Precision Surface Processing and Software Modelling Using Shear-Thickening Polishing Slurries

YUAN CHENG LI

(Tony)

A thesis submitted to the University of Huddersfield
in partial fulfilment for the degree of Doctor of Philosophy

School of Computing and Engineering
The University of Huddersfield

November 2023

(Page left intentionally blank)

*I dedicate this Thesis to my beloved wife
and my wonderful parents.*

(Page left intentionally blank)

Copyright Statement

i. The author of this thesis (including any appendices and/ or schedules to this thesis) owns any copyright in it (the "Copyright") and s/he has given The University of Huddersfield the right to use such Copyright for any administrative, promotional, educational and/or teaching.

ii. Copies of this thesis, either in full or in extracts, may be made only in accordance with the regulations of the University Library. Details of these regulations may be obtained from the Librarian. This page must form part of any such copies made.

iii. The ownership of any patents, designs, trademarks and any and all other intellectual property rights except for the Copyright (the "Intellectual Property Rights") and any reproductions of copyright works, for example graphs and tables ("Reproductions"), which may be described in this thesis, may not be owned by the author and may be owned by third parties. Such Intellectual Property Rights and Reproductions cannot and must not be made available for use without permission of the owner(s) of the relevant Intellectual Property Rights and/or Reproductions.

(Page left intentionally blank)

Acknowledgments

This thesis was only made possible with the help and guidance from numerous patient and generous people around me. Firstly, to my wife – Mikeila, the person who gave me all the necessary encouragements and loving support to carry on, thank you. And to my parents, who sustained me and allowed me to spread my wings halfway across the world, thank you.

Many thanks to Professor David Walker, who mentored me over the course of this journey with his vast knowledge and wisdom. One of the many life lessons that I will always remember from him is "Before we start, let's put the kettle on." Also, many thanks to Dr. Guoyu Yu and Dr. Hongyu Li, who not only had provided continual advice on my research, but they've also given me reception and shown me hospitality.

Countless other colleagues had made an impact on this pilgrimage. Though some more significant than others, their collective influence deserves my utmost gratitude. From the team at the lab: Wang Zhang, Xiao Zheng, Peng Zhang, Xiaolong Li, Xing Su, Lunzhe Wu, Ke Wang, Chenhui An, and Michal Darowski. From the OpTIC Technology Centre: Garry Davies, Rob Evans, and Dale Blackmore. From the University of Huddersfield: Christ Sentence, Helene Pickles, Cathie Raw, Nicola Williams, Chris Dawson, Andrew Longstaff, Rakesh Mishra, and James Williamson. From Sheffield Hallam University: Andrew Alderson. From Innovative Physical Organic Solutions: Olivia Jackson and Rebecca Armitage. From Cannon Instrument Company: Jesse Rameshwaram.

(Page left intentionally blank)

Abstract

Mid-spatial frequency surface error is a known manufacturing defect for aspherical and freeform precision surfaces. These surface ripples decrease imaging contrast and system signal-to-noise ratio. Existing sub-aperture polishing techniques are limited in their abilities to smooth mid-spatial frequency errors. Shear-thickening slurries have been hypothesised to reduce mid-spatial frequency errors on precision optical surfaces by increasing the viscosity at the tool-part interface.

Currently, controlling the generation and mitigating existing mid-spatial frequency surface errors for aspherical and freeform surfaces requires extensive setup and the experience of seasoned workers. This thesis reports on the experimental trials of shear-thickening polishing slurries on glass surfaces. By incorporating shear-thickening slurries with the precessed bonnet technology, the aim is to enhance the ability of the precessions technology in mitigating mid-spatial frequency errors.

The findings could facilitate a more streamlined manufacturing chain for precision optics for the versatile precessions technology from form correction and texture improvement, to MSF mitigation, without needing to rely on other polishing technologies. Such improvement on the existing bonnet polishing would provide a vital steppingstone towards building a fully autonomous manufacturing cell in a market of continual economic growth.

The experiments in this thesis analysed the capabilities of two shear-thickening slurry systems: (1) polyethylene glycol with silica nanoparticle suspension, and (2) water and cornstarch suspension. Both slurry systems demonstrated the ability at mitigating existing surface ripples. Looking at power spectral density graphs, polyethylene glycol slurries reduced the power of the mid-spatial frequencies by ~50% and cornstarch suspension slurries by 60-90%.

Experiments of a novel polishing approach are also reported in this thesis to rotate a precessed bonnet at a predetermined working distance above the workpiece surface. The rapidly rotating tool draws in the shear-thickening slurry through the gap to stiffen the fluid for polishing. This technique demonstrated material removal capabilities using cornstarch suspension slurries at a working distance of 1.0-1.5mm. The volumetric removal rate from this process is ~5% of that of contact bonnet polishing, so this aligns more as a finishing process. This polishing technique was given the term *rheological bonnet finishing*.

The rheological properties of cornstarch suspension slurries were tested using a rheometer and modelled through CFD simulation. Using the empirical rheological data, polishing simulations of the rheological bonnet finishing process were modelled in Ansys to analyse the effects of various input parameters such as working distance, tool headspeed, precess angle, and slurry viscosity.

Table of Contents

Table of Figures

Table of Tables

List of Equations

List of Abbreviations

CFD   Computational fluid dynamics

CMP   Chemical mechanical polishing

CNC   Computer numerical control

CSS   Cornstarch suspension

DNS   Direct numerical simulations

FJP   Fluid jet polishing

HST   Hubble Space Telescope

IBF   Ion beam figuring

IRP   Intelligent Robot Polishers

LES   Large eddy simulations

MR   Magnetorheological

MRF   Magnetorheological finishing

MSF   Mid-spatial frequencies

n-N   Non-Newtonian

NNSP   Non-Newtonian sub-aperture polishing

PEG   Polyethylene glycol

PSD   Power spectral density

PSF   Point spread function

RBF   Rheological bonnet finishing

Re   Reynolds number

RMS   Root mean square

RPM   Revolutions per minute

SCUBA   Submillimetre Common-User Bolometer Array

SST   Shear stress transport

STF   Shear-thickening fluids

TIF   Tool influence function

TPG   Toolpath generator

UDF   User-defined functions

UPMC   Ultra-Precision Machining Centre

VRR   Volumetric removal rate

WD   Working distance

1   Introduction

In the late 19th century, archaeologists unearthed one of the earliest pieces of evidence of optical craftsmanship. This artefact, named the Nimrud lens, is a small piece of a finely polished convex lens dating back to as early as 750B.C. (Layard, 1853; British Museum, n.d.). Archaeologists reason that it would have been of "little to no practical application" as its optical quality was so poor (BBC News, 1999; Discovery Channel Staff, 1999). Although the Nimrud lens most likely served only as decoration, the skilled craftsmanship of this refined, polished, and transparent quartz could still be seen nonetheless.
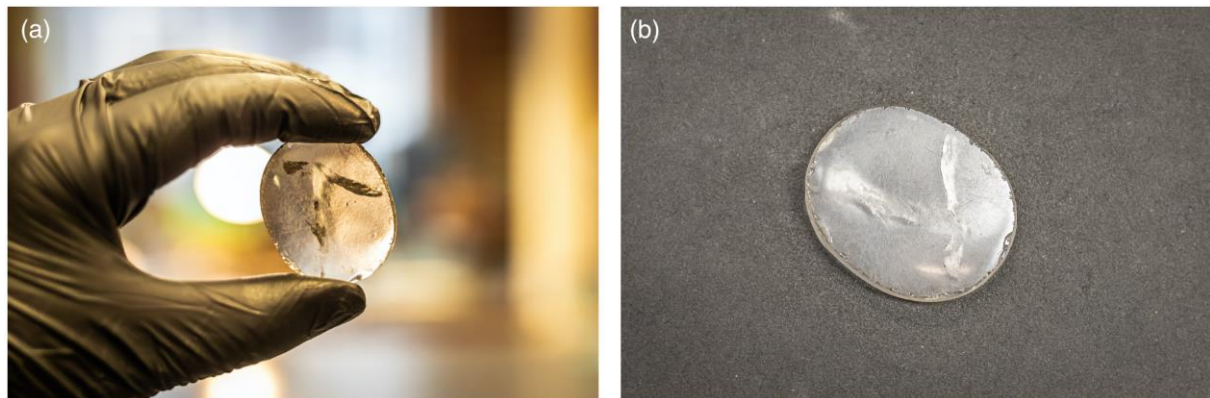
Figure 1-1 The Nimrud lens. (Pictures taken by author at the British Museum)

From ancient Mesopotamia to the modern 21st century, optics had been constantly evolving as the study of the propagation, generation, and detection of visible light. During the recent decades as a result of accelerated technological advancement, new disciplines have branched out of optics, and consequently, new terms have come into use: quantum optics, light-wave technology, electro-optics, optoelectronics, etc. (Saleh & Teich, 2007).

One of the largest fields that emerged was photonics, which arose to represent all fields that utilises photons as the alternative to electrons. While the term *optics* was derived from the Greek term *optikôs*, meaning everything that is visible, the term *photonics* was derived from the Greek term *phôs*, meaning everything that has to do with light (Hoad, 2004a & 2004b). Professor Nikolay Zheludev from the University of Southampton remarked, "In my view, this implies that optics is a much narrower term than photonics. In fact, photonics embraces optics." (Bedrock, 2008). Although complete agreement on the precise usage of these term is somewhat trivial, there is a general consensus regarding their meanings. It is worth noting here that the sources used in *Driving Forward – The Global Photonics Market* and *Defining the Problem –* hold the view that optics is a sub-branch of photonics. However, for the rest of this thesis, "optics*"* is used as the all-encompassing term for the world of light, vision, and photons, which thereupon includes photonics.

1.1 Recent Advancement in Optical Manufacturing

Optical manufacturing had come a long way since the Nimrud lens. Traditionally, the production and measurement of complex aspherical and freeform precision optical surfaces would often be a time-consuming, trial-and-error process done by the hands of a seasoned worker (Jones, 1977). Each step on the process chain would generally require a trained technician, elaborate setup procedures, and highly customised machineries and tooling (Thomas, 2018).

A breakthrough in manufacturing precision optical components was made by Robert A. Jones in 1977. Through computer modelling and using pre-existing experimental data, Jones developed machines to accomplish precise grinding and polishing operations, shown in Figure 1-2 (Jones, 1978). He termed this technology *computer-controlled polishing*. Jones' technology thus paved the way for various innovative techniques using machineries more broadly known as *computer numerical control* (CNC) machines. The advancement of CNC technology over the decades since had three main targets of improvement:

    i.   Lower tooling and process cost;

    ii.   Higher material removal predictability;

    iii.   Greater embedded process control intelligence (D. Kim & S. Kim, 2005).
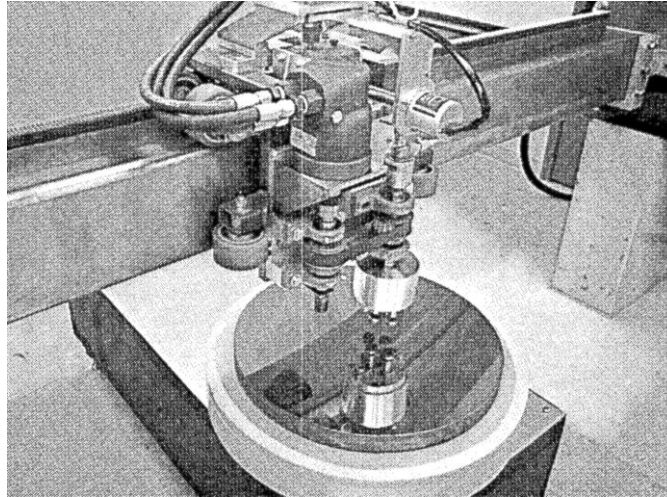
Figure 1-2 The computer-controlled polisher head (Jones, 1977).

The theoretical basis for estimating the polishing removal rates used by most of the CNC processes today can be approximated by the Preston equation (1-1). This empirical equation is very versatile due to the presence of the Preston coefficient, which is dependent on the nature of the process and could be a function of a variety of factors, such as temperature and material. Runnels & Eyman optimised the Preston coefficient by analysing the fluid dynamic pressure (1994). Sundararajan et al. incorporated into the Preston coefficient the formation of a thin lubricating film between the workpiece and tool during wafer planarization (1999).

Kordonski et al. corrected the Preston coefficient during MRF processes due to Bingham flow phenomenon (1998). Téllez-Arriaga et al. integrated into the Preston coefficient the effects of tool friction on the workpiece surface during low traveling speeds (2007).

$$\Delta h(x, y) = k \cdot v(x, y) \cdot p(x, y)$$

<div align="right">(1-1)</div>

Where, $\Delta h(x, y)$ is the material removal rate at point (x, y) on the surface;

$v(x, y)$ is the instantaneous difference in velocity between the tool and the surface;

$p(x, y)$ is the pressure exerted by the polishing tool on the surface;

k is the Preston coefficient, dependent on factors such as temperature and material.

Through the Preston equation, the relationship between the pressure and velocity of the tool, and the removal rate could be simplified. Many CNC technologies today rely on the Preston equation to generate and optimise a dwell-time map for polishing complex surfaces, some of which are introduced in *chapter 2* (Li, 2012). However, the experimental results could differ from the predicted results by the equation (Small & Hoskin, 1986; Cordero-Dávila et al., 2006). Therefore, the equation could only serve as an approximation.

1.2   The Freeform Revolution

An optical system may contain one or more components. Such components could be separated into three general groups: spherical, aspherical, and freeform. Spherical components maintain a constant radius of curvature throughout the optical surface and are essentially a segment taken out of a perfect sphere.

Aspherical and freeform components possess surfaces with a varying radius of curvature. An aspherical component could be described by mathematical means, such as a conic section of revolution (Zheng, 2017). Therefore, aspherical surfaces could be described with at least one axis of rotational symmetry regardless of whether that axis is within or beyond the component boundary. One of the advantages of aspherical surfaces over the traditional spherical counterpart is the correction of spherical aberration, shown in Figure 1-3.

Freeform surfaces do not have any axis of rotational symmetry (Fang et al., 2013). They can fulfil tasks which traditional optics with spherical and aspherical components cannot (Ohl et al., 2004). They had enabled optical systems that were smaller, lighter, simpler, or previously considered unrealistic (Walker, 2019). As technology progressed across the turn of the millennium with the popularisation of CNC processing, the intricacy and performance requirements for optical systems also progressed alongside. The beginning of the 21st century saw the optical research field undergo a much-anticipated transition informally known by some as the *freeform revolution*.
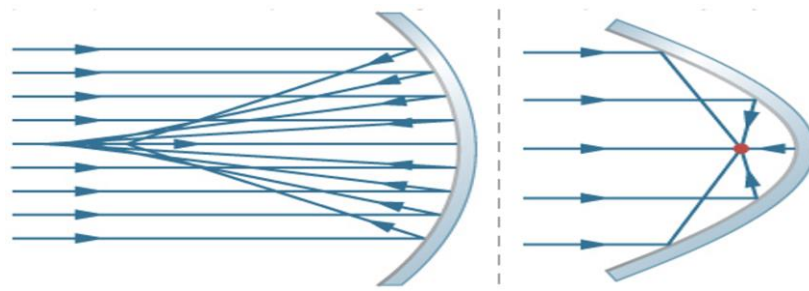
Figure 1-3 Surfaces reflecting incoming parallel light: a spherical surface produces varying focal points (left), and a parabolic asphere focusing onto a single diffraction-limited focal point (right).

The first successful commercialised application of freeform optics was often given to the Polaroid SX-70 single-lens reflex camera in 1972, shown in Figure 1-4. Two freeform lenses in its system made this camera capable of providing well corrected aberrations for its foldable design and off-axis viewing features (Plummer, 1982).

Figure 1-4 The Polaroid SX-70 Single Lens Reflex camera (Plummer, 1982).

Since the success of the Polaroid SX-70, freeform optics had unlocked doors to numerous innovations. Dowski & Cathey incorporated freeform phase plates in microscopes to improve the depth of field through hybrid imaging systems (1995). Drexel University demonstrated a freeform driver-side mirror, shown in Figure 1-5, which was capable of rendering a field of view up to 45° to cover the blind spot with minimal distortion (Hicks, 2008). The second Submillimetre Common-User Bolometer Array (SCUBA) instrument, an integral part of the James Clerk Maxwell Telescope situated in Hawaii, utilised nine aluminium freeform mirrors to inspect large areas of sky up to 1000 times faster than the original SCUBA system. As well, the freeform mirrors provided the SCUBA-2 with a much larger field of view and sky-to-background noise tolerance when compared with the original SCUBA unit (Saunders et al., 2005; Atad-Ettedgui et al., 2006).
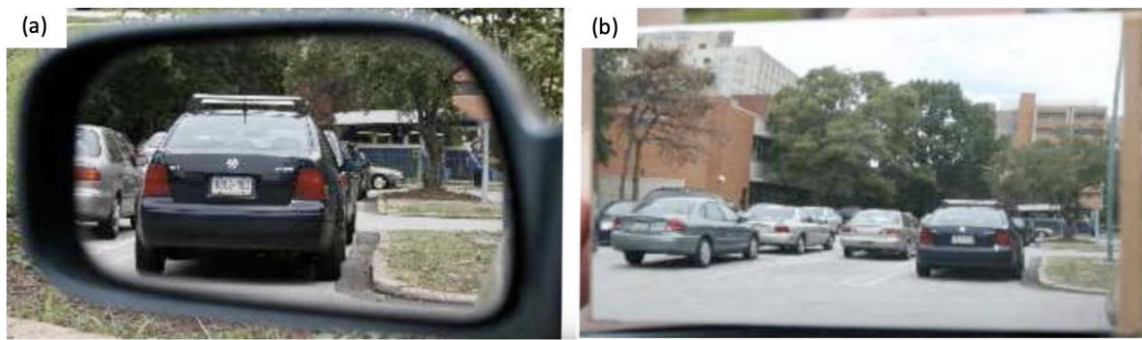
Figure 1-5 Comparison between a conventional flat mirror (a) to a freeform mirror (b) from the same viewing point (Hicks, 2008).

Freeform surfaces had also made an impact in non-imaging applications (Fournier & Rolland, 2008). For example, freeform concentrators for solar energy panels had been devised to accept larger angle of incident light, thus making tracking no longer necessary for solar panels to maintain small incident angles (Winston et al., 2005; Garcia-Botella, Fernandez-Balbuena, & Bernabeu, 2006). Freeform lenses were used to redirect light from LED traffic signals in deterministic ways to ensure a prescribed luminance distribution across the road surface and improve the overall safety of road transportation, as illustrated in Figure 1-6. (Sun, Jin, & Cen, 2009; Feng, Luo, & Han, 2010).
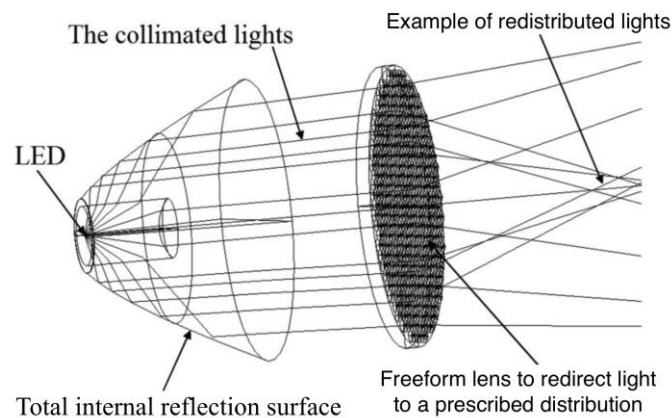
Figure 1-6 Schematic of a freeform lens distributing LED lights (Sun, Jun, & Cen, 2009).

In general, the advantages of employing freeform optics over traditional rotationally symmetrical components include:

- Simplified system structure by reducing part number, mass, cost, and package size (Gregory, Olsen, & Fournier, 2014);
- Increased degrees of freedom of manufacturable surfaces providing optical designers with more flexibility to innovate and scope for novelty (Jiang, Scott, & Whitehouse, 2007);

- Enhanced overall optical performances otherwise impossible to achieve, such as simultaneously correct aberrations, increase depth of field, and expanding field of vision (Saunders et al., 2005; Atad-Ettedgui et al., 2006).

1.3   Driving Forward – The Global Photonics Market

Throughout much of the 20th century, engineering industries such as automotive, electronics, and robotics experienced tremendous growth stimulated by military conflicts and the onset of globalisation. When compared to these industry giants, optical manufacturing still relied much on the seasoned experience of labouring workers. The introduction of CNC polishing technologies in the late 20th century provided a vital lifeline that saw optics come out of the previous developmental infancy.

Surveys on the global photonics market made in recent years suggest the industry holds potential for substantial market growth (Photonics Leadership Group, 2015; Photonics21, 2018; Photonics21, 2021). The photonics industry grew from €228 billion in 2005 to €690 billion in 2019 and is projected to reach €900 billion by 2025, illustrated in Figure 1-7. The current compound annual growth rate of 7% was even higher than the entire Chinese industry, which was estimated at 6%. The UK alone contributed around €15.5 billion to the photonics market in 2019. This was made possible by 1500 companies and 70,040 employees devoted to the photonics market, and these numbers were comparable to the thriving pharmaceutical industry.
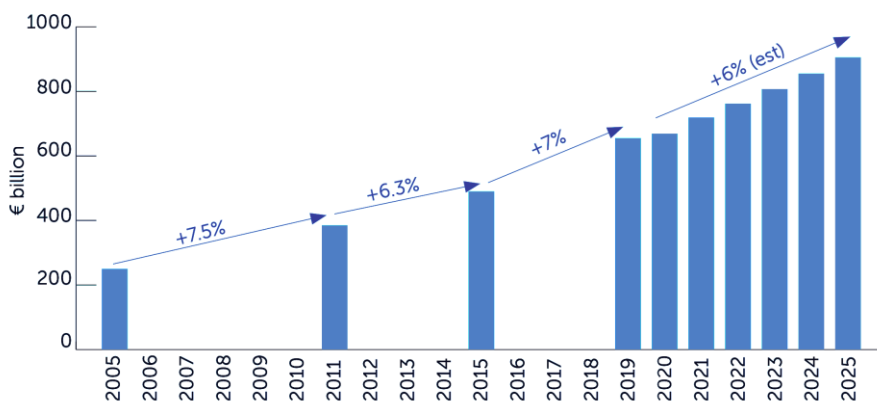
Figure 1-7 Graph of the global photonics market value and projected growth (Photonics21, 2021).

The advancement in photonics enabled competitiveness throughout various related industries such as semiconductors, touch screen displays, lasers, and cameras, leading to greater employment rate, GDP, and exports. Over the years, photonics had been addressing key societal challenges such as generating greener energy, improving energy efficiency, and combating climate change. Furthermore, photonics had been

revolutionary in the detection of counterfeit goods, which were estimated to cost businesses yearly around £3.5 billion in the UK (Monaghan, 2017).

1.4 Defining the Problem – Shrinking Availability of Skilled Workers

Although the optics industry is growing faster than the overall economy, reports suggested that one-fifth of experienced technicians and engineers are approaching retirement (Thomas, 2018; Phtonics21, 2021). The market is pushing optical manufacturing to be faster, cheaper, more precise, and more complex. However, the increasing demand for skilled workers could not be met. In the United States, 75% of skilled optics technician positions were left unfilled annually, and in another survey conducted in Germany of 1700 companies, 75% reported that the lack of skilled workers hindered their innovative activities (Thomas, 2018).

Therefore, the overall direction of prospective research and development emphasises on total process optimisation. This is a long-term vision and a collaborative advancement paralleling tooling, robotics, metrology, engineering, and mathematical techniques, to create and eventually incorporate fully autonomous manufacturing cells for the production of ultra-precision optical components with complex surfaces (Walker & Yu, 2016). This outlook falls in line with the German concept of *smart factories* and the computerisation of manufacturing known as *Industrie 4.0* – the fourth industrial revolution, summarised in Table 1-1 (Maier, 2017).

Table 1-1 Summary of the industrial revolutions.

Revolution	Year	Information
1	~ 1784	Steam, water, mechanical production equipment
2	~ 1870	Division of labour, electricity, mass production
3	~ 1969	Electronics, IT, automated production
4	?	Networks, smart factories, cyber-physical systems

1.5 Identifying an Obstacle – Mid Spatial Frequency Errors

The transition from a predominately hands-on process for manufacturing precision optics of the past, to fully autonomous manufacturing cells of the future is still ongoing. Its path is crowded with problems that need to be solved. Throughout the optical manufacturing chain, a variety of factors such as component material, tool selections, machine speeds, vibrations, and measurement errors could all contribute to irregularities, or errors, on the component surface (Tabenkin, 1999). Surface errors could be corrected along each process on the manufacturing chain, progressively decreasing in amplitude, and ultimately producing a finished surface within specified tolerances. These surface irregularities were given the term *spatial frequencies*.

The irregularity on a surface is a composition of a continuous spectrum of spatial frequencies (Youngworth & Stone, 2000). On optical surfaces, the spatial wavelengths of interest could span from metres for large optics to nanometres (Forbes, 2015). Although there are no distinct boundaries, this continuous spectrum is often decomposed into three regimes for the convenience in classification, analysis, and treatment of the surface errors: high, mid, and low spatial frequencies.

1.5.1   High-Spatial Frequency – Texture

High-spatial frequency, conventionally known as surface *texture* or *finish*, describes the roughness of the surface. The surface texture of a component depends chiefly on the interactions between the abrasive particles used and the microscopic structure of the component surface during grinding and polishing procedures. During processing, each individual abrasive granule leaves its signature on the component surface in relation to its size, shape, and chemistry. With each passing of the grinding or polishing tool, the abrasive particles combine to effectively form millions of tiny cutting tools, each leaving its mark on the surface (Tabenkin, 1999). Prominent high-spatial frequencies could result in overall energy loss of the system, illustrated in Figure 1-8.
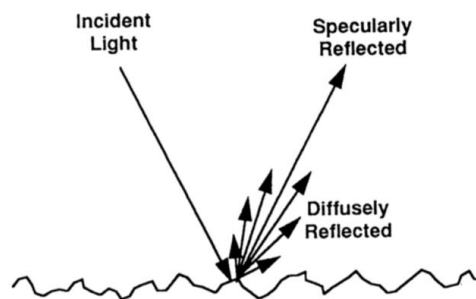
Figure 1-8 Surface roughness resulting in system energy loss through scattering (Harvey & Thompson, 1995).

Roughness on optical surfaces scatter some of the reflected light away from the desired direction, causing the loss of overall energy within the system. This phenomenon, knows as wide-angle scattering, tends to produce a veiling glare in optical imaging systems, which reduces image contrast as well as the signal-to-noise ratio (Harvey & Thompson, 1995). To combat the prominence of high-spatial frequencies, an optimal smoothness could be achieved with the aid of smaller, softer abrasive particles, with the trade-off being a decrease in material removal rate and longer processing time. Surfaces low in high-spatial frequency errors, or super-smooth surfaces, are needed in short-wavelength applications such as x-ray optics and laser gyros (Henking et al., 1995; Yang et al., 2017; Zhang et al., 2018).

1.5.2 Low-Spatial Frequency – Form

On the opposite end of the spectrum, low-spatial frequency characterises the overall curvatures of the component surface, commonly known as *form* or *figure*. This alludes to the incorporation of terms such as astigmatism and coma. Any deviation from the desired form for a component would result in low-spatial frequency errors. Such deviations are customarily described using Zernike polynomials. The Zernike polynomials are a set of mathematical descriptions pioneered by Frits Zernike in 1934, shown by Equation (1-2) and in Figure 1-9 (Zernike & Stratton, 1934).

$$W(\rho, \theta) = \sum_{i=1}^{n} a_i Z_i(\rho, \theta)$$

<div align="right">(1-2)</div>
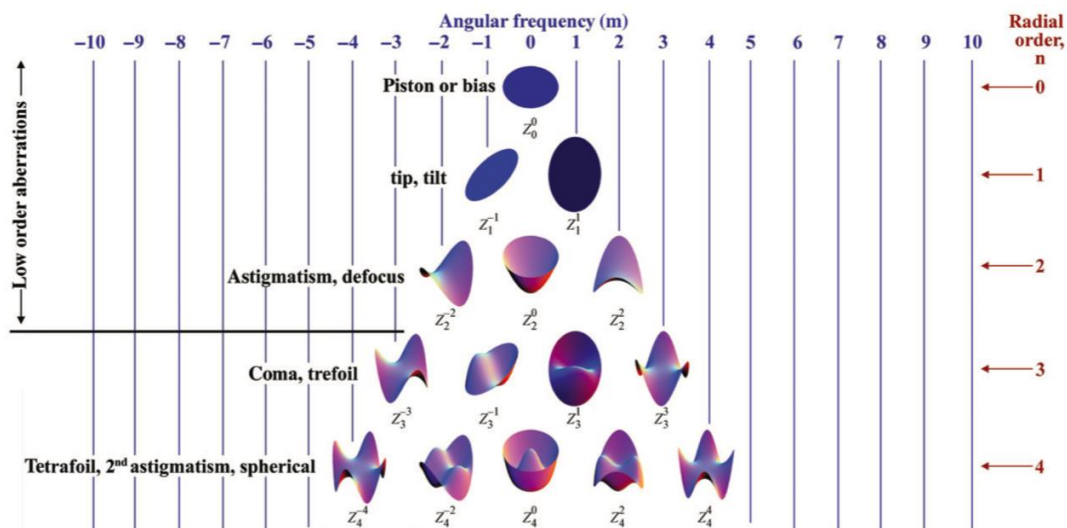
Figure 1-9 Surface plots of Zernike polynomials up to the 4th order (Lakshminarayanan & Fleck, 2011).

Each element in the polynomial represents a particular mode of surface form error, such that coefficients of greater magnitude represent larger contribution of that particular error mode, and consequently greater negative impact on the optical performance (Lakshminarayanan & Fleck, 2011). The predominant advantage of using Zernike polynomials over other mathematical polynomial sequences is the independency of the individual terms, such that additional terms can be added, or subtracted, from the polynomial without impact on terms already computed.

1.5.3 Mid-Spatial Frequency – Ripples

Unlike high-spatial and low-spatial frequencies, which possess their distinct definitions, mid-spatial frequencies (MSF) are more ambiguous in literature. Although precise boundaries of MSF are nebulous, it is widely understood within the field of optics that MSFs are surface ripples that bridges the gap between form and surface texture (Zheng, 2017). The consensus is that MSFs are spatial frequencies too high to be described by the first 37 Zernike polynomials and spatial frequencies too low to be considered energy loss from surface roughness (Hull et al., 2012; Progler & Wong, 2000; Youngworth & Stone, 2000). Figure 1-10 illustrates a few examples of MSF surface error maps from interferometry.
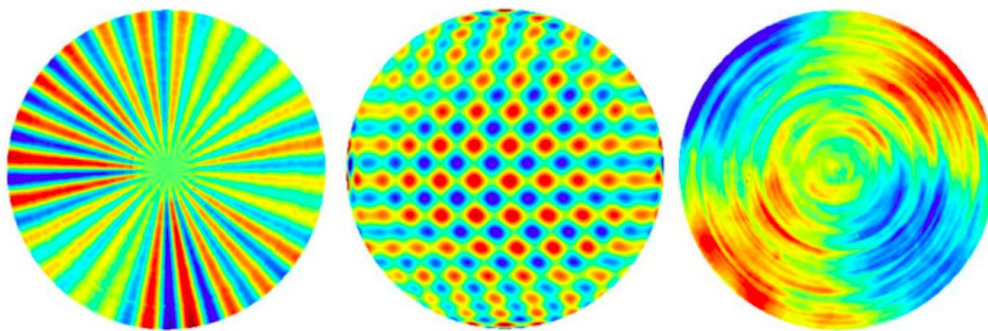
Figure 1-10 Example of azimuthal, Cartesian, and concentric MSF errors (Hosseinimakarem, Davies, & Evans, 2016).

It has become increasingly apparent that simply achieving the desired form and roughness specifications are no longer adequate in precision optics. Form and roughness values describe only the low-spatial and high-spatial frequencies. As modern applications demand tighter surface specifications, MSF errors should also be managed with care.

1.5.4 Effects of Mid-Spatial Frequency Errors on Optical Performance

An ideally smooth optical surface reflects all incoming light with equal angles of incidence and reflection about the local normal. Realistically, the reflection of light, even on a near perfect optical surface, would consist of such specularly reflected component, along with diffusely reflected or diffracted components due to surface imperfections (Harvey & Thompson, 1995). The performance of an optical surface, and the effects of said scattering from surface imperfections, is oftentimes expressed through the *point spread functions (PSF)*. PSF describes the response of an optical system to a point source, and this relationship is shown in Figure 1-11.
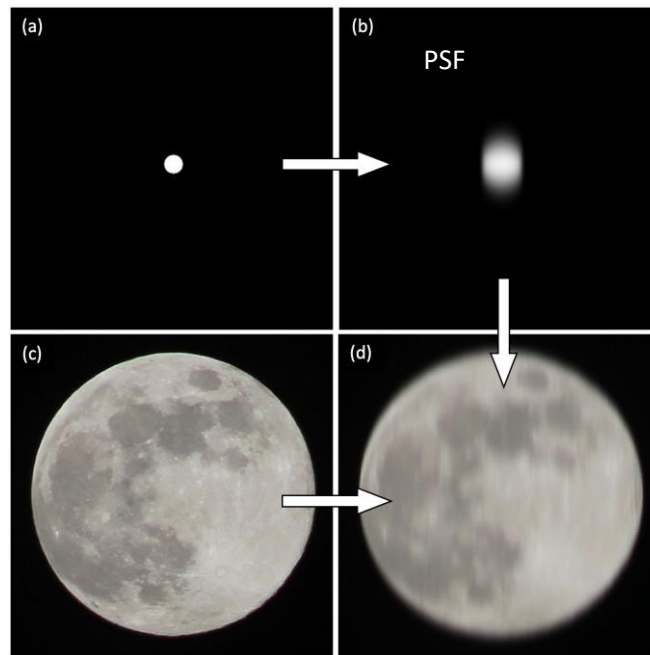
Figure 1-11 (a) A perfect point source. (b) Example PSF of a particular optical imaging system. (c) Ideal image of the moon. (d) Image of the moon seen through the optical imagining system with the PSF. (Pictures by author).

MSF errors tend to produce small angle scattering that decreases resolution by generating image blur (Harvey & Thompson, 1995). Therefore, MSF errors have shown to produce effects that combine the extremities of low and high spatial errors (Parks, 1983; Youngworth & Stone, 2000). Traditional requirements of optical surfaces with form and texture specifications have all too often proved to be inadequate. Therefore, MSF artefacts and its effects on the performance cannot be overlooked. Such optical systems, although satisfying both form and texture specifications, often produced subpar performances (Parks, 2008). A famous example was the primary mirror in the Hubble Space Telescope (HST). Although the HST primary mirror had some form errors, it also exhibits noticeable MSF artefacts, shown in Figure 1-12 (Allen, 1990; Cohen, 2004).

Figure 1-12 MSF features of around 9nm RMS exhibited on the surface map of the HST primary mirror (Cohen & Hull, 2004).

A computer simulation comparing the PSF of the HST primary mirror with and without the 9nm RMS MSF features were made to analyse the effects of the MSF, shown in Figure 1-13. As can be seen, the presence of MSF proved to have an adverse impact on its imaging abilities, causing the mirror to underperform its expectations.
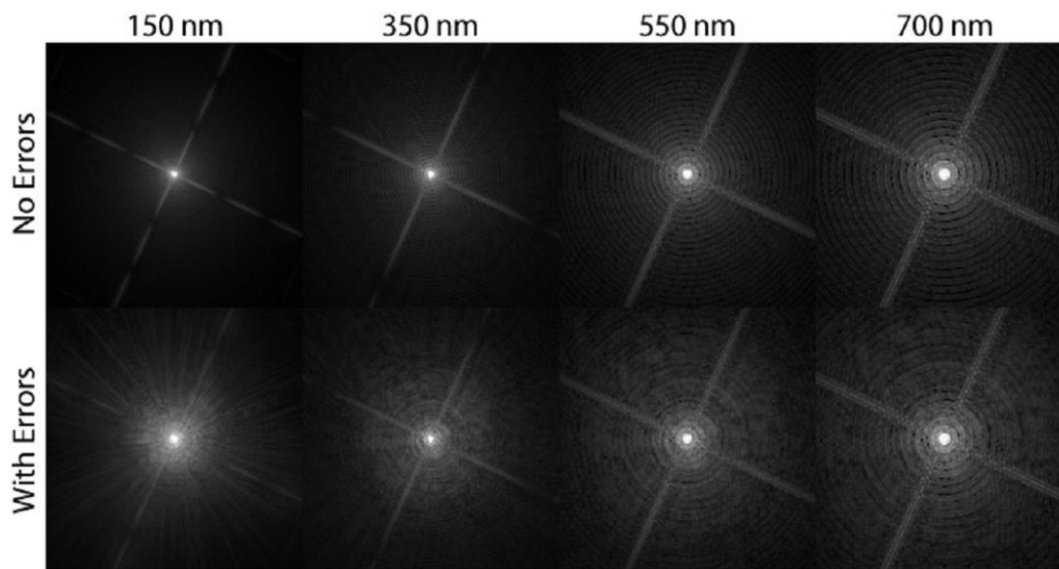
Figure 1-13 Computer simulation of PSF responses of the primary mirror of the Hubble Space Telescope with and without the 9nm RMS MSF errors, with the wavelengths of light expressed across the top (Hull et al., 2012).

In conclusion, the presence of surface spatial errors creates scattering of light that reduces the optical throughput and causes a loss of contrast. It is worth noting here that apart from the negative influences of MSF on optical imaging performances, the presence of MSF also greatly reduces customer appreciation and the potential value of the system, as the human eyes is sometimes capable of detecting MSF artefacts (Zheng, 2017).

1.5.5   Detecting Mid-Spatial Frequencies with Power Spectral Density Functions

The spectral distribution of different spatial frequencies could be represented by *power spectral density* (PSD) functions. Obtained from Fourier transformations, the PSD is a mathematical description that quantifies the distribution of frequencies of a signal's power, with "power" being the square of the amplitude (Youngworth, Gallagher, & Stamper, 2005). Figure 1-14 illustrates an example of a typical logarithmic PSD plot. If a measured component surface had a specific spatial frequency error, its PSD plot would contain a distinct peak of power at the corresponding frequency.
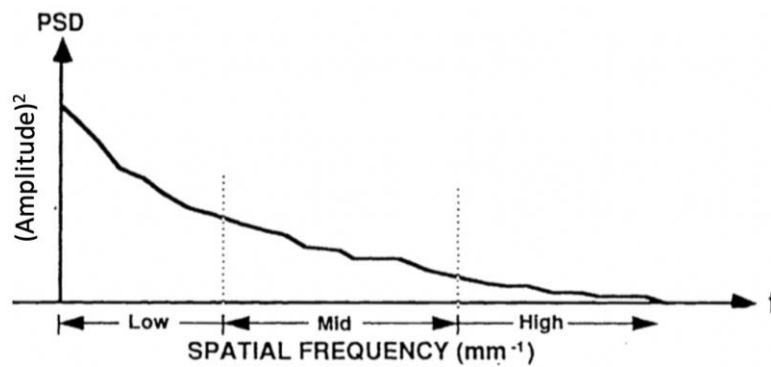
Figure 1-14 Example of a PSD plot, showing distribution of spatial frequencies (Harvey & Thompson, 1995).

While a comprehensive PSD plot covers frequencies over several order of magnitude, generating such data usually demands a variety of metrology instruments ranging from interferometer, to phase measuring microscopes, to atomic force microscopes (Hull, 2012). As the sensitivity of individual metrology instruments only extends across approximately three orders of magnitude of frequencies at best, no one type of instrument is sufficient to analyse the entire spatial frequency profile of a surface. The PSD reaches zero when the spatial frequencies increase beyond the accuracy of the metrology instrument.

1.6 Objective of the Thesis

The objective of this thesis is to examine a new way to mitigate MSF surface errors through physical experiments and software modelling. The research is a proof-of-concept for new proposed polishing media, namely shear-thickening fluids, which was hypothesised to improve process speed and MSF mitigation (introduced in *section 2.6*). In doing so, this research has the potential of filling in a vital piece of the jigsaw and taking another step towards fully autonomous manufacturing cells.

1.7 Geographic Locations

The project has been conducted throughout under the supervision of the primary supervisor – Professor David Walker. This research – with Professor Walker and his group – was based at the OpTIC Centre in North Wales during 2017 and 2018, as shown in Figure 1-15(a). The laboratory relocated to new facilities in the TechSpace One building at the STFC Daresbury Science and Innovation Campus in 2019, shown in Figure 1-15(b).

The move of the group in January 2019 corresponded with the expiry of Huddersfield's lease at OpTIC and was part of a strategic plan to foster strategic links with STFC. The negotiations on leaving OpTIC proved unexpectedly problematic. Under the final settlement, OpTIC retained key metrology equipment required for the work of this thesis (particularly the scanning Profilometer), in exchange for releasing the Zeeko IRP600

machine which was also required. The group decommissioned and packed the equipment at OpTIC in early January 2019, and it then went into temporary storage pending final negotiation of the Daresbury lease, and subsequent fit-out of the new lab. Recommissioning then started at Daresbury in August 2019. The IRP 600 itself was then refurbished by Zeeko Ltd. (funded by the University) to overcome known issues at the beginning of 2020.

Figure 1-15 (a) The OpTIC Centre and (b) TechSpace One.

1.8 Outline of the Thesis

Chapter 1 – Brief introduction of the history of optical manufacturing, the current global market, the drive for fully autonomous manufacturing cells, and the known issue of mid-spatial frequency errors.

Chapter 2 – Overview of the generation and mitigation of mid-spatial frequency errors with respect of current manufacturing techniques; and overview of the definition, classifications, and mechanisms of non-Newtonian materials, as well as a review of prior-art in shear-thickening polishing.

Chapter 3 – Influence function and mid-spatial frequency mitigation experiments using polyethylene glycol-based slurries, as well as the rheological properties of polyethylene glycol-based slurries.

Chapter 4 – Influence function and mid-spatial frequency mitigation experiments using cornstarch suspension slurries.

Chapter 5 – Rheology of cornstarch suspension slurries and using computational fluid dynamics modelling to define material properties.

Chapter 6 – Preliminary experiments with non-contact precess bonnet and shear-thickening slurries in a process termed rheological bonnet finishing, and subsequent computational fluid dynamics modelling of the rheological bonnet finishing process with varying complexity and setup parameters.

Chapter 7 – Conclusions from the experiments and modelling and presenting future work.

2 Mid-Spatial Frequency and Non-Newtonian Polishing

Mid-spatial frequency (MSF) errors are a worldwide challenge in producing complex aspherical and freeform surfaces in the ultra-precision industry. These defects produce undesirable patterns on optical surfaces that cause noise in the system, interfere with oncoming wavefront, and scatter light (Harvey & Thompson, 1995; Parks, 1983; Youngworth & Stone, 2000). An overview of existing optical manufacturing techniques is given in this chapter with regards to their respective abilities to mitigate MSF ripples.

One method to control MSF errors was to adjust slurry mechanics and chemistry at the tool-workpiece interface (Golini, 2004). Non-Newtonian fluids had been incorporated into optical manufacturing techniques, and it was hypothesised that they could aid in MSF mitigation (Li et al, 2015; Walker & Yu, 2016). A brief introduction on non-Newtonian fluids is given, before a brief overview of non-Newtonian polishing prior-art.

2.1 Generation of Mid-Spatial Frequency Artefacts

There are two main groups of tools used in optical manufacturing: rigid and conformal. Both comes with their respective advantages and disadvantages. The optimal type of tooling to use would be largely dependent on the type of surfaces. For flat and spherical surfaces, MSF is relatively easy to control and mitigate when compared to aspheres and freeforms. For these surfaces with constant radius of curvature, a rigid tool with inversely matching curvature would be able to maintain intimate contact with the component across the entire surface. Rigid tools provide greater polishing efficiency than that of conformal tools.

Problems arise when processing aspherical and freeform surfaces. A rigid tool would not be capable of matching the changing curvature of an asphere or freeform component as it travels across the surface, and a phenomenon known as translational tool-shape misfit occurs, illustrated in Figure 2-1. Another mode of misfit is known as rotational tool-shape misfit. A cylindrical rigid tool on a mating cylindrical part would be able to maintain full contact with the component across the entire surface. The misfit would arise when the tool is subjected to rotation.
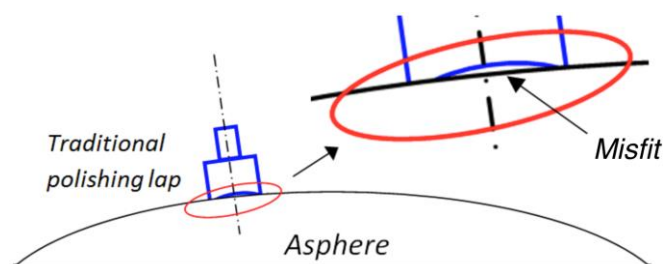
Figure 2-1 Tool-shape misfit between a rigid polishing tool and an aspherical component (Li, 2012).

Thus, for non-spherical components, any given rotating rigid tool would only be sufficient to make intimate contact in one small zone only. Imperfect contact between the tool and the component surface introduces fluctuating pressure regions that leads to zonal errors (Li, 2012). This misfit of curvature is one of the mechanisms for MSF generation.

In some respects, processing of near-spherical surfaces could often be best estimated by the amount of departure from a best-fit sphere (Blalock, Medicus, & Nelson, 2015). There is a rule-of-thumb, which suggests that a small amount of misfit could be overcome by rigid tools, as long as the abrasive particle size was larger than the perceived misfit between the tool and the surface. This criterion implies the abrasive particles would be large enough to bridge the gap between the tool and the surface, creating cushioning. So far, experiments have indicated that this rule-of-thumb between grit size, misfit, and MSF holds validity (Messelink, 2016; Walker et al., 2017, Yu et al., 2019).

Conformal tooling provides greater versatility and adaptability than rigid tools. Illustrated in Figure 2-2, they are capable of polishing aspherical and freeform surfaces without tool-shape misfit, especially sub-aperture conformal tools. Although these tools avoid any MSF generation from misfit, they tend to initiate MSF through another mechanism.
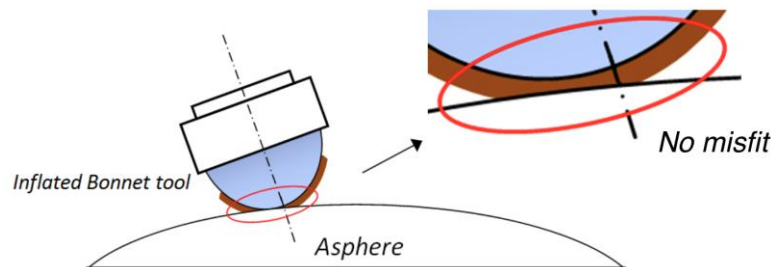
Figure 2-2 Intimate contact between a sub-aperture conformal tool and the component surface (Li, 2012).

The *tool influence function* (TIF) of a particular tool describes the imprint that the tool makes on the workpiece under specific polishing parameters. Due to the nature of conformal tools, their TIFs often resemble a near-Gaussian profile. Referring to Figure 2-3, during polishing processes, the stacking of these TIFs is prone to generate MSF through a "cusping" effect (Li, 2012). The initiation of MSF caused by the stacking of TIFs is extremely sensitive to track spacing. Illustrated in Figure 2-4, processes with track spacing too large could generate such MSF, though the depth of these ripples is shallower (<10μm) when compared to that of the MSF generated from tool-shape misfit (>10μm). However, it is accepted in the field that such generation of MSF can be circumvented when the ratio between the track spacing and TIF width is less than 0.1 (Li, 2012).
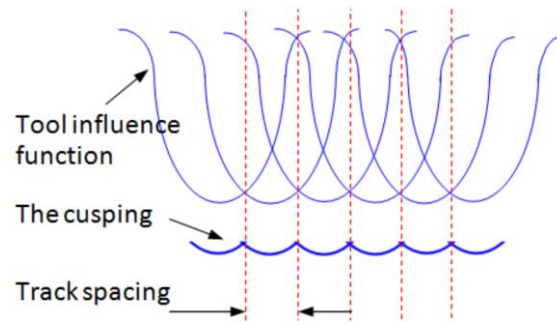
Figure 2-3 The cusping effect of stacked tool tracks (Li, 2012).
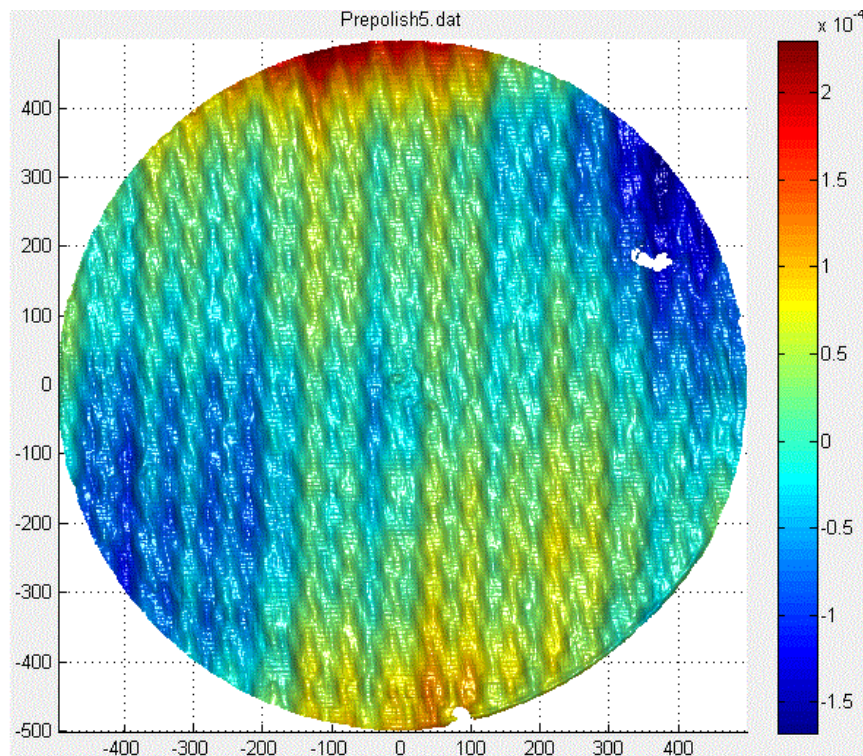
Figure 2-4 MSF ripples created from overlapping of toolpaths (Picture by author).

2.2   Mitigation of Mid-Spatial Frequency Errors Using Rigid Tools

Compared to conformal tools, rigid tools are more capable of mitigating existing MSF surface errors. They smooth down the ripples from the peaks, as illustrated in Figure 2-5. Larger smoothing tools enhance process efficiency and are also capable of smoothing surfaces with peaks further apart. However, with the requirements for more aspherical and freeform surfaces, increasing the tool size comes at the expense of creating greater tool-shape misfit.
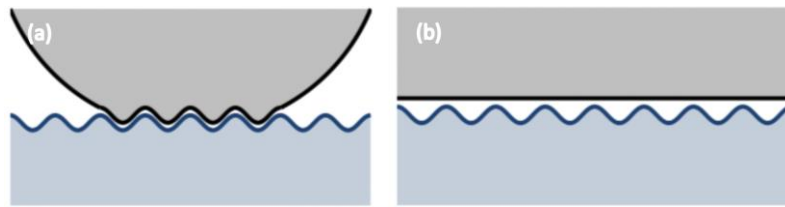
Figure 2-5 (a) The inability for conformal tools to rectify MSF features. (b) The ability for a rigid tool to smooth away the peaks of MSF ripples (Messelink, 2016).

2.2.1 Traditional Lapping Processes

For the majority of optical fabrication history, lapping was the main technique used to process optical surfaces. Lapping takes two surfaces and grinds material away through means of microscopic cutting mechanisms provided by interspersed loose abrasive grains between the surfaces (Marinescu, Uhlmann, & Doi, 2007). This is in contrast with grinding procedures in which the abrasives are fixed in the tool.

The earliest evidence of lapping may be attributed to the stone age, when sticks were used to work away a stone workpiece aided by loose abrasives (Sunanta & Bidanda, 2003). Figure 2-6 illustrates such a setup from archaeologic findings by the Deutsches Museum in Munich. Leonardo da Vinci also drafted lapping machines as a kinematic concept in 1493, shown in Figure 2-7 (da Vinci & Reti, 1974). The sketches from da Vinci served as an inspiration to numerous lapping machines still in use today.

Nearly all materials could be lapped with suitable tools and abrasives: metals, glass, marble, granite, plastics, silicon, germanium, carbon, graphite, gemstones of all kinds, and etc (Marinescu, Uhlmann, & Doi, 2007). One of the most widely used lapping tool in optical polishing is a class of polymer commonly known as pitch. Different types of pitch could be extracted from different sources, such as plants, petroleum, or coal tars. As a result, pitch materials come with an array of diverse properties such as stiffness, softening point, and viscoelastic constants. The earliest utilisation of the pitch lapping could be traced back to Isaac Newton as he attempted to fabricate optical lenses in 1668 (Mills & Turvey, 1979). Figure 2-8 shows a small pitch tool situated on top of an inflatable bonnet.
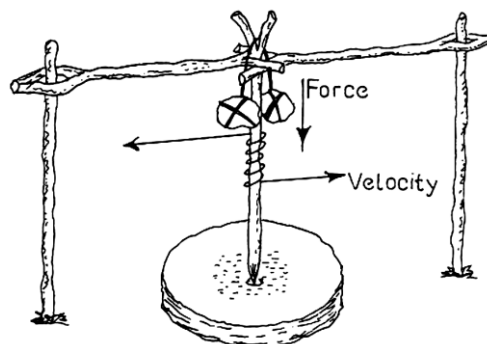
Figure 2-6 Schematic of primitive lapping apparatus from the stone age (Sunanta & Bidanda, 2003).
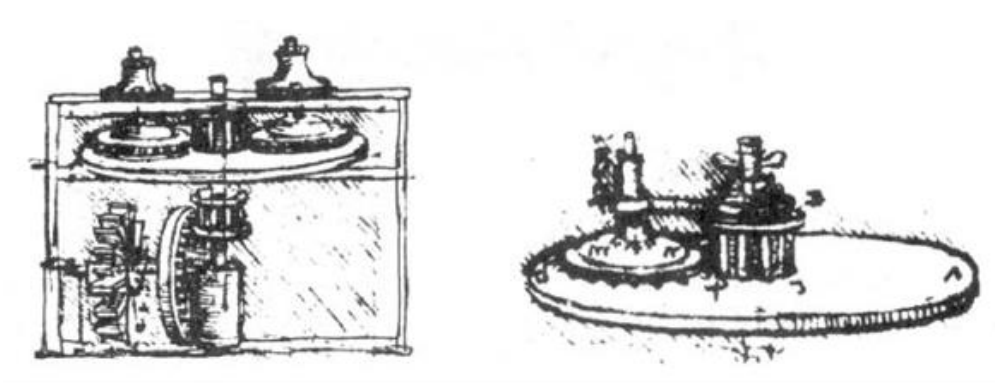
Figure 2-7 Lapping concept by Leonardo da Vinci in 1493 (da Vinci & Reti, 1974).

Figure 2-8 Example of a pitch lapping tool (picture by author).

The main advantage of using pitch is its diversity in the shape of which it could be made. With a low softening point of 55-70°C, pitch could be readily melted down and made into the desired shape. Its low hardness also allows the ease of machining the tool surface to match closely to the surface curvature of the workpiece. However, even with its viscoelastic properties, pitch tools deform much too slowly to overcome surface misfit on non-spherical components (Wang et al., 2016). Its low hardness also means that the volumetric removal rate of pitch tools was lower than that of metal tools by about 2 orders of magnitude (Zheng, 2017). Nonetheless, with ample polishing time, surface texture down to <1 nanometre could be achieved with pitch (Li, 2012; Walker et al., 2012).

Metal lapping tools could be made from a range of alloys such as aluminium, iron, and brass. Figure 2-9 shows a cast iron lapping tool. Such tools are more effective in mitigating MSF than pitch due to their higher volumetric removal rate. The greater hardness of metals ensures the peaks of surface ripples are machined down efficiently with the aid of abrasives such as aluminium oxide and cerium oxide.
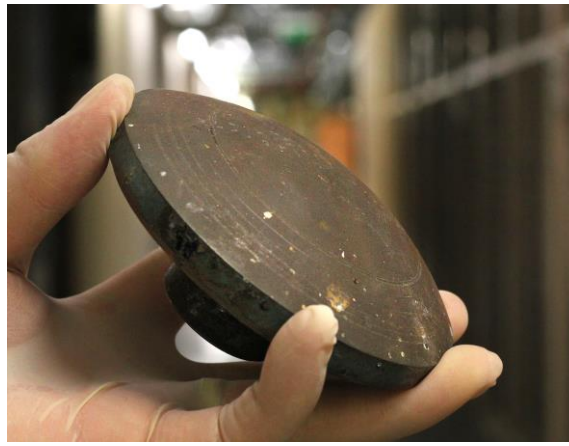
Figure 2-9 Example of a cast iron lapping tool (picture by author).

However, the shortcoming of metal tools includes degrading surface finishing quality. With abrasive particle size ranging from 3μm to 50μm, the texture proceeding metal lapping are around 2 to 3 orders of magnitude worse than that of pitch lapping (Zheng, 2017). The largest disadvantage of metal lapping tools was their incompetence in overcoming surface misfit. Therefore, the usage of metal lapping tools to mitigate MSF was restricted to only spherical and flat surfaces.

2.2.2   Stressed Mirror Polishing

As mentioned before, the main obstacle in rigid tool lapping of aspheric and freeform surfaces is the presence of tool-shape misfit. Stressed mirror polishing bypasses this obstacle through Newton's theory of elasticity. Bernhard Schmidt successfully produced the first Schmidt corrector by methods of elastic deformation at the Hamburg Observatory around 1930 (Lemaître, 1972). It wasn't until 1980 that stressed mirror polishing was trialled by researchers to mitigate MSF during fabricating of non-axisymmetric mirrors (Lubliner & Nelson, 1980; Nelson et al., 1980).

Shown in Figure 2-10, an aspheric or freeform workpiece was stressed through fluid pistons underneath into a spherical form, eliminating any large misfit between the spherical polishing lap and the workpiece. As a result, the surface could be polished as if polishing a spherical part, and based on computer simulations, the workpiece should elastically return to the desired non-spherical form after the forces and moments were released (Mast & Nelson, 1990).

In 1980, this technique was developed and successfully used to polish the parabolic mirror segments of the primary mirror in the Keck Telescope. Through a set of 24 pistons, a traditional spherical pitch lapping tool was able to smooth the mirrors to a form error of around 225nm RMS through stressed mirror polishing (Mast & Nelson, 1980). Since that original manufacturing success, this process had also been successfully applied to produce mirror segments for the European Extremely Large Telescope (McPherson et al., 2012).
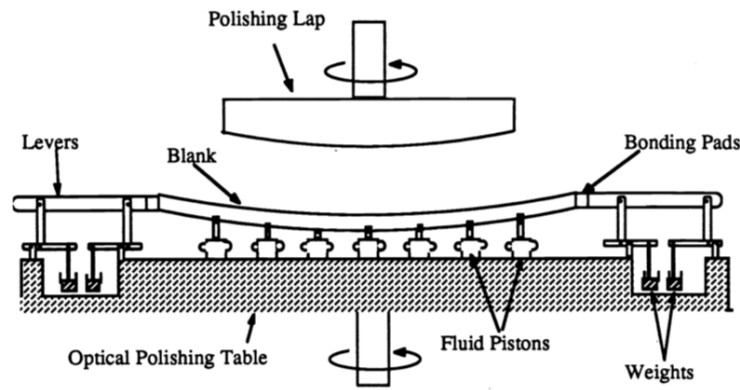
Figure 2-10 Schematic of stressed mirror polishing setup (Mast & Nelson, 1990).

Although stressed mirror polishing worked well in rectifying MSF without tool-shape misfit, the limitations to this process cannot be overlooked. Ductile materials such as some metals and plastics were not suitable for this process due to their lack of inherent material elasticity. As for suitable materials, the shape requirement demanded the thickness of the workpiece to be considerably smaller than its surface area to prevent brittle fractures during stressed polishing. The process was also confined to polish components with relatively simple form specifications, as stressing a component to suit complex form specifications could be difficult.

2.2.3   Stressed Lap Polishing

The Steward Observatory at the University of Arizona innovated the stressed lap polishing technology in the early 1990s (Martin et al., 1990). To mitigate MSF ripples, the researchers bypassed non-spherical tool-shape misfit through real-time alteration of the form of the lapping tool during polishing procedures. The tool was composed of a collection of smaller pitch squares. In contrast to the already developed stressed mirror polishing, this process used computer iterations to influence actuators above the pitch squares in order to modify the shape of the lapping tool in real-time, as shown in Figure 2-11. As the tool travelled across a non-spherical surface, the changing of the tool's form ensured the absence of misfit.

Stressed lap polishing had proved its ability to smooth aspheric figures. It was the core technology employed in the fabrication of the primary mirror in the 25m Gian Magellan Telescope (Martin et al., 2004). Such 8.4m mirror segments possess a 15mm peak-to-valley aspheric departure, and the process produced a surface texture of less than 1nm (Martin et al., 2014). Since then, the Steward Observatory had been improving this technology, and it was utilised again in the manufacturing of the 8.4m primary mirror for the Large Binocular Telescope with an achieved form accuracy of 15nm RMS (Martin et al., 2006).
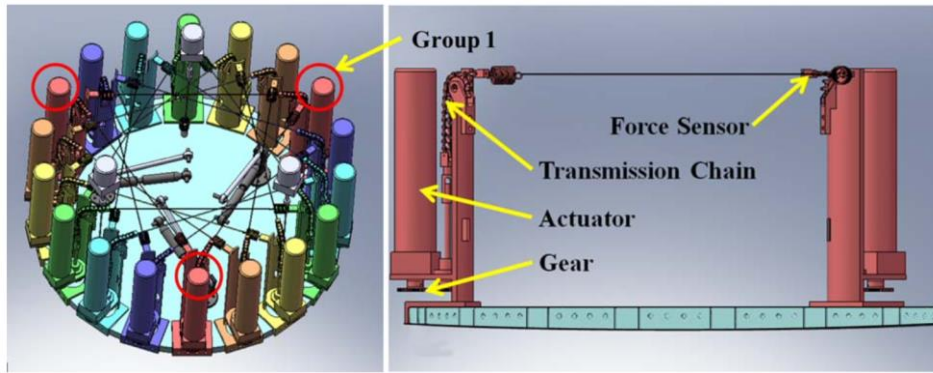
Figure 2-11 Schematic setup of the stressed lap tool (Zhao, 2015).

Over the decades, stressed lap polishing had shown its advantages in large optical component manufacturing in mitigating MSF errors. Nevertheless, due to the complexity of the tool, this technique was not suitable for polishing smaller components, especially parts with steep changes in curvature across the aperture. The construction and maintenance of the tool also proved to be the main drawback for this technology, as it was necessary to design and rebuild a new tool for each specific workpiece (Chen et al., 2010).

2.2.4   Summary of Rigid Tool Polishing

Traditional lapping was mostly performed by the hands of seasoned workers. With decades of experience, they were able to control the pressure and dwell time of the lapping tool on the component surface to ensure effective removal of surface ripples. In the case of tool-shape misfit, they were also able to feel the magnitude of such misfit and adjust accordingly. One of the main limiting factors to machine lapping was the inability to overcome translational and rotational tool-shape misfit. With the market push for autonomous manufacturing, as well as the decrease in number of seasoned technicians, the demand for machine lapping on aspheric and freeform surfaces is expanding (Thomas, 2018).

With the global optics market pushing for aspherical and freeform surfaces, one of the biggest challenges in precision optical manufacturing is the mitigation and prevention of MSF ripples. Although rigid tools have been exceptional in rectifying such surface ripples, their effectiveness were limited to only flat and spherical components.

Novel technologies such as stressed mirror and stressed lap polishing showed capabilities in mitigating MSF errors. These processes avoided non-spherical misfit by altering either the shape of the mirror workpiece or the tool using a matrix of actuators. However, both processes were confined to smoothing only large optics. High cost, demanding maintenances, and complex setup procedures were just few of the deterrence from their manufacturing feasibility. For stressed mirror polishing especially, it requires the workpiece to be thin and elastic.

2.3   Mitigation of Mid-Spatial Frequency Errors Using Conformal Tools

Sub-aperture conformal tools had been utilised in many processes to correct surface form errors that were larger than or similar in size to their contact areas between the tool and the component (Walker et al., 2002; Kordonski, Shorey, & Sekeres, 2003). A key disadvantage of using such conformal tools was their inability to rectify smaller surface errors such as MSF. As those tools adapt to the changing local topography, the peaks and valleys of MSF were polished equally, as seen in Figure 2-5(a).

2.3.1   Precessions Bonnet Polishing

The precessions polishing technology was a novel CNC technique developed in the mid 1990s by University College London. Subsequently, Zeeko Ltd. was founded as a spin out from the research, branding this series of CNC machineries as *Intelligent Robot Polishers* (IRP), depicted in Figure 2-12 (Bingham et al., 2000; Walker et al., 2001). Since its establishment, the IRP series ad been used extensively in innovative research areas, such as ultra-precision surface polishing process for large spec telescope mirrors, as well as commodity production chains (Walker et al., 2006, 2011; Li et al., 2014).

Figure 2-12 Zeeko IRP 400 Polishing Machine (Zeeko LTD., n.d.).

The IRP machines use pressurised rubber bonnets as the polishing tool, and they have the ability to mould around the local topography of the contacting surface, as illustrated previously in Figure 2-2. With the absolute orientation and motion orchestrated by the IRPs' 7-axis CNC system, the IRP machines effectively render the tool "universal" (Walker et al., 2002). The simplicity of the tool was traded for the complexity of the machine to provide a highly versatile system. Suitable polishing cloths, such as polyurethane, could be adhered onto the bonnet, and the polishing work is done via rapidly rotating the tool about its axis with the presence of abrasive slurries.

During polishing, the entire tool is subjected to a precess angle, hence the name *Precessions^TM polishing*. Shown in Figure 2-13, the overriding advantage of precessing the tool to an angle is the distribution of the material removal. As the bonnet rapidly rotates about its axis, the velocity at the centre of the bonnet is effectively zero. A pole-down polishing process leaves a tool influence function (TIF) with centre having zero removal, while a precessed bonnet has the ability to produce a near-Gaussian TIF with no sharp discontinuities (Walker et al., 2001, 2003, 2006).
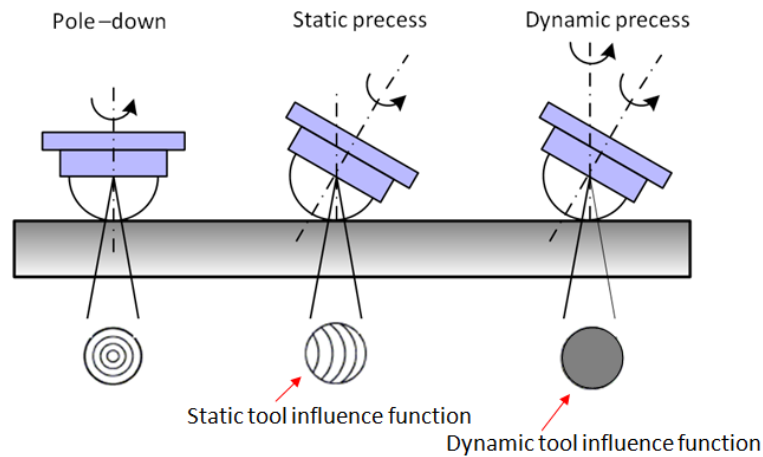
Figure 2-13 Comparison of TIFs regarding precess angles (Li, 2012).

For components with existing MSF ripples on the surface, the precessed bonnet had only limited capability to smooth away such errors. The polishing experiments reported in this thesis used the IRP machines exclusively with precessed inflated bonnets, and their MSF mitigation capabilities are examined and reported in *chapters 3* and *4*.

2.3.2   Magnetorheological Finishing

Led by William Kordonski, a group of researchers first invented *magnetorheological finishing* (MRF) in 1988 at the Luikov Institute of Heat and Mass Transfer (Kordonski et al., 1995, 1996; Golini, 2004). Further development of MRF was made at the Center for Optics Manufacturing at the University of Rochester in 1993, maturing it as an automated CNC process (Jacobs et al., 1995; Pollicove & Golini, 2003). The technology thereupon became the foundation of QED Technologies, a start-up company, which introduced the first marketable MRF CNC machine in 1998 (Golini, 2004). Nowadays, the technology is mainly applied to high quality optical fabrication processes for nonmagnetic materials such as glass, ceramics, and typical semiconductor materials (Arrasmith et al., 2001; Jin & Liu, 2010).

The underlying mechanism of MRF relies on the distinct properties of magnetorheological (MR) fluid, which exhibits a rapidly reversible viscosity change depending on the external applied magnetic field (de Vicente, Klingenberg, & Hidalgo-Alvarez, 2011). Under sufficient magnetic fields, MR fluids were known to demonstrate yield stresses up to 100kPa (Phulé & Ginder, 1998). Shown in Figure 2-14, as the field strength increases, microscopic chains manifests from magnetic suspension particles and quickly combine to produce packs and stacks that eventually bridge the electrode gap (Wen, Zheng, & Tu, 1999).
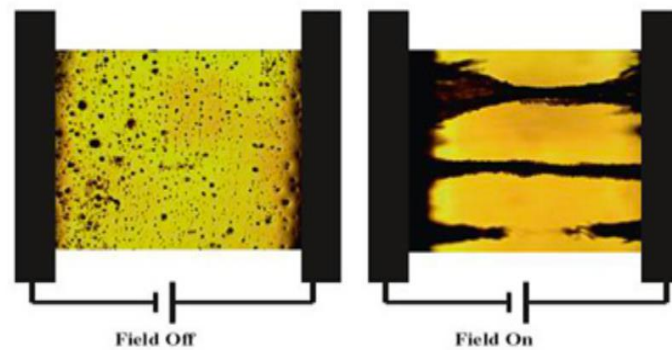
Figure 2-14 Particle suspension of MR fluid with no magnetic field (left) and with magnetic field (right) (Lvovich, 2011).

By combining MR fluids with abrasive particles, the MRF fluid has the ability to be stiffened in a controlled manner through the manipulation of the location and the magnitude of external applied magnetic fields. As a consequence, the process was restricted to polishing only nonmagnetic materials. Depicted in Figure 2-15, material removal occurs at the region where the component was immersed in the stiffened MR fluid ribbon. The process "tool" was effectively the MR fluid, which stiffens and conforms to the topography of the component (Harris, 2011). This characteristic made MRF as a feasible CNC technology that provides a deterministic surface finishing without specialised tooling (Pollicove, 2000).
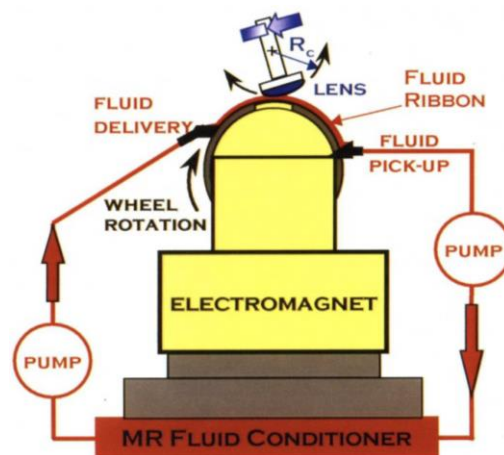
Figure 2-15 Schematic illustration of the MRF process setup (Harris, 2011).

In respect of mitigating MSF artefacts, MRF was not commonly used for controlling MSF errors. Shown in Figure 2-16, the edge of the cross-section of a typical MRF TIF resembled a step-edge, as opposed to a near-Gaussian profile of the inflated bonnet and fluid jet polishing (Ghosh, Dalabehera, & Sidpara, 2018). On the contrary, the process could introduce further MSF through overlapping of influence functions. Although decreasing the track spacing theoretically prevents such initiation of MSF, it would significantly increase the processing time.
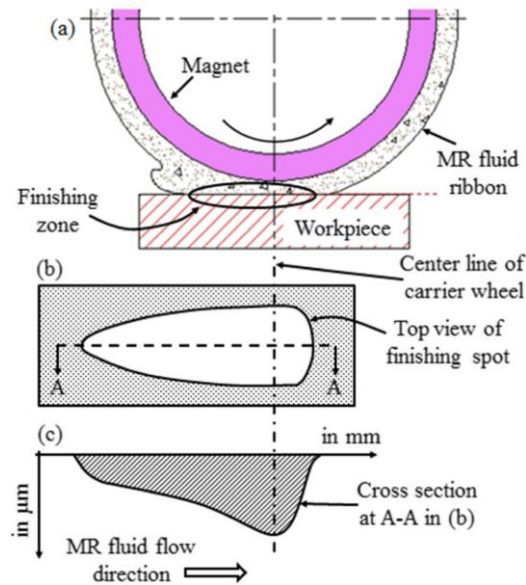
Figure 2-16 TIF schematics of a typical MRF process (Ghosh, Dalabehera, & Sidpara, 2018).

2.3.3 Fluid Jet Polishing

In 1998, Oliver Fähnle, a PhD student from Delft University, experimented and developed a feasible process for precision polishing using a fluid jet (Fähnle, 1998; Fähnle, van Brug, & Frankena, 1998). As shown in Figure 2-17, an abrasive containing slurry was pumped from a holding tank, onto the workpiece, guided through a nozzle. In the absence of a conventional tool, the "tool" in *fluid jet* polishing (FJP) was thus the jet itself. Naturally, the material removal occurs via collision and shearing of the abrasive polishing fluid with the component surface. This liquid "tool" effectively eliminates tool-shape misfit for non-spherical surfaces.

Fähnle's preliminary FJP experiments observed the surface roughness of a BK7 glass part to decrease from 350nm to 25nm RMS after a series of FJP runs using water and 10% 800-grit SiC abrasives (Fähnle, van Brug, & Frankena, 1998). Compared to precessions polishing and MRF, FJP offers lower removal rates, with an upper boundary of around 0.5mm^3/min (Kordonski, Shorey, & Sekeres, 2003). Therefore, the process was mainly used as a surface finishing stage of precision optical fabrication to improve the final surface texture (Zheng, 2017). The volumetric removal rate for FJP was too low to be considered an effective technique in MSF mitigation.
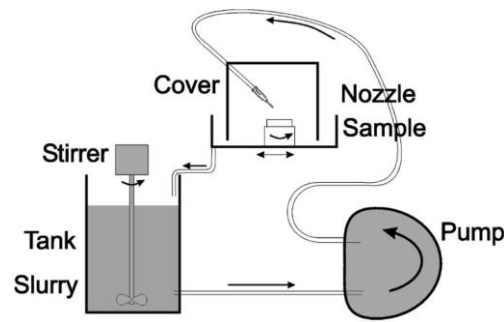
Figure 2-17 Schematic illustration of the FJP process setup (Booji et al., 2002).

2.3.4 Ion Beam Figuring

Experiments in 1965 at the University of Arizona used an energised ion beam to control optical surfaces (Meinel, Bashkin, & Loomis, 1965). *Ion beam figuring* (IBF) removed material by focusing and accelerating high-energy ions towards the workpiece surface, illustrated in Figure 2-18. Through the bombardment of energised ions under a vacuum, IBF could remove material from the workpiece surface on an atomic level. IBF had been developed to process both small and large optics (Drueding et al., 1995; Wilson & McNeil, 1987).
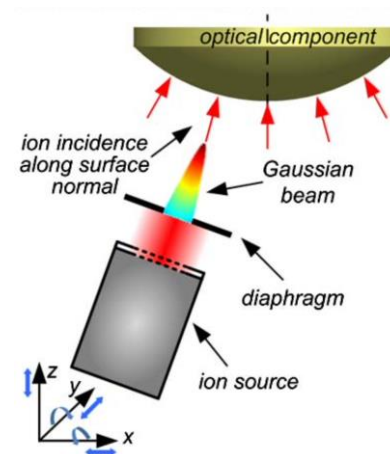
Figure 2-18 Schematic illustration of IBF process (Liao et al., 2014).

In the late 20th century, it was the main finishing method for the manufacturing of the primary mirror for the Keck Telescope. IBF had shown to correct a residual error of 0.762μm RMS leftover from stressed mirror polishing, and the finial residual form error approached 5nm RMS (Mast & Nelson, 1990). However, the entire process required around 14 days to complete, and the exceptionally low material removal rate continues to be one of the biggest drawbacks to IBF technology.

Apart from its inability to correct large form errors, the capital cost of this technology was also very high. Therefore, although IBF theoretically could control MSF artefacts, it was mostly used for final surface finishing only due it its low removal rate, and thus not suitable for smoothing large quantities of MSF ripples.

2.4 Summary of Mid-Spatial Frequency Mitigation in Optical Manufacturing

MSF are undesirable artefacts on the surface of an optical component that reduces signal to noise ratio, disturbs oncoming wavefront, and scatters light (Harvey & Thompson, 1995; Parks, 1983; Youngsworth & Stone, 2000). Current manufacturing technologies continue to struggle in mitigating MSF surface errors. The shortcomings of current CNC techniques could generally be grouped as follows:

i.   Limited smoothing ability to control MSF ripples (i.e. precess bonnet & MRF);

ii.   Not suitable for small components (i.e. stressed mirror & stressed lap polishing);

iii.   Too time consuming and expensive (i.e. FJP & IBF);

Prospective development of optical manufacturing in the direction of MSF mitigation could be a combination of various methods, including, but not limited to:

i.   Eliminating any periodic noise in the system;

ii.   Improving toolpath algorithms (Walker & Dunn, 2008; Hu, Dai, & Peng, 2010);

iii.   Lapping with rigid tools with best fit curvature (Kim, Martin, & Burge, 2013);

iv.   Adjusting slurry mechanics and chemistry at the tool-part interface (Golini, 2004).

As different slurries were required to polish different materials, optimal texture and volumetric removal rate would be dependent on the type of polishing slurry used. It has been proposed that improvement made on polishing slurries could potentially enhance the polishing efficiency for MSF mitigation, namely, the incorporation of a class of materials known as non-Newtonian fluids (Walker & Yu, 2016). *Section 2.7* below summarises the recent progress made on non-Newtonian polishing. However, significant territory is still available for exploration with the combination of non-Newtonian slurries and area-targeted conformal tools to mitigate MSF ripples. Therefore, the research conducted in this thesis focused on the fourth method (adjusting slurry mechanics and chemistry at the tool-part interface).

2.5 Classification of Shear-Thinning and Shear-Thickening Fluids

Non-Newtonian (n-N) materials are a class of materials that exhibit nonlinearity in their relationship between shear stress and shear rate. The viscosity of a fluid is the quotient between the shear stress and the shear rate. Shown in Figure 2-19, n-N materials could be grouped into two categories. Materials that exhibit a decrease in viscosity with increasing shear rate are known as *shear-thinning fluids*. Conversely, materials that exhibit an increase in viscosity with increasing shear rate are known as *shear-thickening fluids* (STF). STFs are often observed in concentrated suspensions (Chhabra & Richardson, 2008). There is a vast range of subclasses of n-N materials, all with their unique definition of properties, such as: pseudoplastic, dilatant, thixotropic, rheopectic, Bingham plastic, viscoplastic, viscoelastic, and etc. Table 2-1 lists a few well-documented examples of n-N materials.
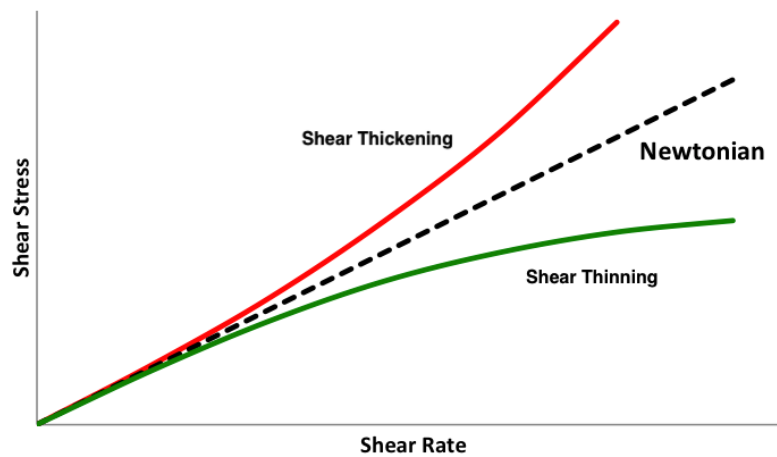
Figure 2-19 Shear stress vs shear rate graph for non-Newtonian materials.

Table 2-1 Examples of non-Newtonian materials and their classifications Chhabra & Richardson, 2008).

Non-Newtonian Material	Classification	Characteristic Significance
Toothpaste	Bingham plastic	Holds shape on brush; behaves like liquid while brushing
Drilling muds	Bingham plastic	Good lubrication properties and ability to convey debris
Non-drip paints	Thixotropic	Thick in the container but thin while on the brush
Wallpaper paste	Pseudoplastic	Good spreadability and adhesive properties
Egg white	Viscoplastic	Easy air dispersion during whipping
Molten polymers	Viscoplastic	Thread-forming properties
Silly Putty®	Viscoplastic	Would flow if stretched slowly, but bounce if hit sharply
Wet cement aggregates	Thixotropic	Small impulses produce settlement
Printing inks	Pseudoplastic	Spread easily in high speed yet do not run at low speed
Waxy crude oil	Thixotropic	Flows readily in a pipe, but difficult to restart the flow
Optician's Pitch	Viscoelastic	Intimately matches surface form, but hard while polishing

There are a few conventional units commonly used for viscosity (μ) (Irgens, 2014):

$$\mu \implies Ns/m^2 = Pa \cdot s = 10P = 1000cP$$

The unit "P" is called Poise, named after Jean Lois Marie Poiseuille, a French physician and physiologist in the early 19th century (Schaschke, 2014). Table 2-2 shows some typical viscosity values at room temperature. An important n-N material that is widely used in optical polishing is known as "optician's pitch". Extracted from plant resin, pitch is a viscoelastic material with a resting viscosity around 2.3×10^{11} mPa·s at room temperature and around 4×10^4 mPa·s at 90°C (Gillman, 1999; DeGroot et al., 2001). Pitch has the ability to flow as a liquid at elevated temperatures (~90°C). At that temperature, the pitch could be moulded to the inverse form of the workpiece that is to be polished. After cooling down, with viscosity in the order of magnitude of 10^{11} mPa·s, pitch behaves similar to a solid, providing the hardness needed for rigid tool polishing.

Table 2-2 Typical viscosity values at room temperature (Chhabra & Richardson, 2008).

Substance	Viscosity (mPa·s)	Substance	Viscosity (mPa·s)
Air	10^{-2}	Olive oil	100
Benzene	0.65	Castor oil	600
Water	1	100% glycerine	1500
Ethyl alcohol	1.20	Honey	10^4
Mercury	1.55	Corn syrup	10^5
Molten lead (673 K)	2.33	Bitumen	10^{11}
Ethylene glycol	20	Optician's pitch	2.3×10^{11}

2.6   Behaviour of Shear-Thickening Slurry During Polishing

For precision optics, it is STFs that are of particular interest. Traditional polishing slurries are Newtonian in nature, while shear-thickening behaviour could offer the potential to enhance polishing efficiency and mitigate MSF errors (Walker & Yu, 2016). As the viscosity of an STF is sensitive to shear rates, the fluid experiences a sharp increase in stiffness as the polishing tool brings the slurry into motion and contacts the workpiece surface. This could aid in the material removal ability of the abrasive particles, as Li et al. proposed a series of snapshots during STF polishing shown in Figure 2-20 (2015).

Snapshot (a) illustrated a shear-thickening polishing fluid under low shear rates. The 'solid particles' refers to the shear-thickening suspensions within the system, such as cornstarch or silica-nanoparticles. With particles

evenly distributed in the slurry, the peaks on the workpiece surface are hard to smooth away due to insufficient forces acting on the abrasive particles. Under such circumstances, the abrasive would have the tendency to rotate or flip over the peaks without cutting.

The shear rate increases starting from snapshot (b) to induce shear-thickening behaviour. As the abrasive-containing STF travels over surface peaks, the local shear rate increases to cause localised shear-thickening. The thickening causes the suspension system to form particle clusters. The effectiveness of STF polishing depends on the hypothesis that such particle clusters provide process enhancement by gripping onto the abrasive particles to shear away the peaks, shown in (c), (d), and (e). As the peaks are smoothed away, localised shear-thickening ceases to occur, and thus the colloidal system breaks apart (f).
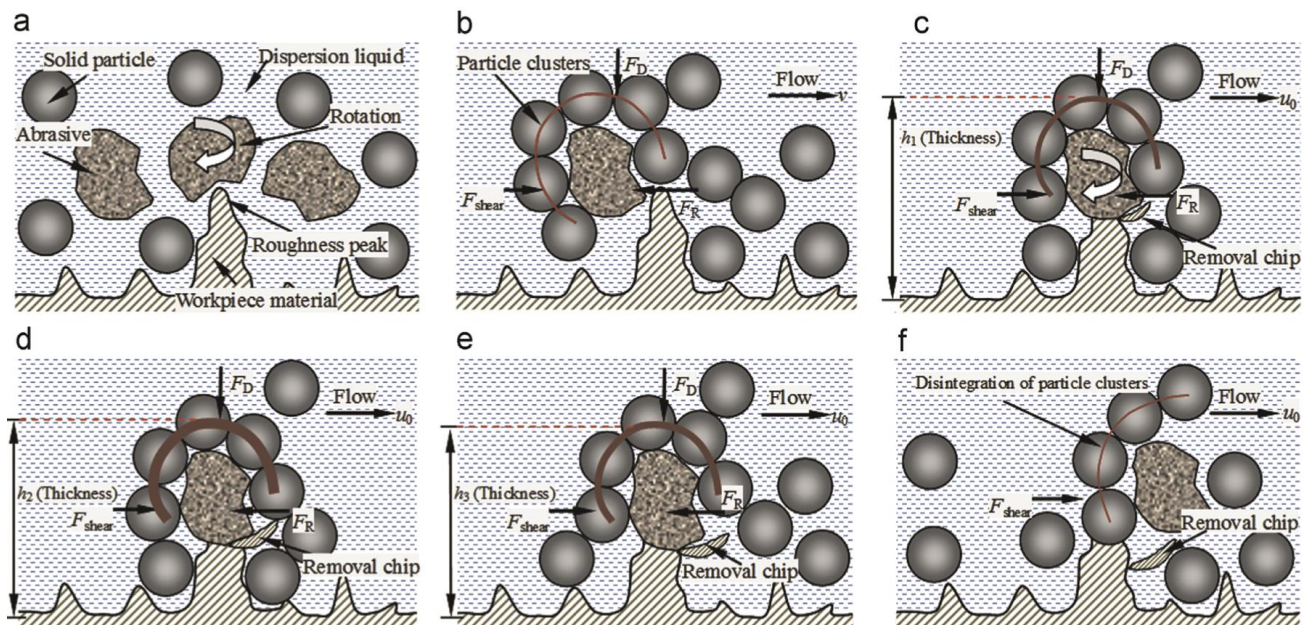
Figure 2-20 Mechanism illustrating the increased ability to shear due to shear-thickening (Li et al., 2015).

2.7   Prior-Art in Non-Newtonian Fluid Polishing

Other prior-art research and development ad explored the potential of STF during polishing processes. During this literature survey, a few patents and publications were discovered, representing applications in lapping and surface finishing.

2.7.1   University of Huddersfield

The University of Huddersfield had been experimenting with STF tooling, namely Silly Putty® tools (Li, 2018). The group rotated the STF tool to target the mitigation of MSF artefacts on aspherical and freeform aluminium mirrors. Figure 2-21 illustrates the construction of the STF tool. A layer of Silly Putty® was

sandwiched between a rigid backing and a compliant diaphragm membrane to construct the semi-rigid tool. A robotic arm was then used to guide the rotating tool across the component surface in a predetermined randomised toolpath (Walker & Dunn, 2008; Zheng, 2017).

The effectiveness of STF tools could be attributed to the shear-thickening effect of the tool as it travels over surface irregularities on the component. The fluid within such tool had the ability to stiffen as the tool travels across surface irregularities. The thickening of the fluid generated increased pressure exertion on the component surface, and according to the Preston equation (1-1), this resulted in greater material removal of MSF ripples (Li et al., 2018b). Furthermore, under more macroscopic traverse conditions, the putty was malleable enough to conform to the aspherical or freeform curvature of the component, bypassing any tool-shape misfit. This tool bridged the gap between rigid and conformal. In doing so, they could retain the benefits from both camps.
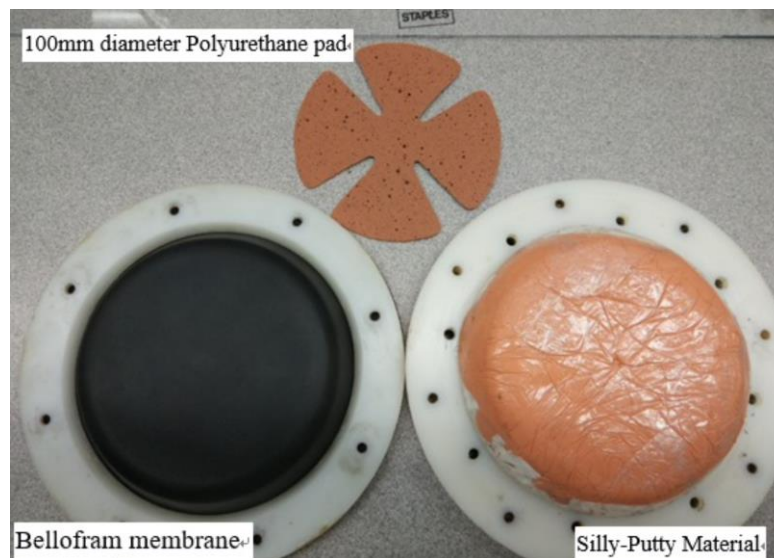
Figure 2-21 Constituents of the Silly Putty® STF polishing tool (Li et al., 2018b).

The results demonstrated a significant improvement on high spatial frequencies on the component surface. For the mitigation of MSF ripples, the results varied depending on the surface's initial condition (depth of the MSF). Experiments carried out by Li et al. found the tool to be effective in mitigating MSF generated by grolishing processes (2018). Surface ripples with depths between ~0.5μm and ~1.5μm were successfully smoothed away after a process time of 4 hours.

2.7.2   University of Sydney

The University of Sydney patented the use of STF to polish components targeting high spatial frequencies, or surface roughness (Chang, Friedrich, & Ye., 2013). The effectiveness of the STF came from "relative

movements" between the STF slurry and the workpiece surface, and such movements could include "rotational, translational, orbital, reciprocating, or randomised motion". The patented technique required the workpiece to be rotated at high speed and submerged under the STF to provide abrasive effects. The slurries mentioned included polymer suspensions such as silica nanoparticle and silicon carbide nanoparticle suspensions in polyethylene glycol.

2.7.3 Zhejiang University of Technology

The Ultra-Precision Machining Centre (UPMC) at the Zhejiang University of Technology made steady advancements in STF polishing over the past decade, resulting in a few Chinese patents. One of the earlier patents explained their success in increasing polishing efficiency by rotating and submerging the workpiece under STF slurries (Lu et al., 2010). Such slurries could be a combination of media (water, oil, or polymer), abrasives (cerium oxide, aluminium oxide, or iron oxide), and tools (0.1-10 mm sized polyurethane balls).

UPMC then patented a way to control actively the viscosity of such STF slurries by means of ultrasonic waves (Lu et al., 2014). A paper was later published by UPMC showcasing their success in utilising STF as a final finishing step, shown in Figure 2-22. This technique involved submerging the component under a rapid current of STF slurry (Li et al., 2015). The shear-thickening effects was generated by the flowing of the slurry around the component. Such a process specifically targets high spatial frequencies and provides approximately uniform polishing to all faces of the component.

Figure 2-22 Workpiece after submergence polishing in STF slurry (Li et al., 2015).

2.7.4 Industrial University of Ho Chi Minh City

The Industrial University of Ho Chi Minh City conducted research similar to that of Zhejiang University of Technology and subsequently published a paper (Nguyen, 2020). The research experimental setup involved submerging a 40mm diameter hardened steel hip joint under STF fluid, illustrated in Figure 2-23. The steel part is rotated within the slurry tank, with Al_2O_3 as the abrasive. The research focused on surface texture and showed a surface roughness of 12nm RMS was obtainable.
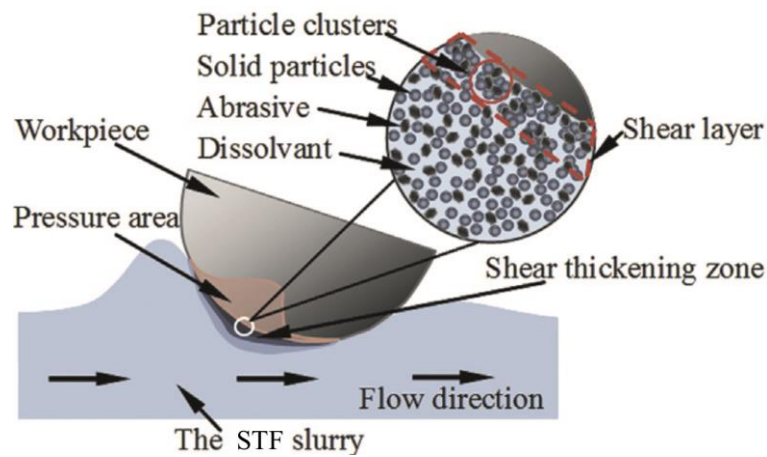
Figure 2-23 Polishing setup by Nguyen (2020).

2.7.5 Centre for Optical Technologies (Germany)

A team in Germany explored polishing of glass using non-Newtonian slurries with focus on improving surface roughness (Schneckenburger, Schiffner & Börret, 2020). Unlike the majority of other research teams, Schneckenburger, Schiffner and Börret employed shear thinning fluids, namely ketchup. They argued that this novel processing should reduce roughness while not affecting shape, opposite to the effect of pitch on glass. This is hypothetically achievable due to the time-dependency shown by tomato ketchup: the longer the ketchup undergoes shear stress, the lower its viscosity. The team used cerium oxide as the abrasive suspended in three different Heinz® ketchup – standard, curry, and organic. The glass was fully submerged under the shear thinning slurry. A rotating tool was attached to a robotic arm, and the tool was lower onto the glass surface for polishing. Experimental results showed that "no improvement in roughness could be achieved" and that "it makes no sense to polish with ketchup."

2.7.6 Kyoto University

A research group at Kyoto University developed a new polishing process called non-Newtonian sub-aperture polishing (NNSP) (Zhu & Beaucamp, 2020). The STF slurry incorporates a mixture of polymer suspension, starch, and Al_2O_3. A nickel-plated part was polished on an IRP 200 machine. The tool used was a 20mm bonnet rotated at 3000 rpm. The tool was kept at a 0.21mm stand-off distance to the nickel part with the STF slurry pumped to the tool-part gap. Under these circumstances, the removal footprint had a maximum depth of 0.5µm and a surface roughness of 3.9nm RMS was achieved. The group also used numerical modelling to explore the polishing capabilities of such STF slurry.

2.7.7 Summary of Prior-Art

A small body of prior-art developing polishing processes with STF demonstrated positive results. The University of Huddersfield focused on tooling, while the University of Sydney, UPMC, and the Industrial University of Ho Chi Minh City directed research efforts to submergence in STF slurries. Kyoto University explored the potential of sub-aperture polishing using STF slurries. However, the combination of STF slurries, along with area-targeted conformal tooling to mitigate MSF ripples for aspheres and freeforms, is still available for a new patent, which leaves a significant territory and incentive for exploitation in this thesis.

2.8   Candidates for Shear-Thickening Polishing Slurries

Through personal discussions with a materials scientist, two potential STF candidates were selected to explore as potential polishing slurries: cornstarch suspension (CSS), and polyethylene glycol (PEG) with silica nanoparticle suspensions.

Experimental trial with CSS was the obvious first step in navigating STF polishing slurries, as cornstarch can be added directly into the existing water-based slurries such as cerium oxide and aluminium oxide polishing slurries. Food grade cornstarch is also readily available at supermarkets. To optimise its performance, additives such as anti-microbial agents and anti-agglomeration agents could be considered.

For PEG systems, the main advantage over cornstarch is the freedom to control more parameters. Variables such as the molecular weight of the PEG medium, and the particle size and shape distribution of the silica nanoparticles could all be controlled to optimise the process. PEG systems had already been widely used in many different applications, such as stabbing-resistant liquid body armour, and medical hydrogel nerve-glue, which is a biocompatible semi-adherent gel-like surgical glue to facilitate nerve repairs (Gong et al., 2014; Isaacs, Klumb, & McDaniel, 2009; Xu et al., 2017; Yu et al., 2012). Therefore, there is much novelty in a polymer-based polishing slurry as the existing cerium oxide and aluminium oxide slurries are all water-based.

2.9   Health and Safety Measures

Experiments in this chapter used substances previously uncommon to the laboratory and its staff, such as PEG and silica nanoparticles. A survey of both substances' health and safety precautions and handling methods had been done via material safety data sheets from various chemical distributors (Acros Organics, 2017; General Engineering and Research, 2015; Roth, 2015; Sigma-Aldrich, 2006; Sigma-Aldrich, 2017; ThermoFisher Scientific, 2017).

PEG came in a variety of different molecular lengths. Depending on the length of the molecules, the rheological properties of PEG could range from a free-flowing liquid to solid. PEG with an average molecular weight of 400 was used for experiments in this chapter, which resembled a free-flowing liquid. According to

Directive 67/548/EEC, PEG-400 is not classified as dangerous (Sigma-Aldrich, 2017). Personal protective equipment such as lab coats, goggles, and gloves are advised, but other equipment such as respiratory protections and ventilation are not required. When in contact with skin, PEG is not toxic, but should be washed away thoroughly with water. Ingestion of PEG could result in gastrointestinal complaints, nausea, and diarrhoea. In case of a PEG-fuelled fire, the advice is to extinguish using foam, dry extinguishing powder, or carbon dioxide.

Silica nanoparticles with specified average particle diameter of 30nm were used for experiments in this chapter. At this size and when handling, any disturbance can cause the particles to become airborne. When handling, any disturbance can cause the particles to become airborne, creating a "cloud" surrounding the bulk substance. Silica nanoparticles have been rated by the Health Management Information System and the National Fire Protection Association to be 0 for both flammability and reactivity, which is of least concern (Sigma-Aldrich, 2006). Prolonged and repeated exposure could result in organ damage and lung cancer. Tests on lab mice showed inflammatory responses and oxidative stress responses in cells (Kaewamatawong et al., 2006; Lin et al., 2006). High concentrations of silica nanoparticles exhibit cytotoxicity by entering cell nuclei and potentially bind to the DNA phosphate backbone (Chen & Vonmikecz, 2005). Therefore, it was essential to limit direct exposure. During the experiments in this chapter, protective measures such as goggles, gloves, lab coats, and masks were used to prevent direct skin contact and inhalation.

2.10   Conclusions

Current optical manufacturing techniques continue to struggle in combatting MSF errors on aspherical and freeform surfaces. For conformal tooling, a trade off exists between fast process time and versatility. Techniques such as stressed mirror and stressed lapping polishing are able to process large aperture components but are not versatile. On the other end of the spectrum, fluid jet polishing and ion beam figuring are able to process complex freeform surfaces but are time consuming and expensive.

Precess bonnets tread the middle ground between fast process time and versatility, though the process has limited smoothing ability to control MSF ripples. Non-Newtonian fluids have been proposed to enhance the ability in MSF mitigation through shear-thickening behaviour at the peaks of the surface ripples. Various prior-art have reported on utilising shear-thickening fluids during polishing, mainly focusing on texture improvements.

A significant territory is available for exploration combining shear thickening slurries with are-targeted conformal tools to mitigate MSF errors. Polyethylene glycol and cornstarch have been proposed as candidates for shear thickening slurries. These are explored in the subsequent chapters.

3   Polishing Tests with Polyethylene Glycol Based Slurries

In the previous chapter, shear-thickening slurries were hypothesised to provide enhanced material removal capabilities during polishing (Li et al., 2015). A few studies had incorporated n-N materials in polishing processes (Burge & Kim, 2012; Li et al., 2018b; Nguyen, 2020). However, the combination of shear-thickening slurries along with area-targeted conformal tooling to mitigate MSF ripples for aspheres and freeforms is still a significant opportunity for exploitation (Walker & Yu, 2016). The experiments in this chapter focused on the novel approach to use PEG as the abrasive carrier. The experiments examined first the material removal rate and then the ability in mitigating existing MSF features. Various abrasives including cerium oxide, aluminium oxide, and diamond nano-powder were suspended in the PEG medium to analyse its polishing potential in both chemical and mechanical means.

3.1   Overview of Materials, Instruments, and Software Used

3.1.1   Glass Workpiece and Its Preparation

The workpiece being polished was a flat 150 x 150mm BK7 glass. This high-quality optical material is a type of borosilicate glass composed mainly of SiO_2 and B_2O_3. Spectroscopy of the material done by Kumar and Singh also showed traces of compounds such as Na_2O, K_2O, BaO, TiO_2, and CaO (2018). The first introduction of borosilicate glass could be found in a catalogue in 1906 under the name O3832 (Glaswerk Schott & Genossen, 1906). The material was subsequently named *BK7* in another catalogue in 1923 (Jenaer Glaswerk Schott & Genossen, 1923).

Since its introduction, BK7 quickly became one of the most popular optical glasses (Campbell et al., 2004; Hartmann, 2012; Jedamzik et al., 2016). In 2014, 1.685 million tons of BK7 was produced, making up for more than 5% of the total industry production of glass in Europe (Li et al., 2016). Due to its high linear optical transmission, good wear resistance, and colourless appearance, BK7 was often used as a standard comparison for other glass materials (Bach & Neuroth, 1998). Therefore, this piece of BK7 glass shown in Figure 3-1 was chosen for the experiments in this chapter.

Before each polishing trial, the glass needed to be returned to the same controlled initial condition. That was achieved through hand-smoothing the glass on a flat cast iron lapping spindle. Aluminium oxide abrasives sized ~10μm (C15) and sized ~6μm (C9) were used (Micro Abrasives, 2011). The larger abrasive C15 were used first to remove any existing features on the glass surface. Due to the brittleness of BK7, large abrasives could cause micro-cracks on the order of 10μm – 100μm to form beneath the surface (Hed & Edwards, 1987). Such subsurface damage could influence negatively the responses of metrology instruments. Therefore, the finer C9 abrasive was used to ensure the absence of any large subsurface damages. Illustrated in Figure 3-1, this lapping practice returned the glass workpiece to a repeatable initial condition.
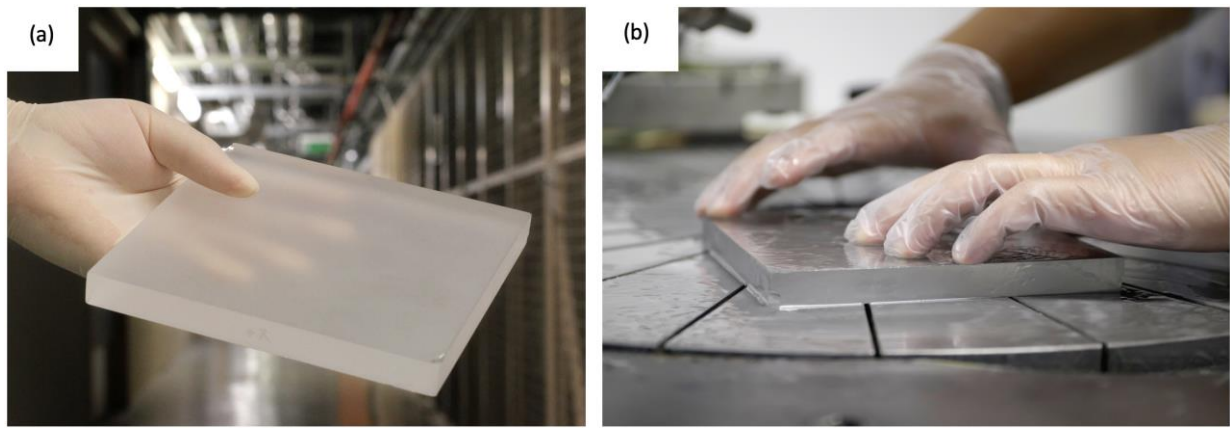
Figure 3-1 (a) The flat BK7 glass component used for experiments; (b) hand smoothing of glass on iron spindle.

3.1.2   Precessed Bonnet Tool

The polishing machine used was the Zeeko IRP 600, which incorporates a precessed sub-aperture inflated bonnet tool. A polyurethane pad was first moulded to match the radius of the bonnet, then cemented onto the bonnet as the polishing cloth, as it is the conventional material to use when polishing BK7 glasses (Li et al., 2014; Mathews, Ross, and Gemballa, 2017; Messelink, 2016). The three main parameters for the precessed bonnet tool are as follows and shown in Figure 3-2:

- Bonnet radius – The radius of curvature of the spherical form of the bonnet.
- Z-offset (bonnet compression) – the distance the bonnet is moved towards the workpiece surface after first-contact with the surface.
- Precess angle – the angle between the bonnet's axis of symmetry (i.e., the rotation axis) and the local normal to the workpiece surface.
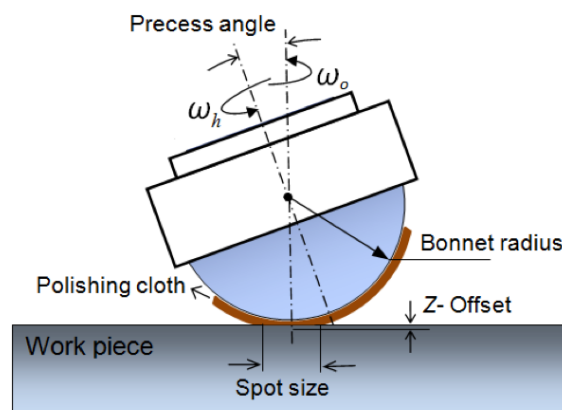
Figure 3-2 Schematic of parameters for the inflated bonnet (Li, 2012).

The bonnet radius and the z-offset work in conjunction to determine the area of contact on the workpiece surface shown by Equation (3-1). A larger bonnet radius and z-offset corresponds to a larger spot size, and vice versa. Greater contact area tends to provide higher material removal rate and greater process speed but lacks the ability to correct surface errors smaller than the contact area. The precess angle determines the velocity profile of the tool on the component surface as illustrated in Figure 3-3.

$$d = 2\sqrt{R^2 - (R - z)^2}$$

Where, d is the diameter of the contact spot;
R is the bonnet radius;
z is the z-offset.
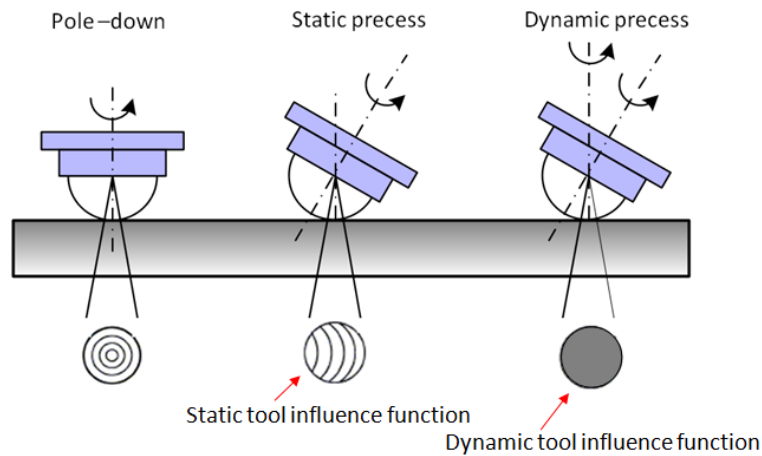
Figure 3-3 Comparison of tool influence functions in regard to precess angles (Li, 2012).

3.1.3 Toolpath Generator Software

The software used to generate the polishing toolpath was Zeeko's Toolpath Generator (TPG). This software is capable of producing toolpaths for tools to travel according to a designed surface profile. There are three main toolpaths that can be generated through TPG: pre-polishing, form correction, and tool influence function (TIF) generation.

The removal rate experiments used the third TPG feature (i.e., TIF) exclusively, in order to polish influence functions onto the glass component. There were a few parameters to be input into the TPG, such as the bonnet radius, z-offset, head speed, feed rate, and tool pressure. Head speed controls the rotational speed of the polishing tool in RPM. Feed rate controls the speed the spindle travels across the component surface in mm/min. The tool pressure controls the pressure within the inflated bonnet tool, usually kept at 1 bar.

3.1.4 Slurry System

The Zeeko IRP 600 machine incorporated a slurry conditioning and re-circulation system. The bulk of the slurry could be contained in a temperature-regulated holding chamber. The holding chamber was equipped with a rotating agitator to ensure the homogeneity of the slurry suspension. A pump drew the slurry from the holding tank and delivered the slurry through nozzles near the tool head. The nozzles could be manually adjusted to aim the slurry at the contact zone between the tool and workpiece. Drainage canals on either side of the polishing table guided the slurry back to the holding tank for recirculation.

Although the IRP 600 machine was equipped with such internal circulation system, it was decided more advantageous to forgo this scheme, because the system was designed to circulate only low-viscosity fluids. Any shear-thickening fluid (STF) could potentially clog pipes, damage the system pump, and increase the difficulties in clean-up procedures. Therefore, a plastic tub was used as an alternative. The slurry under evaluation could be contained during polishing procedures and easily disposed afterwards for clean-up.

As shown Figure 3-4, two 3D printed holders were bolted to the base of the tub, and the glass workpiece was held in place between the holders. The slurry was added to the tub until the glass workpiece was submerged. Air tubes were placed around the base of the tub to induce bubbles. Along with the rapidly rotating tool head, the bubbles served as agitation devices to ensure the homogeneity of the slurry suspension system. The glass component was then polished fully submerged in the slurry. Another advantage of using the tub is the guarantee that the tested slurry would be present at the tool-part interface throughout the polishing processes.
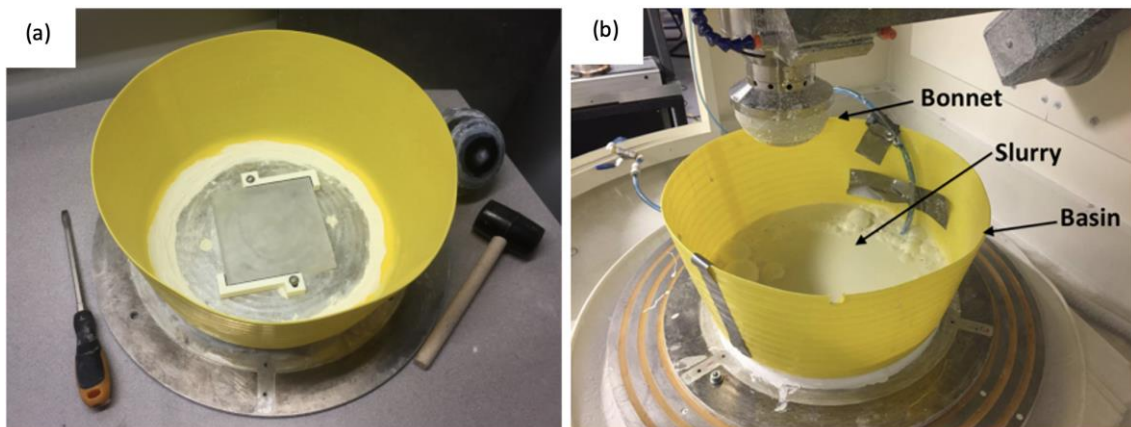
Figure 3-4 (a) Setup of the glass workpiece in the tub; (b) setup of the tub on the IRP 600 with slurry.

3.1.5 Metrology Instruments and Software

Two profilometers were used to measure the glass component before and after each polishing trial. The Taylor Hobson Form Talysurf provided the larger travel distance of the two profilometers with an uncertainty

of measurement of ±0.5μm. While the 50mm traverse Taylor Hobson Intra was limited to a smaller measuring distance, its uncertainty of measurement could approach ±5nm (Taylor Hobson, 2002). They are shown in Figure 3-5.

The profilometry data were processed using Zeeko's Metrology Toolkit software. The software was capable of analysing both 2D profiles and 3D surfaces, removing Zernike polynomials, and determine PSD plots. Existing MATLAB programs were then used to calculate the volumetric removal rate for each process.
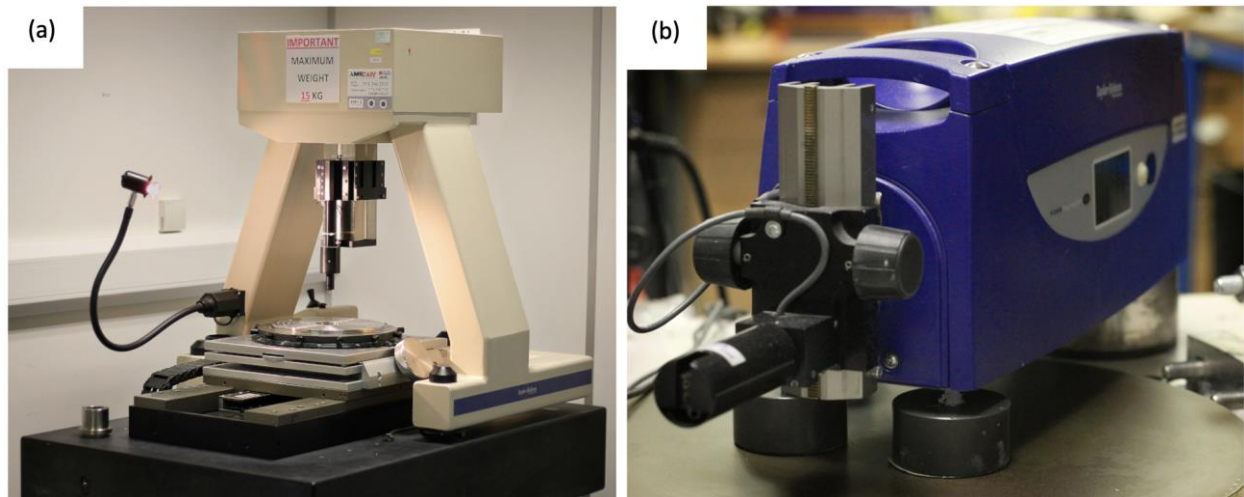
Figure 3-5 (a) The Taylor Hobson Form Talysurf; (b) the 50mm Intra.

3.2   The Control Experiment for Removal Rate Tests

To test the effectiveness of shear-thickening polishing fluids, the polishing results should be compared to conventional polishing slurries such as water-based cerium oxide and aluminium oxide. It was important then to vary the composition of the polishing slurry, while keeping other parameters as constant as was manageable in practice. The volumetric removal rates of the candidate slurries were tested first before experiments on mid-spatial frequency mitigation.

3.2.1   Process Parameters and Toolpath Generation

The main characteristic of STFs is the non-linearity between the shear stress and the shear rate. In order to reflect any n-N behaviour of the slurries, conditions of varying shear rates were introduced. In bonnet polishing, the shear rate was most conveniently varied by changing the bonnet's rotation speed. When the rotation axis was inclined to the local surface-normal (precess angle), the motion of the tool naturally pulled the slurry through the tool-part interface. Therefore, as illustrated in Figure 3-6, six individual parallel trenches were polished onto the glass surface, each possessing a head speed of 500, 600, 700, 800, 900, and

1000 RPM respectively. The influence function of each process was represented by the cross-section profile of the corresponding trench, with the widths equalling the tool's spot size.

Apart from the variation in head speed, all other parameters were kept the same across the 6 trenches. The parameters used on the IRP 600 were as follows: bonnet radius = 80mm; precess angle = 15°; z-offset = 0.7mm; feed rate = 50mm/min. With the selected bonnet radius and z-offset, the spot size was calculated to be ~21mm in diameter using Equation (3-1).
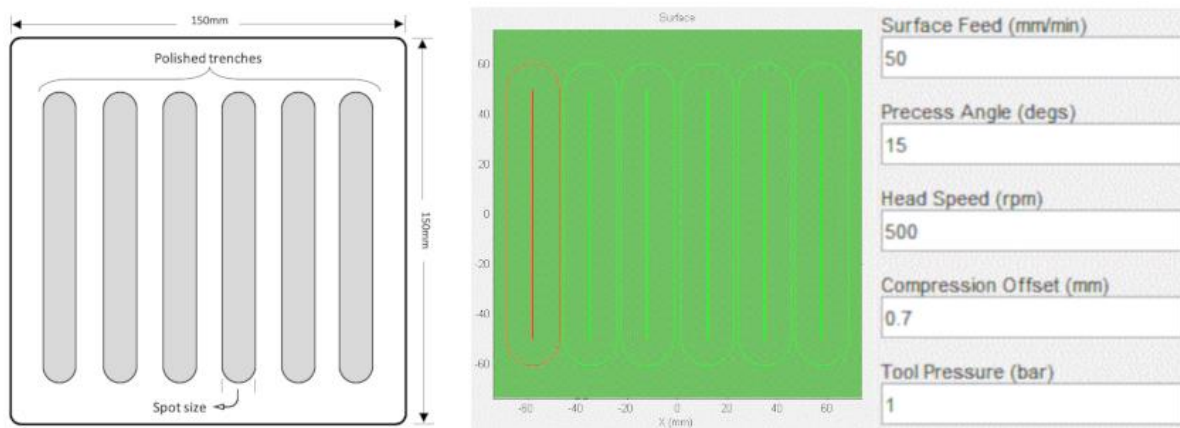
Figure 3-6 Schematic of the 6-trench toolpath on the glass (left) and the screenshot of Zeeko's TPG (right).

3.2.2   Slurry Compositions

Traditional cerium oxide polishing slurry was chosen as the baseline slurry to which the other STF slurries would be compared. Cerium oxide is the conventional polishing abrasive used historically and widely today to provide high-quality glass surfaces (Bouzid, Belkhie, & Aliouane, 2012; Cook, 1990). Glass polished by cerium oxide abrasives can be found in applications such as optical windows, mirrors, computer monitors, prescription eyeglasses, camera lenses, binoculars, integrated circuits, microscopes, and telescopes (Hedrick & Sinha, 1994).

Cerium oxide's excellent removal capability stems from a synergetic combination of chemical and mechanical processes. This process was commonly described as chemical-mechanical polishing (CMP) (Nanz & Camilletti, 1995; Tian et al., 2013). Great advances in recent decades were made to further the comprehension in the underlying mechanisms of CMP, and it has been theorised that cerium ions break down the silica lattice of the glass to form a silica-gel layer (Wang, Zhang, & Biddut, 2011). This hydro-saturated layer is subsequently removed mechanically by the combination of the tool and the abrasive, revealing a "fresh" layer of silica to restart the CMP cycle (Janoš et al., 2016). The chemical interaction is a complex system that hinges on numerous pertinent variables. Nevertheless, the overriding chemical process within the system can be summarised as such (Peng, Guan, & Li, 2014):

$$SiO_2 + 2H_2O \rightarrow Si(OH)_4$$

<div align="right">(3-2)</div>

$$2CeO_2 + 4H_2O \leftrightarrow 2Ce(OH)_3 + H_2O_2$$

<div align="right">(3-3)</div>

$$2Ce(OH)_3 + Si(OH)_4 \rightarrow Ce_2O_3 \cdot SiO_2 + 5H_2O$$
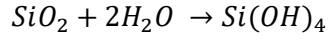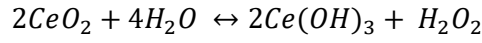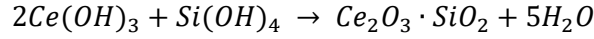
<div align="right">(3-4)</div>

Considering its popularity in high-quality glass processing, cerium oxide was chosen as the abrasive present in the baseline slurry as well as the STF polishing media. A concentration of 26g cerium powder per kilogram of the bulk slurry was chosen. This concentration was normally used in the laboratory due to the trade-off between greater removal rate and higher particle sedimentation rate (information from personal communication with Dr. Guoyu Yu).

3.2.3   Data Collection and Analysis

The BK7 glass workpiece was smoothed before each test (as described in *section 3.1.1*) and measured by the Form Talysurf profilometer to record the initial surface profile, example shown in Figure 3-7. After the influence functions had been polished, the profiles were measured again, as shown in Figure 3-8. The removal profile could then be analysed via Zeeko's Metrology Toolkit software by subtracting the initial profile from the final profile, seen in Figure 3-9. The profile of each individual trench was analysed by an existing MATLAB program called Data Process Utility, developed by a lab colleague. Shown in Figure 3-10, the program calculates the area of the cross section and the volume of the polished trench.
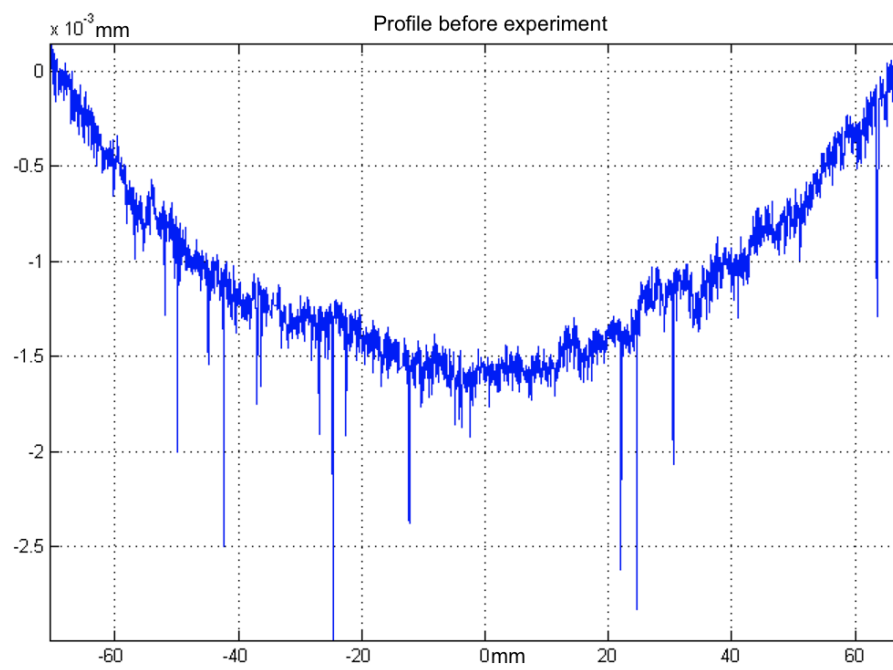
Figure 3-7 Typical initial surface profile across the glass before polishing trials.
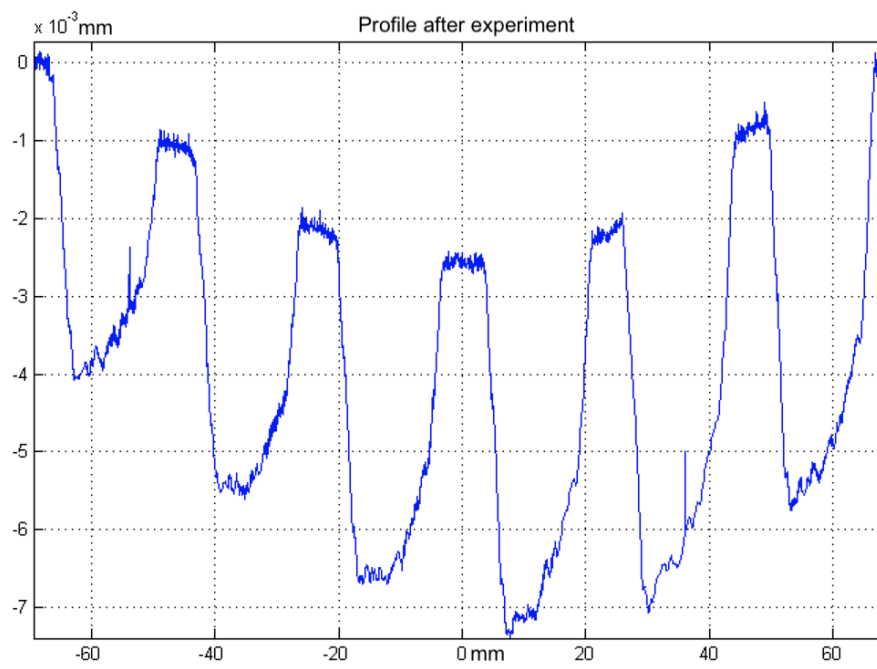
Figure 3-8 Surface profile across the glass after trench polishing.
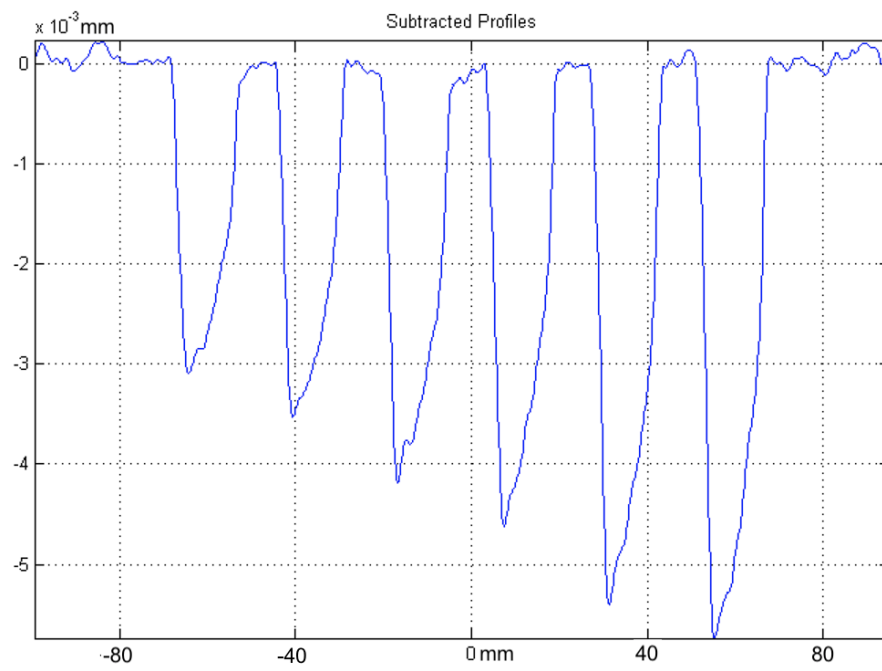
Figure 3-9 Surface profile obtained after subtracting the initial profile from the final profile.
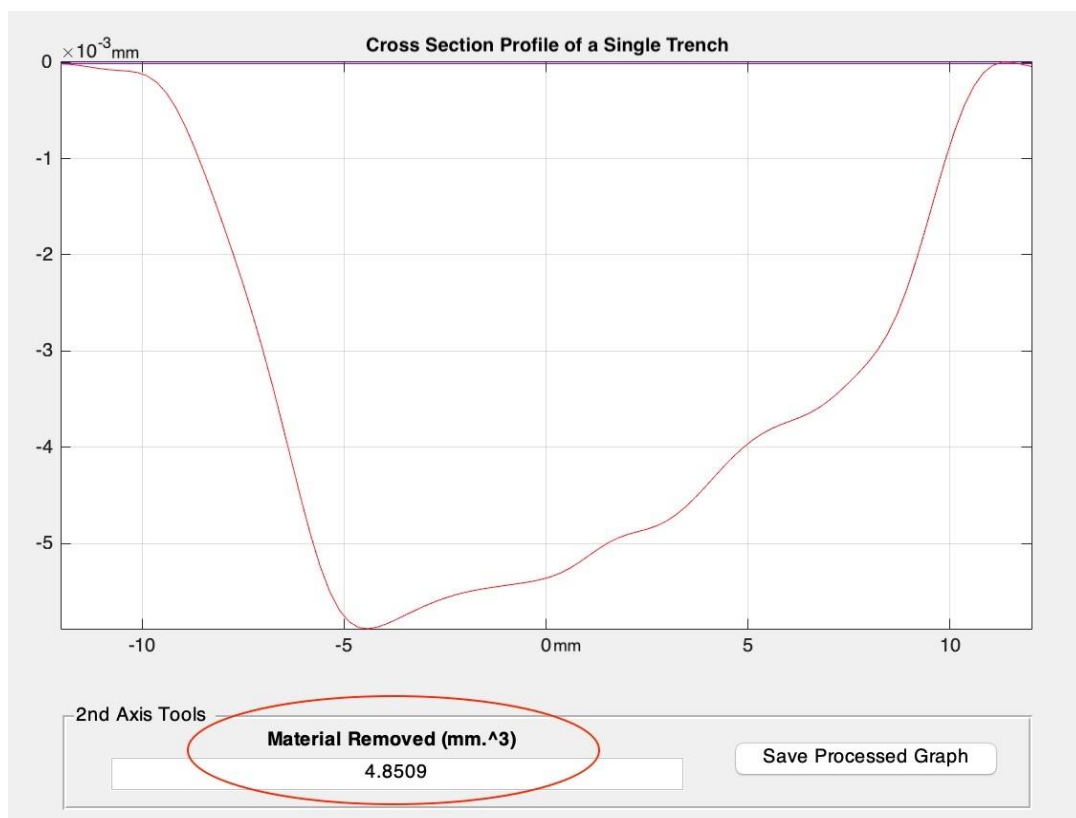
Figure 3-10 Screen capture of MATLAB program used to compute removal area and volume of from a given profile.

3.2.4 Results of the Control Experiments

Four control experiments were completed with the above parameters and procedures, all using cerium oxide. The first two were carried out with the IRP 600 machine's standard slurry circulation system, while the latter two were carried out with the slurry in the tub. Repeating the control experiments four times was not only to test the repeatability of the machine and the process, but also to examine the volumetric removal rate (VRR) responses between the two different slurry delivery systems. The polished surface is depicted in Figure 3-11.

For each test, 10 profilometry scans along parallel tracks were collected across the six trenches to calculate the mean and standard deviation of the experiments. The resulted VRR (mm^3/min) and uncertainty from the 4 control experiments are tabulated in Table 3-1 and compared in Figure 3-12. It was apparent that the tub setup filled with agitated slurry provided similar polishing capabilities to the machine's circulated slurry system. The results conformed to the expected trend that the VRR increases with increasing tool speed.

Figure 3-11 Trenches on the glass surface after polishing trials using a precessed bonnet.

Table 3-1 Mean and standard deviation of volumetric removal rates (mm^3/min) from tests A-D.

Test	Slurry System	500 RPM		600 RPM		700 RPM		800 RPM		900 RPM		1000 RPM	
		Mean	σ	Mean	σ	Mean	σ	Mean	σ	Mean	σ	Mean	σ
A	Circulated	0.858	0.0694	1.17	0.0925	1.46	0.0903	1.71	0.0997	1.92	0.0711	1.99	0.1274
B	Circulated	0.831	0.0925	1.17	0.0906	1.44	0.1052	1.70	0.1419	1.80	0.1746	1.98	0.1402
C	Tub	0.832	0.0834	1.13	0.0909	1.46	0.0622	1.69	0.0722	1.84	0.0775	1.91	0.0902
D	Tub	0.850	0.0750	1.16	0.0326	1.53	0.0689	1.76	0.0512	1.94	0.0833	1.98	0.0569
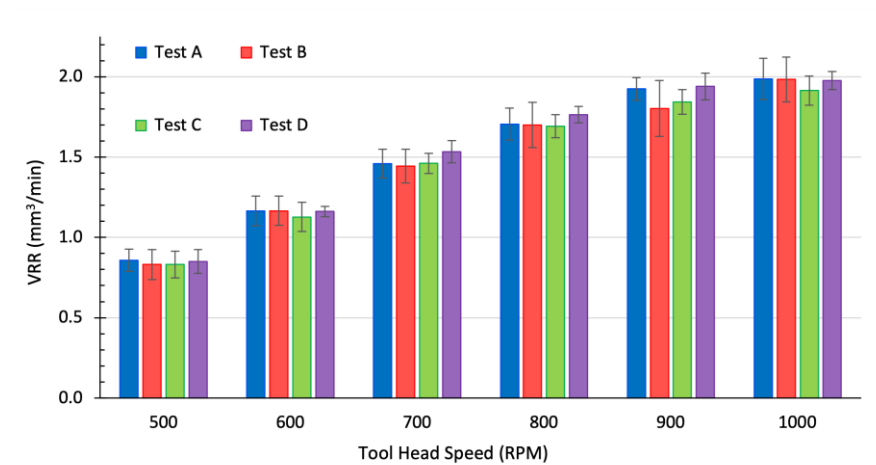
Figure 3-12 Comparison of VRR with standard deviation for tests A-D.

3.3   Volumetric Removal Rate Tests for PEG Slurries

The slurries tested in these trials were made up of three constituents: the polishing medium (PEG), the polishing abrasive (cerium oxide), and the shear-thickening inducing agent (silica nanoparticles). The PEG used had an average molecular length of 400 units (Sigma-Aldrich, 202017). This molecular weight was chosen because higher molecular weight PEG provides more n-N behaviour, while PEGs significantly higher than 400 units start to resemble the consistency of wax. The silica nanoparticles had a specified mean particle size of 30nm. Through small batch experiments, it was found that PEG thickens considerably between 10-15wt% silica nanoparticles while still maintaining a liquid-like state at rest. As before, the mass concentration of cerium oxide in the slurry was kept at 2.6wt%.

Table 3-2 Compositions for tests 1-6 with PEG as media in weight percent.

Test	Mass concentration		Test	Mass concentration	
	CeO_2	SiO_2		CeO_2	SiO_2
1	0%	0%	4	2.6%	0%
2	0%	10%	5	2.6%	10%
3	0%	15%	6	2.6%	15%

A total of 6 tests with various combinations of the three constituents were performed to explore the effects each constituent has on the VRR. Table 3-2 tabulates the compositions and concentrations of the 6 tests.

- Test 1 assessed the removal ability of PEG by itself.
- Test 2 and 3 investigated any polishing potential of silica nanoparticles as the lone suspension.
- Test 4 investigated the removal ability of pure PEG slurry with the addition of cerium oxide.
- Test 5 and 6 investigated the PEG-based slurries with all three constituents.

3.3.1　Results and Discussion

Across the 6 tests, no polishing marks could be seen on the glass surface with visual inspection. When attempting to measure quantitatively using the 50mm Intra profilometer, the trenches, if any, were too shallow to be distinguishable. Illustrated in Figure 3-13, the peak-to-valley height was around 100-200nm. These undulations were most likely either measurement noise or surface texture.
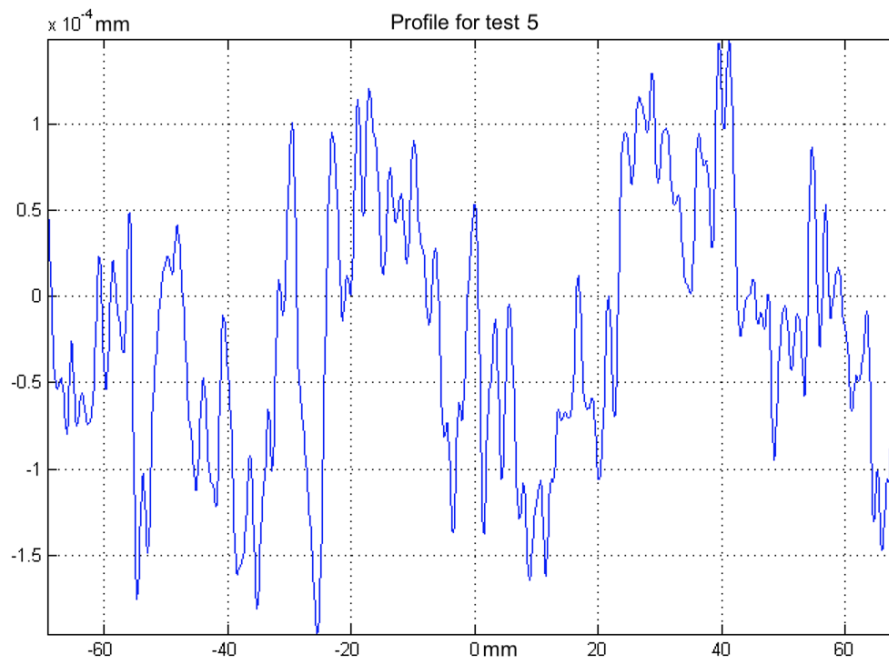
Figure 3-13 Profilometry scan of test 5 after experiment.

As seen from the profilometry trace, there were no discernible trenches of material removal on the surface. The presence of silica nanoparticles and cerium oxide would be expected to provide at least some abrasive effects but showed no benefit in the slurries' material removal abilities across the 6 polishing trials. A few hypotheses were discussed to explain the inability of PEG-cerium slurries for glass polishing.

3.3.2　Absence of Water in the System

One possible explanation for the lack of removal was the absence of water in the system. Without the presence of water, the chemical element of CMP processes could not take place (Wang, Zhang, & Biddut, 2011). For cerium oxide polishing, it is the chemical process of breaking down the crystal lattice of the glass surface that provides this abrasive its superiority over other compounds, and this process relies heavily on the presence of water, alluding to Equations (3-2) and (3-3) (Peng, Guan, & Li, 2014).

Although PEG is a polymer-based medium, it is soluble with water (Gong, 2014). Thus, the polishing capability of PEG-based slurries with the addition of water were tested. The slurry then comprised four constituents: the medium (PEG), the abrasive (cerium oxide), the shear-thickening inducing agent (silica nanoparticles), and the abrasive activator (water). Two tests were subsequently carried out with different concentrations water and silica nanoparticles, shown in Table 3-3. As before, the polishing parameters were all kept the same as the baseline experiments.

Table 3-3 Compositions for tests 7 and 8 with water present in weight percent.

Test	Mass concentration		
	CeO_2	SiO_2	Water
7	2.6%	10%	10%
8	2.6%	15%	50%

The results from tests 7 and 8 were similar to that of the PEG-based slurries without water. Even with the presence of water, there were no signs of removal on the glass surface. The trenches, if any, were too shallow to be discernible from the profilometry data. Figure 3-14 shows a representative example of a profilometry reading, with the undulations most likely due to either measurement noise or surface texture. The addition of water should facilitate the chemical reactions for cerium oxide to achieve CMP. Other factors must be at play to inhibit the material removal capabilities of PEG-based slurries.
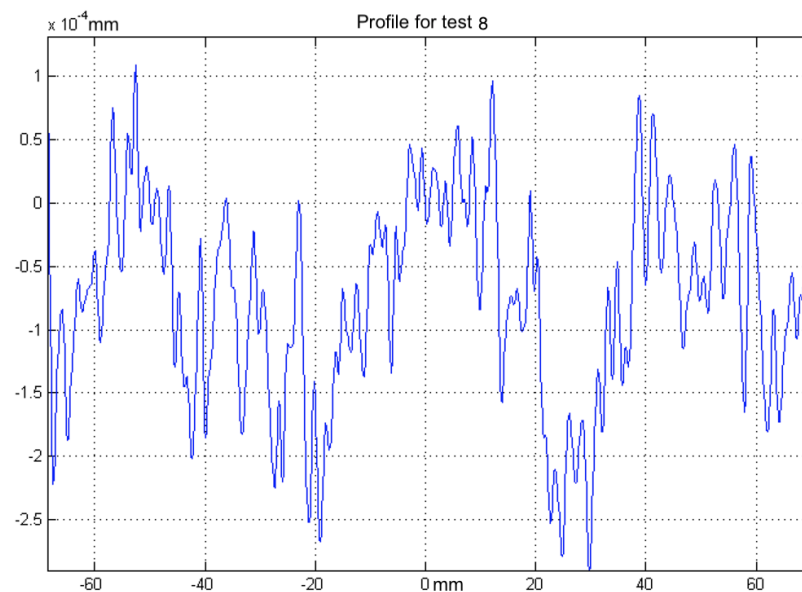
Figure 3-14 Profilometry scan of test 8 after experiment.

3.3.3 Disturbance in Chemistry – Polishing with Aluminium Oxide

It was suspected that the CMP process of the water-based cerium oxide slurry might be hindered by the addition of polymers and silica in the system. Although the major components of the CMP process were all present, its chemistry relied on many other factors such as the pH and ratio of the constituents. For instance, the optimal pH for cerium oxide abrasives to perform CMP was found to be around 8 to 10 (Wang, Zhang, & Biddut, 2011). Under such slight basic environments, cerium oxide abrasives provide higher material removal rate than that in acidic conditions (Lee et al., 2016). The PEG used was slightly acidic in nature, with pH between 5-7 (Sigma-Aldrich, 2017). Therefore, using PEG as the slurry medium could interfere with the CMP ability of the cerium oxide abrasives.

The next step in understanding the polishing potential of PEG-based slurries was to isolate mechanical polishing from the chemical. This was achieved by using aluminium oxide abrasives (Al_2O_3), as aluminium oxide polishing relied solely on the mechanical aspects to grind away at the glass surface. Six trenches were polished onto the glass workpiece using C9 aluminums oxide abrasive particles, which has an average particle size of 10μm (Micro Abrasives, 2011). The tool rotation speed had been lowered to 50, 100, 200, 400, 600, and 800RPM respectively. The feed rate of the bonnet was reduced to 5mm/min. Tests 9, 10, and 11 were conducted to compare the polishing performance of three slurry media: water, vegetable oil, and PEG respectively. Al_2O_3 concentration of 10wt% were used due to trade-off between higher removal ability and higher particle sedimentation rate. For each test, 10 profilometry scans along parallel tracks were collected along each trench to calculate the mean and standard deviation of the experiments. The resulted VRR and uncertainty from the three experiments are tabulated in Table 3-4 and compared in Figure 3-15.

The results show the expected increase in VRR with increasing head speed for the respective tests. For the oil-based slurry (test 10) and the PEG-based slurry (test 11), the increase in VRR slows at higher RPMs. However, the oil-based slurry had consistently lower VRR when compared to that of the water-based slurry, and the PEG-based slurry had consistently lower VRR when compared to both. The mean VRR of the PEG slurry was around 20% of that of the water-based slurry. These results, along with the results from cerium oxide abrasive testing, suggest that PEG is overall an inferior polishing slurry medium when compared to water.

Table 3-4 Mean and standard deviation of volumetric removal rates (mm³/min) from test 9-11.

Test	Slurry Media	50 RPM		100 RPM		200 RPM		400 RPM		600 RPM		800 RPM	
		Mean	σ	Mean	σ	Mean	σ	Mean	σ	Mean	σ	Mean	σ
9	Water	0.096	0.0083	0.154	0.0040	0.237	0.0075	0.290	0.0148	0.339	0.0118	0.450	0.0099
10	Oil	0.097	0.0086	0.131	0.0385	0.170	0.0085	0.197	0.0073	0.199	0.0061	0.209	0.0094
11	PEG	0.018	0.0031	0.026	0.0055	0.051	0.0053	0.063	0.0044	0.073	0.0066	0.075	0.0095
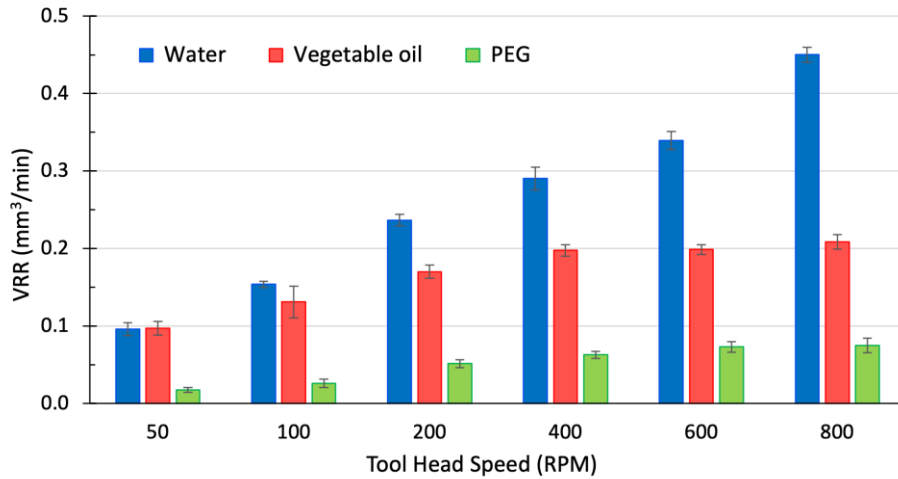
Figure 3-15 Comparison of VRR with standard deviation for tests 9-11.

3.3.4   Coefficient of Friction

The physical feel of the PEG medium resembles that of oils. It is slippery in nature even after the addition of silica nanoparticles to induce n-N behaviours. This slipperiness could contribute negatively to the polishing process as it acts as a lubricant between the tool and the component surface, decreasing its frictional impact. According to the Preston equation (1-1), the decrease in friction directly affects the mechanical removal capability of the slurry by affecting the Preston coefficient (Téllez-Arriaga et al., 2007). A rig was constructed to compare the dynamic frictional coefficient between water, oil, and PEG. Figure 3-16 shows the rig's setup. A weighted vessel was pulled via a metal wire at a constant velocity. A spring-balance was placed between the weighted vessel and metal wire to measure the tension force needed to pull the weighted vessel at a constant velocity. As the vessel travels along the trough, a camera captures the force displayed on the spring-balance.

Tests were performed with water, vegetable oil, and PEG placed into the trough respectively. According to Newton's law of friction, the force needed to overcome friction is proportional to the normal force exerted on the object and the frictional coefficient (μ):

$$F_f = \mu N$$

(3-5)

The measurements from the spring-balance were recorded as the weighted vessel traveled down the trough at a constant speed. As the mass of the weighted vessel remained unchanged, the normal force experienced should remain constant. Therefore, the dynamic friction force should only be affected proportionally by the frictional coefficient. Figure 3-17 shows the comparison of forces recorded by the scale from the three fluids.

73
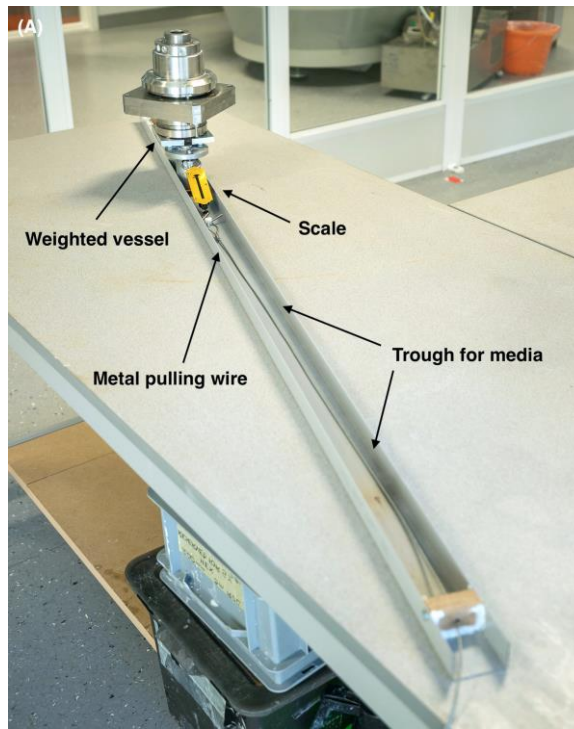
Figure 3-16 Test rig setup for comparing dynamic frictional coefficient.
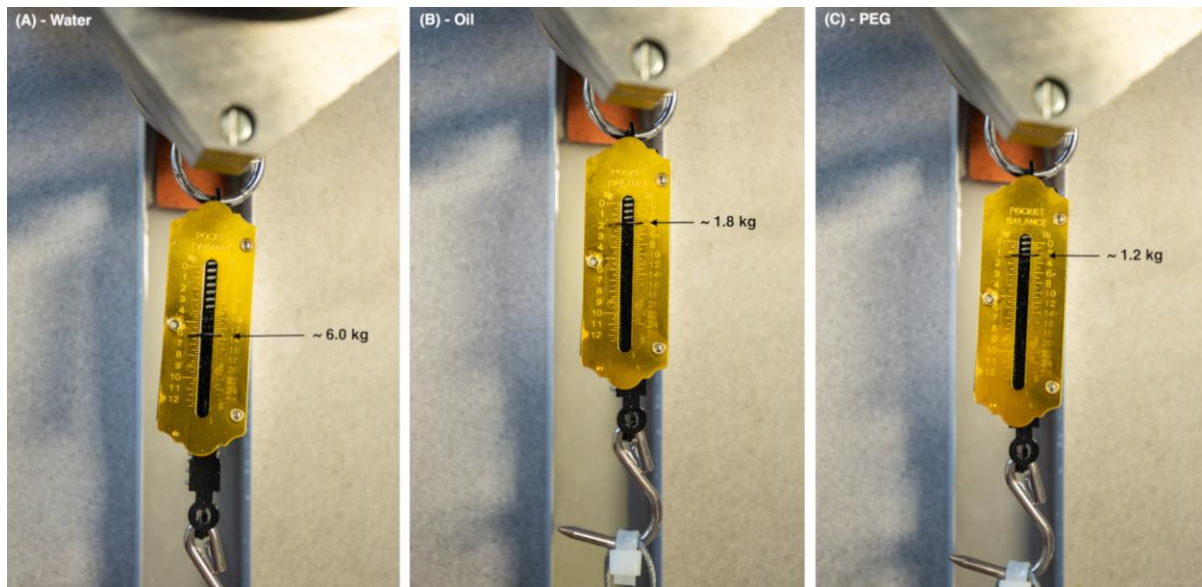
Figure 3-17 Readings from the friction tests on water, oil, and PEG (left to right).

From the spring-balance readings, the frictional force was the largest for water and smallest for PEG, consistent with the trend seen in Figure 3-15. The ratio of frictional coefficient between water and vegetable oil was approximately 3 to 1; and between water and PEG to be approximately 5 to 1. Drawing from the Al_2O_3 polishing results of tests 9 and 11, the ratio of VRR between the water-based slurry and PEG slurry were also approximately 5 to 1, suggesting a possible correlation.

3.4   Rheology of Polyethylene Glycol Based Slurries

Experiments conducted up to this point followed reasonings and assumptions backed up by literature review with regards to fluid properties (Cheng, Friedrich, & Ye, 2013; Gong et al., 2014; Xu et al, 2017). PEG-silica systems were assumed to be shear-thickening. Nonetheless, major differences exist between slurries used in publications and those used in this thesis, such as preservatives, surfactants, methods of mixing, nanoparticle size and shape distribution, PEG molecule lengths, suspension concentrations, and etc.

Although the literature survey provided a springboard for experimental logic, that is no substitute for conducting rheological tests on the slurries to analyse their exact quantitative fluid properties. Knowing their respective rheological characteristics would not only help to better understand the underlying physics at the tool-workpiece interface during polishing, but it would also aid in constructing an accurate software model for computer analytics and process optimisation. Consequently, the rheological results would be able to verify the legitimacy of the previous assumptions.

3.4.1   Parelle-Plate Rheometer Setup

A total of 3 samples tested. The compositions of the samples are summarised in Table 3-5. Cerium Oxide suspension were added across the samples at 2.6wt%. Sample PEG-1 represented the polymer medium with cerium oxide only, which was the slurry used in test 4. Samples PEG-2 and PEG-3 represented a low and high concentration of silica nanoparticles respectively, reflective of slurry used in test 5 and 6.

Table 3-5 Samples tested with PEG as medium in weight percent.

Sample	CeO$_2$	SiO$_2$
PEG-1	2.6%	0%
PEG-2	2.6%	10%
PEG-3	2.6%	15%

The viscosity of each sample was recorded across a shear rate range of $100 - 1000$ s^{-1}. This shear rate range corresponds to an equivalent local surface speed at the interface with the workpiece of an 80mm bonnet precessed at 15° rotating between $100 - 1000$ RPM. The experiments were conducted on a NOVA Rotational Rheometer using the couette geometry (i.e., parallel plate) with the wall and cylinder gap at 1mm. Figure 3-18 illustrates the schematics of a parallel-plate rheometer.
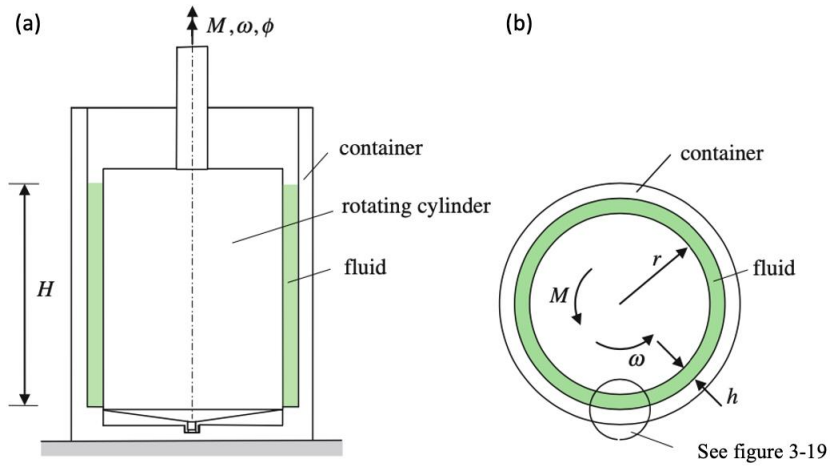
Figure 3-18 Schematics of a rotational rheometer with side view (a) and top view (b) (Irgens, 2014).

During the test, a central cylinder was rotated in a cylindrical container about a shared vertical axis. The liquid being tests was put in between the two concentric cylinders. The shear rate could be calculated from the angular velocity ω of the inner cylinder: Equation (3-6). The shear stress could be calculated from the torque force M applied to the vertical axis of the inner cylinder: Equation (3-7). The viscosity could then be calculated: Equation (3-8). The local shear situation of the fluid is shown in Figure 3-19. However, some assumptions were first made:

   i.   The relation between the cylinder walls can be approximated as two parallel plates, as the distance h is relatively small compared to the radius r of the cylinder that the motion of the liquid may be considered to be like the flow between two parallel plane surfaces.

   ii.   The boundary condition states that the velocity of the fluid immediately in contact with the cylinder walls is equal to the velocity of the cylinder walls (i.e., no-slip boundary conditions).

   iii. The fluid is evenly distributed across the rheometer (i.e., ignoring centrifugal forces causing density differences among the fluid).

$$\dot{\gamma} = \frac{d\gamma}{dt} = \frac{dv_x}{dy} = \frac{v}{h} = \frac{\omega r}{h}$$

(3-6)

$$\tau = \frac{F}{A} = \left(\frac{M}{r}\right)\left(\frac{1}{2\pi r H}\right) = \frac{M}{2\pi r^2 H}$$

(3-7)

$$\mu = \frac{\tau}{\dot{\gamma}} = \left(\frac{M}{2\pi r^2 H}\right)\left(\frac{h}{\omega r}\right) = \frac{h}{2\pi r^3 H}\left(\frac{M}{\omega}\right)$$

(3-8)
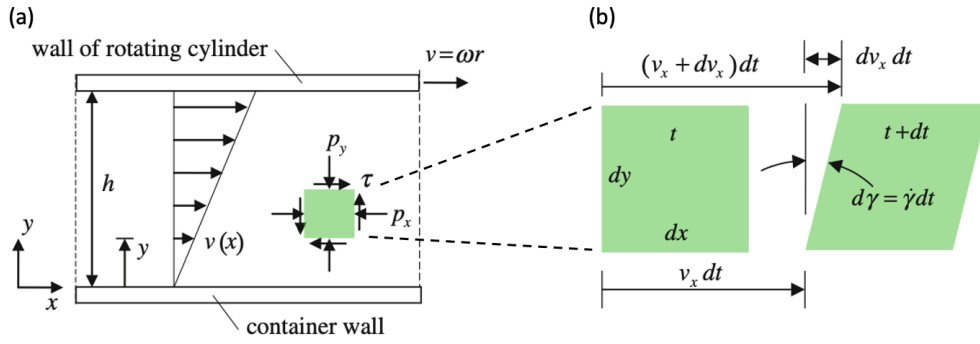
Figure 3-19 (a) Simple shear flow. (b) Fluid element (Irgens, 2014).

3.4.2   Results and Data Analysis

Each sample was tested three times for repeatability. Sample PEG-3 was placed in a vacuum oven for 2 hours at room temperature to remove trapped air bubbles. Each sample were subjected to a shear rate of ~400 s^{-1} for 10 minutes to allow for temperature equilibration to 20°C.

The rheological experiments yielded the flow curves, and the plot of each run could be fitted the power-law model, an established n-N mathematical model (Chhabra & Richardson, 2008). Ostwald was the first to use the power law model to describe fluid characteristics in his publication in *Colloid and Polymer Science*, so this model is sometimes also referred to as the *Ostwald de Waele model* (1929). The power law model is expressed in the following equation:

$$\mu = \frac{\tau}{\dot{\gamma}} = m(\dot{\gamma})^{n-1}$$

(3-9)

Where, m is the fluid consistency coefficient in Pa·s^n;

n is the flow behaviour index;

$n < 1$, the fluid exhibits shear-thinning behaviour;

$n = 1$, the fluid exhibits Newtonian behaviour;

$n > 1$, the fluid exhibits shear-thickening behaviour.

For each sample, the fluid consistency coefficients and flow behaviour indexes across the 3 runs were averaged to produce the final power law model variables for each of the 3 samples. These values serve a vital purpose in constructing an accurate model for computational fluid dynamics. The variables are tabulated in Table 3-6.

*Table 3-6 Coefficients for the power law models. (*not used in calculating average).*

Sample	Test	m (Pa·s^n)	n	Average m	Average n
PEG-1	1	48.421	1.062	48.539	1.061
	2	48.716	1.060		
	3	48.490	1.060		
PEG-2	1	1570.1	0.790	1782.2	0.773
	2	1574.8	0.790		
	3	2201.8	0.740		
PEG-3	1	34388	0.468	31835.5	0.481
	2	2967937*	-0.360*		
	3	29283	0.493		
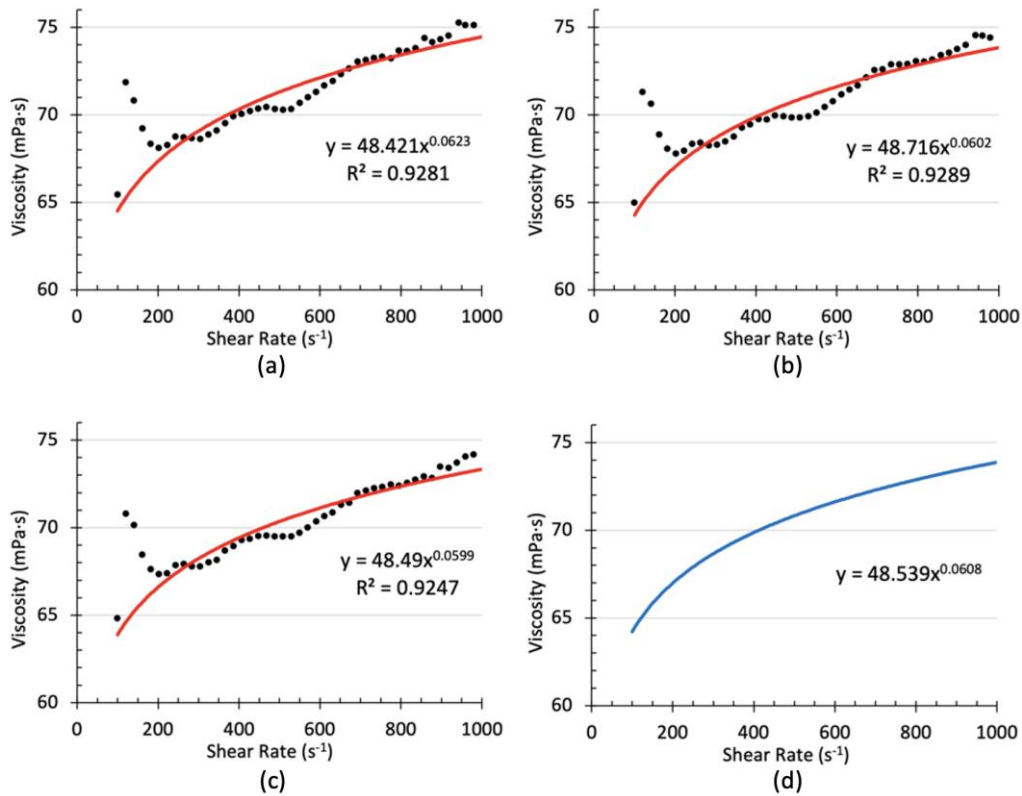
Figure 3-20 (a), (b), and (c) Rheology for sample PEG-1. (d) Projection of the averaged power law coefficients.
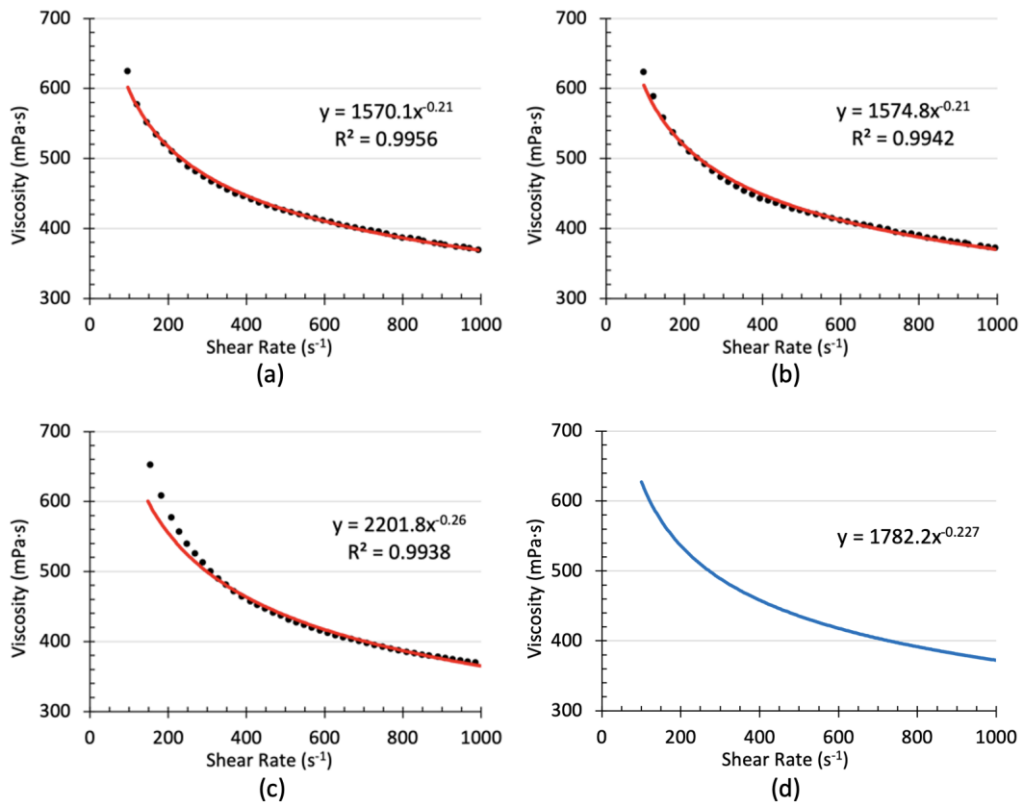
Figure 3-21 (a), (b), and (c) Rheology for sample PEG-2. (d) Projection of the averaged power law coefficients.
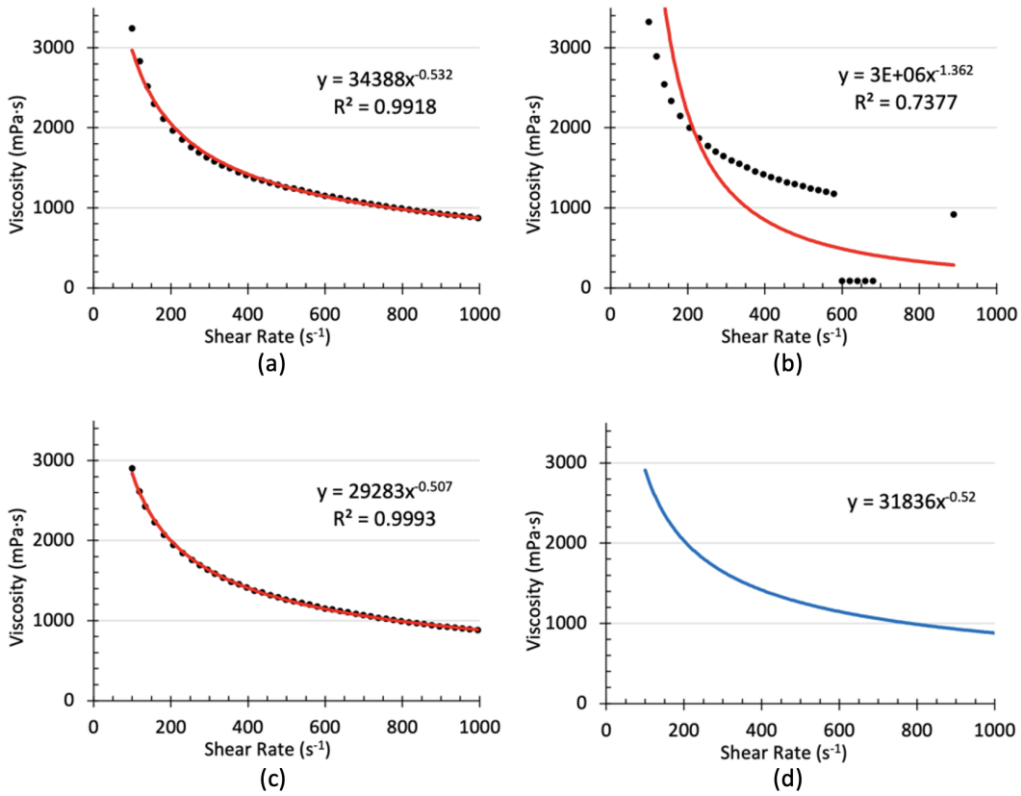
Figure 3-22 (a), (b), and (c) Rheology for sample PEG-3. (d) Projection of the averaged power law coefficients.

Figure 3-20, Figure 3-21, and Figure 3-22 show the individual runs and the averaged power law models for the three samples respectively. The peak around 175s^{-1} on the Sample PEG-1's flow curves were most likely due to turbulence in the fluid at the beginning of each test before settling down to laminar flow. Therefore, data points around the peaks were excluded in fitting the power law model for sample PEG-1. There was a loading error for run 2 of sample PEG-3. The rheometer had not been cleaned properly following run 1, therefore data from run 2 were incorrect and not used in the power law model for sample PEG-3.

3.4.3 Discussion

Preliminary literature review yielded numerous accounts of applications that utilised the shear-thickening properties of PEG and silica nanoparticle systems (Mankarious & Radwan, 2020; Xu et al., 2017; Yu et al., 2012). With only cerium oxide suspended in pure PEG medium, sample PEG-1 exhibited shear-thickening properties. However, rheology data suggested PEG-silica systems were inherently shear thinning. This was contrary to the expected shear-thickening behaviour, though the overall viscosity was over an order of magnitude higher than that of pure PEG. Upon further literature review, this discrepancy could be attributed to two reasons – filler concentration and shear rate regimes.

Two publications made by Shanghai Jiao Tong University and Thapar University respectively tested the rheological properties of PEG systems with varying silica nanoparticle sizes (Yu et al., 2018; Singh et al., 2019). Figure 3-23 shows the flow curves of 30nm silica particles in varying concentrations in PEG medium. Samples PEG-2 and PEG-3 corresponded to the 10% and 15% curves in Figure 3-23. It was apparent that at these filler loadings, the system was shear thinning across the entire shear rate range.
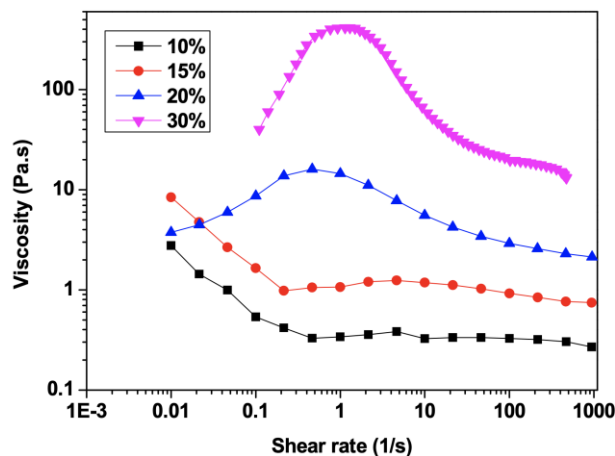
Figure 3-23 Flow curve of PEG-Silica system tested by Yu et al, 2018.

The maximum concentration of silica that PEG could uptake is affected by the particle size. Smaller particles possess higher free surface energy, which results in a lower maximum concentration of silica (Xu et al., 2017). The method in which silica nanoparticles are introduced to the PEG also plays a significant role in sample preparation. According to reports in the literature, higher filler loading in literature was achieved using a combination of vacuum chambers, ultrasonic agitation, and magnetic stirring, all of which were not available in the lab at the time (Gong et al., 2014; Gürgen & Sofuoglu, 2020); Mankarious & Radwan, 2020). Without such preparation methods, 25wt% silica nanoparticles were added in one instance at the lab, and the system quickly turned from a liquid to a foam-like consistency. This is shown in Figure 3-24.
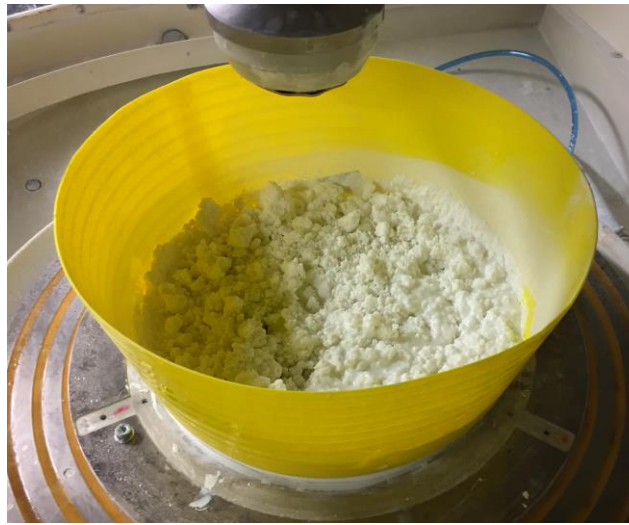
Figure 3-24 Too much silica nanoparticles turned PEG into a foam-like consistency.

Referring to Figure 3-23, filler loadings of 20% and 30% were capable of exhibiting thickening behaviour only at shear rate below ~1s^{-1}. Even if preparation methods such as vacuum chambers and ultrasonic agitation were made available, slurries with higher filler loading would still exhibit shear thinning behaviour at the high shear rates induced by a rapidly rotating bonnet. Shear thinning behaviour of PEG-silica systems at high shear conditions was evidentially a contributing factor to PEG-bases slurries' ineffectiveness in high-speed bonnet polishing.

3.5   Mid-Spatial Correction Using Polyethylene Glycol Based Slurries

The negative effects of mid-spatial frequency (MSF) surface errors were introduced in *section 1.5*, and the limited ability for sub-aperture precessed bonnets to rectify existing MSF features is summarised in *section 2.1*. It was hypothesised that n-N slurries, in particular shear-thickening slurries, could have a positive effect on mitigating surface ripples in conjuncture with precessed bonnets (Walker, 2016). Despite PEG-silica

systems demonstrating close to negligible polishing capability, and exhibited shear thinning behaviour at high shear rates, PEG-based slurries were tested for their ability to mitigate pre-existing MSF ripples.

3.5.1   Experimental Setup and Mid-Spatial Frequency Generation

The same glass workpiece and preparation process was used as outlined previously in *section 3.1.1*. After the workpiece was returned to the same initial state, MSF ripples were generated onto the workpiece surface using a precessed bonnet. This was achieved by using a raster toolpath with a 40mm radius bonnet at a track spacing of 2mm. This created a 2mm periodic surface ripple shown by profilometry in Figure 3-25(a). Data could also be presented through power spectral density (PSD) graphs, which was introduced in *section 1.5.5.* The PSD plot after the MSF generation is shown in Figure 3-25(b), and it shows a clear spike at 2mm wavelength.

To mitigate the MSF generated, a combination of 4 raster toolpaths perpendicular to the ripples were used. Each toolpath precessed the bonnet at 15° leaning towards +x, -x, +y, and -y direction respectively. Each toolpath also utilised varying track spacing of 0.5mm, 0.6mm, 0.43mm, and 0.57mm in order to stager the raster and prevent the generation of any new surface ripples. The surface profile was measured after the second mitigation toolpath (run 2) and after the fourth mitigation toolpath (run 4).
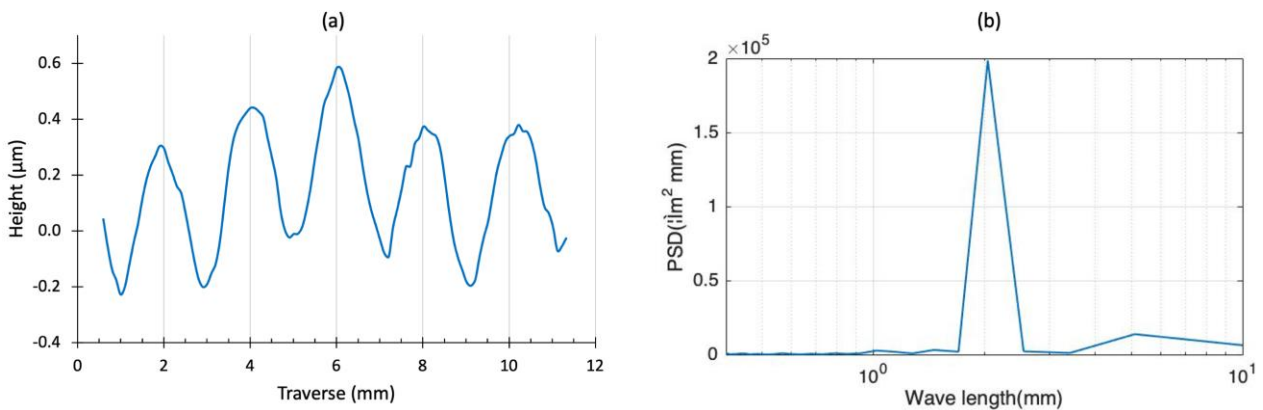
Figure 3-25 (a) Profilometry showing 2mm MSF generation; (b) PSD showing presence of 2mm frequencies.

3.5.2   Slurry Compositions

Section 3.3 examined the various hypotheses for the incompatibility between PEG and cerium oxide, namely the lack of CMP polishing. Therefore, only mechanical polishing was considered for MSF mitigation tests. Aluminium oxide abrasive (C9) was used and compared with diamond nano-powder abrasive. Given PEG's slippery nature, PEG could act as the carrier fluid for diamond nano-powder, as diamond nano-powder had

the precedence of being suspended in oily media providing purely mechanical surface removal, especially in metal finishing (Hird & Field, 2004; Schuelke & Grotjohn, 2013; Lu et al., 2017).

Four tests were conducted with the slurry composition summarised in Table 3-7. The diamond nano-powder use supplied by Hongwu International Group Ltd., with average particle size of 40nm and purity of 99% (Xuzhou Jiechuang New Material Technology Co, 2019). Tests 12 and 13 examined the ability of aluminium oxide with and then without silica nanoparticles respectively. Tests 14 and 15 examined the ability of diamond abrasives with and then without silica nanoparticles respectively.

Table 3-7 Compositions for tests 12-15 in weight percent.

Test	Media	Abrasive	Abrasive concentration	SiO_2 concentration
12	PEG	Al_2O_3	5%	0%
13	PEG	Al_2O_3	5%	10%
14	PEG	Diamond	5%	0%
15	PEG	Diamond	5%	10%

3.5.3   Results and Discussion

Figure 3-26 to Figure 3-29 show the progression of tests 12 to 15. Each graph compares the MSF ripples generated to the resulting profiles and PSD after the second raster polish (run 2) and the fourth raster polish (run 4). MSF mitigation could be difficult to decipher from the clustered profile trace data, thus the PSD plots painted a clearer picture of the effectiveness of each slurry. The absolute value of the PSD peaks may vary from test to test, but the focus is the amount of reduction of the peaks after the experiments. The reduction of the peaks is summarised in Table 3-8.
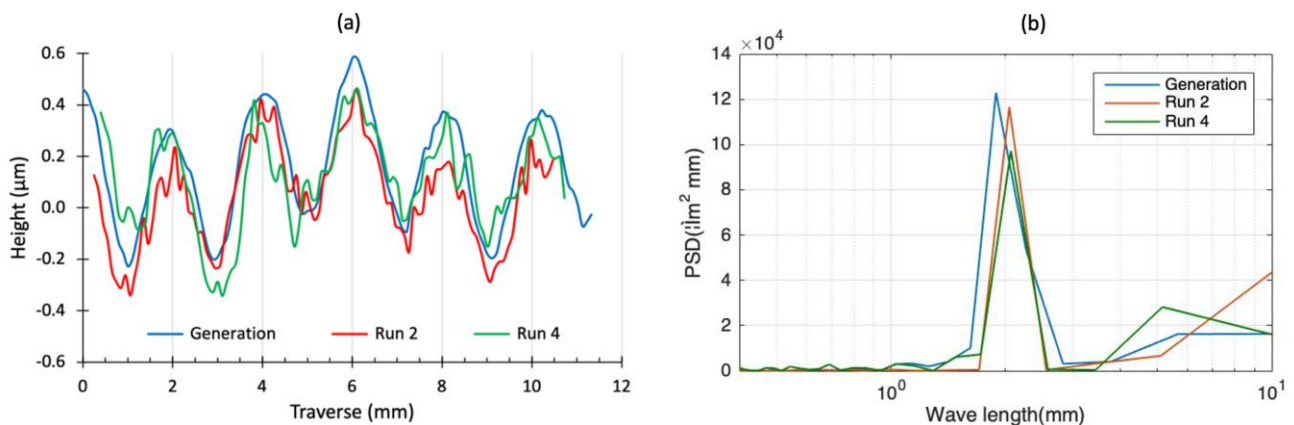
Figure 3-26 Profile traces (a) and PSD plot (b) for test 12.
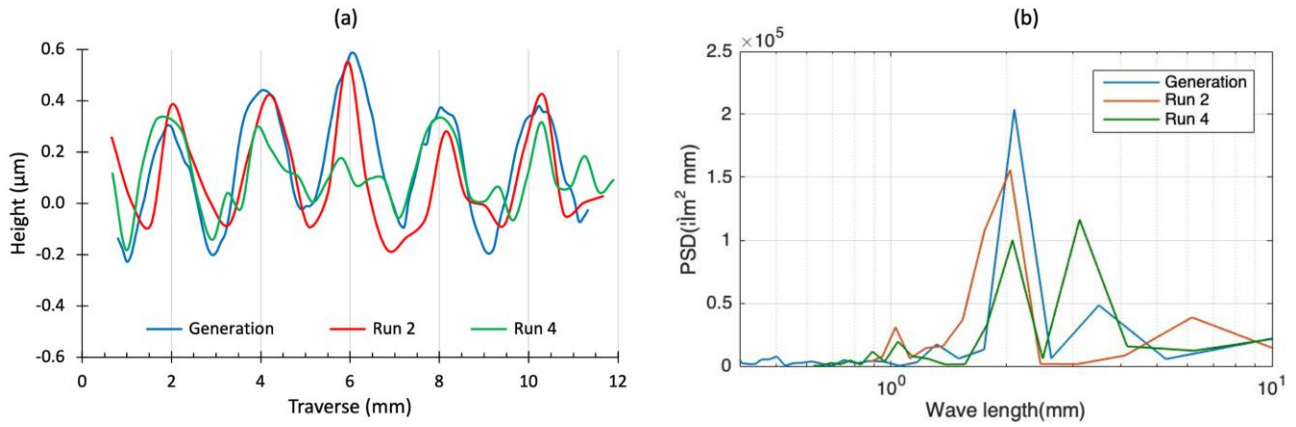
Figure 3-27 Profile traces (a) and PSD plot (b) for test 13.
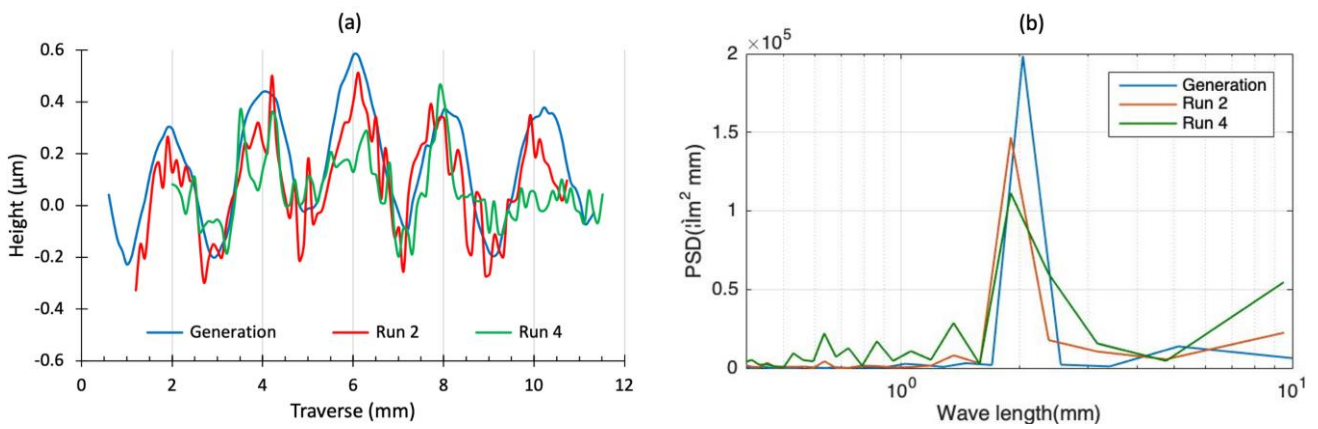
Figure 3-28 Profile traces (a) and PSD plot (b) for test 14.
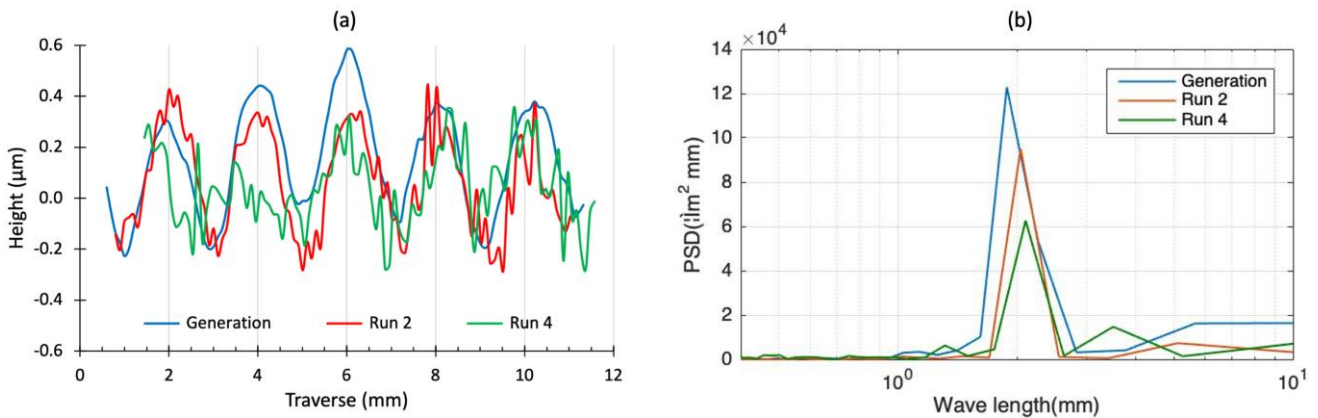
Figure 3-29 Profile traces (a) and PSD plot (b) for test 15.

Every slurry showed some capability in mitigating existing MSF features on the glass surface. Comparing tests 12 and 13, the addition of silica nanoparticles had a positive effect, with peak reduction of 25% after the second raster toolpath and 50% reduction after the fourth. Note regarding test 13, referring to Figure

3-27(a), the data processing threshold for high frequency pass was set too high, resulting in too much smoothing, and excluded some surface texture features. Comparing tests 14 and 15, the introduction of silica nanoparticles appears to have no effect on the diamond slurries' polishing ability. Comparing the tests 12 and 14, tests 13 and 15, both aluminium oxide and diamond abrasives performed similarly, though the diamond had slightly higher removal without silica nanoparticles in the system. These experiments demonstrated some promising effects of PEG-based slurry's ability at smoothing exiting MSF surface ripples.

Table 3-8 PSD peak values and reductions for tests 12-15, with peak unit of lm^2 mm x 10^4.

Test	Generation	Run 2		Run 4	
	Peak	Peak	Reduction	Peak	Reduction
12	12	11.5	4%	9.5	21%
13	20	15	25%	10	50%
14	20	15	25%	11	45%
15	12	9	25%	6	50%

3.6 Conclusions on Polyethylene Glycol as Polishing Medium

From the volumetric removal experiments, the polishing efficiency of PEG-based slurries was very low. Compared to the water-cerium normal, which under the same parameters produced influence function depth of 5μm, the PEG slurries showed low to negligible removal (< 200nm peak-to-valley). This was the case for both cerium oxide and aluminium oxide abrasives. A few hypotheses exist to explain the inferiority of PEG slurries such as absence of CMP, change in system pH, and decrease of the friction coefficient.

The rheological property of PEG systems was measured. PEG-silica nanoparticle systems were assumed to be shear-thickening from applications found in literature, but later rheological testing showed shear-thickening behaviour was limited to low shear rate conditions. Under the high shear rate of surface polishing, PEG systems exhibit shear thinning behaviour, which could contribute negatively to overall polishing efficiency.

PEG was used as the carrier fluid for aluminium oxide and diamond nano-powder abrasives for means of purely mechanical smoothing of existing MSF surface ripples. Under the parameters used, both abrasives showed similar effectiveness at decreasing the amplitude of the ripples, with 50% reduction of the PSD peaks. Therefore, although PEG based slurries would not be suitable for overall form correcting polishing due to low material removal efficiency, they demonstrated some viability in MSF correction.

4   Polishing Tests with Cornstarch Suspension Slurries

Mid-spatial frequency (MSF) errors degrade the performances of optical surfaces, and it continues to present challenges in mitigation using conformal tools on aspherical and freeform surfaces. STFs had been hypothesised to enhance material removal and MSF mitigation efficiency (Li et al., 2015; Walker & Yu, 2016). *Chapter 2* provided an overview on n-N fluids and prior arts in incorporation with polishing. *Chapter 3* explored the novel approach of utilising PEG as slurry carrier in conjunction with silica nanoparticles to induce n-N rheological effects. This chapter returns to water as the slurry medium. Cornstarch was chosen as the suspension to induce the desired shear-thickening behaviour to the system. Cornstarch suspension (CSS) was selected due to the readily availability of food-grade cornstarch and can be easily added directly into the conventional water-based polishing slurries without the need for surfactants, agitators, or vacuum chambers. Moreover, the intensity of the shear-thickening behaviour could be precisely controlled by the concentration of cornstarch in the system. This chapter investigates the preservation, the volumetric removal rate (VRR), the MSF mitigation abilities, and the achievable texture of CSS slurries.

4.1   Preservation of Cornstarch Suspension

Wetted cornstarch is subject to spoilage from moulds, yeasts, and bacteria. CSS could degrade rapidly in a matter of days. To combat such degradation, preservatives were added to the CSS polishing slurry for conservation and storage. Potassium sorbate ($C_6H_7KO_2$) is a common preservative used not just in foods, but also in pharmaceuticals and cosmetics to prevent the growth of microbials (Saraiva et al., 2017; Wang, et al., 2012). Starch films containing potassium sorbate had exhibited strong inhibitory effects on E coli (Shen et al., 2010). Although excess use in foodstuffs could lead to metabolic acidosis, convulsions, and hyperpnoea, it was considered a safe food additive at low concentrations (Fujiyoshi et al., 2018; Mohammadzadeh-Aghdash et al., 2018). The European Food Safety Authority prescribed maximum permitted levels of potassium sorbate as food additives ranging from 20-6000 mg/kg depending on the food product (European Food Safety Authority, 2015).

A simple test was conducted to visually examine and demonstrate the ability of potassium sorbate to preserve CSS in the presence of cerium oxide. Referring to Figure 4-1, three glass vessels containing varying composition was used. Vessel (a) represented the conventional polishing slurry. Vessel (b) represented CSS, with the addition of cornstarch and cerium oxide. Potassium sorbate was added to vessel (c) for comparison with vessels (a) and (b). Two sets of the test were carried out, one with the vessels covered with cling film and the other uncovered, yielding a total of 6 vessels. The vessels were left at room temperature untouched and unstirred. Picture shown in Figure 4-2 were taken when the test began on day 0, after a week on day 7, and once more on day 20.
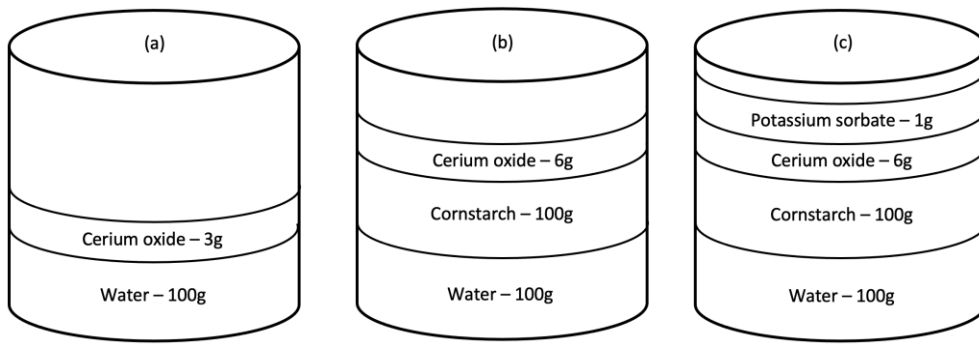
Figure 4-1 Setup of the potassium sorbate test for CSS polishing slurry.
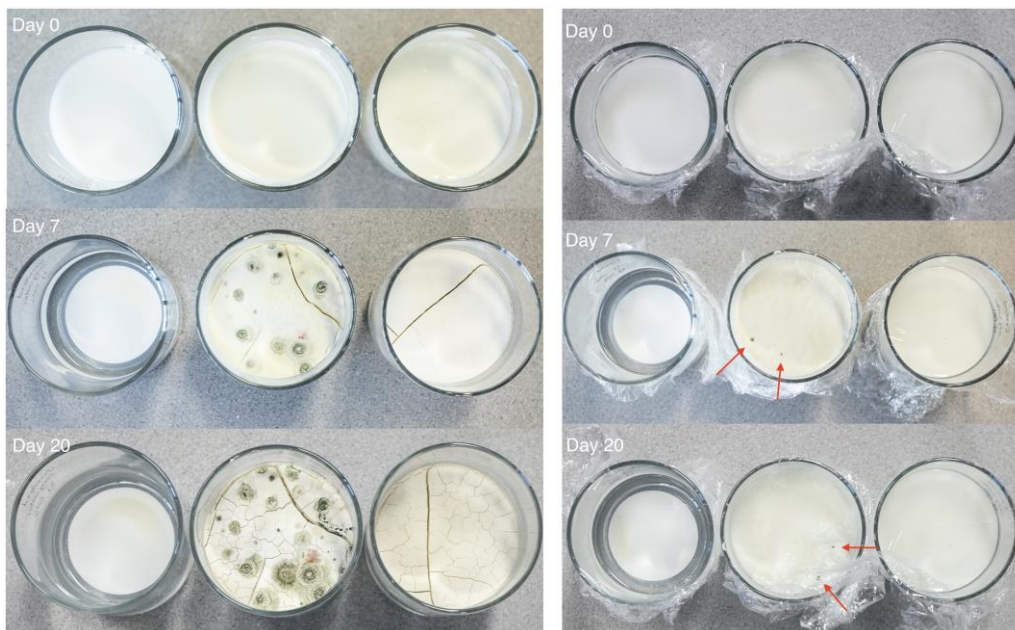
Figure 4-2 Preservation test of potassium sorbate with vessels uncovered (left) and covered (right).

Vessels (a), which contained only inorganic cerium oxide, were left without microbial growth. Vessels (b) showed very apparent microbial growth. Cling film provided some protection, but spots could still be seen after 7 days. The vessels (c) with the presence of potassium sorbate were left free of microbial growth. It can be concluded that small addition of potassium sorbate provides the necessary preservation needed for the CSS slurry.

4.2   Experimental Setup and the Control Experiment

The workpiece, instruments, and software used were outlined in *section 3.1*. The process parameters, toolpath, and data analysis were outlined in *section 3.2*, where four tests (tests A-D) were conducted as the control with just water and cerium oxide as the slurry. The effect of potassium sorbate on the overall performance of cerium oxide slurry required testing and comparison, with ~5g/kg$_{slurry}$ of potassium sorbate

added to the conventional slurry and polished in the tub. Two tests were performed for repeatability, and the results were compared to test D.

Referring to both Table 4-1 and Figure 4-3, the addition of potassium sorbate did not affect the VRR in a meaningful way. Taking the standard deviation into consideration, the three tests offer similar VRR across the head speed ranges. Therefore, for all subsequent CSS tests, 5g/kg$_{slurry}$ of potassium sorbate were added to the slurry. Test F was used as the control experiment in the subsequent sections, and it is referred to as Test 0.

Table 4-1 Mean and standard deviation of volumetric removal rates (mm3/min) from tests D-F.

Test	Potassium sorbate	500 RPM		600 RPM		700 RPM		800 RPM		900 RPM		1000 RPM	
		Mean	σ	Mean	σ	Mean	σ	Mean	σ	Mean	σ	Mean	σ
D	No	0.832	0.0834	1.13	0.0909	1.46	0.0622	1.69	0.0722	1.84	0.0775	1.91	0.0902
E	Yes	0.914	0.0649	1.19	0.0495	1.52	0.0555	1.72	0.0513	1.90	0.0715	1.94	0.0490
F (0)	Yes	0.848	0.0799	1.18	0.1193	1.48	0.1102	1.75	0.1194	1.92	0.0923	1.98	0.1295
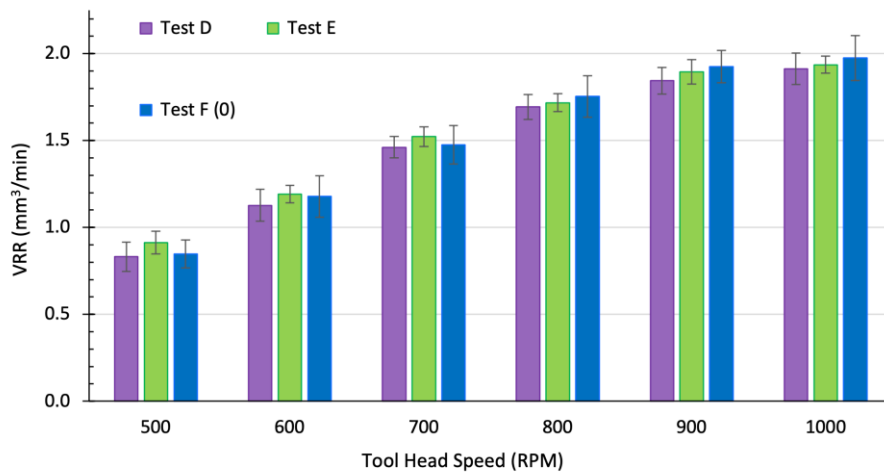
Figure 4-3 Comparison of VRR with standard deviation for tests D-F.

4.3 Volumetric Removal Rate Tests for Cornstarch Suspension Slurries

The slurries tested in these trials were made up of four constituents: the polishing medium (water), the polishing abrasive (cerium oxide), the shear-thickening agent (cornstarch), and the preservative (potassium sorbate). By adding more cornstarch into the existing Newtonian cerium oxide slurry, the slurry should exhibit increasingly shear-thickening behaviour. Eight tests with increasing concentrations of cornstarch were performed, tabulated in Table 4-2.

Table 4-2 Cornstarch to water weight ratios for tests 0 and 16-23

Test	Ratio	Test	Ratio	Test	Ratio
0	0	18	0.1875	21	0.5
16	0.0625	19	0.25	22	0.75
17	0.125	20	0.375	23	1

With the addition of cornstarch to the original slurry containing 2.6wt% of cerium oxide, the total mass increases, and the concentration of cerium oxide was effectively diluted. Thus, in order to maintain a comparable abrasive concentration to the baseline experiments, more cerium oxide was added to recover the 26g/kg$_{slurry}$ cerium oxide. It should be noted that the available scale measures weight to the nearest gram, leading to a nominal uncertainly in measured weight of ±0.5 grams.

4.3.1   Results and Discussion

After each experiment, 10 profilometric scans of trench depths were collected along parallel tracks using the Form Talysurf and the VRR values calculated. The mean and the standard deviation of the resulted VRR are shown in Table 4-3 and plotted in Figure 4-4. Figure 4-5 shows some representative profilometry readings showing the effects of cornstarch addition. Contrary to expectation, the addition of cornstarch into the slurry contributed negatively to the VRR. A few potential explanations were proposed such as drag induced on the tool head and the particle size difference between the abrasive and the starch.

Table 4-3 Mean and standard deviation of volumetric removal rates (mm^3/min) from tests 0 and 16-23.

Test	500 RPM		600 RPM		700 RPM		800 RPM		900 RPM		1000 RPM	
	Mean	σ	Mean	σ	Mean	σ	Mean	σ	Mean	σ	Mean	σ
0	0.848	0.080	1.178	0.119	1.476	0.110	1.754	0.119	1.925	0.092	1.975	0.129
16	0.716	0.086	1.060	0.112	1.268	0.095	1.461	0.109	1.608	0.080	1.741	0.095
17	0.651	0.077	0.950	0.100	1.098	0.116	1.251	0.089	1.293	0.106	1.361	0.100
18	0.584	0.054	0.806	0.059	1.041	0.044	1.177	0.097	1.223	0.059	1.176	0.057
19	0.625	0.044	0.812	0.044	0.955	0.036	1.135	0.056	1.159	0.061	1.142	0.085
20	0.574	0.092	0.766	0.041	0.903	0.062	1.149	0.070	1.126	0.084	1.077	0.088
21	0.612	0.026	0.797	0.095	0.888	0.076	1.040	0.098	1.028	0.082	1.066	0.082
22	0.576	0.050	0.730	0.055	0.898	0.059	1.100	0.061	1.047	0.053	1.032	0.057
23	0.592	0.060	0.730	0.062	0.929	0.057	1.103	0.073	0.998	0.077	1.044	0.122
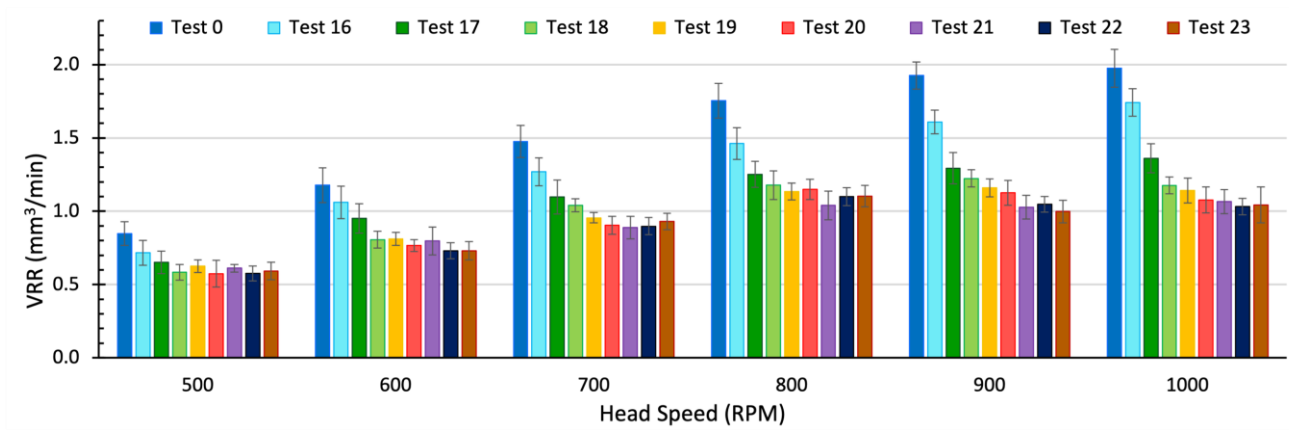
Figure 4-4 Comparison of VRR with standard deviation for tests 0 and 16-23.
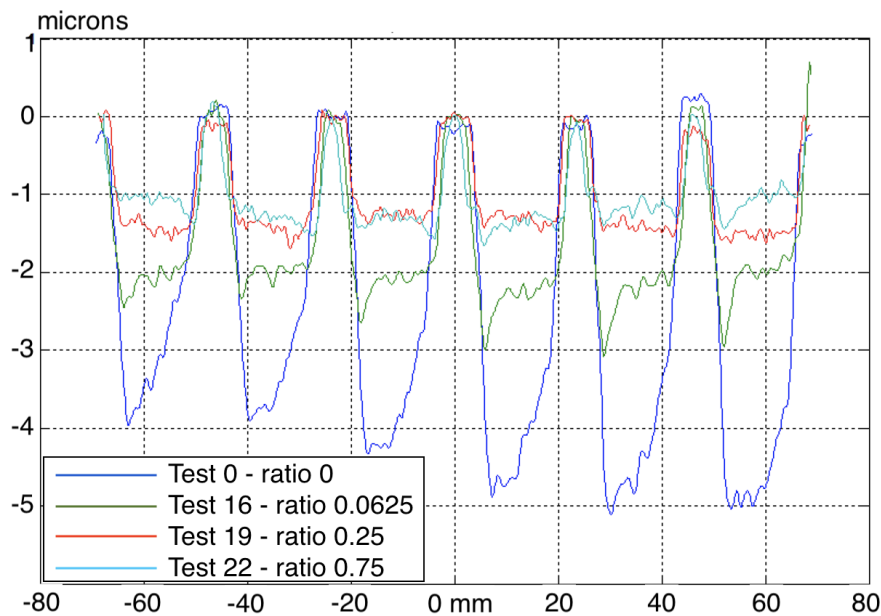
Figure 4-5 Stacked profiles from tests 0, 16, 19, and 22.

4.3.2 Spindle Speed Test

It was suspected that the shear-thickening behaviour of the slurry could have had a dragging effect on the tool spindle. As the slurry became increasingly viscous, it could potentially slow down the tool rotation speed, therefore explaining the sharp decrease in VRR. To test this theory, the true RPM of the tool spindle was independently measured in 20 RPM intervals by a Neiko tachometer with an uncertainty of ±0.05% RPM. The head speed at different input values were counted using this external counter under two scenarios: one where the tool was spinning in low-viscosity Newtonian slurry of test 0, and the other where the tool was spinning in the viscous CSS slurry of test 23. This is plotted in Figure 4-6. The readings from the external tachometer showed that the spindle had less than 1% decrease in RPM when spinning in shear-thickening slurry. Such slight differences weren't sufficient to explain the decrease in VRR.
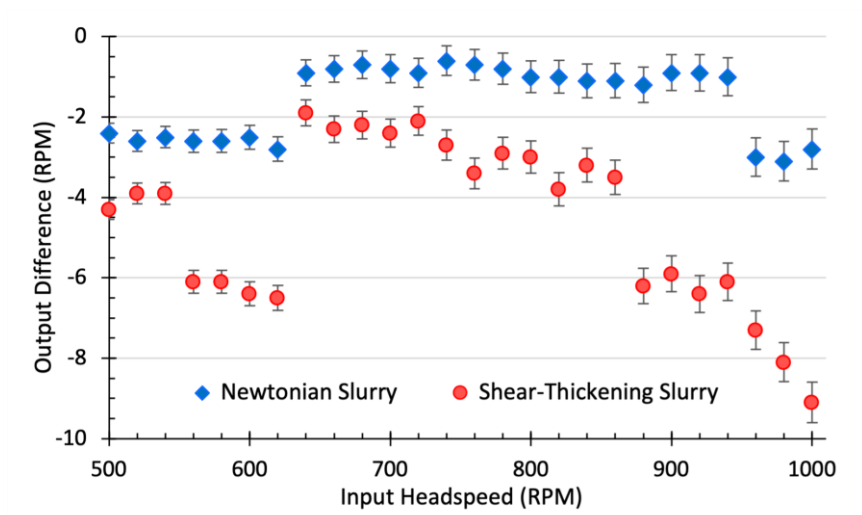
Figure 4-6 Decrease in spindle speed of the machine spindle under Newtonian and shear-thickening CSS slurries.

4.3.3   Particle Size Differences

Another possible explanation was the difference in the sizes of the suspended particles. The cerium oxide powder used was around 1.5-3.0μm in diameter (Solvay, n.d.). The cornstarch particles, however, were roughly 15μm to 20μm in diameter (Cui et al., 2014; Hossen et al., 2011). The particle size of cornstarch was confirmed using a white-light interferometer, shown in Figure 4-7. The blue circle represents what a cerium oxide particle would look like beside the cornstarch.
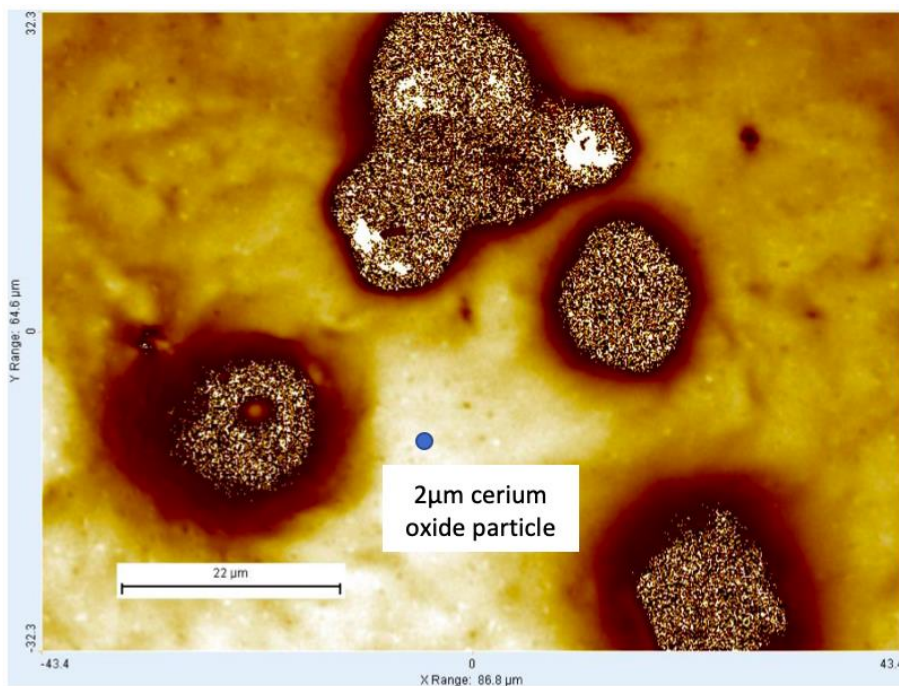
Figure 4-7 White-light interferometer image of cornstarch particles compared with a cerium oxide particle.

Being approximately an order of magnitude different in diameter, effectively three orders of magnitude larger in volume, the cornstarch particles could act as a cushion between the tool and the workpiece, preventing sufficient CMP processes from cerium oxide particles (Walker et al., 2017). One possible solution for future work would be milling the cornstarch to a finer particle size. Smaller particle size of cornstarch could provide different rheological properties, as well as interfere less with cerium oxide abrasives.

4.4   Mid-Spatial Correction Using Cornstarch Suspension Slurries

The addition of cornstarch into the system had a negative effect on the efficiency of the slurry to removal material during polishing. When compared to the traditional baseline slurry, highly shear-thickening CSS slurry provided around half the VRR. However, a system with lower VRR could nonetheless potentially show good ability in MSF mitigation, as both are not mutually exclusive. Therefore, CSS slurries' ability to mitigate existing MSF errors were tested, as well as the achievable texture.

4.4.1   Experimental Setup and Mid-Spatial Frequency Generation

The workpiece and setup of these experiments differed from those used for VRR experiments. This was to facilitate parallel data collection for another project at the Daresbury Laboratory for Ultra Precision Surfaces. A flat 100 x 100mm BK7 glass was used as the workpiece. It was returned to a controlled initial condition after each test through hand-smoothing on a flat cast iron lapping spindle using aluminium oxide abrasives. Shown in Figure 4-8, the workpiece was mounted and secured onto a 3D-printed holding tray. The holding tray had an indentation slot of nominally 100 x 100mm, larger than the workpiece by approximately 0.3mm so that the glass was effectively laterally constrained without being stressed. The underside of the holding tray was mounted via a spigot onto a bespoke force-measuring table through a Schunk chuck. The force table comprised a system of nested flexures and six load cells to provide real-time feedback of cartesian forces and torques during active polishing. The force and torque data-collection project ran in conjunction with the MSF generation and mitigation experiments.

The force table was kinematically mounted onto the horizontal turntable of the Zeeko IRP 600 CNC machine, and a 40mm radius inflated bonnet tool was used. The smaller bonnet (c.f. 80mm used previously) was chosen to facilitate MSF ripple generation, as a small tool provided better-defined tool signature. Polyurethane polishing cloth was adhered on to bonnet face. Shown in Figure 4-9, the glass surface was divided into three zones. Zones A and B were used to generate MSF surface ripples with two different spatial frequencies. Zone C was used to test the surface texture achieved using various slurries, and this is analysed in *section 4.5*. Referring to Figure 4-9, raster tool paths were used along the y direction, and profile scans were conducted along the x direction. Table 4-4 summarises the bonnet parameters used. Figure 4-10 and Figure 4-11 show the resulted MSF profile scan and the PSD conversion.
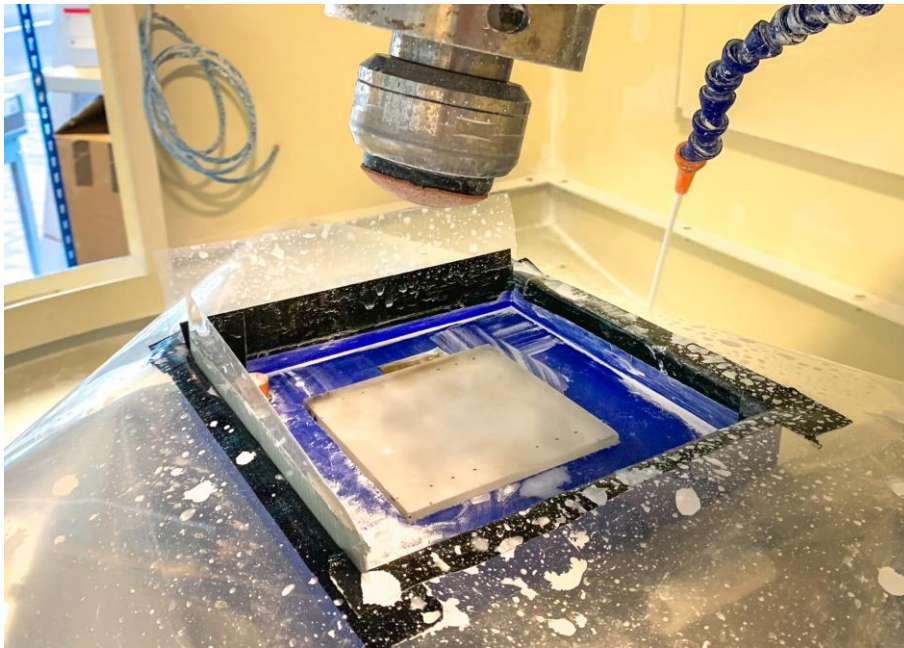
Figure 4-8 Setup for MSF mitigation tests with holding tray.

Table 4-4 Toolpath parameters for MSF generation.

Zone	Precess angle	Headspeed RPM	z-offset mm	Tool spot size mm	Track spacing mm	Feed rate mm/min
A	15°	800	0.2	7.99	1.2	90
B	15°	800	0.4	11.29	2	80
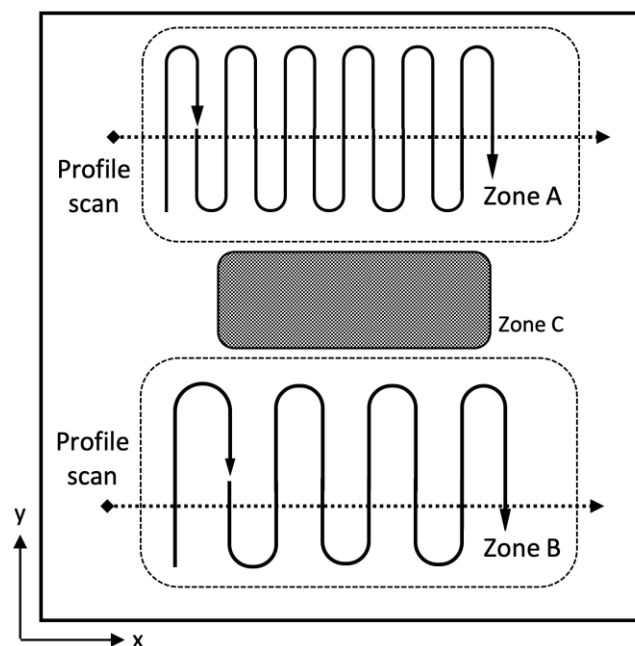
Figure 4-9 Workpiece surface toolpath allocation, with profilometry along x, and raster along y. (Not to proportion)
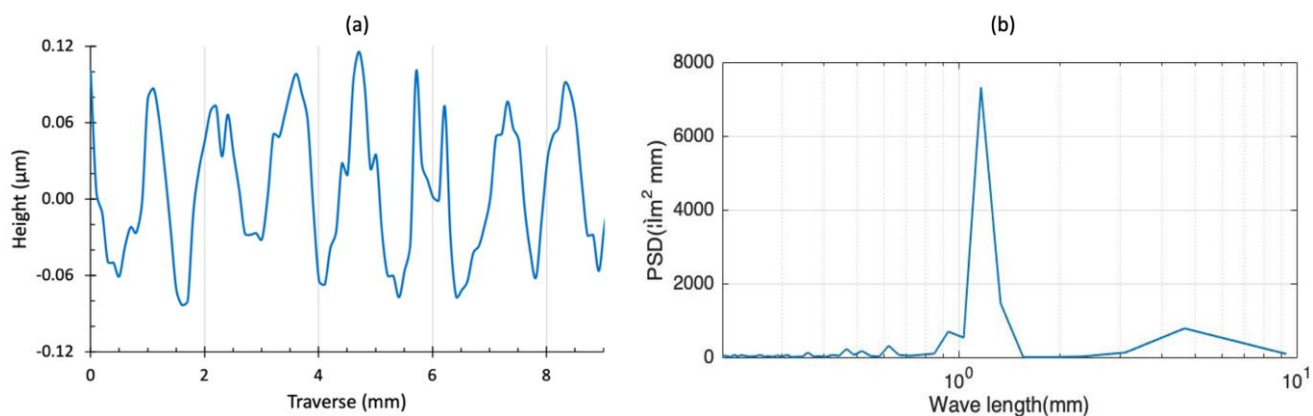
Figure 4-10 Profile (a) and PSD (b) of the 1.2mm MSF generation in zone A.
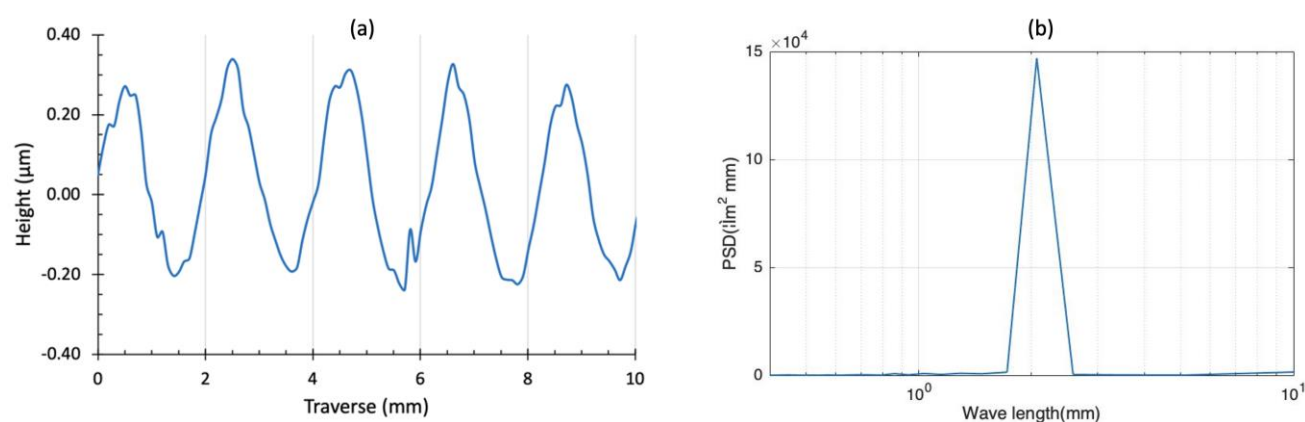
Figure 4-11 Profile (a) and PSD (b) of the 2mm MSF generation in zone B.

4.4.2   Toolpaths and Slurry Compositions

For each zone A and B, four raster toolpaths along the x direction (perpendicular to the ripples generated) were used in attempt to mitigate MSF features. The bonnet was used at a standard precess angle of 15°, headspeed of 800RPM, and z-off set of 0.5mm for a spot size of 12.61mm. Each toolpath utilised different track spacing, feed rate, and precess direction to stager the raster and prevent the generation of any new surface ripples. The parameters are summarised in Table 4-5.

Two abrasives were tested, cerium oxide and aluminium oxide. As in the *section 4.3*, the cerium oxide slurries were composed of 4 constituents: water, cornstarch, cerium oxide, and potassium sorbate. The cornstarch to water ratio was increased to reflect increasing shear-thickening behaviour. The cerium oxide concentration was kept at 2.6wt%, and the potassium sorbate concentration was kept at 0.5wt%. Six cerium oxide tests were conducted with the slurry composition summarised in Table 4-6. Three aluminium oxide slurries were also tested, and their compositions are summarised in Table 4-7.

Table 4-5 Toolpath parameters for MSF mitigation.

Zone	Raster run	Precess direction	Track spacing mm	Feed rate mm/min
A	1	+x	0.40	300
	2	-y	0.50	250
	3	-x	0.38	320
	4	+y	0.47	260
B	1	+x	0.50	300
	2	-y	0.60	175
	3	-x	0.43	280
	4	+y	0.57	200

Table 4-6 Cornstarch to water weight ratio for tests 24-29.

Test	Ratio	Test	Ratio	Test	Ratio
24	0	26	0.25	28	0.75
25	0.125	27	0.5	29	1

Table 4-7 Composition for tests 30-32 with aluminium oxide abrasives in weight concentration.

Test	Aluminium oxide	Cornstarch
30	5%	0%
31	5%	12.5%
32	5%	25%

4.4.3 Results and Discussion

Each test yielded profile traces and PSD plots for zones A and B respectively. The resulted figures are compiled in *Appendix A*. The MSFs generated were compared after the second raster polishing (run 2) and the fourth raster polishing (run 4). A good indication of MSF mitigation is the eroding of the PSD peak at the ripple frequency. The PSD peak values for each of the tests are summarised in Table 4-8 for zone A and Table 4-9 for zone B, and the percent reduction is compared graphically in Figure 4-12.

Test 24 to 29 increased in cornstarch concentration, with test 24 serving as the control experiment, without the presence of cornstarch. From the PSD data, all slurries demonstrated ability to decrease existing MSF ripples for both 1.2mm and 2mm spatial frequencies. There appeared to be a step change in polishing performance around cornstarch to water weight ratio of 0.25. Small addition of cornstarch did not have a notable effect on MSF mitigation, but higher concentration of cornstarch had consistently lower smoothing

efficiency when compared to the normal. This phenomenon could be explained with the particle size difference hypothesis explored in *section 4.3.3.*

Aluminium oxide abrasive particles used were ~9μm in diameter, so the size difference with starch particles were smaller. From the PSD data for tests 30 to 32, the addition of cornstarch had a positive effect on the mitigation of MSF ripples. All three slurries showed roughly equal ability to reduce the PSD peak by 81-87% after the four raster toolpaths. The main contribution made by the addition of cornstarch was the enhancement of performance by run 2. At 25wt% for test 32, the PSD reduction of run 2 almost reached the final achievable reduction of run 4. This suggests that in the presence of aluminum oxide, the addition of cornstarch aided the polishing efficiency of the slurry in reducing MSF ripples.

Table 4-8 PSD peak values and reductions for tests 24-32 of zone A, with peak unit of lm^2 mm.

Test	Generation	Run 2		Run 4	
	Peak	Peak	Reduction	Peak	Reduction
24	7200	1800	75%	500	93%
25	2000	400	80%	100	95%
26	1900	450	76%	200	89%
27	2200	1250	43%	900	59%
28	1000	600	40%	400	60%
29	2100	1300	38%	850	60%
30	2650	1300	51%	500	81%
31	2700	1350	50%	400	85%
32	2300	400	83%	350	85%

Table 4-9 PSD peak values and reductions for tests 24-32 of zone B, with peak unit of lm^2 mm x 10^4.

Test	Generation	Run 2		Run 4	
	Peak	Peak	Reduction	Peak	Reduction
24	15	5	67%	2.5	83%
25	10.5	3	71%	1.4	87%
26	9.7	5.4	44%	3.5	64%
27	12	5.8	52%	3.6	70%
28	8.3	5	40%	3.3	60%
29	15.3	11.8	23%	6	61%
30	14	8	43%	2.2	84%
31	11.5	3.2	72%	1.5	87%
32	14	2	86%	1.8	87%
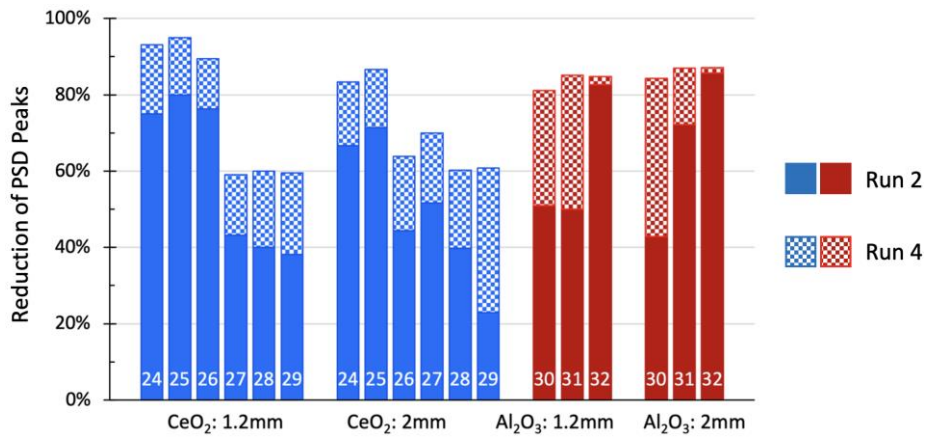
Figure 4-12 Comparison of PSD peak reduction for tests 24-32 with solid colours for run 2 and checkered for run 4.

4.5 Texture Achieved with Cornstarch Suspension Slurries

Referring to Figure 4-9, the workpiece was divided into three zones, with zone C reserved for texture measurements. The six CCS slurries with cerium oxide abrasive were tested, with slurry composition of test 24 to 29 summarised previously in Table 4-6. Zone C was 600mm^2 in area, and it was subjected to a total of 36 minutes of polishing with the 40mm bonnet precessed at 15° with 800rpm headspeed. The texture interferometer measured a circular area of 0.1mm in diameter. Figure 4-13 serves as a representative image showing the interferometer interface and measurement result. After each test, 5 texture measurements were taken at different locations on zone C to calculate an average and standard deviation. The results are summarised in Table 4-10 and compared in Figure 4-14.

Basic Statistics (ISO)	
PV	61.214 nm
RMS	5.370 nm
Sa	4.311 nm
Zernike Tilt	221.748 nm
Zernike Power	-4.310 nm
Power Deviation	-8.620 nm
Zernike Astig	13.645 nm
Zernike Coma	2.704 nm
Zernike Spherical	-1.236 nm
Part Diameter	0.108 mm
Part Width	0.102 mm
Part Height	0.083 mm
Part Center X	0.055 mm
Part Center Y	0.045 mm
Meas Wv	635.000 nm
Display Wv	632.800 nm
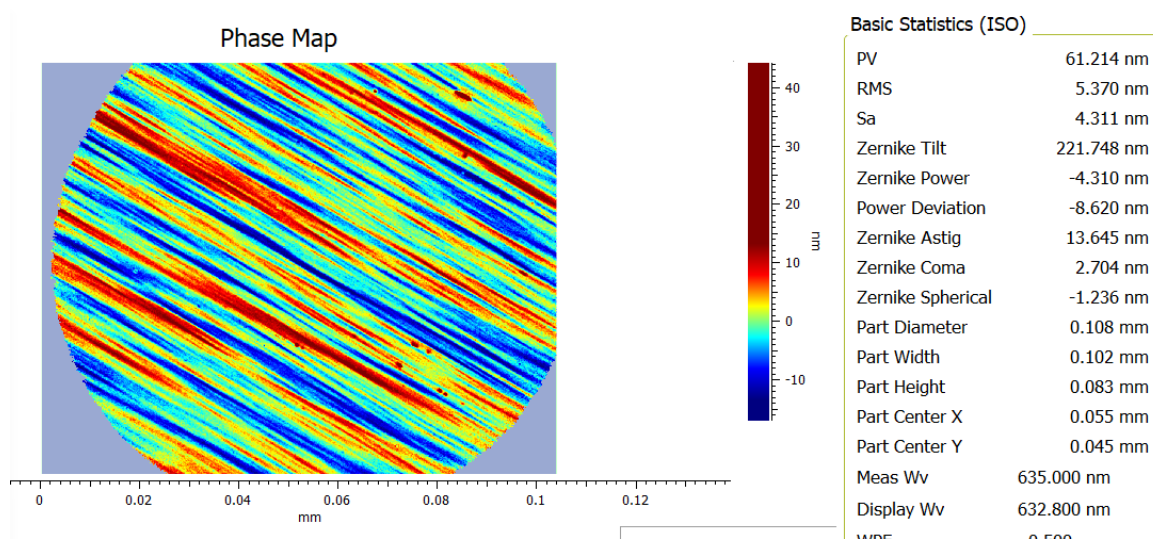
Figure 4-13 Texture measurement after test 26.

Table 4-10 Mean and standard deviation of texture Sa (nm) from tests 24-29.

Test	Average	St. Dev.	Test	Average	St. Dev.
24	2.95	0.193	27	4.82	0.266
25	3.63	0.327	28	6.23	0.447
26	5.01	0.319	29	9.04	0.358
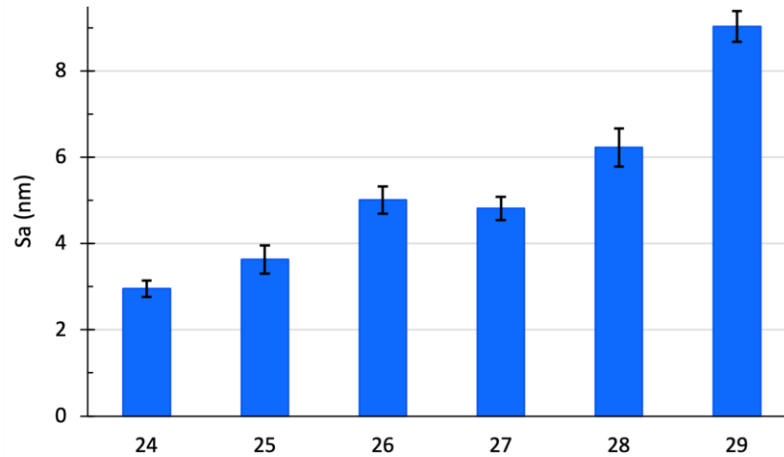
Figure 4-14 Mean and standard deviation of texture Sa (nm) from tests 24-29.

Texture could be quantitatively represented by either the arithmetical mean height (Sa) or the root mean square height (RMS). Sa was chosen as the criterion for this section. Test 24 served as the control for the texture measurements. Without cornstarch, the conventional cerium oxide slurry achieved texture of under 3nm. This was consistent with the texture achievable in literature with polyurethane cloth on an inflatable bonnet (Li, 2012; Walker et al., 2011; Walker et al., 2019). With each increase of cornstarch in the system, the achieved texture worsened. This correlation could be explained by the large particle size of the starch particles, causing deep gashes onto the workpiece surface.

4.6   Conclusions

The polishing performance of CSS slurries were tested. First the VRR of cerium oxide slurries with varying cornstarch concentration were examined, and the addition of cornstarch had a negative impact on the VRR. This was contrary to the hypothesis that a shear-thickening slurry would enhance material removal rate. This phenomenon could be attributed to the difference of particle size. Cerium oxide abrasives were 2μm in diameter on average. Cornstarch particles were 20μm in diameter. This is confirmed using a white light interferometer and confirmed through literature in *section 4.3.3*. Cornstarch particles being 1000 times greater in volume than cerium oxide particles could cause a shielding effect that prevents the abrasive from coming into contact with the glass surface.

The CSS slurries' ability to mitigate existing MSF artefacts were then tested with two abrasives: cerium oxide and aluminium oxide. Similar to the VRR tests, the addition on cornstarch had an inhibitory effect on MSF mitigation for the cerium oxide abrasive. The CSS cerium oxide slurries were tested for their achievable texture. Due to the large particle size of the starch, increasing cornstarch concentration had a negative effect on the final texture. One possible solution for future work would be milling the cornstarch to a finer particle size. Smaller particle size of cornstarch could interfere less with cerium oxide abrasives.

However, there was evidence that the addition of cornstarch enhanced the efficiency of the aluminium oxide slurry. The slurry was able to smooth away ripples quicker than its standard Newtonian counterpart. The final PSD peak reduction produced from aluminium oxide slurries was 87% after 4 runs, but the reduction already could reach 86% after the initial 2 runs. This was in line with the hypothesis regarding STF slurries and warrants future experiment to explore further the role of STF slurries with aluminium oxide abrasives. This is an important result, as aluminium oxide slurries are widely used to "smooth" glass surfaces, before polishing, and after milling the base form using bound-abrasive grinding-wheels on traditional CNC machines.

5   Rheology and CFD Modelling of Cornstarch Suspension Slurries

The viscosity of non-Newtonian (n-N) materials changes with respect to shear rate. A subclass of n-N materials known as shear-thickening fluids (STFs) increases in viscosity with increasing shear rate. They are hypothesised ability to enhance polishing efficiency, improve surface texture, and mitigate mid-spatial frequency (MSF) ripples. Surfaces with MSFs scatter light, reduce optical throughput, and decrease system signal-to-noise ratio. Mitigation of MSFs continues to pose a technical challenge in aspherical and freeform surface manufacturing with area-targeted sub-aperture polishing.

Two STF systems were explored in *chapter 3* and *4* – polyethylene glycol (PEG) and cornstarch suspension (CSS) respectively. While PEG systems showed limited polishing capabilities, CSS systems demonstrated some abilities in mitigating existing MSF ripples. Current progress on STF polishing had been largely process-driven (Burge & Kim, 2012; Li et al., 2015; Nguyen, 2020). This leaves a significant incentive to explore the underlying mechanisms, through rheology and computational fluid dynamics (CFD) modelling, to paint a more complete picture of STF polishing.

A robust understanding of the viscous behaviour of CSS systems is essential to build an accurate CFD model of STF polishing. This chapter focuses on the rheology of CSS slurries and the simulation of material properties in CFD modelling. The rheological properties of the simulated STFs were then compared to the physical rheology data.

5.1   Introduction to Rheology

Eugene Bingham was a professor in the Department of Chemical Engineering at Lafayette College in the early 1900s. The research field which Bingham explored was originally called *the mechanics of continuous media*. As a chemistry professor, Bingham humorously remarked, "No, such a designation will frighten away the chemists!" (Reiner, 1964). By consulting a fellow professor in classical languages, Bingham arrived at the new designation of *rheology* (πάντα ῥεῖ) which was inspired by the motto of Heraclitus, a pre-Socratic Greek philosopher, meaning *everything flows* (Reiner, 1964). Nowadays, the term rheology is used to describe the study of the deformation and flow of matter (Law and Rennie, 2015a).

5.1.1   Apparent Viscosity

In an edition of *Principia*, Sir Isaac Newton hypothesised, "the resistance which arises from the lack of slipperiness of the part of the liquid, other things being equal, is proportional to the velocity with which the parts of the liquid are separated from one another." (1687). The "lack of slipperiness" mentioned by Newton is known as apparent viscosity. It measures the flow resistance, which is influenced by the fluid's velocity

gradient (shear rate), flow characteristics, and geometry. Viscosity μ is defined as the ratio between stress τ and shear rate $\dot{\gamma}$ (6-1), and the shear rate is the change in strain $d\gamma$ in a given amount of time dt (6-2).

$$\mu = \frac{\tau}{\dot{\gamma}}$$

(5-1)

$$\dot{\gamma} = \frac{d\gamma}{dt}$$

(5-2)

Figure 5-1 illustrates the relationship between viscosity and shear rate over several orders of magnitude for n-N materials. For most materials, the shear-thickening and shear thinning region extended over just a few orders of magnitude of shear rates. In the limit of very low and very high shear rates, the viscosity was observed to be constant. These two extremes are known as the lower and upper Newtonian region respectively (Barnes, Hutton, & Walters, 1993).
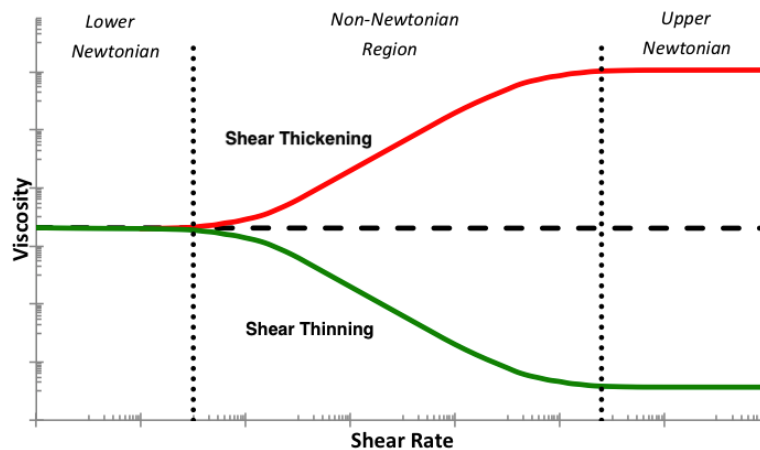
Figure 5-1 Viscosity vs shear rate graph for n-N materials on log-log scales.

The viscosity of a Newtonian fluid by definition is constant and independent of shear rate. However, changes in flow characteristic could still alter the apparent viscosity of Newtonian fluids. For example, when laminar flow transitions to turbulent, the streamline flow breaks down into vortices and turbulences. These flow regimes require more energy, and the apparent viscosity of the liquid increases (Barnes, 1993). Unless otherwise stated, apparent viscosity in this chapter will simply be referred to as "viscosity".

5.1.2 Molecular Mechanism for Shear-Thickening Behaviour

STFs are generally high-concentration suspension systems. At low shear rate, the fluid medium is sufficient in providing ample lubrication for the motion of suspended particles to flow past one another, and the resulting shear stress is low. The onset of shear-thickening occurs when the shear force applied overcomes the repulsive interparticle forces (Boersma, Laven, & Stein, 1990). The fluid under high shear rates tends to dilate slightly, given rise to another name for STFs – dilatants, shown by Figure 5-2.
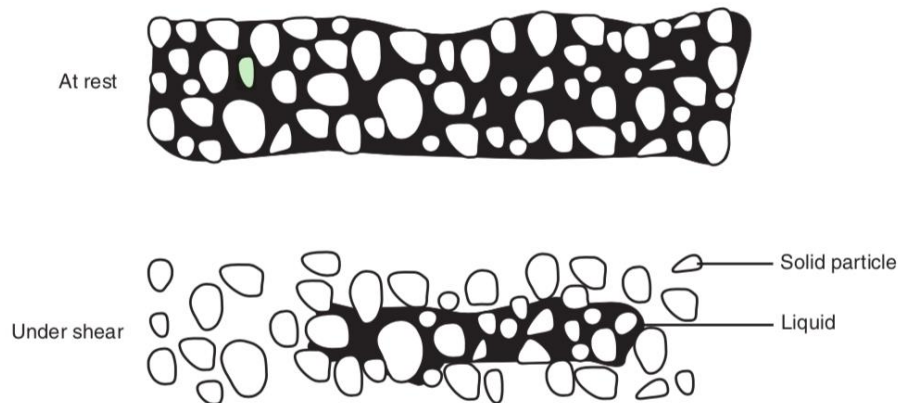
Figure 5-2 Representation of shear-thickening and dilation behaviour (Chhabra & Richardson, 2008).

The dilation causes micro-voids to form in the fluid, and the medium is insufficient to fill the voids fast enough. The direct solid-solid contact between particles results in the formation of particle aggregates through hydrodynamic forces (Cheng et al., 2011; Li et al., 2018a). The particle aggregates then collide with each other as shown in Figure 5-3, coalescing into hydroclusters in a mechanism known as the 'hydrocluster theory' (Brady & Bossis, 1985; Branda et al., 2007). This hinders the flow of the fluid, thus increasing the viscosity of the system (Chhabra & Richardson, 2008).
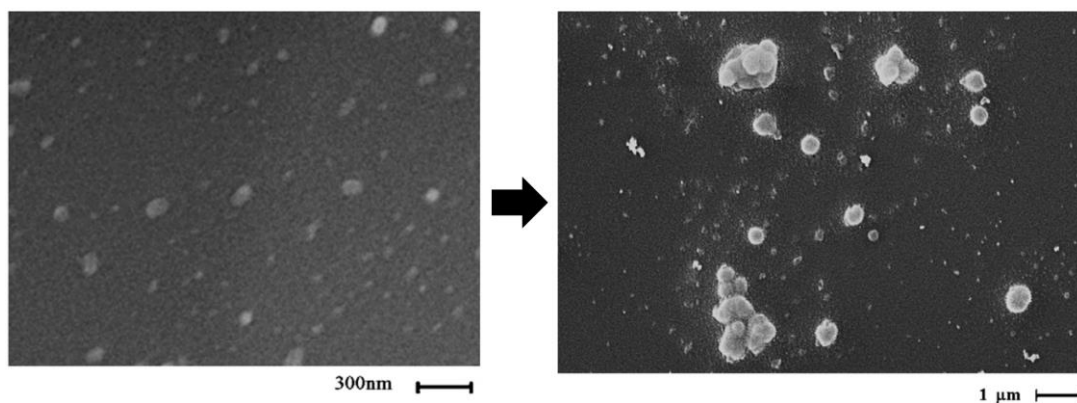
Figure 5-3 SEM imaging of hydrocluster formation from particle aggregates (Branda et al., 2007).

5.1.3 Flow Regimes

The flow regime, or characteristics, of a fluid in motion depends on the setup of the system, such as geometry, flow speed, fluid density, and viscosity. There are two main types of flow regimes: laminar and turbulent flow. The flow characteristic is said to be laminar when the fluid flows in smooth and infinitesimal parallel layers in the direction of bulk flow. The flow characteristic is said to be turbulent when the fluid motion is chaotic and irregular, often accompanied by eddies and vortices.

$$Re = \frac{\rho V L}{\mu}$$

(5-3)

Where, ρ is the density of the fluid in kg/m^3

V is the speed of the fluid in m/s

L is the characteristic length in m

μ is the dynamic viscosity of the fluid in Pa·s

The flow regime can be predicted by the Reynolds number (*Re*) (Reynolds, 1883). *Re* is a dimensionless number calculated through Equation (5-3). A system with *Re* smaller than 2300 is most likely to conserve laminar flow, while *Re* greater than 2900 dictates turbulent flow (Schlichting & Gersten, 2018). The characteristic length *L* depends on the geometry. For example, when predicting the characteristics of pipe flow, the characteristic length would be the diameter of the pipe.

5.2   Rheology of Cornstarch Suspension Slurries

Experiments in *section 3.5* showed the potential of CSS slurries in MSF mitigation. To better understand the underlying mechanisms, seven samples were sent for viscosity analysis. These samples consisted of four components, which were reflective of CSS slurries used in *chapter 4*: water, cornstarch, cerium oxide, and potassium sorbate. The compositions are summarised in Table 5-1.

Sample 1 was pure de-ionised water, and this served as a known Newtonian normal. Sample 2 was the conventional cerium oxide polishing slurry, with cerium oxide concentration of 2.6wt% in water. Samples 3 to 7 gradually increased in cornstarch concentration in water to induce shear-thickening behaviour, with the addition of potassium sorbate as the preservative at 0.005wt%.

Table 5-1 Cornstarch to water weight ratio for samples CSS-1 to CSS-7.

Sample	Cerium oxide	Ratio	Sample	Cerium oxide	Ratio
CSS-1	/	0	CSS-5	2.6wt%	0.5
CSS-2	2.6wt%	0	CSS-6	2.6wt%	0.75
CSS-3	2.6wt%	0.125	CSS-7	2.6wt%	1
CSS-4	2.6wt%	0.25			

5.2.1   Cone-Plate Rheometer Theory

A cone-plate rheometer was used to test the seven samples. During testing, the fluid was placed on the bottom plate, with the top cone rotating at predetermined speeds. Referring to Figure 5-4, the top cone used an angle θ of 2°, and a radius R of 25mm. The cone and plate gap at the centre was kept at 0.07mm. The rotational shear stress τ could be calculated as a function of the torque M, sensed by the plate sensor. The shear rate could be calculated from the input angular velocity ω of the cone. Combining with Equation (5-1), the viscosity at various shear rates could be calculated as a function of torque and angular velocity – Equation (5-9).
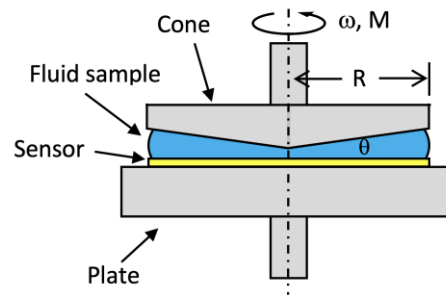
Figure 5-4 Schematic of the cone-plate rheometer (picture by author and not to scale).

$$\tau = \frac{M}{rA} = \frac{dM}{r\,dA} = \frac{dM}{2\pi r^2\,dr}$$

(5-4)

$$\int_0^M dM = 2\pi\tau \int_0^R r^2 dr$$

(5-5)

$$M = \frac{2}{3}\pi\tau R^3$$

(5-6)

$$\tau = \frac{3M}{2\pi R^3}$$

(5-7)

$$\dot{\gamma} = \frac{d\dot{\gamma}}{dt} = \frac{V_r}{R} = \frac{\omega r}{r \sin\theta} = \frac{\omega}{\sin\theta}$$

$$\mu = \left(\frac{3\sin\theta}{2\pi R^3}\right)\frac{M}{\omega}$$

5.2.2   Apparent Viscosity Profiles from Rheometer

The samples were tested at 25°C (±0.5°C). The shear rate was ramped from 100 s^{-1} to 1000 s^{-1}. This shear rate range corresponded to an equivalent local surface speed at the interface with the workpiece of an 80mm bonnet precessed at 15°C rotating between 100 – 1000 RPM. Each sample was tested three times for repeatability, but sample 7 was only tested once due to coagulation over time because of high suspension loading. The data of the three repeats for samples 1-6 were averaged, and the resulted viscosity curve is given in Figure 5-5.

Sample 1 served as a known Newtonian normal. The theoretical viscosity of should be 1 mPa·s independent of shear rate at room temperature. The rheometer data showed an increase in viscosity, which potentially could be caused by a combination of factors such as turbulence, calibration error, or system geometry.

5.2.3   Flow Regimes in the Rheometer

The flow characteristic of the fluid influences the viscosity measured. Even for a Newtonian fluid, turbulence flow creates small eddies and vortices that induces drag and increases the viscosity. The rheology data from all seven samples exhibited some degree of shear-thickening, and some of that phenomenon could potentially be explained by turbulence flow in the rheometer.

The flow regime of a system could be predicted by *Re*, introduced in *section 5.1.3*. The speed of the flow was taken as the outer radius of the rotating cone, where the flow was quickest and least stable. The characteristic length *L* was taken as double the height between the edge of the cone and the plate. Using the viscosity data collected, the Reynolds number was calculated for each sample at various shear rates, and these are summarised in Table 5-2.

All of the Reynolds number calculated were below 2300, which suggests that the characteristic within the rheometer conserved laminar flow across the seven samples. Under laminar flow, the viscosity of water (sample 1) should remain at 1 mPa·s. The increase of viscosity shown from the data then suggests a possible calibration error of the rheometer.
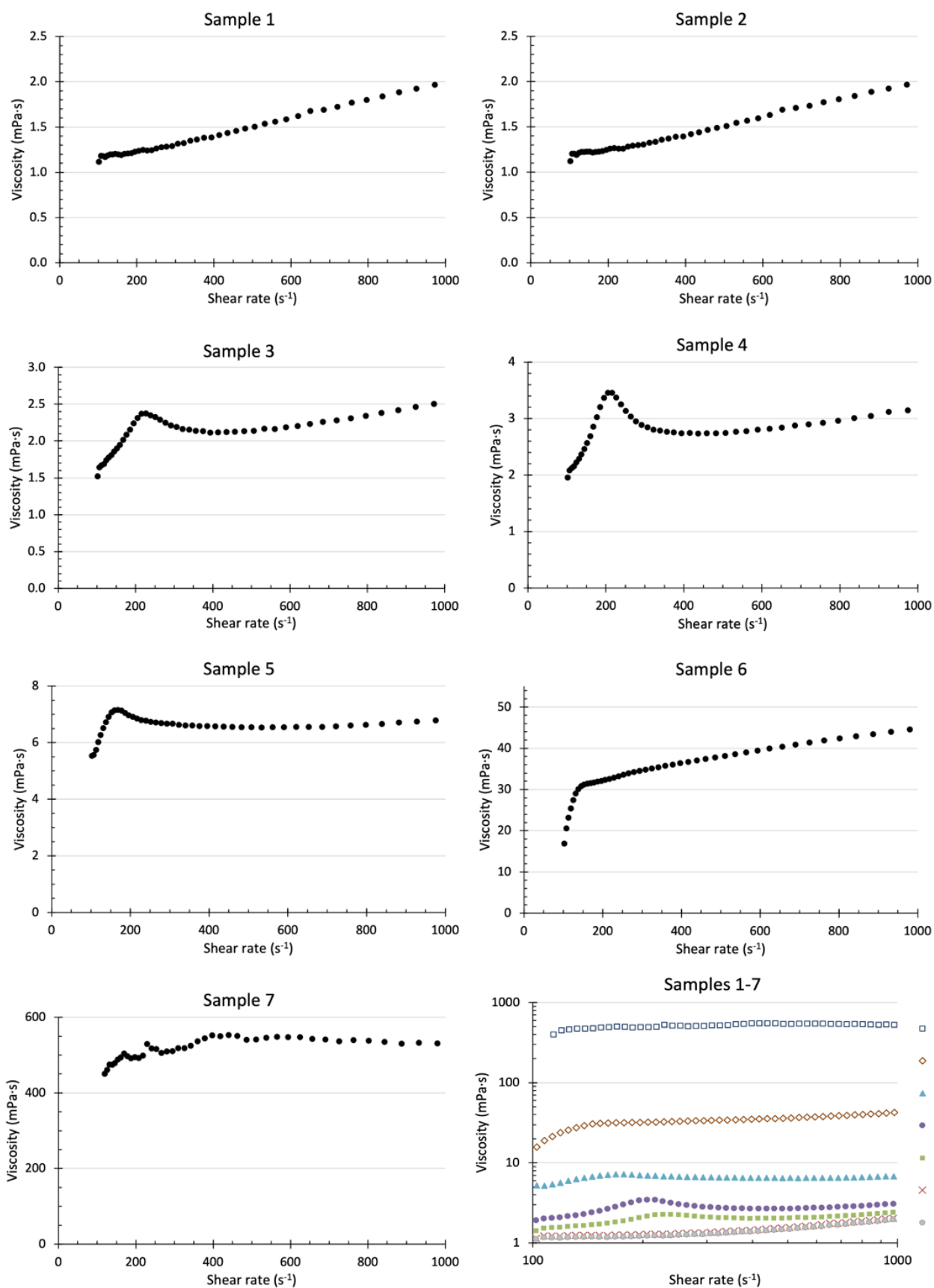
Figure 5-5 Viscosity profiles for samples CSS-1 to CSS-7. (Note the logarithmic nature of the last graph)

Table 5-2 Reynolds number calculations for samples CSS-1 to CSS-7.

Sample & ρ (kg/m³)	μ (mPa·s) & Re	Shear rate (s⁻¹)				
		100	200	400	600	1000
1	μ	1.12	1.24	1.39	1.62	1.97
1000	Re	159	288	513	658	903
2	μ	1.15	1.28	1.45	1.66	2.05
1003	Re	156	279	493	646	870
3	μ	1.43	2.17	2.04	2.10	2.42
1033	Re	129	169	361	524	759
4	μ	1.92	3.49	2.70	2.77	3.10
1065	Re	99	109	281	411	611
5	μ	5.27	7.07	6.55	6.51	6.84
1096	Re	37	55	119	180	285
6	μ	15.8	32.1	35.1	37.6	42.6
1126	Re	13	12	23	32	47
7	μ	105	495	553	548	531
1153	Re	1.95	0.83	1.48	2.25	3.86

5.2.4 Calibration of Viscosity Profiles and Discussion

Sample 1 was used as the normal to calibrate the rheometer data. The viscosity readings were adjusted accordingly for samples 2-7. This resulted an overall downwards shift on the viscosity profiles, and the calibrated data are presented in Figure 5-6.

The rheometer data for sample 2 closely resembled that of sample 1 with deviations withing ±0.020% of water. This suggests that the conventional cerium oxide polishing slurry could be assumed as Newtonian in nature. Samples 3-7 gradually increased in cornstarch concentration. An initial shear-thickening phase could be seen between 100 – 200 s⁻¹. Samples 3, 4 and 5 exhibited a peak in viscosity at around 200 s⁻¹. Between shear rates of 400 – 1000 s⁻¹, the viscosities of samples 3-7 followed an almost linear trend.

5.3 Computational Fluid Dynamics Modelling of Cornstarch Suspension Slurries

Prior-art in n-N polishing were mostly experimental-driven, leaving a significant area of exploration in the underlying rheology and CFD modelling of shear-thickening polishing slurries (Burge & Kim, 2012; Li et al., 2015; Nguyen, 2020). A valid CFD model of polishing would rely heavily on the correct material definition of the n-N used. This section aims to construct accurate material definitions of CSS slurries using the Ansys Fluent 2019 R1 software.
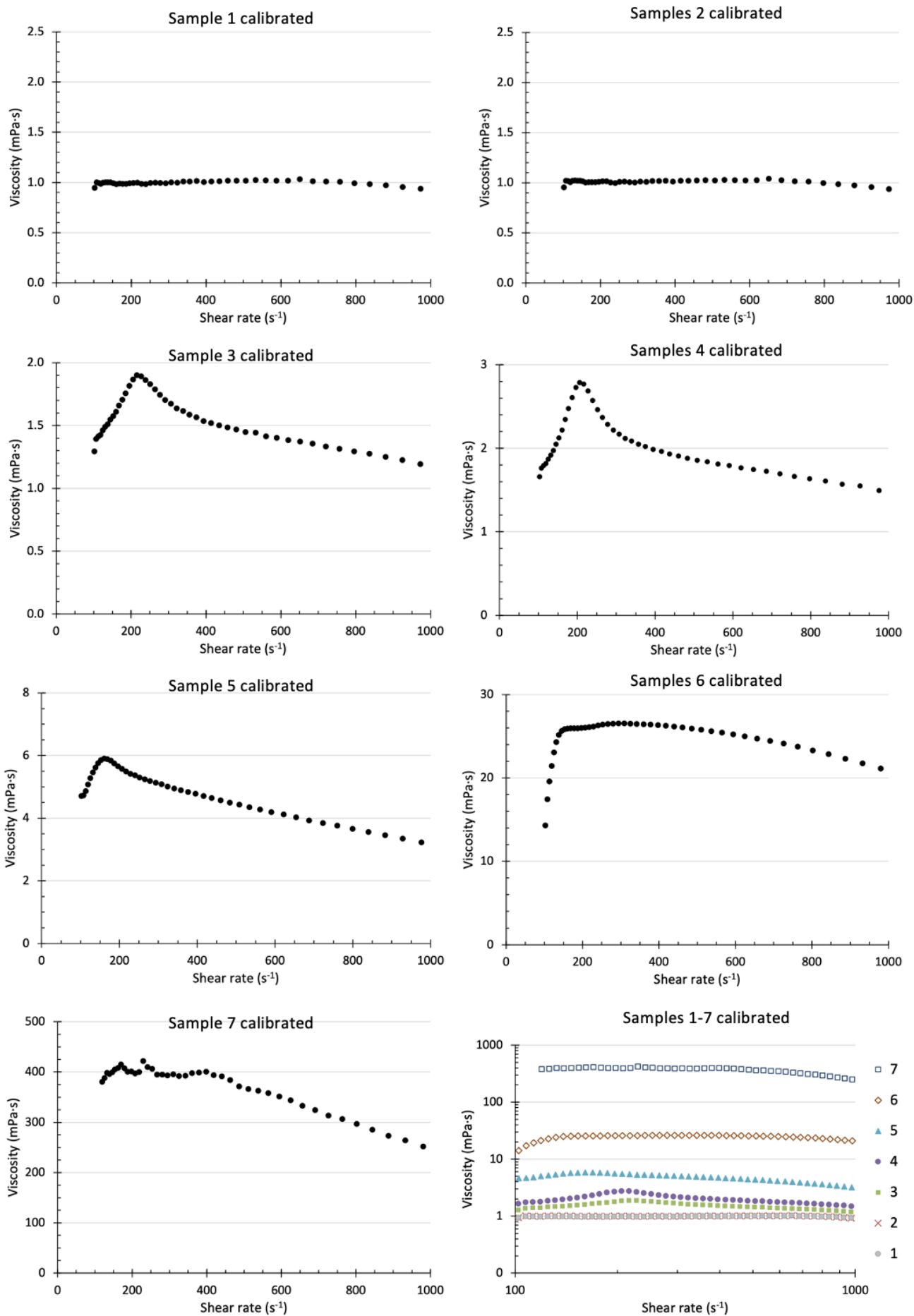
Figure 5-6 Calibrated viscosity profiles for samples CSS-1 to CSS-7. (Note the logarithmic nature of the last graph)

5.3.1 Boundary Conditions and Meshing

Referring to the geometry of the fluid sample shown in Figure 5-4, the 3D fluid domain was constructed in Solidworks® and imported into Ansys, with the cross section shown in Figure 5-7. The top surface of the fluid domain reflected the shape of the cone and was made to have a rotational boundary condition. The bottom surface represented the plate sensor of the rheometer and was made to remain stationary. The boundary condition for both the cone and plate surfaces were set to no-slip wall. No-slip boundary condition deemed the full transfer of momentum from the surface onto the fluid layer in contact.
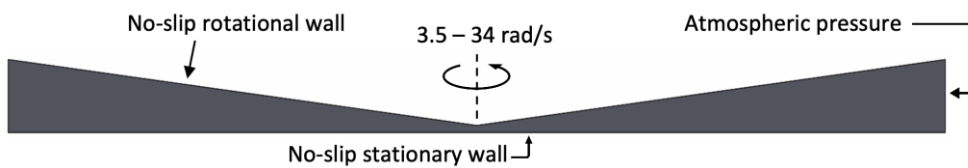
Figure 5-7 Cross section of the fluid domain with boundary conditions. (Not to proportion)
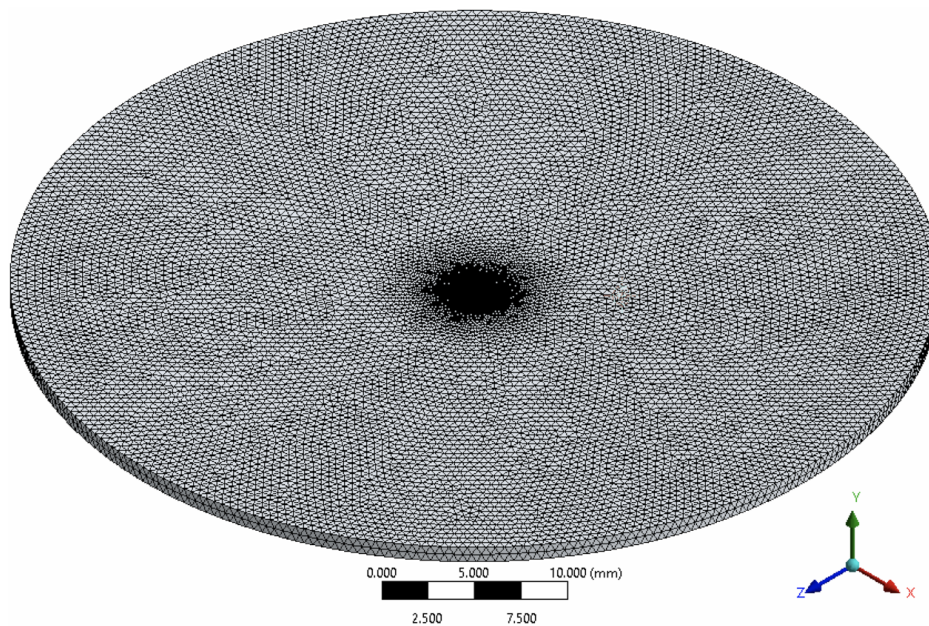
Figure 5-8 Meshing of the 3D fluid domain.

Ansys solver employed finite element analysis when computing results, and the meshing procedure divided the project into small elements. Such elements could be set to either triangular/tetrahedron or square/cubic. The element size determined the number of elements in the mesh. There was a trade-off between total element number and computational time. A finer mesh produced a more accurate model at the expense of computation time. Targeted mesh refinements could be made at strategic areas of interest to decrease the strain on computational power, such as stress concentrations or fluid exchange interfaces. Optimal element

size depended on the flow characteristics of the fluid as well as the complexity of the geometry. Guided by literature survey, an element size of 0.5mm was chosen for the mesh to generate a total of ~164,000 elements and nodes (Argyropoulos & Markatos, 2015; Chauhan, Bhalla, & Danish, 2019).

5.3.2 Material Property Definition

Ansys had a comprehensive database of materials of well-studied properties, with the majority being homogenous fluids such as water, ethylene glycol, and engine oil. For heterogenous suspension systems that were not within the material database, such as CSS-ceria slurries, the user could define new materials through input of various properties such as the density and viscosity profile. There were four options when defining the viscosity profile of a new material, shown in Figure 5-9: constant, temperature dependent, shear rate dependent, and user-defined function (UDF).

The constant viscosity profile was designed for fluids that behave in a Newtonian manner. Temperature dependent viscosities did not apply, as the experiments in this thesis exclusively examined the relationship between viscosity and shear rate under constant temperature. There were many curve-fitting models provided by Ansys for shear rate dependent viscosities, such as the power law model, the Carreau model, and the Herschel-Bulkley model. The power law model was introduced and used previously in *section 3.5* for samples PEG-1 to PEG-3. For samples CSS-1 to CSS-7, especially the latter five, the viscosity profiles did not follow any of the shear rate dependent models provided by Ansys. Therefore, the last option was utilised for viscosity definition – UDFs.
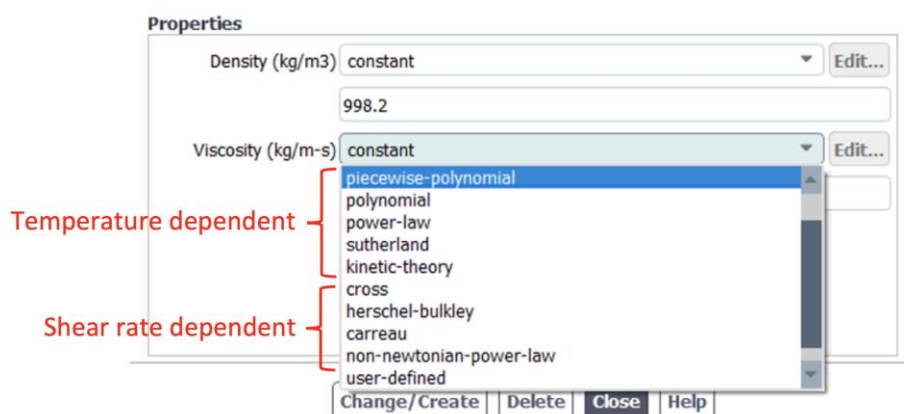
Figure 5-9 Ansys user interface for viscosity profile input.

Material property definition made by UDFs employed the C coding language. Referring to Figure 5-5, the Excel curve-fitting trendline function was used to generate the best fit equations for each of the samples. For samples 1 and 2, a linear relationship was used between the viscosity and shear rate. For samples 3-7, a

combination of linear, polynomial, and power law equations were used. The viscosity profile for sample 1 is given in Figure 5-10. The C code for samples 2-7 can be found in *Appendix B*.

```c
#include "udf.h"

DEFINE_PROPERTY(cellViscosity,c,t)
{
    double mu; /* This is the viscosity variable */
    double shRate = C_STRAIN_RATE_MAG(c,t);
    mu = (shRate * 0.000001558 + 0.9996) / 1000;
    return mu;
}
```

Figure 5-10 User-defined function for sample CSS-1.

5.3.3   Modelling of Sample CSS-1 – The Control Experiment

Sample 1, being water, should exhibit Newtonian viscosity across all shear rates under laminar flow. Viscosity data from rheology in *section 5.2.2* showed sample 1 to increase in viscosity. Calibration of the viscosity profile was carried out, and Ansys CFD was then used to validate the calibration and the UDF definition.

Ansys provided a selection of flow regime models. As the Reynolds number calculations from the previous section predicted exclusively laminar flow, the laminar flow model was chosen. The viscosity profile for the samples was defined through UDFs due to the empirical nature of the rheological data. While CSS slurries were not within the Ansys material database (samples 2-7), water could be defined using the database. Therefore, a comparison experiment was conducted to compare the accuracy of the CFD model between using a Newtonian definition (μ = 1 mPa·s) and the empirical definition (UDF) of the viscosity of sample 1.
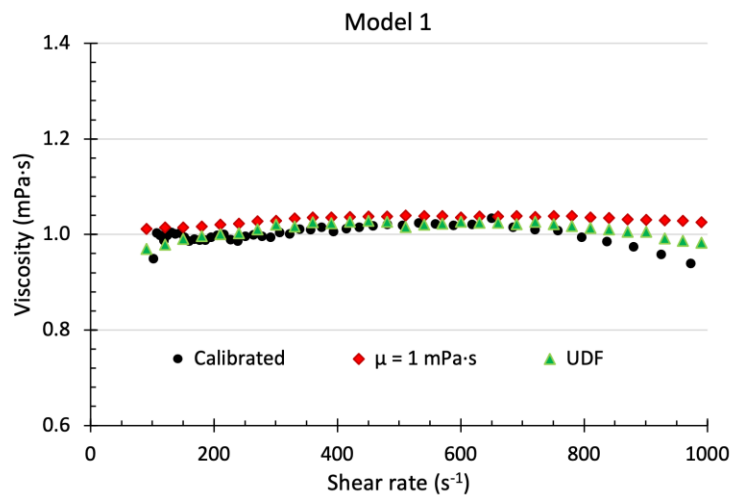
Figure 5-11 CFD results for model 1, comparing 2 methods of material definition.

Figure 5-11 shows the resulted viscosity profile from the CFD model. When using the material definition of μ = 1 mPa·s, the result deviated from the rheometer data by 5.11%. In contrast, the UDF deviated by 3.40%, suggesting that the UDF is a valid method in material definition for the empirical data collected from the rheometer.

5.3.4   Modelling of Samples CSS-2 to CSS-7

Following the logic of the previous section, CFD simulation of samples 2 to 7 employed laminar flow regime and used the empirical viscosity profiles from the UDFs. Each sample corresponded to models 2 to 7 respectively, and the simulated results are shown in Figure 5-12. The CFD simulations produced viscosity results indicative of the rheometer data. There were some discrepancies and the average deviation between the model and rheometry are summarised in Table 5-3. The models produced average deviations smaller than 4.8%.

5.4   Conclusions

Rheology of 7 samples, 5 of which contained cornstarch, showed increasing shear-thickening behaviour with increasing cornstarch concentration. The empirical viscosity data collected were used to create the viscosity profiles for material definitions in Ansys CFD modelling. A model of the rheometer was built within the CFD, and the simulation results were compared with the rheological data. The two data sets closely resembled one another with average deviation lesser than 4.8%.

The above simulation exercises confirmed a few key aspects in building a robust software model for non-Newtonian polishing with CSS slurries. Firstly, the experiments confirmed the legitimacy of user-defined functions – materials not within the internal database could be defined using C-code to produce accurate results. Secondly, the flow characteristics within the rheometer was most likely laminar by confirming with CFD modelling. Thirdly, the entire CFD process chain (building the geometry, defining the material, setting the flow regime, and calculating the resulting values) produced results indicative of the real world.

Referring to Figure 5-6, samples 3, 4, and 5 showed a local viscosity maximum at shear rate of ~$200s^{-1}$. Both increase in viscosity and tool headspeed could results in higher material removal. Further CFD modelling in the next chapter explores which factors could be the larger influencer in the process efficiency. This study of numerical simulation of shear-thickening fluids provided vital steppingstones for more comprehensive CFD models of non-Newtonian polishing, which is explored in the next chapter.
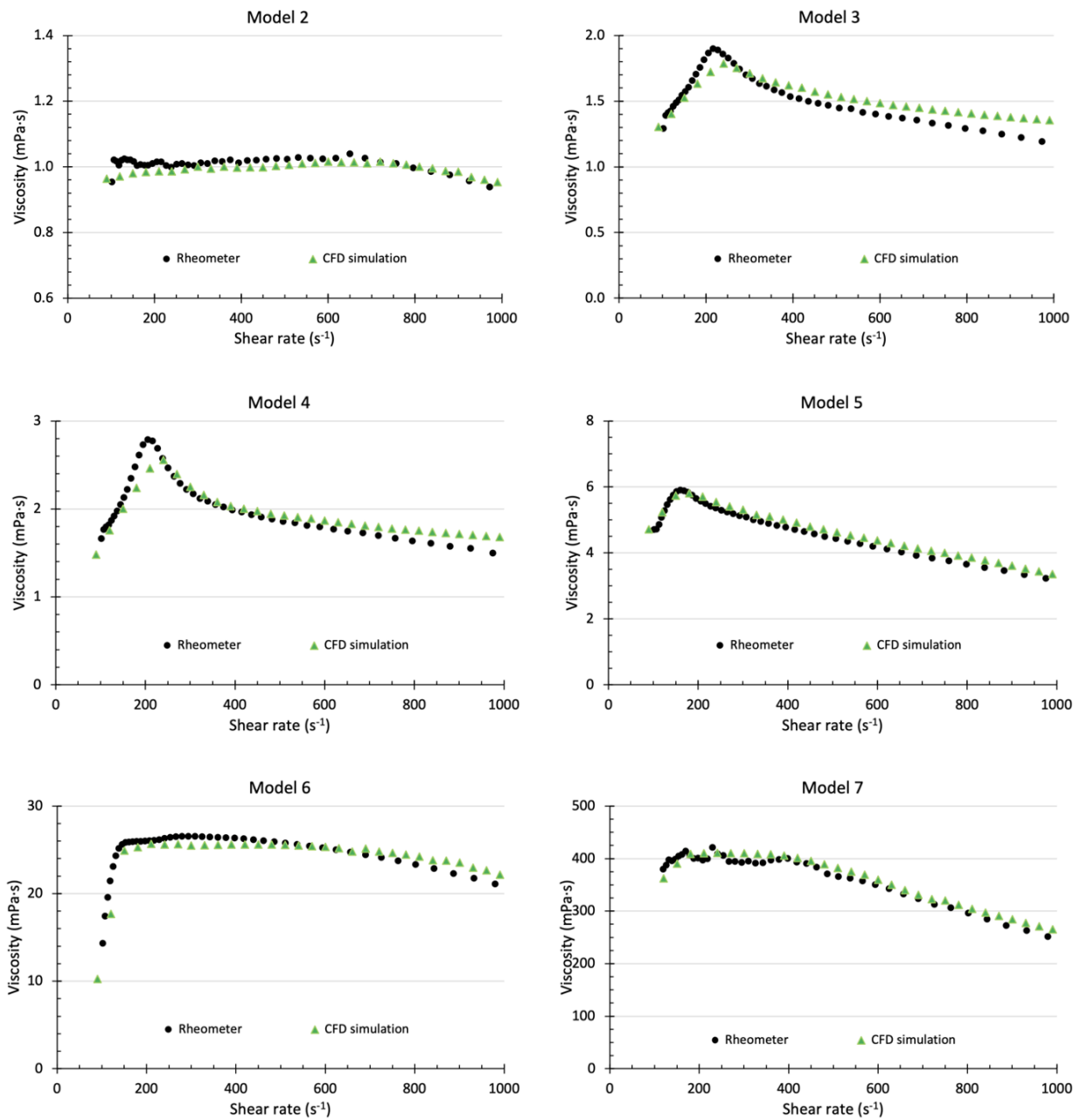
Figure 5-12 CFD results for models 2-7.

Table 5-3 Deviation of CFD simulation from rheometer data for models 1-7.

Model	Deviation	Model	Deviation
1	3.40%	5	3.58%
2	3.36%	6	3.61%
3	4.74%	7	3.51%
4	4.67%		

6   Rheological Bonnet Finishing Trials and CFD Modelling

Mid-spatial frequency (MSF) errors continue to be a limiting factor in optical manufacturing. *Chapter 2* provided an overview of existing manufacturing processes available to control MSF errors. There is a constant trade-off between process efficiency and versatility. Precessed bonnet polishing combines the process-speed advantage of stressed mirror and stressed lap polishing, with the adaptability of magneto-rheological finishing (MRF) and ion beam figuring. However, regarding MSF errors, precessed bonnet polishing is incapable on its own of mitigating spatial frequencies smaller than its tool influence function (Messelink, 2016). Drawing inspiration from MRF, which utilises magnetically stiffened fluid as the process tool, a novel approach to use stiffened shear-thickening slurry as the process tool is explored in this chapter.

6.1   Introduction to Rheological Bonnet Finishing

MRF is a polishing process introduced in *section 2.3.2*. It stands apart from other processes by utilising magnetorheological (MR) fluids. During polishing, the workpiece is kept at a set distance from the electromagnet with MR fluid filling the gap. By controlling the magnetic fields, the process is able to control the stiffness of the MR fluid in real-time (Harris, 2011). Effectively, the stiffened fluid becomes the tool for polishing the workpiece surface.

Non-magnetorheological finishing is a novel approach developed by the present author seeking to polish and correct MSF errors on surfaces by using stiffened fluids as the effective polishing tool. While MRF uses MR fluids and electromagnets, this process utilises shear-thickening fluids (STF) and precessed bonnets and was given the name 'rheological bonnet finishing' (RBF). Figure 6-1 shows the schematics of the established MRF process and the proposed RBF process.
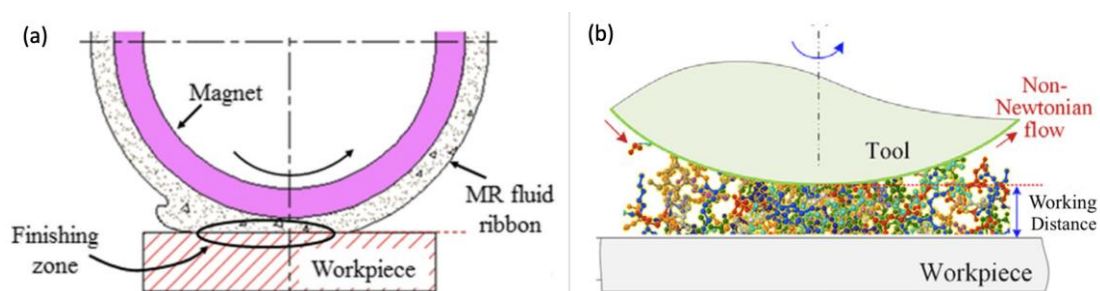
Figure 6-1 (a) the MRF process (Ghosh, Dalabehera, & Sidpara, 2018); and (b) the RBF process (Zhu & Beaucamp, 2020).

Unlike traditional contact bonnet polishing that was utilised in the previous three chapters, where the tool is pressed against the workpiece via setting the z-offset, the bonnet was kept at a working distance (WD) above the workpiece up to 1.5mm. The STF filled the gap between the bonnet and workpiece surface. Under high-

speed tool rotation, the bonnet induced shear stress to the STF and drew the shear-thickening slurry through the gap. This should theoretically provide polishing capabilities like that of MRF. The tool influence function of RBF could be controlled through adjusting the WD, slurry viscosity, and tool speed. Due to the non-contact nature of RBF, the process was suspected to provide less volumetric removal rate than its traditional contact bonnet polishing, rendering RBF more of a finishing process.

6.2   Rheological Bonnet Finishing Polishing Trials Using a Disc Tool

Shown in Figure 6-2, a disc shaped tool was first considered for the initial RBF trials. The main reasoning for trialling this tool was its resemblance to the setup of the MRF electromagnetic wheel. The disc tool had a diameter of 200mm and a width of 10mm. Strips of polyurethane were adhered onto the perimeter of the disc with gaps between the strips to facilitate drawing of the slurry when then disc rotates. It was mounted onto the spindle axis of the IRP600 CNC machine at 90°C precess angle. The disc was normal to the working plane, resembling that of the MRF process.
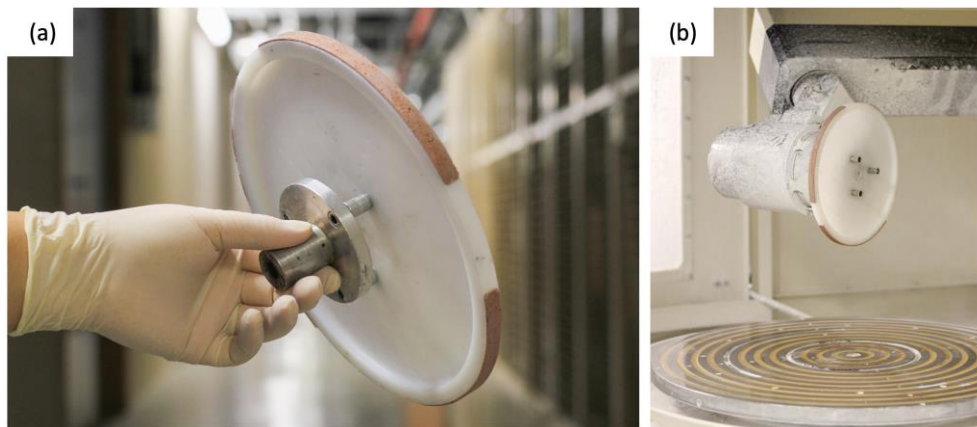
Figure 6-2 (a) Disc tool used for the initial RBF trials. (b) The disc tool mounted on the IRP600 CNC spindle.

As the RBF process had never been trialled before, the parameters of the initial tests were chosen based on past polishing experiences. The workpiece and setup of the tests used the same BK7 glass and yellow tub as described in *section 3.1.4*. The test slurry filled the tub with the workpiece submerged, and the tool lowered and polished following a generated tool path, shown in Figure 6-3.

The toolpath used resembled that of *section 3.2.1*. Six trenches were polished onto the glass surface with tool feedrate of 5mm/min, shown in Figure 6-4. Unlike the experiments in *chapters 3* and *4* that varied tool headspeed across the six polished trenches, the WD was varied, shown in Figure 6-5. The spindle rotation speed was set to 100RPM, which resulted in a tool surface speed of 1047mm/s. Higher rotational speed than that caused the plastic disc to wobble and become unstable.
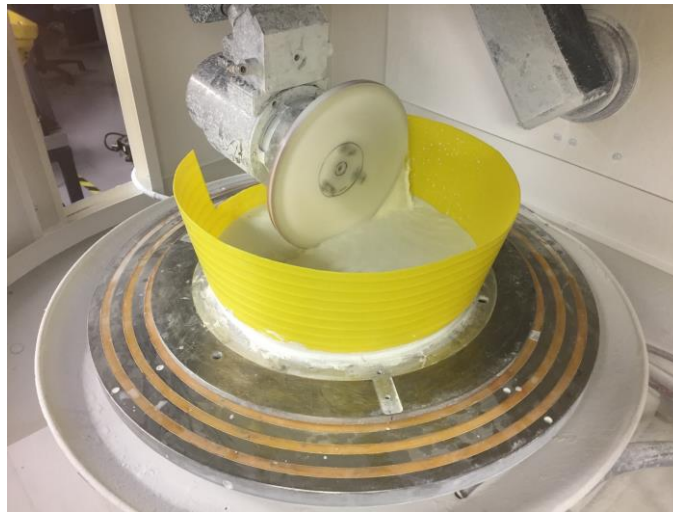
Figure 6-3 RBF polishing experiments with the disc tool.
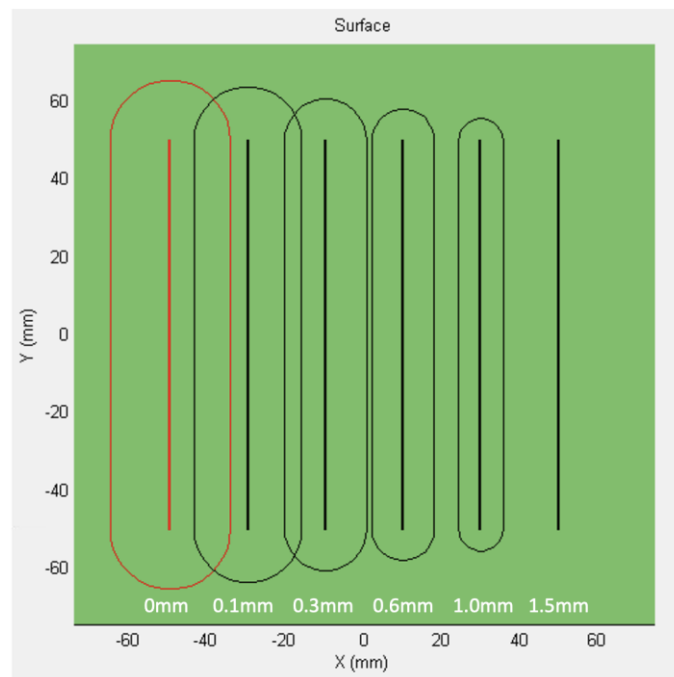
Figure 6-4 Toolpath visualisation for the RBF experiments.
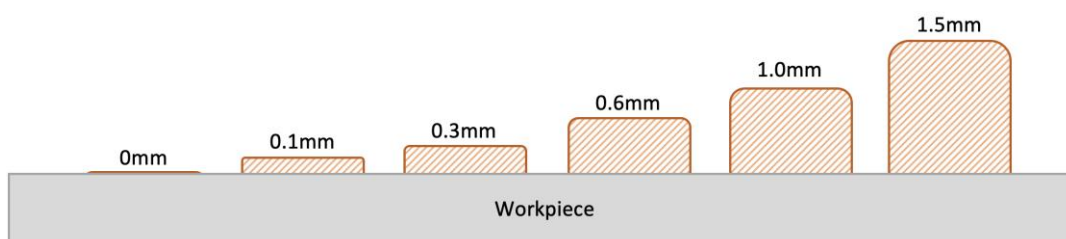
Figure 6-5 Side view of the toolpath and workpiece illustrating the varying WD. (Note: heights of the WD are not to scale.)

Three tests were conducted with cornstarch suspension (CSS) slurries. Their compositions are tabulated in Table 6-1. Test 33 was the conventional water-cerium oxide polishing slurry. Tests 34 and 35 had the addition of cornstarch. The concentration of cerium oxide was kept constant at 2.6wt% across the three tests.

Table 6-1 Cornstarch to water ratio for tests 33-35.

Test	33	34	35
Ratio	0	0.25	1

For all three tests, the glass workpiece surface did not show any sign of material removal. The Form Talysurf profilometer could not detect any tool influence functions. Shown in Figure 6-6, the undulations of the surface profile were most likely surface roughness and instrument noise. There were a few possible explanations for the lack of material removal. Firstly, the process time could have been insufficient to demonstrate material removal capability. As mentioned above, non-contact polishing was suspected to produce smaller removal rate than that of traditional contact polishing. Secondly, the height of the WD could have been unsuitable to facilitate the desired shear-thickening effects induced by the rotating disc. Thirdly, the disc tool had a width of 10mm, which could have been too narrow to pull the shear-thickened slurry through the WD gap.
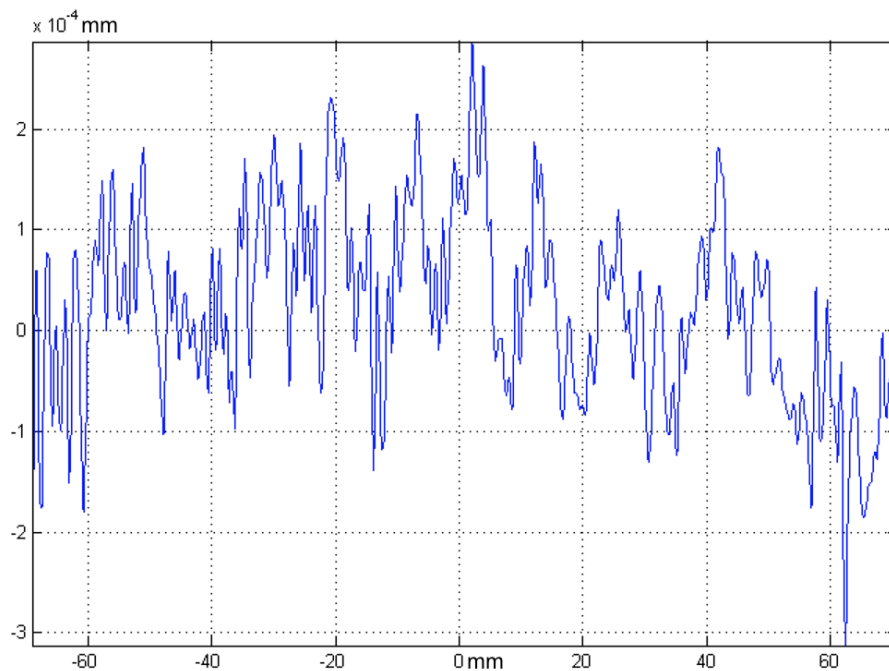
Figure 6-6 Profilometer reading after test 35.

6.3   Rheological Bonnet Finishing Polishing Trials Using a Precessed Bonnet

Subsequent experiments of RBF used a precessed bonnet as the rotating tool instead of the plastic disc for three reasons. Firstly, the polyurethane strips glued onto the perimeter of the disc tool regularly detached during processing. The adhesive was not strong enough, possibly due to the narrowness of the tool and the glossy nature of the plastic surface.

Secondly, the bonnet tool was superior to the disc tool in build quality, consistency, and versatility. The high-grade 6082 T6 aluminium bonnet tools were designed specifically for the IRP series of CNC machines within 10μm manufacturing tolerance (information from personal contact with Zeeko's managing director). On the other hand, the plastic tool was an available part without any manufacturing information. The bonnet tool provided more controllable parameters such as the precess angle, bonnet size, and headspeed. It is capable of headspeeds of over 1000RPM, at which the plastic disc would likely warp.

Thirdly, the standardised bonnet tools are widely used with the IRP machines in the precision surfaces industry across the globe (Acangeli et al., 2019; Huang et al., 2020; Walker et al, 2011). Experimental setup and results from the RBF experiments could be readily replicated and scrutinised by other researchers. Taking these reasons into consideration, the bonnet tool was chosen over the disc tool.

Three more RBF tests (36-38) were conducted. The experimental setup, toolpaths, and slurry compositions were identical to that of tests 33-35, outlined previously in *section 6.2*. The only difference between this trio of tests and the previous was the rotating tool. The 80mm radius bonnet was used at 15° precess angle with a headspeed of 1000RPM. While tests 36 and 38 showed no measurable material removal on the workpiece surface, test 37 (0.25:1 cornstarch to water ratio) showed visible and measurable material removal for both the 1.0mm and 1.5mm WD trench. Figure 6-7 shows the visible marks on the workpiece surface from test 37. Figure 6-8 shows the profilometry data of the 1.0mm and 1.5mm WD trenches.
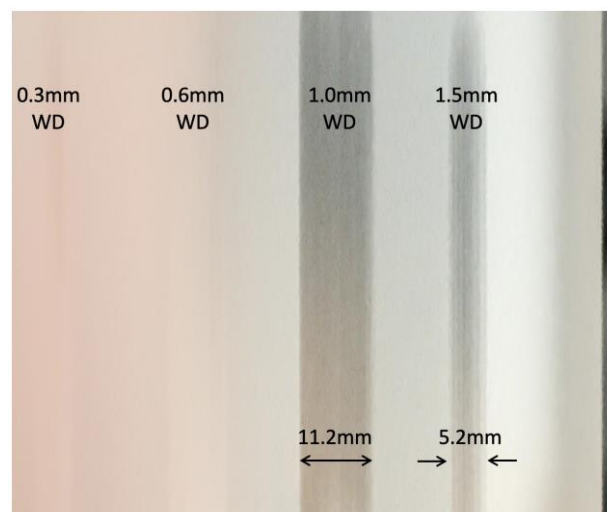
Figure 6-7 Polishing marks on the workpiece after test 37.
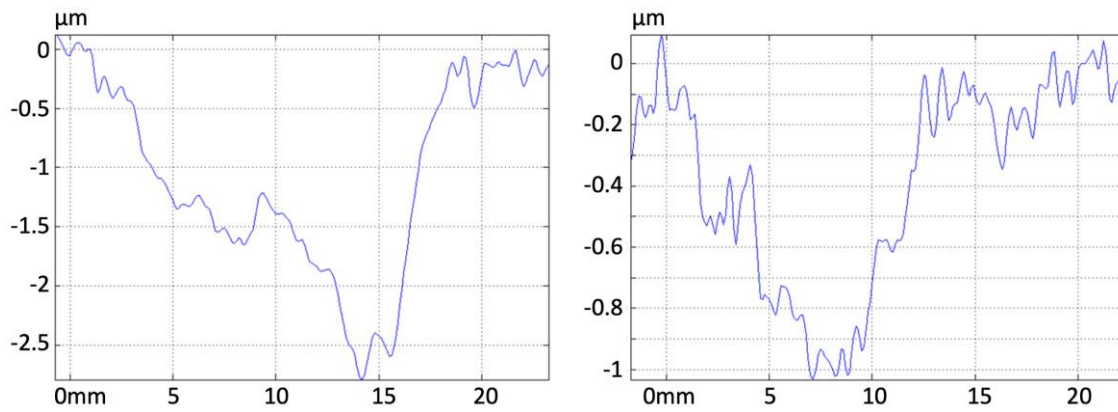
Figure 6-8 Profilometer readings for test 38: 1.0mm WD trench (left), and 1.5mm WD trench (right).

The trenches were measured 10 times along parallel tracks to obtain a mean and standard deviation for the volumetric removal rate (VRR). Test 37 used a tool headspeed of 1000RPM and slurry with cornstarch to water ratio of 0.25:1 by weight. The VRR for the two RBF trenches from 37 were compared with that of contact bonnet polishing from *chapter 4*: the 1000RPM control experiment with standard cerium oxide slurry (test 0), and the 1000RPM experiment with cornstarch to water ratio of 1:1 (test 23). The VRR comparison is visualised in Figure 6-9 and summarised in Table 6-2.
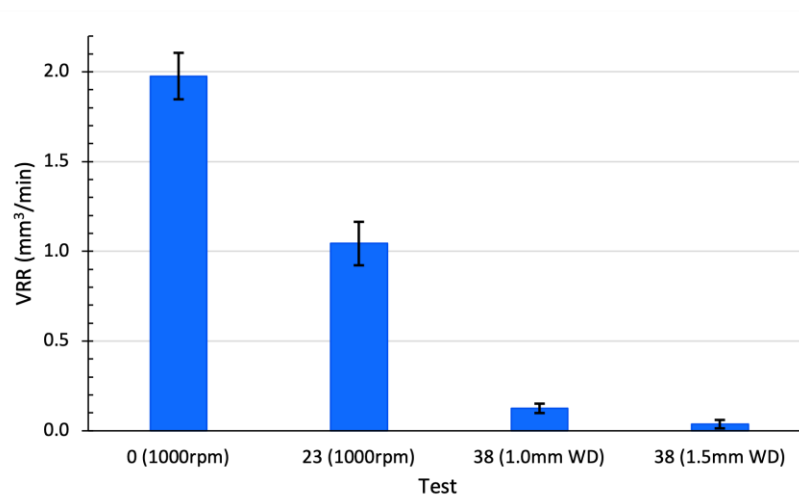
Figure 6-9 Comparison of VRR between tests 0, 23, and 37 with standard deviation.

As expected, the material removal capability of the RBF processed were much lower than that of the contact polishing. The RBF processes produced VRR values between 2% and 7% of the contact polishing VRR. However, as a proof of concept, the RBF demonstrated material removal capability, and could be potentially suitable as a final stage finishing process.

Table 6-2 Comparison of VRR (mm³/min) between tests 0, 23, and 38 with standard deviation.

Test	Tool Influence Trench	Slurry	Mean	σ
0	1000RPM	Traditional cerium oxide	1.975	0.129
23	1000RPM	CSS ratio 1:1	1.044	0.122
37	1.0mm WD	CSS ratio 0.25:1	0.126	0.025
37	1.5mm WD	CSS ratio 0.25:1	0.038	0.023

Although test 38 showed promising signs, it gave an inconclusive result ultimately. The IRP 600 machine used for the experiments developed mechanical calibration errors in its z-axis, along with other faults, which required maintenance and repair by trained technician from Zeeko. The absolute z-axis values set across the 6 WDs for test 38 were likely offset by some tenths of millimetres, but the relative differences in working distances between the trenches were still correct. Test 38 showed that removal rate had a clear maximum at a certain WD above the workpiece. Therefore, this does not invalidate the proof of concept for the RBF process. This test should be repeated in future work, as well as conducting experiments to find the WD that optimises for removal rate.

6.4 Switching Focus from Physical Experiments to Software Modelling

Test 38 showed a proof of concept of the RBF process. Software modelling had been used to optimise and verify experimental results in polishing (Chauhan, Bhalla, & Danish, 2910; Zheng, 2017; Zhu & Beaucamp, 2020). Building an accurate model would not only aid in understanding the fundamental mechanisms in a quantitative manner, but it would also serve as a useful tool to interpret future experimental results by correlations to the simulation models.

Chapter 5 explored the rheological properties of the cornstarch suspension slurries. The apparent viscosity profiles were first tested by a rheometer before comparing with CFD modelling. The models confirmed the legitimacy of the material definition through user-defined C codes. The subsequent sections seek to build upon the model and to provide in-depth analysis on the capability and potential of the RBF process. Modelling of the RBF process used Ansys Fluent 2019 R1 software. Two-dimensional models were first built as a steppingstone before advancing onto 3D modelling.

6.5 Preliminary Two-Dimensional Modelling for Rheological Bonnet Finishing

Modelling of the RBF process should reflect the experimental setup from *section 6.3*. Ansys CFD simulations required the construction of the fluid domain – the area/volume in which the fluid resides. Referring to Figure 6-10, the experimental setup (a) could be simplified down to the rotating bonnet and the glass

workpiece (c). The fluid domain was taken as the space between the tool and the workpiece (d). The fluid domain as a preliminary model can be further simplified and approximated as pipe flow (e). The fluid domain had a height of 1mm, reflecting the RBF working distance, and a length of 20mm.
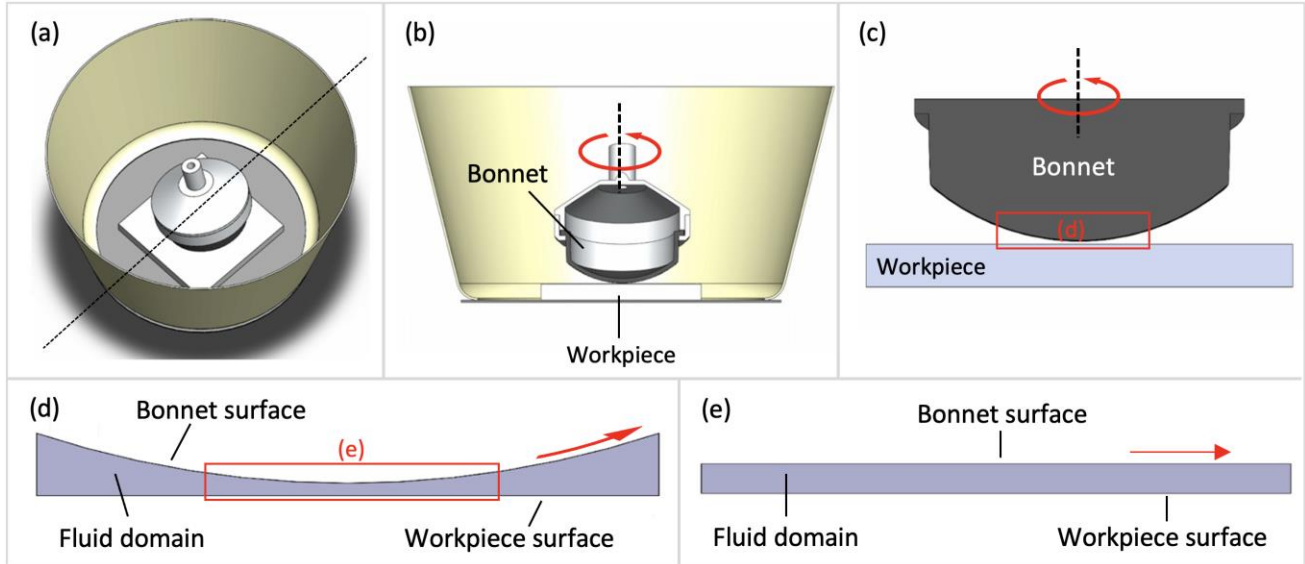
Figure 6-10 (a) The full RBF setup with the dotted line depicting the cross section. (b) Cross section view of the RBF setup. (c) Simplified 2D schematic of the rotating bonnet above the workpiece. (d) Fluid domain between the bonnet and the workpiece with the red arrow indicating bonnet movement. (e) Approximating fluid domain as rectangular, resembling 2D flow of a half-pipe.

Boundary conditions were set to simulate the experimental dynamics of RBF. Referring to Figure 6-10(e), the top surface of the fluid domain reflected the rotation of the bonnet. Its boundary condition was set as a no-slip translational wall. The line speed of the bonnet surface parallel to the workpiece-plane could be calculated from Equation (6-1). With an 80mm radius bonnet rotating at 1000RPM and 15° precess angle, the speed of the bonnet boundary was set to 2168 mm/s travelling from left to right.

$$speed = \frac{\pi}{30} HR \cdot sin(\phi)$$

(6-1)

Where, H is the headspeed in RPM;

R is the bonnet radius in mm;

ϕ is the bonnet precess angle in degrees.

Referring to Figure 6-10(e), the left and right boundaries were set to pressure inlet and outlet respectively. Due to the lack of an active inlet and outlet, such as the case of traditional pipe flow problems, a residual pressure of 0 Pa was set for those boundaries (Burlutskii, 2018; Lim, Adam, & Ahmad, 2018). The bottom boundary of the fluid domain reflected the workpiece surface. Its boundary condition was set as a stationary wall with *slip* condition. A no-slip condition would deem the full transfer of momentum from the surface onto the adjacent fluid layer. Polishing could only occur with a pressure and velocity difference between the fluid and the workpiece surface; therefore, the *slip* condition was selected. It was acknowledged that this was a necessary compromise, as the real-life workpiece surface operates in neither the ideal no-slip nor slip conditions.

Figure 6-11 shows the fluid domain after the general meshing and the refined meshing. A global square meshing of size 0.333mm was first used, before a sizing refinement was made on the bonnet boundary surface for 0.05mm. The final meshing generated ~19,000 elements and nodes.
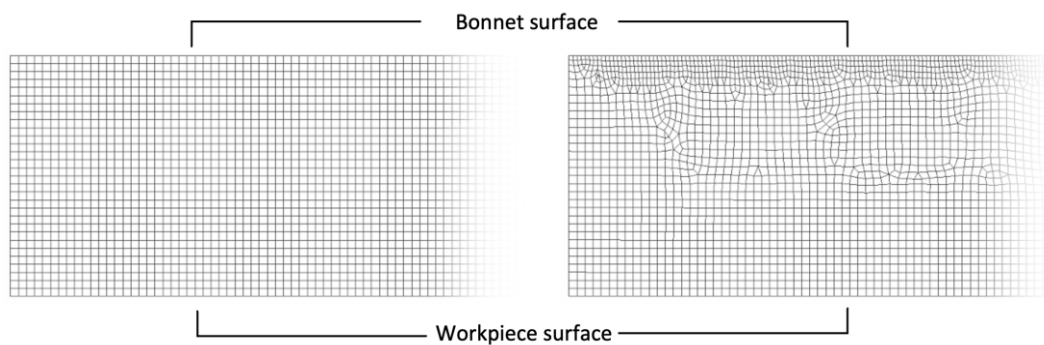
Figure 6-11 Illustration of meshing results for global meshing (left) and refined meshing of top boundary (right).

Three simulations were executed using different fluids. Referring to Table 6-3, the fluids used corresponded to the cornstarch suspension slurries used in polishing experiments (*chapter 4*) and were defined using user-defined functions (*chapter 5*). The flow characteristics of each model were calculated using the Reynolds number – equation (6-3). With *Re* smaller than 2300 for all three models, laminar flow regime was selected for the simulations.

Ansys provided two modes of CFD problem solving – steady-state and transient. In steady-state mode, a final result was reached when the difference between iterations fell below specified values called residuals. If no steady state condition was reached, then the program terminated at a specified maximum number of iterations. In transient mode, the program solved each iteration regardless of residual values, until it is either manually terminated by the operator or reaches the specified maximum number of iterations. For the 2D simulations, steady-state was chosen first to see if the problem reached convergence. All three models reached steady-state convergence between 100 to 120 iterations.

Table 6-3 Fluid composition and Reynolds number for models 8-10.

Model	Cornstarch to water ratio	Chapter 6 sample	Density (kg/m³)	Viscosity (mPa·s)	Reynolds number
8	0	CSS-2	1003	2.05	979
9	0.25	CSS-4	1065	3.10	687
10	0.5	CSS-5	1096	6.84	320

The Preston equation (1-1) provided the theoretical basis for estimating the polishing removal rate used by most of the CNC process (Téllez-Arriaga et al., 2007; Li, 2012). The Preston equation predicts the volumetric removal rate through the speed of the tool/slurry on the workpiece surface and the pressure exerted on the workpiece, and it has been used previously to model the behaviours of non-Newtonian fluids during polishing procedures (Li et al., 2015). Therefore, the velocity and pressure gradient of the CFD results are reported. Figure 6-12 shows the simulation results for models 8-10.
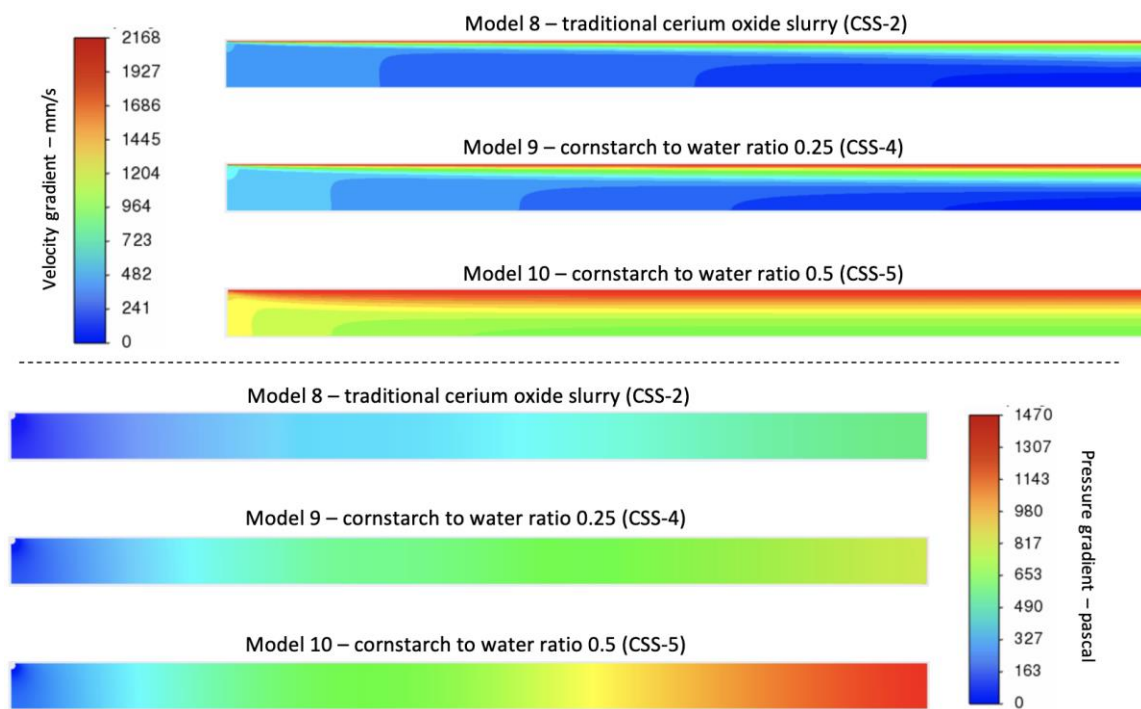
Figure 6-12 CFD simulation results for models 8-10.

The velocity gradients of the models showed the fluid layer adjacent to the top boundary (the bonnet) moved at the same speed as the specified translational no-slip boundary condition. As the cornstarch concentration increased, and effectively increasing shear-thickening behaviour, the fluid adjacent to the bottom boundary (the workpiece) experienced higher velocity. The pressure gradients were a result of the fluid motion, and it describes the kinetic energy per unit volume. As the fluid became more shear-thickening, high pressure was predicted from simulation.

6.6 Refined Two-Dimensional Modelling for Rheological Bonnet Finishing

The next step to improve the model was to modify the top surface of the fluid domain to resemble the curvature and movement of the bonnet. Such shape resembled Figure 6-10(d). The working distance was set at 1mm (i.e., the minimum distance between the bonnet and the workpiece surfaces). The boundary conditions for the refined 2D model were identical to that of the preliminary 2D model except for the motion of the bonnet boundary. The bonnet boundary motion was changed from translational to rotational, with rotation axis set at (0,81) as a bonnet radius of 80mm was simulated. This created motion on the surface tangential to the curvature.

Meshing and geometry for the refined 2D model is shown in Figure 6-13. A mesh size of 30μm was used to create ~200,000 elements and nodes for the CFD. Three simulations were rendered (models 11-13) using the same fluids from models 8-10 respectively. Their composition was summarised above in Table 6-3. All other parameters in Ansys were kept consistent with those used for the preliminary 2D model.
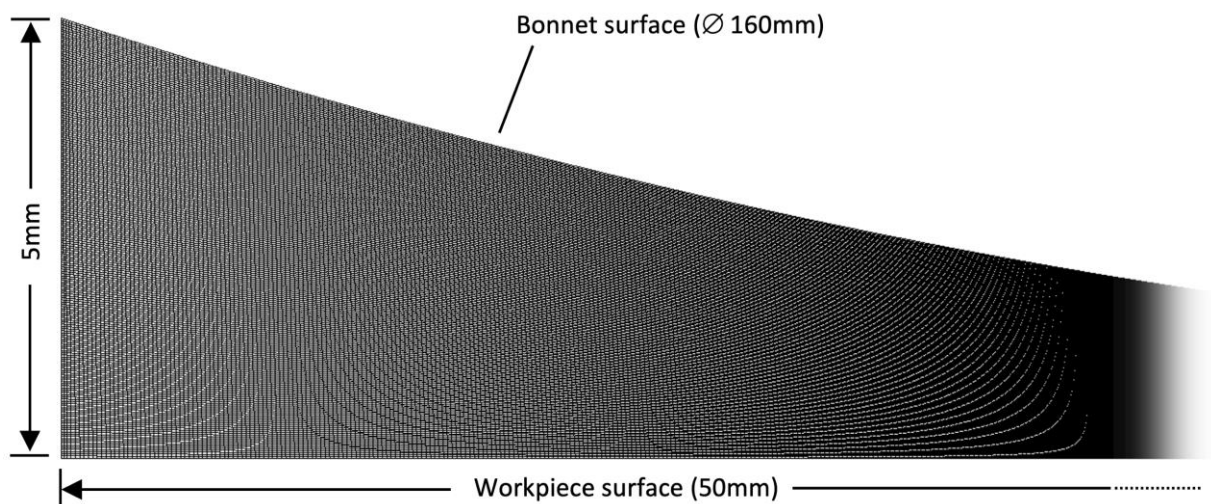
Figure 6-13 Meshing of the refined 2D model, zoomed in to the left side. Note that individual element might be too fine to show on print.

Figure 6-14 shows the simulation results for models 11 to 13. Model 11, being the conventional water-cerium oxide slurry, showed the smallest velocity and pressure gradient. Model 13, being the higher concentration of cornstarch suspension, showed the greatest gradients. This was expected as increasing shear-thickening behaviour should cause the fluid to behave more viscous. The highest velocity on the workpiece boundary was shown to be 1634.9mm/s. These 2-dimensional CFD models demonstrated the potential of simulations to predict RBF processes and served as vital steppingstones to 3-dimensional models.
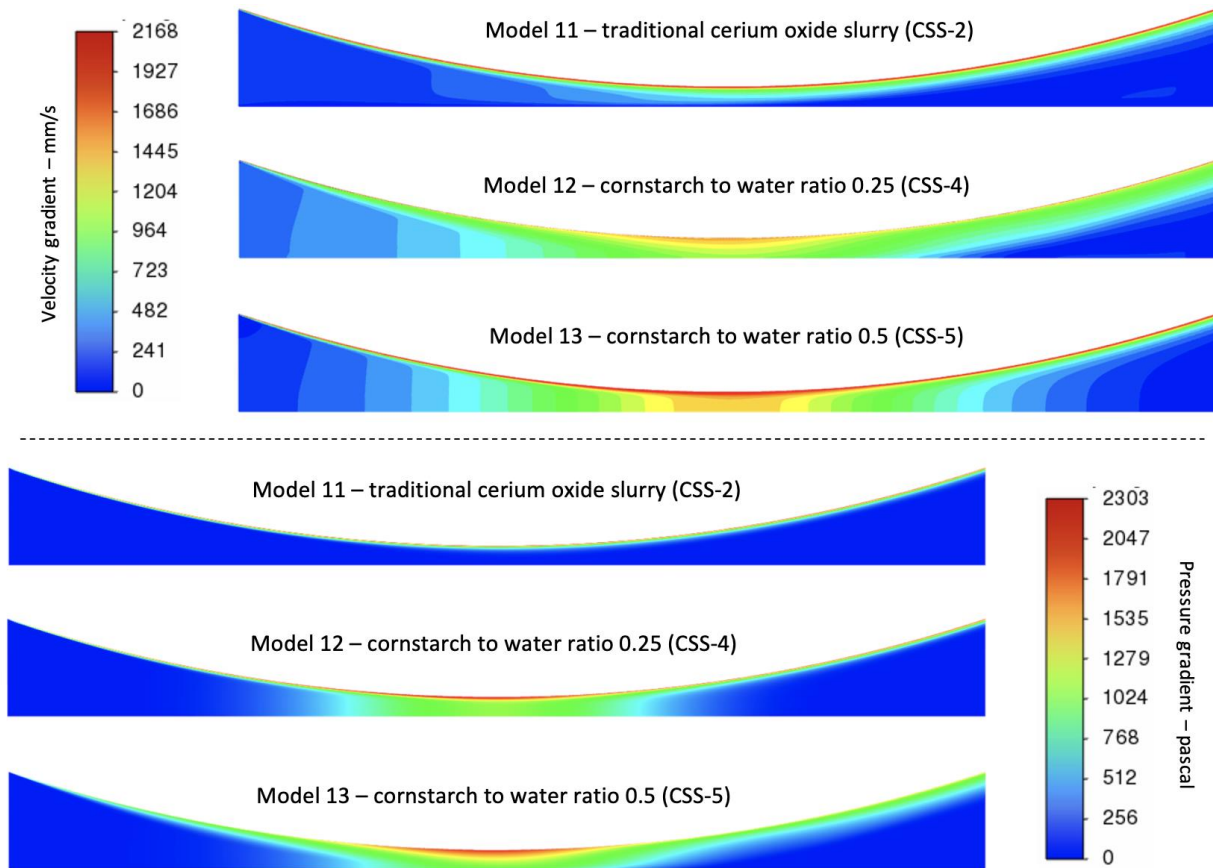
Figure 6-14 CFD simulation results for models 11-13.

6.7 Three-Dimensional Modelling of Rheological Bonnet Finishing

Building on the progress made with the 2D models, 3-dimensional models of the RBF were constructed. Note that all 3D isometric view of the modelling is presented with coordinate system shown in Figure 6-15, and all bird's-eye view is presented for the x-z plane. Referring to Figure 6-16, the geometry of the RBF process were first made in Solidworks before importing into Ansys for meshing and simulations. An assumption was made in Figure 6-16(b) that the entire bottom surface was the workpiece surface, as opposed to the 150 x 150mm workpiece in reality. The thickness of the fluid domain shown by Figure 6-16(c) and (d) represented the depth of the polishing slurry. This was set to 5mm to conserve computation time.
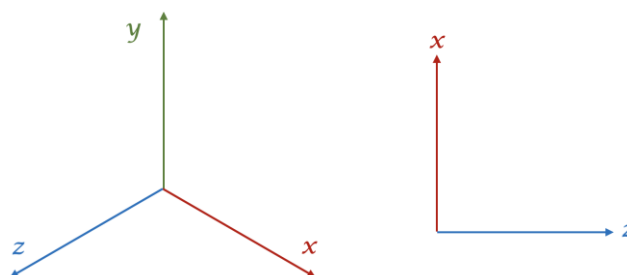
Figure 6-15 Coordinate system used for illustrating in 3D isotropic view (left) and 2D bird's-eye view (right).
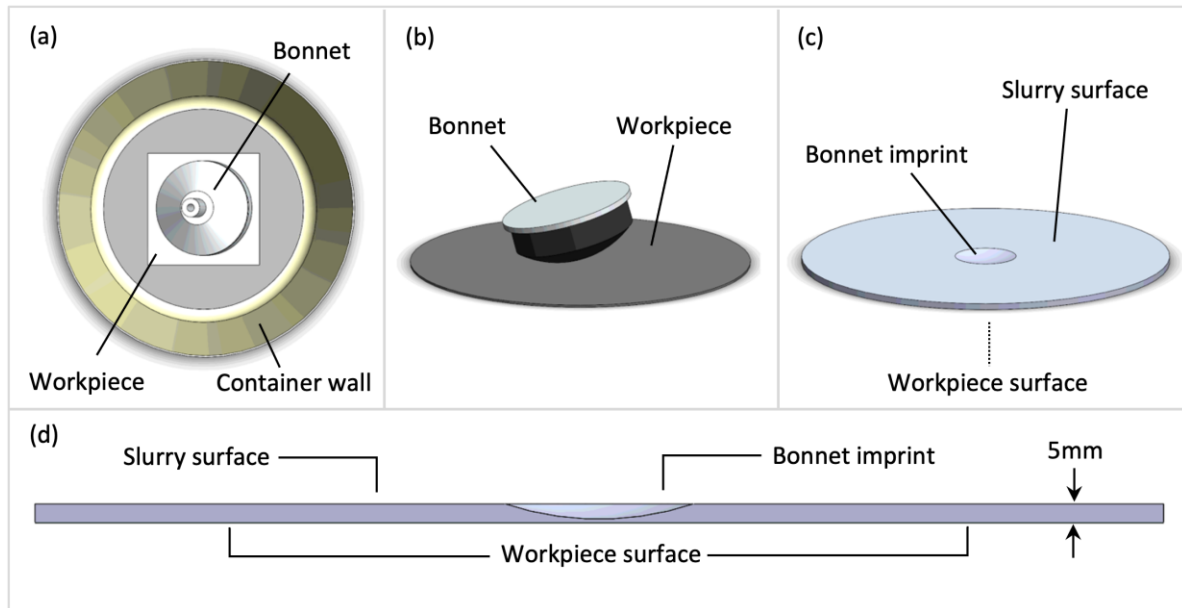
Figure 6-16 (a) Bird's-eye view of full RBF setup. (b) Isometric view of simplified bonnet on workpiece surface with WD. (c) Isometric view of the fluid domain with thickness of 5mm. (d) Cross-section view of the fluid domain.

6.7.1 Domain Shape and Size for the 3D model

Larger domain size decreases meshing density, thus hinders the accuracy of the simulation. Minimising model size while conserving the simulation accuracy should be considered and optimised. Therefore, different shapes and sizes of the fluid domain were explored to evaluate their influences on simulation results. Three domains were considered and depicted in Figure 6-17. The first option was to model for the entire size of the physical 150mm radius yellow tub used in the experiments. The second option was to model for a smaller circular domain base with 75mm radius. Halving the diameter effectively quarters the volume of the domain, resulting in higher meshing density. The third option modelled a square domain base with equal size as the glass workpiece used, with side length 150mm. This was to explore the effect of boundary shape on simulation results. The three domains have been given the name: r150, r75, and s150 respectively for convenience (models 14-16).
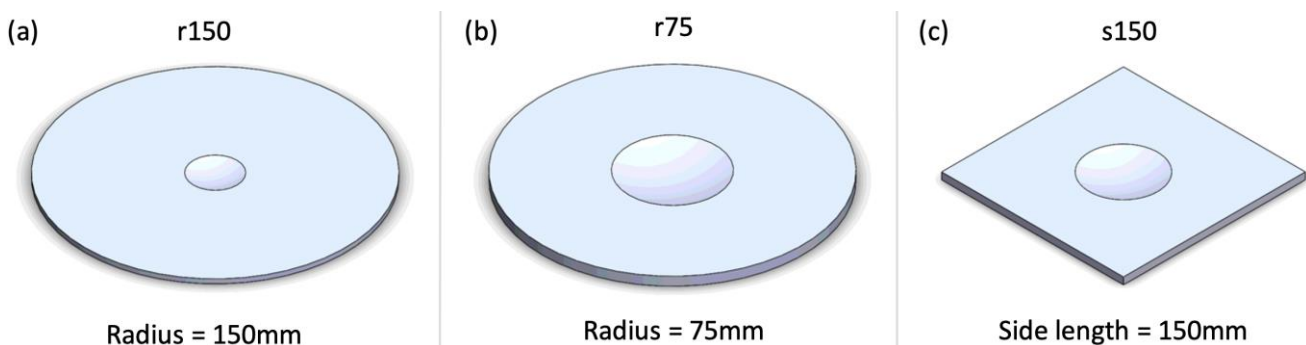
Figure 6-17 (a) r150: Fluid domain reflecting the actual tub size. (b) r75: Fluid domain with half the diameter for higher mesh density. (c) s150: Square fluid domain to explore the effect of boundary shape.

6.7.2   Meshing of the 3D Domains

Meshing of the fluid domains incorporated three zones with varying mesh resolutions. An example is shown in Figure 6-18. Note that the meshing sizes shown were set relatively large in order to portray the idea of the 3-zone meshing and were not used in actual modelling. The entire fluid domain was first subjected to a global meshing size. Then, an *area of influence* sizing constraint was used to increase meshing resolution near the centre of the domain. Lastly, a final refinement was made on the bonnet boundary. The *refinement* setting in Ansys Fluent halves every line segment, effectively quadruples the number of elements on the selected surface (Thompson & Thompson, 2017).
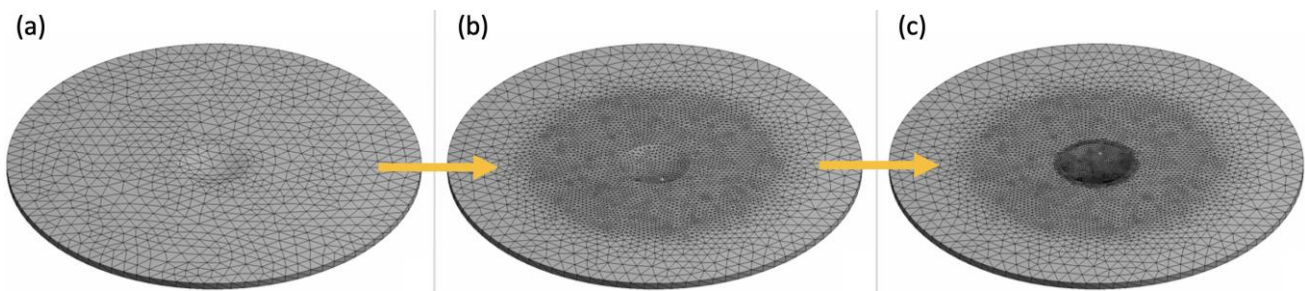
Figure 6-18 Three-zone meshing with increasing resolution. (a) Global meshing. (b) Addition of area of influence. (c) Addition of refinement.

Figure 6-19 shows the final result of the meshing, and Table 6-4 summarises the variables used for meshing of the three domains. These particular numbers were chosen in order to maximise the final element size without exceeding the limit of 512k elements, which was imposed by the academic version of Ansys.
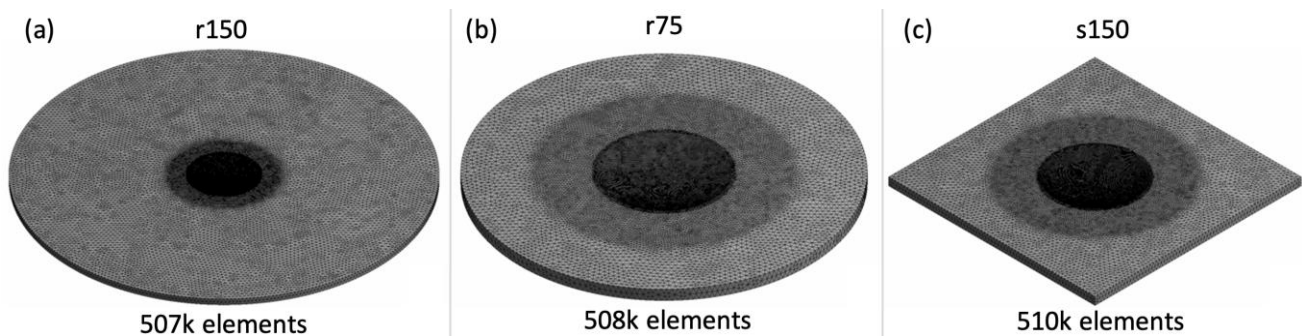
Figure 6-19 Finished mesh of the three fluid domains.

Table 6-4 Variables for meshing of the three domains.

Model	Domain name	Global mesh size (mm)	Area of influence radius (mm)	Area of influence mesh size (mm)	Total number of elements
14	r150	2.67	38	1	507k
15	r75	2	47	1	508k
16	s150	2.1	45	1	510k

6.7.3   Boundary Conditions for the 3D Domains

The boundary conditions used were similar to that of the 2D models. For all 3 domains, the bonnet boundary was set as a rotational moving wall with the centre of rotation at (0,81,0). This reflected the 80mm radius bonnet at 1mm working distance above the workpiece surface. The rotational axis directly reflected the precess angle of the bonnet. For example, in a pole-down process (i.e., 0° precess angle), the rotational axis would have a vector of (0,1,0). For the precess angle, the *x* component of the vector could be calculated using Equation (6-2). At 15° precess angle, the vector used was (0.26795,1,0).

$$vector_x = \tan \phi$$

(6-2)

Where, ϕ is the bonnet precess angle in degrees ($-90° < \phi < 90°$).

The workpiece boundary (the underside of the domain) was set as stationary wall with *slip* condition. The top boundary that represented the fluid surface was set to atmospheric pressure with 0 residual pressure. For the r150 domain, the outer circular boundary was set as a stationary wall with *no slip* condition, which reflected the physical wall of the tub used. For the r75 and s150 domain, the outer circular/square boundaries were set as pressure outlets with 0 residual pressure.

Steady-state mode was chosen for the comparison of the 3 domains. Traditional cerium oxide slurry (CSS-2) was used for the simulation, and a laminar flow regime was chosen. The bonnet boundary rotated at a speed of 1000RPM. A precess angle of 15° was simulated. Figure 6-20 reports the velocity and pressure gradients for models 14-16 on the workpiece surface of the fluid domain. This would represent the motion of the fluid and the pressure exerted by the fluid onto the workpiece surface as the bonnet rotates. Table 6-5 summarises the maximum velocity and pressure values from the results.
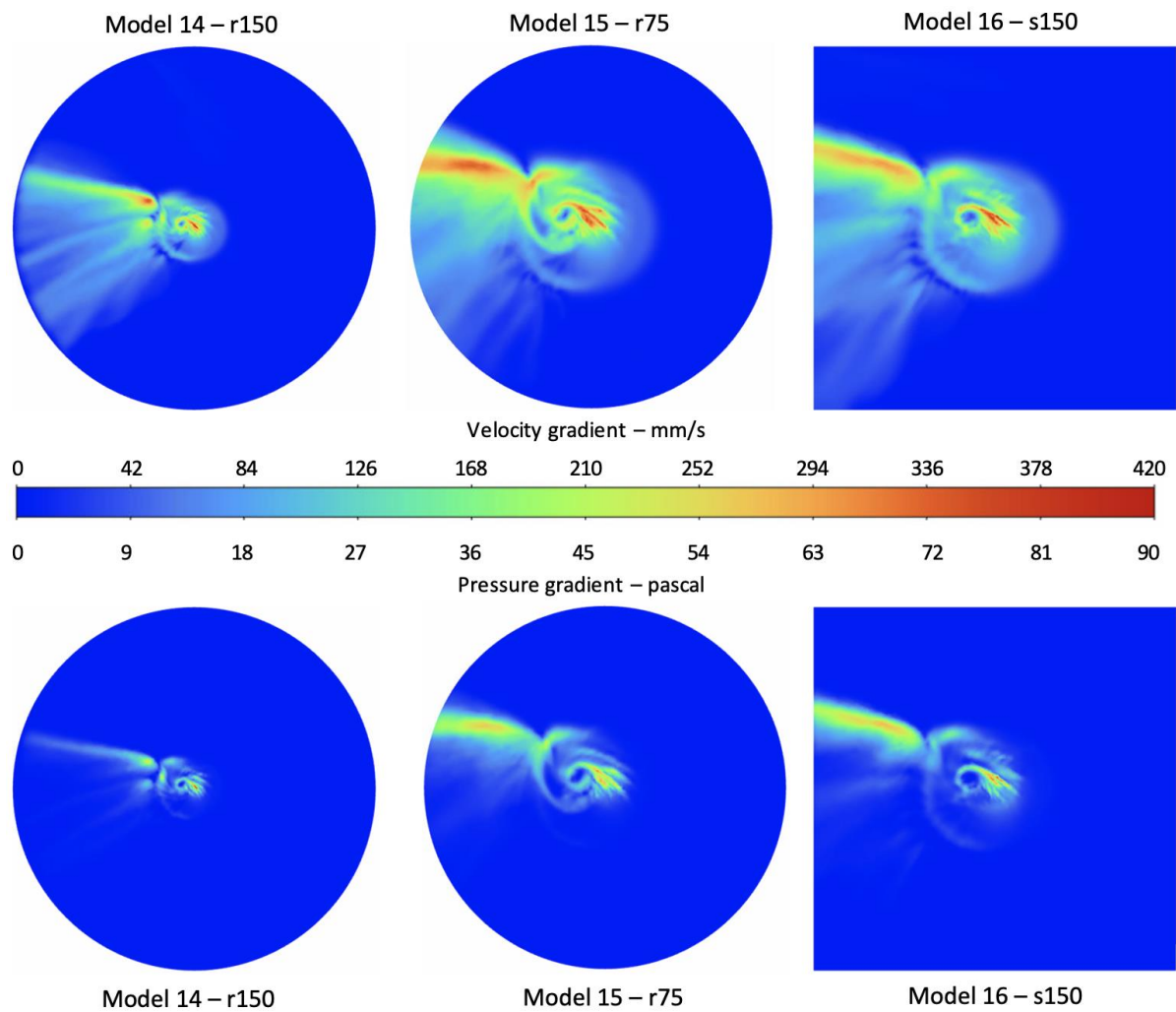
Figure 6-20 CFD simulation results for models 14-16.

Table 6-5 Maximum velocity and pressure on the workpiece surface for models 14-16.

Model	Domain name	Maximum velocity (mm/s)	Maximum pressure (Pa)
14	r150	416.4	86.2
15	r75	407.2	84.5
16	s150	408.4	86.3

The simulations modelled the bonnet precessed 15° towards the *+x* direction (↑), causing the fluid motion to be ejected in the *-z* direction (←) due to bonnet rotation. The models accurately reflected this dynamic, showing a "tail" of fluid outwash trailing from the centre of the fluid domains. The three domains produced similar results, with maximum velocity and pressure varying within ±3%. The r150 domain's main drawback was its large domain size, decreasing its meshing density and potentially decreasing the model accuracy. The four corners of the s150 domain most likely were not necessary contributors to overall accuracy of the model, as fluid motion at the corners were negligible. Therefore, the r75 was chosen and used as the domain shape and size for subsequent CFD modelling.

6.7.4 Effects of Precess Angle

Previous models all incorporated an equivalent precess angle of 15° for the bonnet boundary condition, as this reflected the precess angle most commonly used in industry as well as all the physical experiments in this thesis. Previously introduced in *section 2.3.1*, a pole-down process (0° precess angle) would produce zero material removal at the centre of the tool influence function, as the velocity at the centre of the bonnet is effectively zero. (In reality, there is a trajectory of the influence function along the toolpath so the removal at the centre of the track is not zero.)

The rheological bonnet finishing (RBF) experiments were initially inspired by the setup of the existing magnetorheological finishing (MRF) process. The tool and fluid motion of the MRF process rotates around an axis perpendicular to the workpiece surface normal. Although difficult to achieve in real-life, this dynamic could be modelled by CFD using an equivalent precess of 90° for the bonnet boundary condition.

Previously, model 15 was already simulated with 15° precess angle. Two more models (models 17 and 18) were simulated to explore the effects of the precess angle on the workpiece surface. Table 6-6 summarises a few key parameters. Traditional cerium oxide slurry (CSS-2) was used for the fluid domain. Steady-state and laminar flow regime were chosen for the simulation. Figure 6-21 shows the bonnet surface velocity profile, and Figure 6-22 reports the velocity and pressure gradients on the workpiece surface.

*Table 6-6 Parameters for models 17, 15, and 18. (*Speed at the point closest to workpiece)*

Model	Precess angle	Precess angle vector	Bonnet surface speed* mm/s	Reynolds number
17	0°	(0,1,0)	0	/
15	15°	(0.26795,1,0)	2168	979
18	90°	(1,0,0)	8377	1716
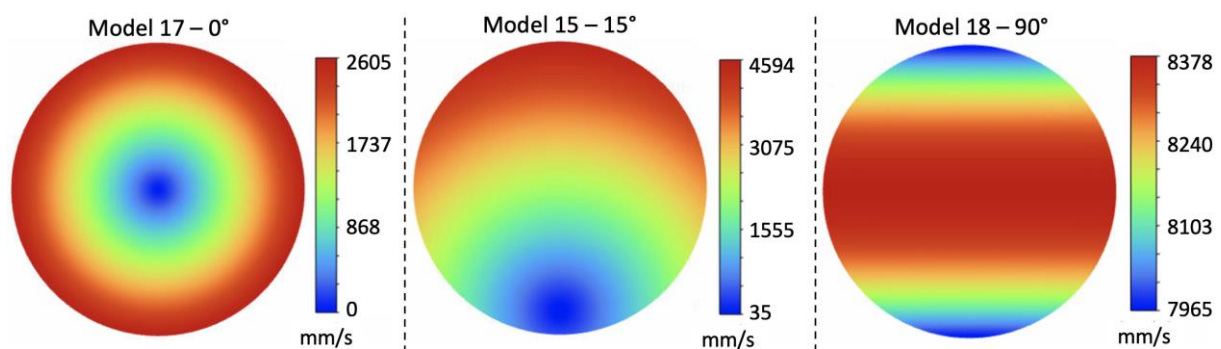
Figure 6-21 Bonnet surface velocity profile with varying precess angle.

The depicted results from the models matched the expected bonnet surface velocity distribution. The pole-down model showed the expected lack of fluid motion at the centre of the tool influence region for a stationery influence function. Though hard to achieve with physical bonnets, the 90° precess angle model showed the largest velocity and pressure values on the workpiece surface. The maximum values for both the velocity and pressure were doubled that of the 15° precess angle model. These simulations proved the models' ability to predict the bonnet surface motion. Moving forward, 15° precess were used to reflect the physical RBF experiments in *section 6.3*.

Model 17 – 0°   Model 15 – 15°   Model 18 – 90°

Velocity gradient – mm/s

90°:	0	85	170	255	340	425	510	595	680	765	850
15°:	0	42	84	126	168	210	252	294	336	378	420
0°:	0	42	84	126	168	210	252	294	336	378	420

0°:	0	9	18	27	36	45	54	63	72	81	90
15°:	0	9	18	27	36	45	54	63	72	81	90
90°:	0	26	52	78	104	130	156	182	208	234	260

Pressure gradient – pascal

Model 17 – 0°   Model 15 – 15°   Model 18 – 90°
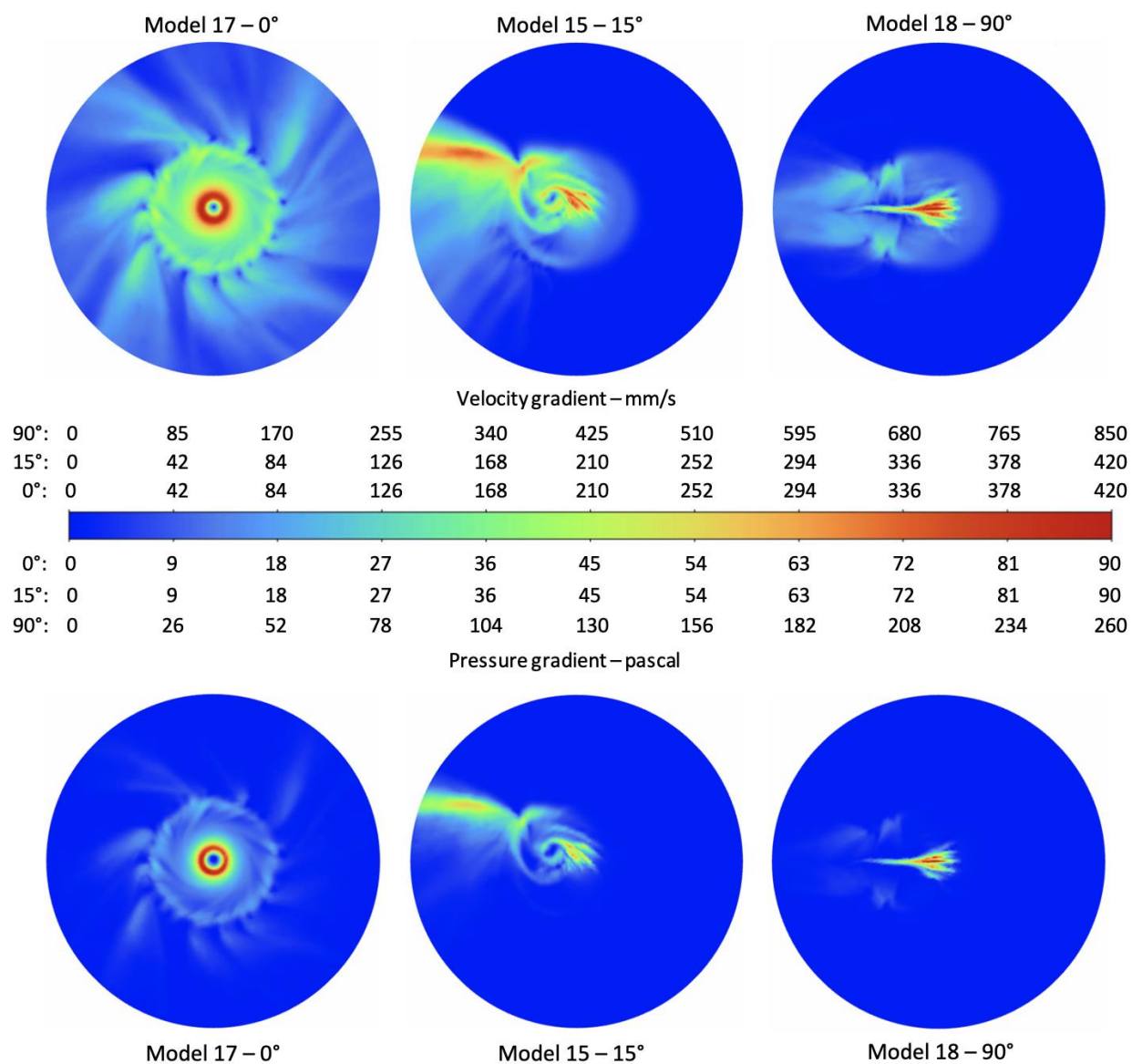
Figure 6-22 CFD simulation results for models 17, 15, and 18.

6.7.5 Effects of Working Distance

The working distance (WD) of the RBF process describes the smallest distance between the bonnet tool and the workpiece surface. Unlike traditional contact bonnet polishing, the tool rotated at a WD above the workpiece surface, drawing the shear-thickening slurry through the "bottle neck". This motion stiffened the shear-thickening fluid and demonstrated ability in material removal. *Section 6.3* reported the polishing capability of RBF using cornstarch suspension (CSS) slurries. Using a slurry with cornstarch to water ratio of 1:1, tool influence functions were generated when WD was set to 1.0mm and 1.5mm.

CFD modelling was conducted to explore the effects of WD on the workpiece surface using various slurries. Three slurries were simulated, and each at three different WDs. The rheological properties of these slurries could be found in *chapter 5*, and the fluid properties were input into Ansys using user-defined C-codes (*Appendix B*). These models all used 15° precess angle, steady-state, and laminar flow regime. The models are summarised in Table 6-7.

Slurry with higher cornstarch content could not be modelled correctly in Ansys due to the error message "floating point exception". This error could be caused by many factors such as division by zero, improper mesh size, and boundary conditions. Various attempts had been made to circumvent this issue, but the error message persisted. This was most likely due to the increase in viscosity and shear-thickening behaviour that overloaded the academic version of Ansys. Figure 6-23 depicts the attempted modelling of CSS-6, which was unstable and produced diverging results that overwhelmed the allocated computer memory. Therefore, although physical experiments used slurry with cornstarch to water ratio of 1 (CSS-7), simulation could only go as far as a ratio of 0.5 (CSS-5). To potentially overcome this problem would require access to the full version of the Ansys modelling software.

Table 6-7 Fluid compositions and working distances for models 15 and 19-26.

Model	Cornstarch to water ratio	Chapter 6 Sample	Working distance (mm)
19	0	CSS-2	0.5
15	0	CSS-2	1.0
20	0	CSS-2	1.5
21	0.25	CSS-4	0.5
22	0.25	CSS-4	1.0
23	0.25	CSS-4	1.5
24	0.5	CSS-5	0.5
25	0.5	CSS-5	1.0
26	0.5	CSS-5	1.5

Figure 6-24, Figure 6-25, and Figure 6-26 illustrate the modelling results for CSS-2, CSS-4, and CSS-5 slurries respectively. Each slurry was simulated with three WDs. There were a few general trends that emerged from the simulations. Firstly, increasing cornstarch content produced higher velocity and pressure values on the workpiece surface. This was most likely due to the better ability of more viscous fluid to transfer momentum from the rotating tool onto the workpiece surface. Secondly, smaller WDs produced the higher velocity and pressure values. Thirdly, the maximum velocity and pressure values for 0.5mm WD resided in the regions beneath the bonnet, whereas that of the 1.5mm WD resided in the outwash region to the side. The 1.0mm WD appeared to be a transitional phase where the maximum values were in both the region beneath the bonnet and the outwash region. This suggests that the overall shape of the tool influence functions of the RBF process could be altered through the WD.

The maximum velocity and pressure values are summarised in Table 6-8. For each matching WD, the velocity and pressure for CSS-4 slurry were 1.3 to 2.5 times that of the traditional cerium oxide slurry. The largest increase could be seen for the pressure values of the CSS-5 slurry, which reached over 24 times that of the traditional cerium oxide slurry. These simulations suggest and support the hypothesis that shear-thickening slurries could increase the material removal rate of RBF polishing processes.

Table 6-8 Maximum velocity and pressure on workpiece surface for models 15 and 19-26.

Model	Slurry sample	WD (mm)	Max. velocity (mm/s)	Max. pressure (Pa)	Velocity increase	Pressure increase
19	CSS-2	0.5	789.2	311.2	/	/
15	CSS-2	1.0	407.2	84.5	/	/
20	CSS-2	1.5	344.7	59.4	/	/
21	CSS-4	0.5	1238	765.4	1.57	2.46
22	CSS-4	1.0	562.5	158.0	1.38	1.87
23	CSS-4	1.5	549.5	149.3	1.59	2.51
24	CSS-5	0.5	2850	4619	3.61	14.84
25	CSS-5	1.0	1922	2098	4.72	24.82
26	CSS-5	1.5	1538	1343	4.46	22.61
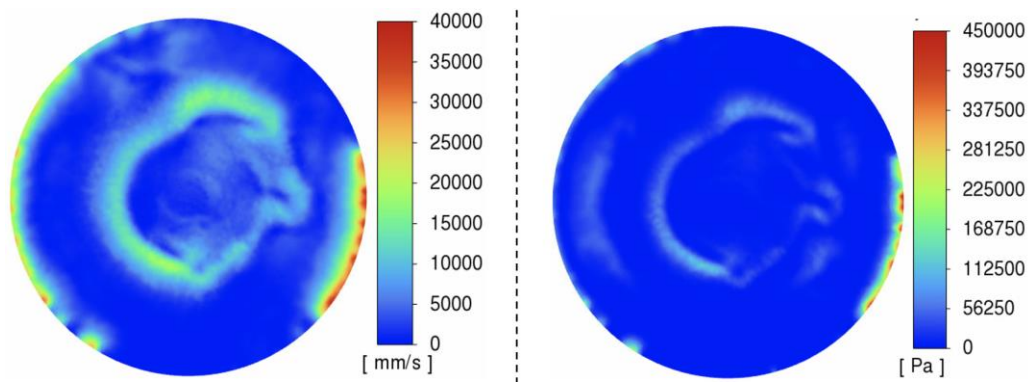
Figure 6-23 Modelling of CSS-6 before error message: velocity gradient (left) and pressure gradient (right).

Model 19 – WD 0.5mm   Model 15 – WD 1.0mm   Model 20 – WD 1.5mm

Velocity gradient – mm/s

WD											
1.5:	0	35	70	105	140	175	210	245	280	315	350
1.0:	0	42	84	126	168	210	252	294	336	378	420
0.5:	0	80	160	240	320	400	480	560	640	720	800

WD											
0.5:	0	31	62	94	125	156	187	218	250	218	312
1.0:	0	9	18	27	36	45	54	63	72	81	90
1.5:	0	6	12	18	24	30	36	42	48	54	60

Pressure gradient – pascal

Model 19 – WD 0.5mm   Model 15 – WD 1.0mm   Model 20 – WD 1.5mm
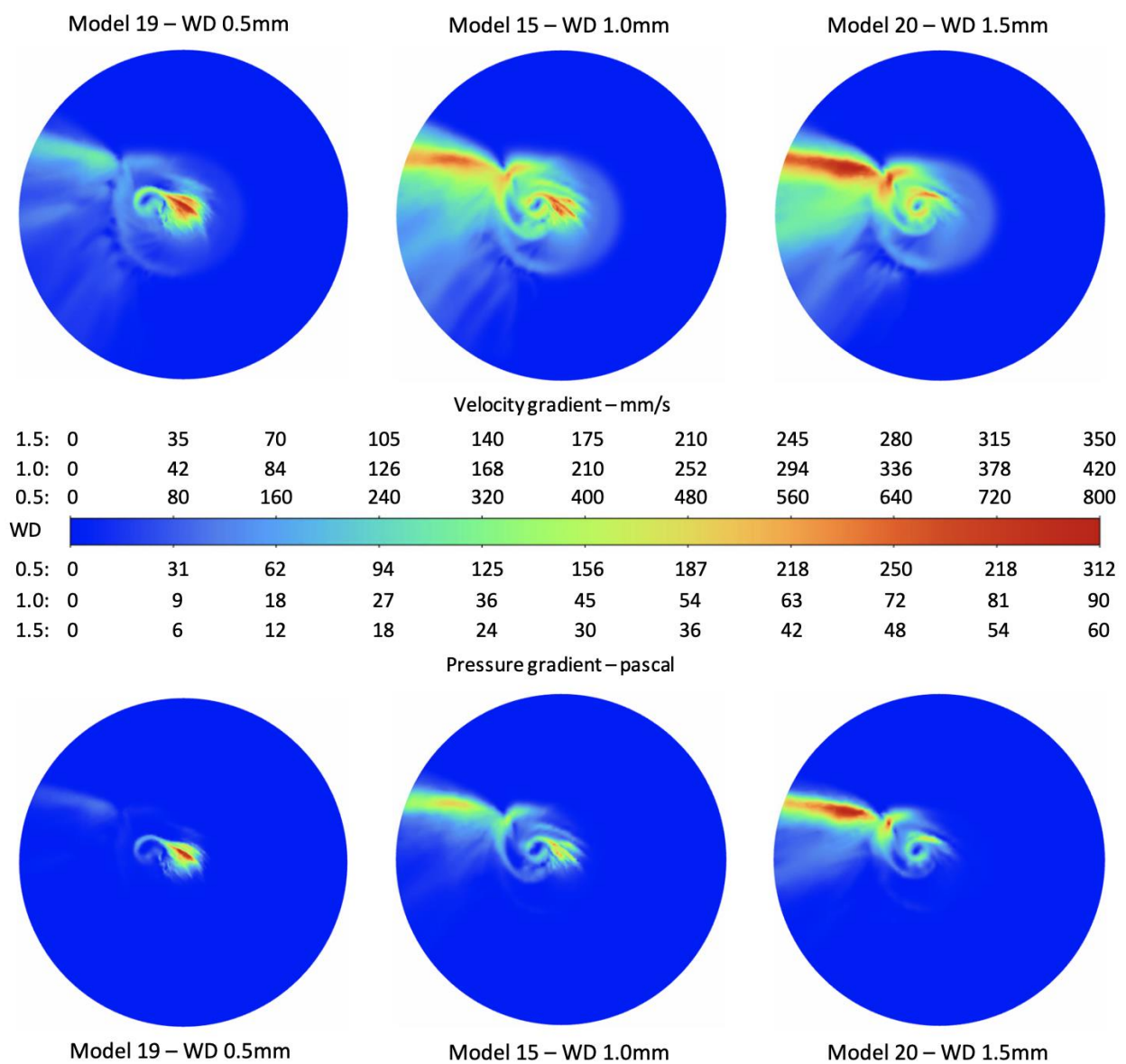
Figure 6-24 CFD simulation results for models 19, 15, and 20 (traditional cerium oxide slurry – CSS-2).

Model 21 – WD 0.5mm   Model 22 – WD 1.0mm   Model 23 – WD 1.5mm

Velocity gradient – mm/s

WD	0										
1.5:	0	55	110	165	220	275	330	385	440	495	550
1.0:	0	57	114	171	228	285	342	399	456	513	570
0.5:	0	125	250	375	500	625	750	875	1000	1125	1250

0.5:	0	77	154	231	308	385	462	539	616	693	770
1.0:	0	16	32	48	64	80	96	112	128	144	160
1.5:	0	15	30	45	60	75	90	105	120	135	150

Pressure gradient – pascal

Model 21 – WD 0.5mm   Model 22 – WD 1.0mm   Model 23 – WD 1.5mm
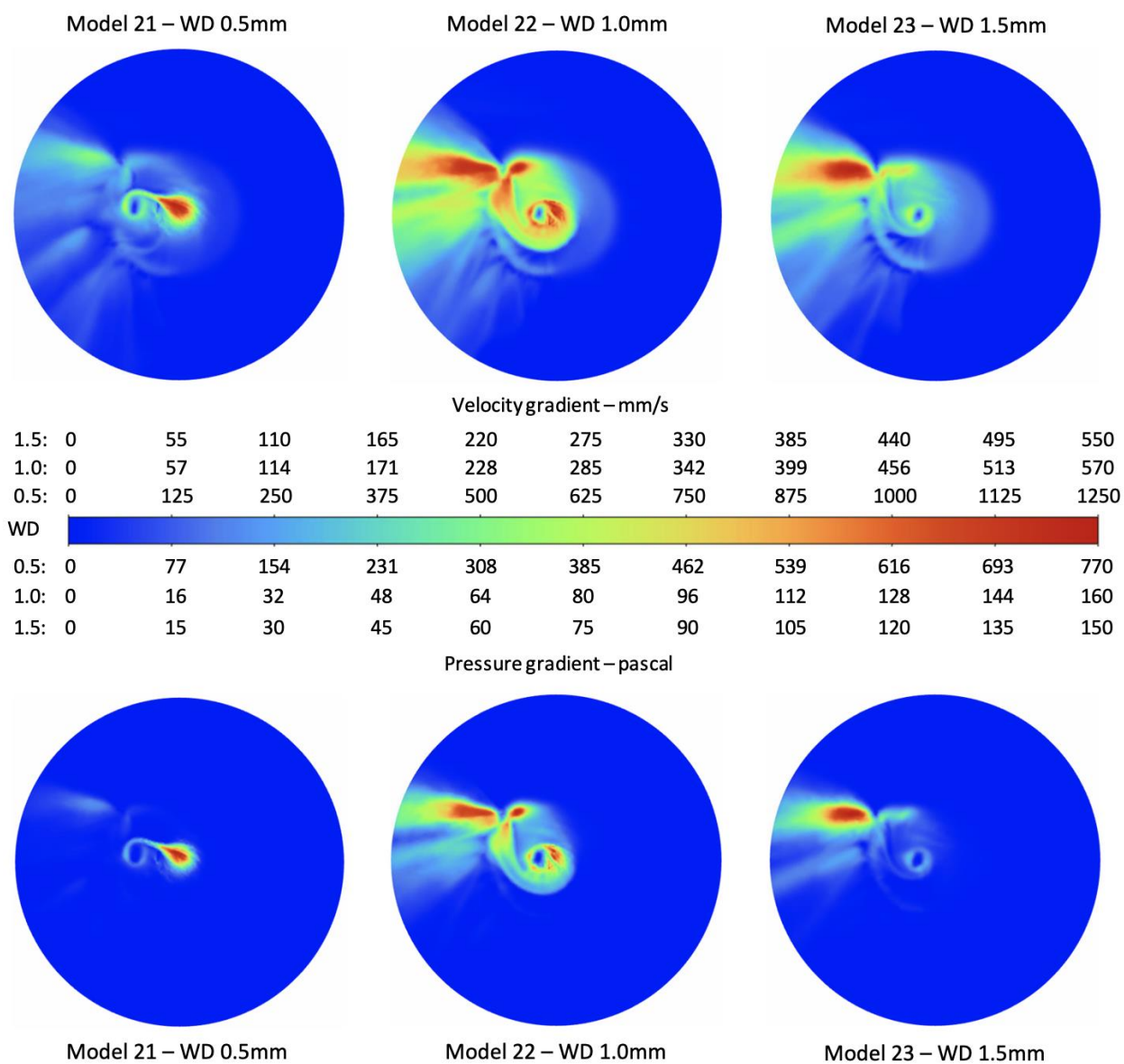
Figure 6-25 CFD simulation results for models 21-23 (cornstarch to water ratio 0.25 – CSS-4).

Model 24 – WD 0.5mm   Model 25 – WD 1.0mm   Model 26 – WD 1.5mm

Velocity gradient – mm/s

1.5:	0	155	310	465	620	775	930	1085	1240	1395	1550
1.0:	0	195	390	585	780	975	1170	1365	1560	1755	1950
0.5:	0	285	570	855	1140	1425	1710	1995	2280	2565	2850
WD											
0.5:	0	462	924	1386	1848	2310	2772	3234	3696	4158	4620
1.0:	0	210	420	630	840	1050	1260	1470	1680	1890	2100
1.5:	0	135	270	405	540	675	810	945	1080	1215	1350

Pressure gradient – pascal

Model 24 – WD 0.5mm   Model 25 – WD 1.0mm   Model 26 – WD 1.5mm

Figure 6-26 CFD simulation results for models 24-26 (cornstarch to water ratio 0.5 – CSS-5).

6.7.6 Effects of Tool Headspeed

The tool rational speed (headspeed) of the bonnet directly affects the rheological properties of the shear-thickening slurries by introducing shear to the system. *Chapter 5* reported on the rheological properties of the CSS slurries used, and the relationship between their viscosities and shear rates were analysed. Referring back to Figure 5-12, the viscosity plots for CSS-4 and CSS-5 showed a local maximum at ~200s^{-1} shear rate and a local minimum at ~400s^{-1}. At 1mm working distance, this would be an equivalent motion of the bonnet headspeed rotating at 200 and 400RPM respectively.

Higher slurry viscosity was hypothesised to enhance polishing performance, and this theory was supported by the models from the previous section (6.7.5). On the other hand, higher headspeed should produce higher velocity and pressure gradients on the workpiece surface. This exercise aimed to examine the competing factors of slurry viscosity and headspeed and to determine which is the more dominant factor. Combining with the 1000RPM models from the previous section, three slurries each with three difference headspeeds were modelled and summarised in Table 6-9. Figure 6-27, Figure 6-28, and Figure 6-29 illustrate the modelling results for CSS-2, CSS-4, and CSS-5 slurries respectively with the three headspeeds.

The overall distribution of the velocity and pressure gradient across the three headspeed for each of the slurry were not too dissimilar to each other. The values of the velocity and pressure gradient increased with increasing headspeed. Although the CSS-4 and CSS-5 have a local minimum of viscosity at 400s^{-1} (400RPM), the simulated viscosity and pressure values were still higher than that of the 200RPM simulations. Therefore, it could be concluded that to enhance polishing efficiency, the process should focus on using higher tool headspeed, rather than to operate within the slurry's local viscosity maximum.

Table 6-9 Headspeeds and viscosity values for models 15, 22, 25, and 27-32.

Model	Cornstarch to water ratio	Chapter 6 sample	Headspeed (RPM)	Apparent viscosity (mPa·s)
27	0	CSS-2	200	1.01
28	0	CSS-2	400	1.01
15	0	CSS-2	1000	0.92
29	0.25	CSS-4	200	2.75
30	0.25	CSS-4	400	1.97
22	0.25	CSS-4	1000	1.45
31	0.5	CSS-5	200	5.59
32	0.5	CSS-5	400	4.75
25	0.5	CSS-5	1000	3.17
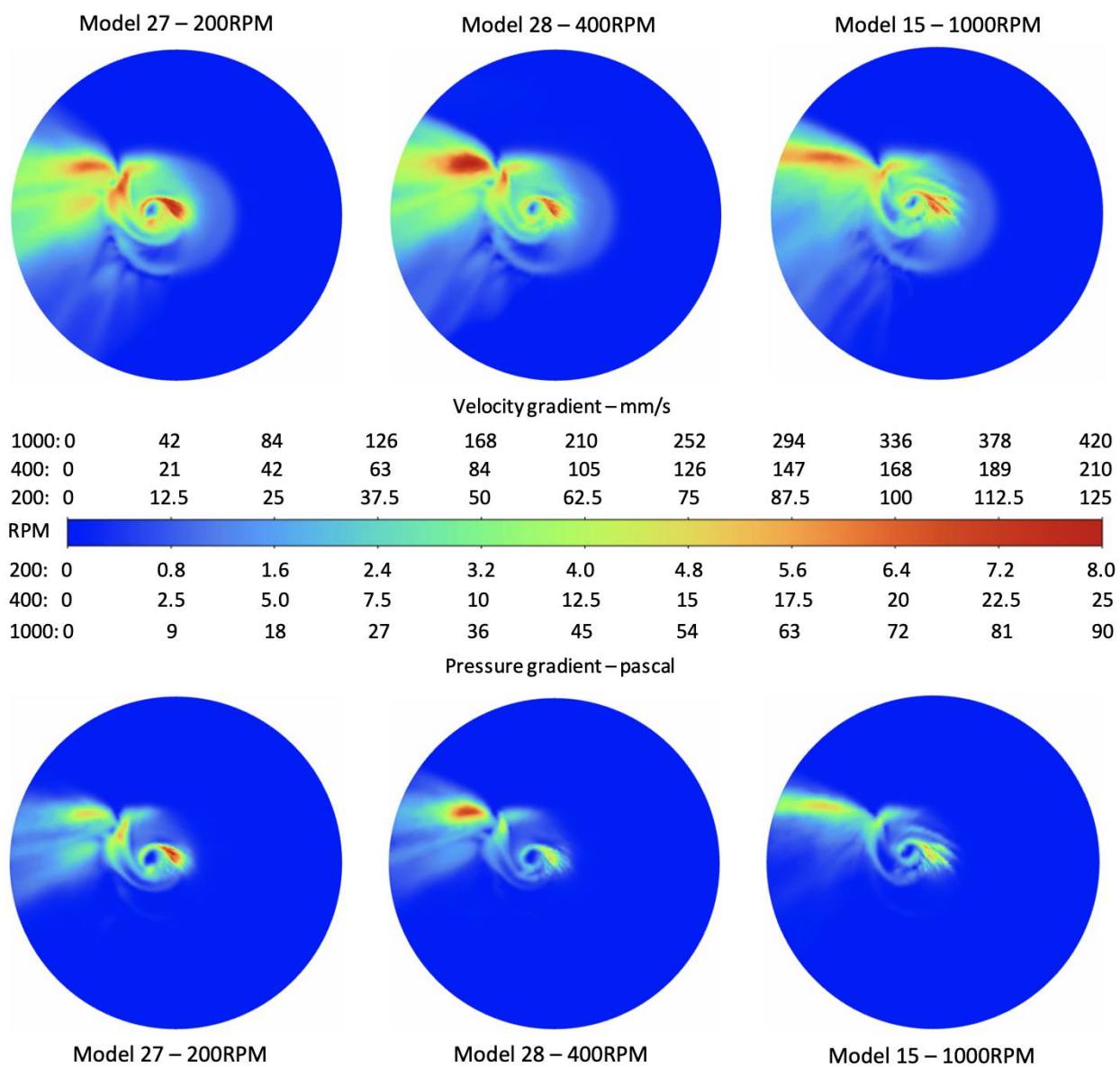
Figure 6-27 CFD simulation results for models 27, 28, and 15 (traditional cerium oxide slurry – CSS-2).

| Model 29 – 200RPM | Model 30 – 400RPM | Model 22 – 1000RPM |

Velocity gradient – mm/s

1000:	0	57	114	171	228	285	342	399	456	513	570
400:	0	37.5	75	112	150	187	225	262	300	338	375
200:	0	28.5	57	85.5	114	142	171	199	228	257	285

RPM

200:	0	4	8	12	16	20	24	28	32	36	40
400:	0	7	14	21	28	35	42	49	56	63	70
1000:	0	16	32	48	64	80	96	112	128	144	160

Pressure gradient – pascal

| Model 29 – 200RPM | Model 30 – 400RPM | Model 22 – 1000RPM |
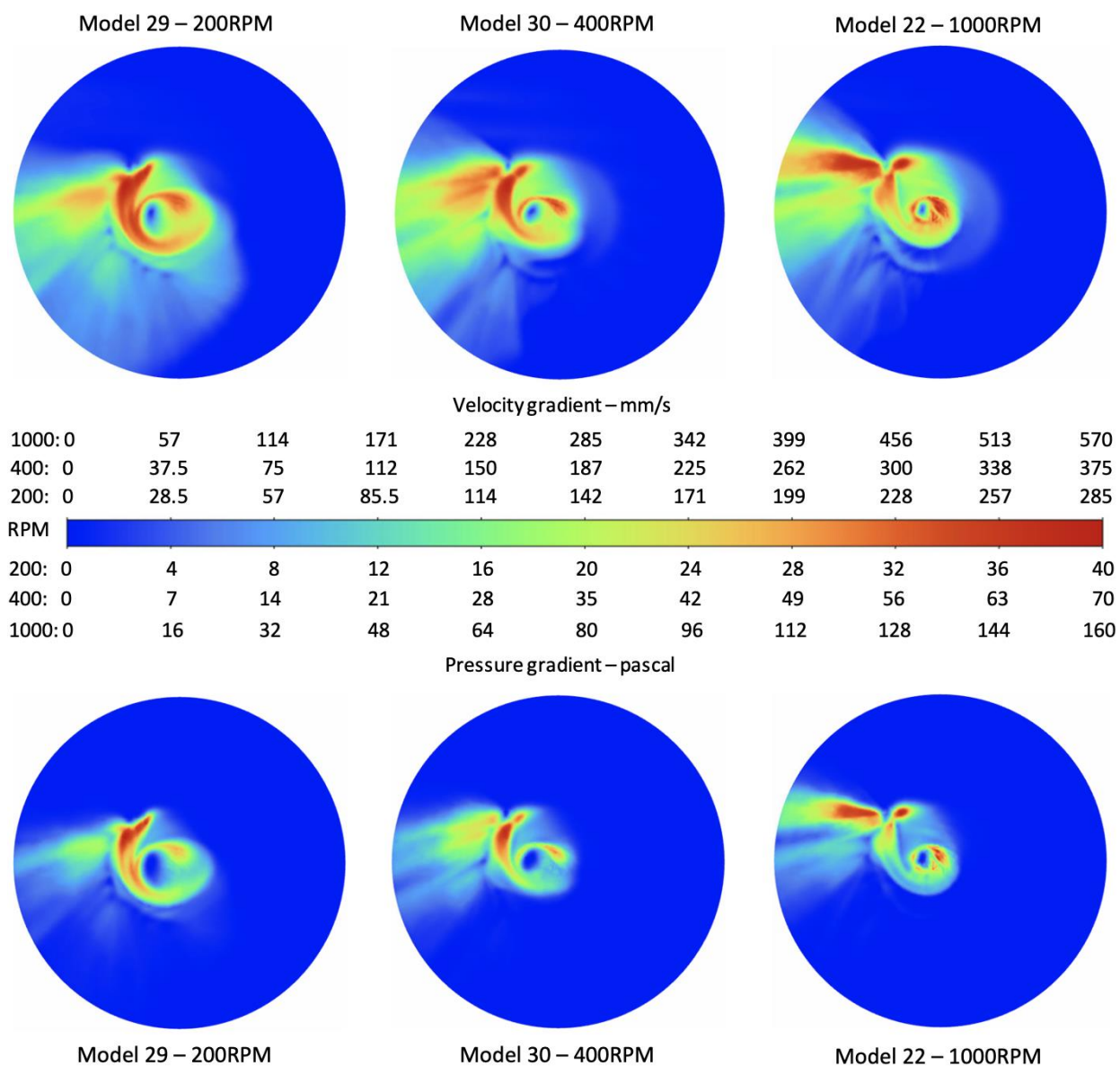
Figure 6-28 CFD simulation results for models 29, 30, and 22 (cornstarch to water ratio 0.25 – CSS-4).

Velocity gradient – mm/s										
1000: 0	195	390	585	780	975	1170	1365	1560	1755	1950
400: 0	100	200	300	400	500	600	700	800	900	1000
200: 0	60	120	180	240	300	360	420	480	540	600
RPM										
200: 0	20	40	60	80	100	120	140	160	180	200
400: 0	58	116	174	232	290	348	406	464	522	580
1000: 0	210	420	630	840	1050	1260	1470	1680	1890	2100
Pressure gradient – pascal										
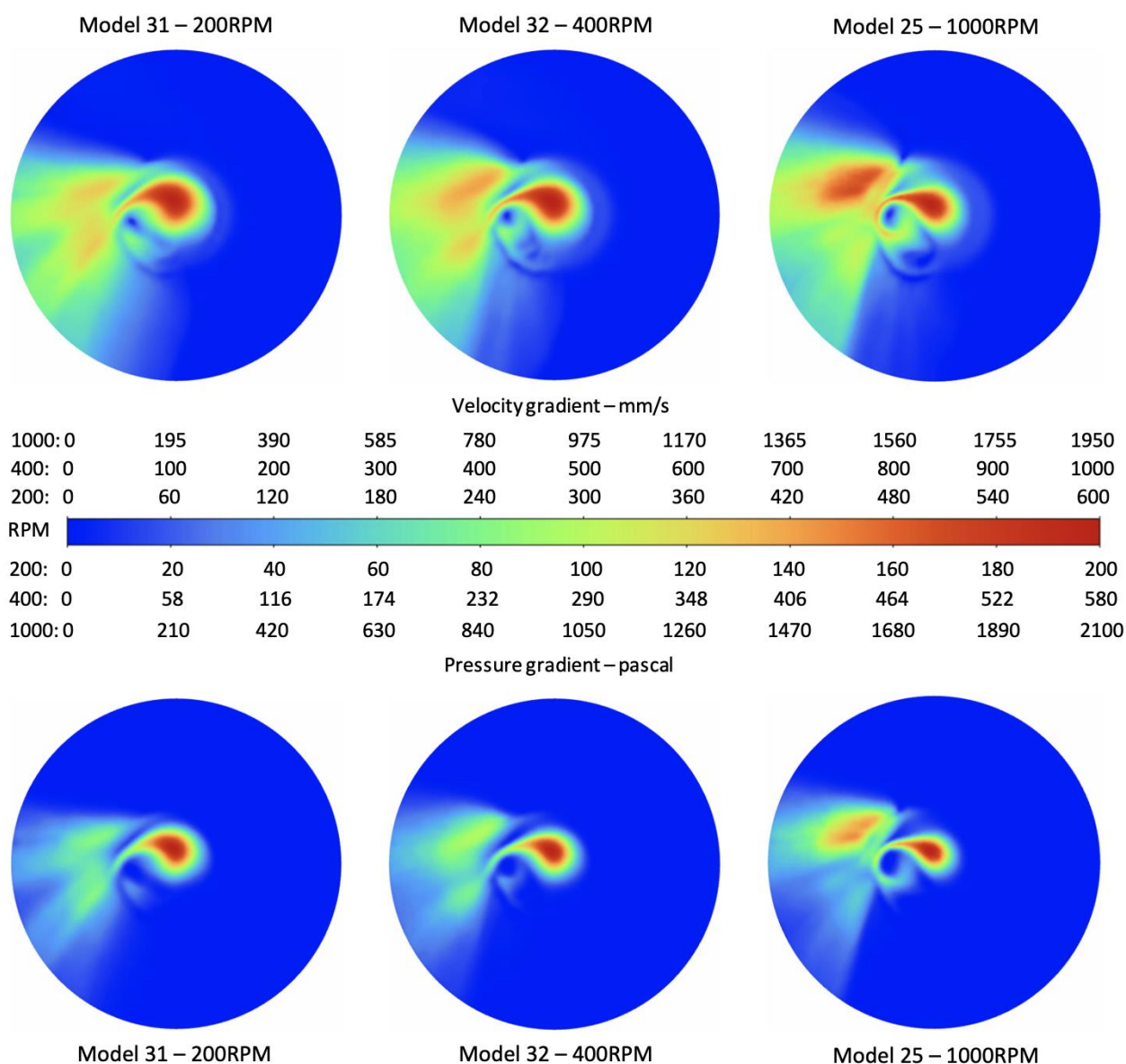
Figure 6-29 CFD simulation results for models 31, 32, and 25 (cornstarch to water ratio 0.5 – CSS-5).

6.8   Modelling Removal Rate Using the Preston Equation

The Preston equation (1-1) was first introduced in *section 1.1*. The equation described the relationship between velocity and pressure, and removal rate on the workpiece surface, with the addition of the Preston coefficient. This coefficient could be a function of a variety of factors such as temperature and material, and it could be empirically obtained through experiments and modelling. Many CNC technologies today are generating dwell-time maps for polishing complex surfaces by utilising the Preston equation. The calculation of the Preston coefficient then serves as a vital step in process optimisation.

CFD model 22 from *section 6.7.5* is representative of the preliminary experiments (test 37) reported in *section 6.3*. Both used a slurry composition of 0.25:1 cornstarch to water ratio, working distance of 1mm, precess angle of 15°, and bonnet rotation of 1000RPM. Model 22 predicted a maximum velocity and pressure

of 562.5 mm/s and 158.0 Pa respectively. Test 37 showed a volumetric removal rate of 0.126 mm³/min. The Preston coefficient could be calculated, shown by equation (6-3).

$$k = \frac{\Delta h(x,y)}{v(x,y) \cdot p(x,y)} = \frac{0.126mm^3/min}{562.5mm/s \cdot 158.0Pa} = 2.36 \times 10^{-8}mm^2/Pa$$

Using the calculated Preston coefficient, the volumetric removal rate predicted by the various models are summarised in Table 6-10. When compared with model 22, which was indicative of the physical experiment, models 24-26 saw the most increase in predicted removal rate. These three models utilised a higher concentration of cornstarch to water ratio, giving the slurry a higher viscosity. This suggests that the viscosity of the slurry is the highest contributing factor in process optimisation.

Table 6-10 Summary of CFD models and their predicted removal rates.

Model	Domain	Precess angle	Cornstarch: Water	WD (mm)	Headspeed (RPM)	Max. velocity (mm/s)	Max. pressure (Pa)	Removal rate (mm³/min)
14	r150	15°	0	1.0	1000	416	86	0.051
15	r75	15°	0	1.0	1000	407	85	0.049
16	s150	15°	0	1.0	1000	408	86	0.050
17	r75	0°	0	1.0	1000	420	90	0.053
18	r75	15°	0	1.0	1000	850	260	0.313
19	r75	90°	0	0.5	1000	789	311	0.348
20	r75	15°	0	1.5	1000	345	59	0.029
21	r75	15°	0.25	0.5	1000	1238	765	1.341
22	r75	15°	0.25	1.0	1000	563	158	0.126
23	r75	15°	0.25	1.5	1000	550	149	0.116
24	r75	15°	0.5	0.5	1000	2850	4619	18.63
25	r75	15°	0.5	1.0	1000	1922	2098	5.707
26	r75	15°	0.5	1.5	1000	1538	1343	2.923
27	r75	15°	0	1.0	200	125	8	0.001
28	r75	15°	0	1.0	400	210	25	0.007
29	r75	15°	0.25	1.0	200	285	40	0.016
30	r75	15°	0.25	1.0	400	375	70	0.037
31	r75	15°	0.5	1.0	200	600	200	0.170
32	r75	15°	0.5	1.0	400	1000	580	0.821

6.9   Conclusions on Rheological Bonnet Finishing

Rheological bonnet finishing (RBF) is a novel polishing technique. It uses a rapidly rotating bonnet tool at a set working distance (WD) above the workpiece surface to draw shear-thickening slurries through the gap to perform polishing. Due to its non-contact nature, the material removal rate of RBF was more than 10 times smaller than that of contact polishing. The ability of RBF to mitigate existing mid-spatial frequency errors should be tested, but experimental work was halted due to the onset of the COVID-19 pandemic. Efforts were then shifted towards software modelling.

CFD simulations were carried out using the academic version of Ansys. Two-dimensional modelling preceded three-dimensional modelling. Various models were simulated by varying shape, geometry, meshing, slurry viscosity, precess angle, WD, and headspeed. The simulations examined the resulting velocity and pressure gradients experienced by the workpiece surface, which are the two key factors for the Preston equation (1-1) that predicts material removal rate during CNC polishing. The models confirmed the pre-existing hypotheses that shear-thickening slurry would enhance the material removal capability. Higher tool headspeed and smaller WD also increased the velocity and pressure values on the workpiece surface.

Models of high cornstarch concentration could not be simulated successfully. Cornstarch to water ratio of up to 0.5 (CSS-5) were simulated. However, physical experiments of RBF used a cornstarch to water ratio of 1. The models showed promising abilities of material removal for the RBF, nevertheless.

The laboratory was reopened for regular work with the passing of the COVID-19 pandemic. The focus then transitioned away from software simulation and back to unfinished physical experiments (*sections 3.5* and *4.4*). The RBF process remains a large potential for exploration on both the experimental and CFD front. The next chapter summarises a few prospects for future work.

(Page left intentionally blank)

7   Conclusions and Future Work

This thesis reported on the material removal rate and MSF mitigation abilities of shear thickening slurries in conjunction with precessed bonnet polishing. Water-based cornstarch suspension (CSS) slurries were the main test subject in both physical experiments and CFD modelling.

Mid-spatial frequency (MSF) reduction experiments demonstrated that shear thickening CSS slurries with aluminium oxide abrasives enhanced the process efficiency. An increase in cornstarch concentration allowed the slurry to reach the achievable MSF reduction with less process time when compared to traditional Newtonian slurry. This has the potential to equip the precessed bonnet polishing process with ability to rectify existing MSF surface errors.

The novel rheological bonnet finishing (RBF) process was introduced, and it differed from traditional bonnet polishing in that the bonnet is suspended and rotated at a working distance above the workpiece surface. Preliminary tests showed volumetric removal rate of 0.126 ± 0.025 mm^3/min. This process eliminates the need for polishing pads on the tool surface, and it could result in a scratch-free surface. RBF provided the precessions technology another tool to improve area-targeted surface quality.

The rheological properties for CSS slurries were tested and modelled through CFD analysis. Subsequent models were constructed to examine the various mechanisms for the RBF technique, through altering process parameters. The models suggest the shear thickening slurries had a positive effect on the material removal rate. This confirmed the results obtained from the preliminary RBF experiments.

The above findings could facilitate a more streamlined manufacturing chain for precision optics for the versatile precessions technology from form correction and texture improvement, to MSF mitigation, without needing to rely on other polishing technologies. Such improvement on the existing bonnet polishing would advance the technology yet another step towards total autonomous manufacturing cells of the future.

The experimental and CFD results for non-Newtonian MSF mitigation and the RBF process showed promise. Nevertheless, both fronts leave a significant area for exploration. A few key areas are proposed for future analysis:

1. The food-grade cornstarch particles had a diameter of ~20µm, which is over 10 times that of the cerium oxide abrasives. Being 1000 times larger in volume, the addition of cornstarch was suspected to interfere with the abrasive, shielding the cerium oxide from the workpiece surface. Future experiments could be conducted by milling the cornstarch particles first, to produce a finer particle size.

2. Non-contact bonnet polishing had been proposed to provide a 'scratch-free' surface (Zhu & Beaucamp, 2020). The achievable texture for RBF should be tested, by optimising process

parameters, such as varying the tool headspeed and the working distance. This could be analysed using the Taguchi method.

3. The MSF mitigation ability of the RBF process should be both modelled and tested. Surface ripples could be modelled onto the CFD domain to analyse the velocity and pressure gradients on the workpiece surface.

4. Rheology could be conducted to examine the flow properties of CSS slurries with other abrasives, such as aluminium oxide. As well, further rheology experiments could be conducted to expand the tested shear rate range below $100s^{-1}$ and above $1000s^{-1}$. Referring to Figure 5-6, detailed experimental work could be done around $200s^{-1}$ shear rate, to utilise the shear-tchicking property at the viscosity maximum, and to decouple the effect of thickening from other parameters such as tool headspeed and took working distance.

List of Publications

1. Li, H., Walker, D., Yu, G., Dunn, C., Li, Y., Zhang, W., & Zheng, X. (2018). Advanced techniques for robotic polishing of aluminum mirrors. SPIE: Optical Fabrication, Testing, and Metrology VI, 10692. doi:10.1117/12.2311625
2. Li, H., Walker, D. D., Zheng, X., Su, X., Wu, L., Reynolds, C., Yu, G., Li, Y., & Zhang, P. (2019). Mid-spatial frequency removal on aluminum free-form Mirror. Optics Express, 27(18), 24885. https://doi.org/10.1364/oe.27.024885
3. Yu, G., Wu, L., Su, X., Li, Y., Wang, K., Li, H., & Walker, D. (2019). Rigid aspheric smoothing tool for mid-spatial frequency errors on aspheric or freeform optical surfaces. Journal of the European Optical Society-Rapid Publications, 15(1). https://doi.org/10.1186/s41476-019-0114-3

List of References

Acros Organics. (2017, January 27). *Poly(ethylene glycol), average M.W. 300*. Retrieved December 5, 2018, from Safety Data Sheet.

Allen, L. N., Keim, R. E., Lewis, T. S., & Ullom, J. R. (1992). Surface error correction of a Keck 10-m telescope primary mirror segment by ion figuring. *SPIE: Advanced Optical Manufacturing and Testing II,1531*. doi:10.1117/12.134862

Allen, L.N., Angel, R., Mangus, J. D., Rodney, G. A., Shannon, R. R., & Spoelhof, C. P. (1990). *The Hubble Space Telescope Optical Systems Failure Report*. *The Hubble Space Telescope Optical Systems Failure Report*. NASA - National Aeronautics and Space Administration.

Argyropoulos, C. D., & Markatos, N. C. (2015). Recent advances on the numerical modelling of turbulent flows. *Applied Mathematical Modelling*, *39*(2), 693–732. https://doi.org/10.1016/j.apm.2014.07.001

Arrasmith, S. R., Jacobs, S. D., Lambropoulos, J. C., Maltsev, A., & Golini, D. (2001). Use of magnetorheological finishing (MRF) to relieve residual stress and subsurface damage on lapped semiconductor silicon wafers. *SPIE: Optical Manufacturing and Testing IV, 4451*. doi:10.1117/12.453627

Atad-Ettedgui, E., Peacocke, T., Montgomery, D., Gostick, D., McGregor, H., Cliff, M., . . . Van Venrooji, B. (2006). Opto-Mechanical Design of SCUBA-2. *SPIE: Optomechanical Technologies for Astronomy,6273*. doi:10.1117/12.669231

Bach, H., & Neuroth, N. (1998). *Properties of optical glass* (2nd ed.). New York: Springer. doi:10.1007/978-3-642-57769-7

Barnes, H. A., Hutton, J. F., & Walters, K. (1993). *An Introduction to Rheology*. Amsterdam, Netherlands: Elsevier.

BBC. (1999, July 1). World's oldest telescope? *BBC News*.

Bedrock, C. (2008). *Optics or Photonics: What's in a Name*. Retrieved January 27, 2018, from http://optics.org/article/32348

Bingham, R. G., Walker, D. D., Kim, D., Brooks, D., & Freeman, R. (2000). Novel Automated Process for Aspheric Surfaces. *SPIE: Current Developments in Lens Design and Optical Systems Engineering, 4093*. doi:10.1117/12.405237

Blalock, T., Medicus, K., & Nelson, J. D. (2015). Fabrication of Freeform Optics. *SPIE: Optical Manufacturing and Testing XI, 9575*. doi:10.1117/12.2188523

Boersma, W. H., Laven, J., & Stein, H. N. (1990). Shear thickening (dilatancy) in concentrated dispersions. AIChE Journal, 36(3), 321–332. https://doi.org/10.1002/aic.690360302

Booij, S. M., van Brug, H., Braat, J. J. M., & Fähnle, O. W. (2002). Nanometer deep shaping with fluid jet polishing. *Optical Engineering, 41*(8), 1926-1931. 10.1117/1.1489677

Bouzid, D., Belkhie, N., & Aliouane, T. (2012). Optical glass surfaces polishing by cerium oxide particles. *IOP Conference Series: Materials Science and Engineering, 28*, 12007. doi:10.1088/1757-899X/28/1/012007

Brady, J. F., & Bossis, G. (1985). The rheology of concentrated suspensions of spheres in simple shear flow by numerical simulation. Journal of Fluid Mechanics, 155, 105. https://doi.org/10.1017/s0022112085001732

Branda, F., Silvestri, B., Luciani, G., & Costantini, A. (2007). The effect of mixing alkoxides on the Stöber particles size. *Colloids and Surfaces A: Physicochemical and Engineering Aspects*, *299*(1–3), 252–255. https://doi.org/10.1016/j.colsurfa.2006.11.048

Brikov, A., & Markin, A. (2015). Rheological Properties of Polyethylene Glycol Solutions and Gels. *Industrial Chemistry,01*(01). doi:10.4172/2469-9764.1000102

British Museum. (n.d.). *The Nimrud Lens / The Layard Lens*. Retrieved March 15, 2018, from https://www.britishmuseum.org/research/collection_online/collection_object_details.aspx?objectId=369215&partId=1

Browning, P. E. (1917). *Introduction to the Rare Elements* (4th ed.). New York: John Wiley & Sons.

Burge, J. H., & Kim, D. (2012). *U.S. Patent No. 20120040590 A1*. Washington, DC: U.S. Patent and Trademark Office.

Burlutskii, E. (2018). CFD study of oil-in-water two-phase flow in horizontal and vertical pipes. *Journal of Petroleum Science and Engineering*, *162*, 524–531. https://doi.org/10.1016/j.petrol.2017.10.035

Campbell, J. H., Hawley-Fedder, R. A., Stolz, C. J., Menapace, J. A., Borden, M. R., Whitman, P. K., . . . Hackel, R. P. (2004). NIF optical materials and fabrication technologies: An overview. *SPIE: Optical Engineering at the Lawrence Livermore National Laboratory II: The National Ignition Facility,5341*. doi:10.1117/12.538471

Chang, L., Friedrich, K., & Ye, L. (2013). *U.S. Patent No. WO2013016779 A1*. Washington, DC: U.S. Patent and Trademark Office.

Chauhan, V., Bhalla, N. A., & Danish, M. (2019). Numerical modelling of shear-thickening fluid in nanosilica dispersion. *Vibroengineering PROCEDIA*, *29*, 260–265. https://doi.org/10.21595/vp.2019.21123

Chen, M., & Vonmikecz, A. (2005). Formation of nucleoplasmic protein aggregates impairs nuclear function in response to SiO nanoparticles. *Experimental Cell Research*, *305*(1), 51–62. doi: 10.1016/j.yexcr.2004.12.021

Chen, M., Feng, Y., Wan, Y., Li, Y., & Fan, B. (2010). Neural network based surface shape modeling of stressed lap optical polishing. *Applied Optics, 49*(8), 1350-1354. doi:10.1364/AO.49.001350

Cheng, X., McCoy, J. H., Israelachvili, J. N., & Cohen, I. (2011). Imaging the microscopic structure of shear thinning and thickening colloidal suspensions. *Science*, *333*(6047), 1276–1279. https://doi.org/10.1126/science.1207032

Chhabra, R.P., & Richardson, J.F. (2008). *Non-Newtonian Flow and Applied Rheology: Engineering Applications* (2nd ed.). Oxford: Butterworth-Heinemann.

Cohen, E., & Hull, T. (2004). Selection of a mirror technology for the 1.8-m Terrestrial Planet Finder demonstrator mission. *SPIE: Optical Fabrication, Metrology, and Material Advancements for Telescopes, 5494*. doi:10.1117/12.552329

Cook, L. M. (1990). Chemical processes in glass polishing. *Journal of Non-Crystalline Solids, 120*(1), 152-171. doi:10.1016/0022-3093(90)90200-6

Cordero-Dávila, A., Cabrera-Peláez, V., Cuautle-Cortés, J., González-García, J., Robledo-Sánchez, C., & Bautista-Elivar, N. (2006). Experimental results and wear predictions with free-pinned petal tools. *SPIE: ICO20: Optical Design and Fabrication,6034*. doi:10.1117/12.668116

Cui, L., Dong, S., Zhang, J., & Liu, P. (2014). Starch granule size distribution and morphogenesis in maize (Zea mays L.) grains with different endosperm types. *Australian Journal of Crop Science,8*(11), 1560-1565.

DaVinci, L.., & Reti, L. (1974). *The madrid codices*. New York: McGraw-Hill.

de Vicente, J., Klingenberg, D. J., & Hidalgo-Alvarez, R. (2011). Magnetorheological Fluids: A review. *Soft Matter*, 7(8), 3701. doi:10.1039/c0sm01221a.

Degroote, J. E., Jacobs, S. D., Gregg, L. L., Marino, A. E., & Hayes, J. C. (2001). Quantitative characterization of optical polishing pitch. *SPIE: Optical Manufacturing and Testing IV*, *4451*. doi: 10.1117/12.453619

Discovery Channel Staff. (1999, June 29). The world's oldest telescope. *EXN Science Wire*.

Dowski, E. R., & Cathey, W. T. (1995). Extended depth of field through wave-front coding.*Applied Optics, 34*(11), 1859. doi:10.1364/AO.34.001859

Drueding, T. W., Fawcett, S. C., Wilson, S. R., & Bifano, T. G. (1995). Ion beam figuring of small optical components. *Optical Engineering, 34*(12), 3565-3571. doi:10.1117/12.215648

European Food Safety Authority. (2015). Scientific Opinion on the re-evaluation of sorbic acid (E 200), potassium sorbate (E 202) and calcium sorbate (E 203) as food additives. *EFSA Journal*, *13*(6).

Fähnle, O. W. (1998). *Shaping and finishing of aspherical optical surfaces* (PhD thesis). Proefschrift Technische Universiteit Delft.

Fähnle, O. W., van Brug, H., & Frankena, H. J. (1998). Fluid jet polishing of optical surfaces. *Applied Optics, 37*(28), 6771. 10.1364/AO.37.006771

Fang, F. Z., Zhang, X. D., Zhang, G. X., Weckenmann, A., & Evans, C. (2013). Manufacturing and measurement of freeform optics. *CIRP Annals - Manufacturing Technology, 62*(2), 823-846. doi:10.1016/j.cirp.2013.05.003

Feng, Z., Luo, Y., & Han, Y. (2010). Design of LED freeform optical system for road lighting with high luminance/illuminance ratio. *Optics Express, 18*(21), 22020-22031. doi:10.1364/OE.18.022020

Forbes, G. (2015). Never-ending struggles with mid-spatial frequencies. *SPIE: Optical Measurement Systems for Industrial Inspection IX,* 9525. doi:10.1117/12.2191135

Fournier, F., & Rolland, J. (2008). Design methodology for high brightness projectors. *Journal of Display Technology, 4*(1), 86-91. doi:10.1109/JDT.2007.907110

Fujiyoshi, T., Ikami, T., Kikukawa, K., Kobayashi, M., Takai, R., Kozaki, D., & Yamamoto, A. (2018). Direct quantitation of the preservatives benzoic and sorbic acid in processed foods using derivative spectrophotometry combined with micro dialysis. *Food Chemistry*, *240*, 386–390. doi: 10.1016/j.foodchem.2017.07.108

Gao, F., Leach, R. K., Petzing, J., & Coupland, J. M. (2008). Surface measurement errors using commercial scanning white light interferometers. *Measurement Science and Technology, 19*(1), 015303. doi:10.1088/0957-0233/19/1/015303

Garcia-Botella, A., Fernandez-Balbuena, A., & Bernabeu, E. (2006). Elliptical concentrators. *Applied Optics, 45*(29), 7622-7627.

General Engineering and Research. (2015, September 16). *Silica Nanoparticle Powder*. Retrieved December 5, 2018, from Safety Data Sheet.

Ghosh, G., Dalabehera, R. K., & Sidpara, A. (2018). Parametric study on influence function in magnetorheological finishing of single crystal silicon. *The International Journal of Advanced Manufacturing Technology*, *100*(5-8), 1043–1054. doi: 10.1007/s00170-018-2330-1

Gillman, B. E., & Tinker, F. (1999). Fun facts about pitch and the pitfalls of ignorance. *SPIE: Optical Manufacturing and Testing III*, *3782*. doi: 10.1117/12.369240

Glaswerk Schott & Genossen (1906). *Catelog: "Optisches Glas".* Jena.

Golini, D. (2004). A Brief History of QED Technologies. In C. Stroud (Ed.), *A jewel in the crown: Essays in honor of the 75th anniversary of the Institute of Optics* (pp. 313-318). Rochester, NY: Meliora Press.

Gong, X., Xu, Y., Zhu, W., Xuan, S., Jiang, W., & Jiang, W. (2014). Study of the knife stab and puncture-resistant performance for shear-thickening fluid enhanced fabric. *Journal of Composite Materials, 48(6)*, 641-657. doi:10.1177/0021998313476525

Gregory, G., Olson, C., & Fournier, F. (2014). Freeform optics. *Optical Engineering, 53*(3) doi:10.1117/1.OE.53.3.031301

Gürgen, S., & Sofuoğlu, M. A. (2020). Vibration attenuation of sandwich structures filled with shear thickening fluids. Composites Part B: Engineering, 186, 107831. https://doi.org/10.1016/j.compositesb.2020.107831

Hariharan, P. (2003). *Optical interferometry* (2nd ed.). Amsterdam; Boston; Academic Press.

Harris, D. C. (2011). History of magnetorheological finishing. *SPIE: Window and Dome Technologies and Materials XII, 8016*. doi:10.1117/12.882557

Hartmann, P. (2012). 110 years BK7: Optical glass type with long tradition and ongoing progress. *SPIE: Optical Systems Design 2012,8550*. doi:10.1117/12.981784

Harvey, J. E., & Thompson, A. K. (1995). Scattering effects from residual optical fabrication errors. *SPIE. 2576(1)* 155-174. 10.1117/12.215588

Hasman, E., Davidson, N., & Friesem, A. A. (1991). Holographic optical profilometer. *SPIE: 7th Mtg in Israel on Optical Engineering, 1442*. doi:10.1117/12.49077

Hed, P., & Edwards, D. (1987). optical-glass fabrication technology .2. relationship between surface-roughness and subsurface damage. *Applied Optics, 26*(21), 4677-4680. doi:10.1364/AO.26.004677

Hedrick, J. B., & Sinha, S. P. (1994). Cerium-based polishing compounds: Discovery to manufacture. *Journal of Alloys and Compounds, 207*, 377-382. doi:10.1016/0925-8388(94)90243-7

Henking, R., Ristau, D., Alvensleben, F. V., & Welling, H. (1995). Optical characteristics and damage thresholds of low loss mirrors. *SPIE: Laser-Induced Damage in Optical Materials: 1994*, *2428*. doi: 10.1117/12.213744

Henselmans, R. (2009). *Non-contact measurement machine for freeform optics* (PhD Thesis). Eindhoven University of Technology.

Hicks, R. (2008). Controlling a ray bundle with a free-form reflector. *Optics Letters, 33*(15), 1672-1674. doi:10.1364/OL.33.001672

Hird, J. R., & Field, J. E. (2004). Diamond polishing. *Proceedings of the Royal Society of London. Series A: Mathematical, Physical and Engineering Sciences*, *460*(2052), 3547–3568. https://doi.org/10.1098/rspa.2004.1339

Hoad, T. F. (2004a). Optic. *The Concise Oxford Dictionary of English Etymology*. Oxford: Oxford University Press. Retrieved March 14, 2018.

Hoad, T. F. (2004b). Photo-. *The Concise Oxford Dictionary of English Etymology*. Oxford: Oxford University Press. Retrieved March 14, 2018.

Hosseinimakarem, Z., Davies, A. D., & Evans, C. J. (2016). Zernike polynomials for mid-spatial frequency representation on optical surfaces. *SPIE: Reflection, Scattering, and Diffraction from Surfaces V*, 9961. doi:10.1117/12.2236520

Hossen, S., Sotome, I., Takenaka, M., Isobe, S., Nakajima, M., & Okadome, H. (2011). Effect of Particle Size of Different Crop Starches and Their Flours on Pasting Properties. *Japan Journal of Food Engineering,12*(1), 29-35.

Hu, H., Dai, Y., & Peng, X. (2010). Restraint of tool path ripple based on surface error distribution and process parameters in deterministic finishing. *Optics Express, 18*(22), 22973-22981. doi:10.1364/OE.18.022973

Huang, W., Tsai, T., Lin, Y., Kuo, C., Yu, Z., Ho, C., Hsu, W., & Young, H. (2020). Experimental investigation of mid-spatial frequency surface textures on fused silica after computer numerical control bonnet polishing. *The International Journal of Advanced Manufacturing Technology*, *108*(5-6), 1367–1380. https://doi.org/10.1007/s00170-020-05388-6

Hull, T., Riso, M., Barentine, J., & Magruder, A. (2012). Mid-spatial frequency matters: Examples of the control of the power spectral density and what that means to the performance of imaging systems. *SPIE: Infrared Technology and Applications XXXVIII*,8353. doi:10.1117/12.921097

Irgens, F. (2014). *Rheology and Non-Newtonian Fluids*. Cham: Springer International Publishing. doi:10.1007/978-3-319-01053-3.

Isaacs, J., Klumb, I., & McDaniel, C. (2009). Preliminary investigation of a polyethylene glycol hydrogel "nerve glue". *J Brachial Plex Peripher Nerve Inj, 4*(1), e98-e102. doi:10.1186/1749-7221-4-16

Jacobs, S., Golini, D., Hsu, Y., Puchebner, B., & Strafford, D. (1995). Magnetorheological finishing: A deterministic process for optics manufacturing. *SPIE: International Conference on Optical Fabrication and Testing, 2576*. doi:10.1117/12.215617

Janmey, P. A., & Schliwa, M. (2008). Rheology. *Current Biology*, 18(15), R639-R641. doi:10.1016/j.cub.2008.05.001.

Janoš, P., Ederer, J., Pilařová, V., Henych, J., Tolasz, J., Milde, D., & Opletal, T. (2016). Chemical mechanical glass polishing with cerium oxide: Effect of selected physico-chemical characteristics on polishing efficiency. *Wear, 362-363, 114-12*0. doi:10.1016/j.wear.2016.05.020

Javan, A., Bennett, W. R., & Herriott, D. R. (1961). Population inversion and continuous optical maser oscillation in a gas discharge containing a He-Ne mixture. *Physical Review Letters, 6*(3), 106-110. doi:10.1103/PhysRevLett.6.106

Jedamzik, R., Petzold, U., Dietrich, V., Wittmer, V., & Rexius, O. (2016). Large optical glass blanks for the ELT generation. *SPIE: Advances in Optical and Mechanical Technologies for Telescopes and Instrumentation II,9912*. doi:10.1117/12.2230647

Jenaer Glaswerk Schott & Genossen (1923). *Catelog: "Jenaer Glas für die Optik"*. Jena.

Jiang, X., Scott, P., & Whitehouse, D. (2007). Freeform surface characterisation - A fresh strategy. *CIRP Annals - Manufacturing Technology, 56*(1), 553-556. doi:10.1016/j.cirp.2007.05.132

Jin, N., & Liu, W. (2010). Thinning of PLZT ceramic wafers for sensor integration. *SPIE: Detectors and Imaging Devices: Infrared, Focal Plane, Single Photon, 7780*. doi:10.1117/12.858610

Jones, R. A. (1977). Optimization of computer-controlled polishing. *Applied Optics, 16*(1), 218. 10.1364/AO.16.000218

Jones, R. A. (1978). Fabrication using the computer-controlled polisher. *Applied Optics, 17*(12), 1889. 10.1364/AO.17.001889

Kaewamatawong, T., Shimada, A., Okajima, M., Inoue, H., Morita, T., Inoue, K., & Takano, H. (2006). Acute and Subacute Pulmonary Toxicity of Low Dose of Ultrafine Colloidal Silica Particles in Mice after Intratracheal Instillation. *Toxicologic Pathology*, *34*(7), 958–965. doi: 10.1080/01926230601094552

Kim, D. W., & Burge, J. H. (2010). Rigid conformal polishing tool using non-linear visco-elastic effect. *Optics Express*, *18*(3), 2242. doi: 10.1364/oe.18.002242

Kim, D. W., Martin, H. M., & Burge, J. H. (2013). Optical surfacing process optimization using parametric smoothing model for mid-to-high spatial frequency error control. *SPIE: Optifab 2013,8884*. doi:10.1117/12.2028816

Kim, D., & Kim, S. (2005). Static tool influence function for fabrication simulation of hexagonal mirror segments for extremely large telescopes. *Optics Express, 13*(3), 910-917. 10.1364/OPEX.13.000910

Kordonski, W. I., Golini, D., Dumas, P., Hogan, S. J., & Jacobs, S. D. (1998). Magnetorheological-suspension-based finishing technology. *SPIE: Smart Structures and Materials 1998: Industrial and Commercial Applications of Smart Structures Technologies,3326*. doi:10.1117/12.310670

Kordonski, W. I., Prokhorov, I. V., Gorodkin, S. R., Gorodkin, G. R., Gleb, L. K., & Kashevsky, B. E. (1995). *U.S. Patent No. US 5449313A*. Washington, DC: U.S. Patent and Trademark Office.

Kordonski, W.I., Shorey, A. B., & Sekeres, A. (2003). New magnetically assisted finishing method: Material removal with magnetorheological fluid jet. *SPIE: Optical Manufacturing and Testing V,5180*. doi:10.1117/12.506280

Kumar, S., & Singh, A. K. (2018). Magnetorheological nanofinishing of BK7 glass for lens manufacturing. *Materials and Manufacturing Processes, 33*(11), 1188-1196. doi:10.1080/10426914.2017.1364759

Lakshminarayanan, V., & Fleck, A. (2011). Zernike polynomials: A guide. Journal of Modern *Optics, 58(7)*, 545-561. doi:10.1080/09500340.2011.554896

Lawson, J. K., Wolfe, C. R., Manes, K. R., Trenholme, J. B., & Aikens, D. M. (1995). Specification of Optical Components using the power spectral density function. *SPIE: Optical Manufacturing and Testing, 2536*. doi:10.1117/12.218430

Layard, A. H. (1853). *Discoveries among the ruins of Nineveh and Babylon: with maps, plans and illustrations*. New York 10 Park Place: G.P. Putnam and Co.

Lee, Y., Seo, Y. J., Lee, H., & Jeong, H. (2016). Effect of diluted colloidal silica slurry mixed with ceria abrasives on CMP characteristic. *International Journal of Precision Engineering and Manufacturing-Green Technology*, *3*(1), 13–17. doi: 10.1007/s40684-016-0002-x

Lemaître, G. (1972). New Procedure for Making Schmidt Corrector Plates. *Applied Optics*, *11*(7), 1630. doi: 10.1364/ao.11.001630

Li, D., Wang, R., Liu, X., Fang, S., & Sun, Y. (2018a). Shear-thickening fluid using oxygen-plasma-modified multi-walled carbon nanotubes to improve the quasi-static stab resistance of Kevlar Fabrics. *Polymers*, *10*(12), 1356. https://doi.org/10.3390/polym10121356

Li, H. (2012). *Research on Manufacturing Mirror Segments for an Extremely Large Telescope* (PhD thesis). University College London.

Li, H. N., Yu, T. B., Zhu, L. D., & Wang, W. S. (2016). Evaluation of grinding-induced subsurface damage in optical glass BK7. *Journal of Materials Processing Tech, 229*, 785-794. doi:10.1016/j.jmatprotec.2015.11.003

Li, H., Walker, D., Yu, G., Dunn, C., Li, T., Zhang, W., & Zheng, X. (2018b). Advanced techniques for robotic polishing of aluminum mirrors. *SPIE: Optical Fabrication, Testing, and Metrology VI, 10692.* doi:10.1117/12.2311625

Li, H., Zhang, W., Walker, D., & Yu, G. (2014). Active edge control in the precessions polishing process for manufacturing large mirror segments. *SPIE: 7th International Symposium on Advanced Optical Manufacturing and Testing Technologies: Large Mirrors and Telescopes, 9280*. doi:10.1117/12.2069790

Li, M., Lyu, B., Yuan, J., Dong, C., & Dai, W. (2015). Shear-thickening polishing method. *International Journal of Machine Tools & Manufacture, 94*, 88-99. Retrieved October 1, 2018.

Liao, W., Dai, Y., Xie, X., & Zhou, L. (2014). Mathematical modeling and application of removal functions during deterministic ion beam figuring of optical surfaces. part 1: Mathematical modeling. *Applied Optics, 53(19), 4266-4274*. doi:10.1364/AO.53.004266

Lim, C. L., Adam, N. M., & Ahmad, K. A. (2018). Cryogenic pipe flow simulation for liquid nitrogen with vacuum insulated pipe (VIP) and Polyurethane (PU) foam insulation under steady-state conditions. *Thermal Science and Engineering Progress*, *7*, 302–310. https://doi.org/10.1016/j.tsep.2018.07.009

Lin, W., Huang, Y.W., Zhou, X.D., & Ma, Y. (2006). In vitro toxicity of silica nanoparticles in human lung cancer cells. *Toxicology and Applied Pharmacology*, *217*(3), 252–259. doi: 10.1016/j.taap.2006.10.004

Lu, B., Dong, C., Dai, W., Weng, H., & Yuan, J. (2014). *U.S. Patent No. CN104191320 A*. Washington, DC: U.S. Patent and Trademark Office.

Lu, B., Wu, J., Zhu, C., Fan, H., & Yuan, J. (2010). *U.S. Patent No. CN101844320 A*. Washington, DC: U.S. Patent and Trademark Office.

Lu, J., Luo, Q. F., Mao, X. Y., Xu, X. P., Wang, Y. H., & Guo, H. (2017). Fabrication of a resin-bonded ultra-fine diamond abrasive polishing tool by electrophoretic co-deposition for SIC processing. *Precision Engineering*, *47*, 353–361. https://doi.org/10.1016/j.precisioneng.2016.09.009

Lubliner, J., & Nelson, J. E. (1980). Stressed mirror polishing 1: A technique for producing nonaxisymmetric mirrors. *Applied Optics, 19*(14), 2332. doi:10.1364/AO.19.002332

Lvovich, V. (2011). *Electrochemical impedance spectroscopy (EIS) characterization of electrorheological fluids (ERF)*. Norwich, NY: Knovel.

Magyar, G., & Mandel, L. (1963). Interference fringes produced by superposition of two independent maser light beams. *Nature, 198*(4877), 255-256. doi:10.1038/198255a0

Maier, J., Smith, P., Stokes, D., Fairburn, C., Connor, R., Roberts, N., … Benzecry, O. (2017). Made Smarter Review. *Department for Business, Energy & Industrial Strategy*.

Mankarious, R. A., & Radwan, M. A. (2020). Shear-thickening Fluids Comparative Analysis Composed of Silica Nanoparticles in Polyethylene Glycol and Starch in Water. *Journal of Nanotechnology*, *2020*, 1–7. https://doi.org/10.1155/2020/8839185

Marinescu, I. D., Uhlmann, E., & Doi, T. K. (2007). *Handbook of lapping and polishing* (1st ed.). Boca Raton, FL: CRC Press.

Martin, H. M., Allen, R. G., Burge, J. H., Davis, J. M., Davison, W. B., Johns, M., . . . Zhou, P. (2014). Production of primary mirror segments for the Giant Magellan Telescope. *SPIE: Advances in Optical and Mechanical Technologies for Telescopes and Instrumentation,9151*. doi:10.1117/12.2057012

Martin, H. M., Allen, R. G., Cuerden, B., Hill, J. M., Ketelsen, D. A., Miller, S. M., . . . Warner, S. (2006). Manufacture of the second 8.4 m primary mirror for the Large Binocular Telescope. *SPIE: Optomechanical Technologies for Astronomy,6273*. doi:10.1117/12.672454

Martin, H. M., Anderson, D. S., Angel, J., Nagel, R. H., & West, S. C. (1990). Progress in the stressed-lap polishing of a 1.8m f/1 mirror. *SPIE: Advanced Technology Optical Telescopes IV,1236*. doi:10.1117/12.19235

Martin, H. M., Burge, J. H., Cuerden, B., Miller, S. M., Smith, B., & Zhao, C. (2004). Manufacture of 8.4-m off-axis segments: A 1/5-scale demonstration. *SPIE: Optical Fabrication, Metrology, and Material Advancements for Telescopes,5494*. doi:10.1117/12.552306

Mast, T. S., & Nelson, J. E. (1990). Fabrication of large optical surfaces using a combination of polishing and mirror bending. *SPIE: Advanced Technology Optical Telescopes IV,1236*. doi:10.1117/12.19234

Matthews, G., Ross, J., & Gemballa, J. (2017). Freeform optics manufacturing. *SPIE: Optifab, 10448*. doi:10.1117/12.2279808

McPherson, A., Spyromilio, J., Kissler-Patig, M., Ramsay, S., Brunetto, E., Dierickx, P., & Cassali, M. (2012). E-ELT update of project and effect of change to 39m design. *SPIE: Ground-based and Airborne Telescopes IV,8444*. doi:10.1117/12.927787

Meinel, A. B., Bashkin, S., & Loomis, D. A. (1965). Controlled figuring of optical surfaces by energetic ionic beams. *Applied Optics, 4*(12), 1674. doi:10.1364/AO.4.001674

Messelink, W. A. (2016). Aspheric mismatch of rigid tools. *SPIE: Third European Seminar on Precision Optics Manufacturing,10009*. doi:10.1117/12.2235536

Micro Abrasives. (2011, January 11). *Microgrit WCA/Aluminum Oxide-Alumina powder*. Retrieved October 23, 2018, from Micro Abrasives Corporation.

Mills, A., & Turvey, P. (1979). newton telescope - examination of the reflecting telescope attributed to newton,isaac in the possession of the royal-society. *Notes and Records of the Royal Society, 33*(2), 133-133.

Mohammadzadeh-Aghdash, H., Sohrabi, Y., Mohammadi, A., Shanehbandi, D., Dehghan, P., & Dolatabadi, J. E. N. (2018). Safety assessment of sodium acetate, sodium diacetate and potassium sorbate food additives. *Food Chemistry*, *257*, 211–215. doi: 10.1016/j.foodchem.2018.03.020

Monaghan, C. (2017, January 25). *Photonics Industry*. Retrieved March 10, 2017, from http://hansard.parliament.uk/commons/2017-01-25/debates/17012525000002/Photonicsindustry

Nanz, G., & Camilletti, L. E. (1995). Modeling of chemical-mechanical polishing: A review. *IEEE Transactions on Semiconductor Manufacturing, 8(4), 382-389.* doi:10.1109/66.475179

Nelson, J. E., Gabor, G., Hunt, L. K., Lubliner, J., & Mast, T. S. (1980). Stressed mirror polishing 2: Fabrication of an off-axis section of a paraboloid. *Applied Optics, 19*(14), 2341. doi:10.1364/AO.19.002341

Newton, I. (1687). Principia. *Imprimatur*.

Nguyen, D.-nam. (2020). Simulation and experimental study on polishing of spherical steel by non-Newtonian fluids. *The International Journal of Advanced Manufacturing Technology*, *107*(1-2), 763–773. https://doi.org/10.1007/s00170-020-05055-w

Ohl, R. G., Dow, T. A., Sohn, A., & Garrard, K. (2004). Highlights of the ASPE 2004 Winter Topical Meeting on Free-Form Optics: Design, Fabrication, Metrology, Assembly. *SPIE: Optical Fabrication, Metrology, and Material Advancements for Telescopes, 5494*. doi:10.1117/12.551469

Ostwald, W. (1929). Ueber die rechnerische darstellung des strukturgebietes der viskosität. *Colloid and Polymer Science, 47*(2), 176-187. https://doi.org/10.1007/BF01496959

Ott, W. R. (2001). 100 years of optical science and metrology at NIST. *SPIE: Harnessing Light: Optical Science and Metrology at NIST*, 4450. doi:10.1117/12.431243

Parks, R. (2008). Specifications: Figure and finish are not enough. *SPIE: An Optical Believe It or Not: Key Lessons Learned, 7071*. doi:10.1117/12.798223

Parks, R. E. (1983). Optical Specifications and Tolerances for Large Optics. *SPIE: Optical Specifications: Components and Systems, 0406*. doi:10.1117/12.935675

Peng, W., Guan, C., & Li, S. (2014). Material removal mechanism of ceria particles with different sizes in glass polishing. *Optical Engineering, 53*(3), 035104-035104. doi:10.1117/1.OE.53.3.035104

Photonics Leadership Group. (2015, June 01). *Future Growth Opportunity Roadmap*. Retrieved March 10, 2017, from https://photonicsuk.files.wordpress.com/2015/06/uk-photonics-future-growth1.pdf

Photonics21. (2018, September). *Market Research Study Photonics 2017* (Rep. No. 3). Retrieved October 31, 2018, from Photonics Public Private Partnership www.photonics21.org

Photonics21. (2021). *Market Data and Industry Report 2020*. Retrieved July 11, 2021, from European Technology Platform https://www.flipsnack.com/Photonics21/photonics-market-data-and-industry-report-2020.html

Phulé, P., & Ginder, J. (1998). The materials science of field-responsive fluids. *Mrs Bulletin, 23*(8), 19-21. 10.1557/S0883769400030761

Plummer, W. T. (1982). Unusual optics of the polaroid SX-70 land camera. *Applied Optics, 21*(2), 196. doi:10.1364/AO.21.000196

Pollicove, H. M. (2000). Next-generation optics manufacturing technologies. *SPIE: Advanced Optical Manufacturing and Testing Technology 2000,4231*. doi:10.1117/12.402758

Pollicove, H., & Golini, D. (2003). Deterministic manufacturing processes for precision optical surfaces. *Key Engineering Materials, 238-239*, 53-58. 10.4028/www.scientific.net/KEM.238-239.53

Preston, F. W. (1927). The theory and design of plate glass polishing machines. *J. Glass, 11*.

Progler, C., & Wong, A. (2000). Zernike coefficients: Are they really enough? *SPIE: Optical Microlithography XIII, 4000*. doi:10.1117/12.389042

QED Technologies. (n.d.). MRF Polishing. Retrieved November 16, 2018, from https://qedmrf.com/en/mrfpolishing/mrf-products

Reynolds, O. (1883). In An experimental investigation of the circumstances which determine whether the motion of water shall be direct or sinuous: and of the law of resistance in parallel channels (pp. 941–942). essay, Royal Society of London.

Rigden, J., & White, A. (1963). The interaction of visible and infrared maser transitions in the helium-neon system. *Proceedings of the IEEE, 51*(6), 943-945. doi:10.1109/proc.1963.2341

Roth. (2015, December 09). *Polyethylene glycol 400*. Retrieved from Safety Data Sheet.

Runnels, S., & Eyman, L. (1994). Tribology analysis of chemical-mechanical polishing. *Journal of the Electrochemical Society, 141*(6), 1699-1701.

Saleh, B. E. A., & Teich, M. C. (2007). *Fundamentals of photonics (2nd ed.)*. Hoboken, N.J: Wiley-Interscience

Saraiva, G., Maia, J., Lima, J., Nogueira, C., Freire, P., Sousa, F. D., … Filho, J. M. (2017). Pressure induced transformations in sorbic acid. *Spectrochimica Acta Part A: Molecular and Biomolecular Spectroscopy*, *184*, 327–334. doi: 10.1016/j.saa.2017.05.019

Saunders, I. J., Ploeg, L., Dorrepaal, M., & Venrooij, B. V. (2005). Fabrication and metrology of freeform aluminum mirrors for the SCUBA-2 instrument. *SPIE: Optical Manufacturing and Testing VI, 5869*. doi:10.1117/12.612998

Schaschke, C. (2014). Non-Newtonian Fluids. In *A Dictionary of Chemical Engineering*. Oxford University Press, USA. Retrieved March 23, 2017.

Schlichting, H., & Gersten, K. (2018). *Boundary-layer theory*. Springer Berlin. https://doi.org/10.1007/978-3-662-52919-5

Schneckenburger, M., Schiffner, M., & Börret, R. (2020). High precision glass polishing with ketchup. *SPIE: Seventh European Seminar on Precision Optics Manufacturing*, *11478*. https://doi.org/10.1117/12.2564867

Schuelke, T., & Grotjohn, T. A. (2013). Diamond polishing. *Diamond and Related Materials*, *32*, 17–26. https://doi.org/10.1016/j.diamond.2012.11.007

Schultz, G. (1987). Imaging performance of aspherics in comparison with spherical surfaces. *Applied Optics, 26*(23), 5118-5124. 10.1364/AO.26.005118

Shen, X. L., Wu, J. M., Chen, Y., & Zhao, G. (2010). Antimicrobial and physical properties of sweet potato starch films incorporated with potassium sorbate or chitosan. *Food Hydrocolloids, 24*(4), 285–290. doi: 10.1016/j.foodhyd.2009.10.003

Sigma-Aldrich. (2006, November 09). *Aldrich - 637238*. Retrieved December 5, 2018, from Safety Data Sheet.

Sigma-Aldrich. (2017, October 09). *Aldrich - P3265*. Retrieved December 5, 2018, from Safety Data Sheet.

Singh, M., Verma, S. K., Biswas, I., & Mehta, R. (2019). Rheology of fumed silica and polyethylene glycol shear-thickening suspension with nanoclay as an additive. Defence Science Journal, 69(4), 402–408. https://doi.org/10.14429/dsj.69.12420

Small, D. W., & Hoskins, S. J. (1986). An Automated Aspheric Polishing Machine. *SPIE: Optical Manufacturing, Testing and Aspheric Optics,0645*. doi:10.1117/12.964488

Solvay. (n.d.). Super Cerox™ 1663 High Performance Polishing Powder. *Cerox™ material data sheet*.

Sun, L., Jin, S., & Cen, S. (2009). Free-form microlens for illumination applications. *Applied Optics, 48*(29), 5520-5527. doi:10.1364/AO.48.005520

Sunanta, O., & Bidanda, B. (2003). Flat surface lapping: Process modeling in an intelligent environment. *IIE Annual Conference. Proceedings*, 1.

Sundararajan, S., Thakurta, D., Schwendeman, D., Murarka, S., & Gill, W. (1999). Two-dimensional wafer-scale chemical mechanical planarization models based on lubrication theory and mass transport. *Journal of the Electrochemical Society, 146*(2), 761-766.

Tabenkin, A. (1999). *Surface finish: A machinist's tool. A design necessity*. Cincinnati: Gardner Publications, Inc.

Taguchi, G. (1995). Quality engineering (Taguchi methods) for the development of electronic circuit technology. *IEEE Transactions on Reliability*, *44*(2), 225–229. https://doi.org/10.1109/24.387375

Taylor Hobson. (2002). *Form Talysurf Intra* (5th ed., Vol. 1). Leicester, England.

Téllez-Arriaga, L., Cordero-Dávila, A., Robledo-Sánchez, C. I., & Cuautle-Cortés, J. (2007). Correction of the Preston equation for low speeds. *Applied Optics,46*(9), 1408. doi:10.1364/ao.46.001408

Thalmann, R., & Dandliker, R. (1985). Holographic contouring using electronic phase measurement. *Optical Engineering, 24*(6), 246930-246930. doi:10.1117/12.7973605

ThermoFisher Scientific. (2017, March 24). *Carbowax PEG 400 (NF)*. Retrieved December 5, 2018, from Safety Data Sheet.

Thomas, K. (2018, February 26). Optics and photonics jobs: what it needs, what it takes. *SPIE Newsroom*. Retrieved from https://spie.org/news/optics-and-photonics-jobs-what-it-needs-what-it-takes?SSO=1

Thompson, M. K., & Thompson, J. M. (2017). *Chapter 6 - meshing*. (pp. 181-199). Elsevier Inc.

Tian, Y., Ang, Y., Zhong, Z., Xu, H., & Tan, R. (2013). Chemical mechanical polishing of glass disk substrates: Preliminary experimental investigation. *Materials and Manufacturing Processes, 28*(4), 488-494. doi:10.1080/10426914.2011.654161

Urone, P. P., Hinrichs, R., Dirks, K., & Sharma, M. (2018, January 25). 2.2: Spherical Mirrors. Retrieved October 17, 2018, from https://phys.libretexts.org/TextMaps/General_Physics_TextMaps/Map:_University_Physics_(OpenStax)/Map:_University_Physics_III_(OpenStax)/2:_Geometric_Optics_and_Image_Formation/2.2:_Spherical_Mirrors

Walker, D. D., & Dunn, C. R. (2008). Pseudo-Random Tool Paths for CNC Sub-Aperture Polishing and Other Applications. *Frontiers in Optics 2008/Laser Science XXIV/Plasmonics and Metamaterials/Optical Fabrication and Testing*. doi:10.1364/oft.2008.othb1

Walker, D. D., & Yu, G. (2016). Optimised Polishing Media – A new Approach. *University of Huddersfield*.

Walker, D. D., Atkins, C., Baker, I., Evans, R., & Hamidi, S. (2011). Technologies for Producing Segments for Extremely Large Telescopes. *SPIE: Optical Manufacturing and Testing IX,8126*. doi:10.1117/12.893360

Walker, D. D., Beaucamp, A. T. H., Doubrovski, V., Dunn, C., Freeman, R., McCavana, G., . . . Wei, X. (2005). New results extending the precessions process to smoothing ground aspheres and producing freeform parts. *SPIE: Optical Manufacturing and Testing VI, 5869*(1) 58690E-58690E-9. doi:10.1117/12.617067

Walker, D. D., Beaucamp, A. T., Brooks, D., Freeman, R., & King, A. (2002). Novel CNC polishing process for control of form and texture on aspheric surfaces. *SPIE: Current Developments in Lens Design and Optical Engineering III, 4767*. doi:10.1117/12.451322

Walker, D. D., Beaucamp, A. T., Doubrovski, V., Dunn, C., & Freeman, R. (2006). New developments in the precessions process for manufacturing free-form, large-optical, and precision-mechanical surfaces. *SPIE: 2nd International Symposium on Advanced Optical Manufacturing and Testing Technologies: Large Mirrors and Telescopes, 6148*. doi:10.1117/12.674039

Walker, D. D., Beaucamp, A., Evans, R., Fox-Leonard, T., Fairhurst, N., Gray, C., Hamidi, S., Li, H., Messelink, W., Mitchell, J., Rees, P., & Yu, G. (2012). Edge-control and surface-smoothness in sub-aperture polishing of mirror segments. *SPIE Proceedings*, *8450*. https://doi.org/10.1117/12.926183

Walker, D. D., Brooks, D., Freeman, R., King, A., Mccavana, G., Morton, R., Riley, D., Simms, J. (2001). First aspheric form and texture results from a production machine embodying the precession process. *SPIE: Optical Manufacturing and Testing IV, 441*. doi:10.1117/12.453652

Walker, D. D., Brooks, D., King, A., Freeman, R., Morton, R., McCavana, G., & Kim, S. (2003). The 'precessions' tooling for polishing and figuring flat, spherical and aspheric surfaces. *Optics Express, 11*(8), 958-964. 10.1364/OE.11.000958

Walker, D. D., Hsing-Yu, W., Yu, G., Li, H., Zhang, W., & Lu, C. (2017). Insight into aspheric misfit with hard tools: Mapping the island of low mid-spatial frequencies. *Applied Optics,56*(36), 9925. doi:10.1364/ao.56.009925

Walker, D. D., Yu, G., Li, H., Myer, B. W., Beaucamp, A. T., Namba, Y., & Wu, L. (2019). Title advances in optical fabrication for astronomy. *Monthly Notices of the Royal Astronomy Society*, *485*, 2071–2082. doi: 10.1093/mnras/sty3255

Wang, J., Hou, X., Wan, Y., Shi, C., & Zhong, X. (2016). Research on controlling middle spatial frequency error of high gradient precise aspheric by pitch tool. *SPIE: Nanoengineering: Fabrication, Properties, Optics, and Devices XIII,9927*. doi:10.1117/12.2236800

Wang, P., Ding, X., Li, Y., & Ang, U. (2012). Simultaneous Determination of Eleven Preservatives in Cosmetics by Micellar Electrokinetic Chromatography. *Journal of AOAC International*, *95*(4), 1069–1073. doi: 10.5740/jaoacint.11-043

Wang, Y. G., Zhang, L. C., & Biddut, A. (2011). Chemical effect on the material removal rate in the CMP of silicon wafers. *Wear, 270*(3), 312-316. doi:10.1016/j.wear.2010.11.006

Wang, Y., Su, P., Parks, R. E., Oh, C. J., & Burge, J. H. (2012). Swing arm optical coordinate-measuring machine: High precision measuring ground aspheric surfaces using a laser triangulation probe. *Optical Engineering, 51*(7), 073603-073603. doi:10.1117/1.OE.51.7.073603

Weckenmann, A., Estler, T., Peggs, G., & McMurtry, D. (2004). Probing systems in dimensional metrology. *CIRP Annals - Manufacturing Technology, 53*(2), 657-684. doi:10.1016/S0007-8506(07)60034-1

Wen, W., Zheng, D., & Tu, K. (1999). Chain/column Evolution and Corresponding Electrorheological Effect. *Journal of Applied Physics, 85*(1), 530-533. doi:10.1063/1.369485.

Wieloszyńska, A., & Strakowski, M. (2016). Optical Profilometer. *SPIE: Photonics Applications in Astronomy, Communications, Industry, and High-Energy Physics Experiments, 10031*. doi:10.1117/12.2248123

Wilson, S. R., & McNeil, J. R. (1987). Neutral Ion Beam Figuring of Large Optical Surfaces. *SPIE: Current Developments in Optical Engineering II,0818*. doi:10.1117/12.978903

Winston, R., Welford, W. T., Miñano, J. C., & Benítez, P. (2005). *Nonimaging optics* (1st ed.). Burlington, MA: Elsevier Academic Press.

Xu, Y., Chen, X., Wang, Y., & Yuan, Z. (2017). Stabbing resistance of body armour panels impregnated with shear-thickening fluid. *Composite Structures, 163*, 465-473. doi:10.1016/j.compstruct.2016.12.056

Xuzhou Jiechuang New Material Technology Co. (2019, February 25). *Diamond powder – CAS7782-40-3*. Retrieved October 5, 2022, from Hongwu International Group Ltd.

Yang, L., Pan, F., Xiao, W., & Cao, R. (2017). Surface quality inspection of laser gyro mirrors using digital holographic microscopy. *SPIE: International Conference on Optical and Photonics Engineering (IcOPEN 2016)*, *10250*. doi: 10.1117/12.2267106

Youngworth, R. N., & Stone, B. D. (2000). Simple estimates for the effects of mid-spatial-frequency surface errors on image quality. Applied Optics, 39(13), 2198. 10.1364/AO.39.002198

Youngworth, R. N., Gallagher, B. B., & Stamper, B. L. (2005). An overview of power spectral density (PSD) calculations. *SPIE: Optical Manufacturing and Testing VI, 5869*. doi:10.1117/12.618478

Yu, G., Wu, L., Su, X., Li, Y., Wang, K., Li, H., & Walker, D. (2019). Rigid aspheric smoothing tool for mid-spatial frequency errors on aspheric or freeform optical surfaces. *Journal of the European Optical Society-Rapid Publications*, *15*(1). https://doi.org/10.1186/s41476-019-0114-3

Yu, K., Cao, H., Qian, K., Sha, X., & Chen, Y. (2012). Shear-thickening behavior of modified silica nanoparticles in polyethylene glycol. *Journal of Nanoparticle Research, 14(3).* doi:10.1007/s11051-012-0747-2

Yu, M., Qiao, X., Dong, X., & Sun, K. (2018). Shear-thickening effect of the suspensions of silica nanoparticles in PEG with different particle size, concentration, and shear. *Colloid and Polymer Science*, *296*(7), 1119–1126. https://doi.org/10.1007/s00396-018-4325-8

Zeeko LTD. (n.d.). IRP 400. Retrieved November 16, 2018, from http://www.zeeko.co.uk/products.html

Zernike, F., & Stratton, F. J. M. (1934). Diffraction theory of the knife-edge test and its improved form, the phase-contrast method. *Monthly Notices of the Royal Astronomical Society, 94(5),* 377-384. doi:10.1093/mnras/94.5.377

Zhang, P., Li, J., Yu, G., & Walker, D. D. (2016). Development of swinging part profilometer for optics. *SPIE: Optics and Measurement International Conference 2016, 10151*. doi:10.1117/12.2256295

Zhang, W. W., Allgood, K. D., Biskach, M. P., Hlinka, M., Solly, P. M., Chan, K.-W., … Saha, T. T. (2018). Astronomical x-ray optics using mono-crystalline silicon: high resolution, light weight, and low cost. *SPIE: Space Telescopes and Instrumentation 2018: Ultraviolet to Gamma Ray*, *10699*. doi: 10.1117/12.2312879

Zhao, H., Li, X., Fan, B., & Zeng, Z. (2015). Deformation verification and surface improvement of active stressed lap for 4 m-class primary mirror fabrication. *Applied Optics, 54*(10), 2658-2664. doi:10.1364/AO.54.002658

Zheng, X. (2017). *Mid-spatial Frequency Control for Automated Functional Surface Processing* (PhD thesis). University of Huddersfield.

Zhu, W., & Beaucamp, A. (2020). Non-Newtonian fluid based contactless sub-aperture polishing. *CIRP Annals - Manufacturing Technology*, *69*(1), 293–296. https://doi.org/10.1016/j.cirp.2020.04.093

Appendix A

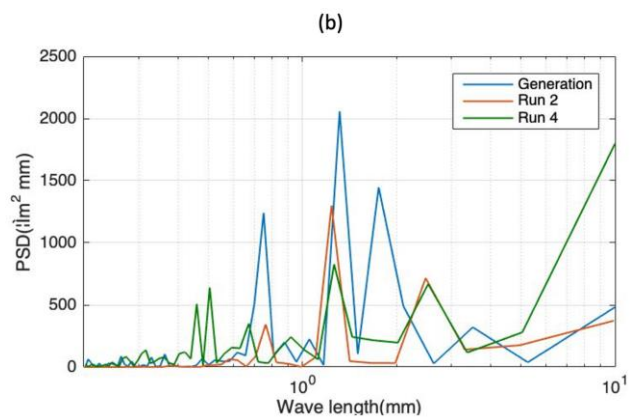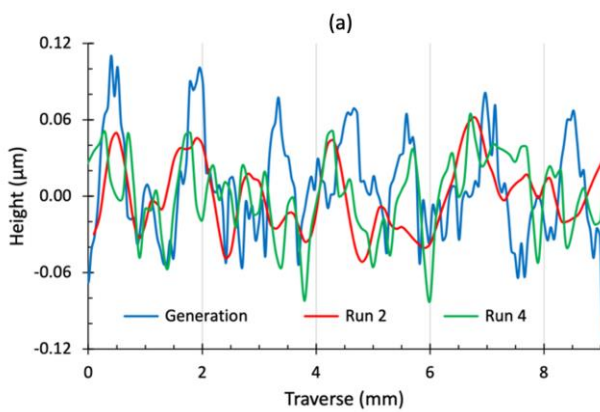*Figure A-1 Profile traces (a) and PSD plot (b) for test 24 zone A: cerium at 1.2mm.*
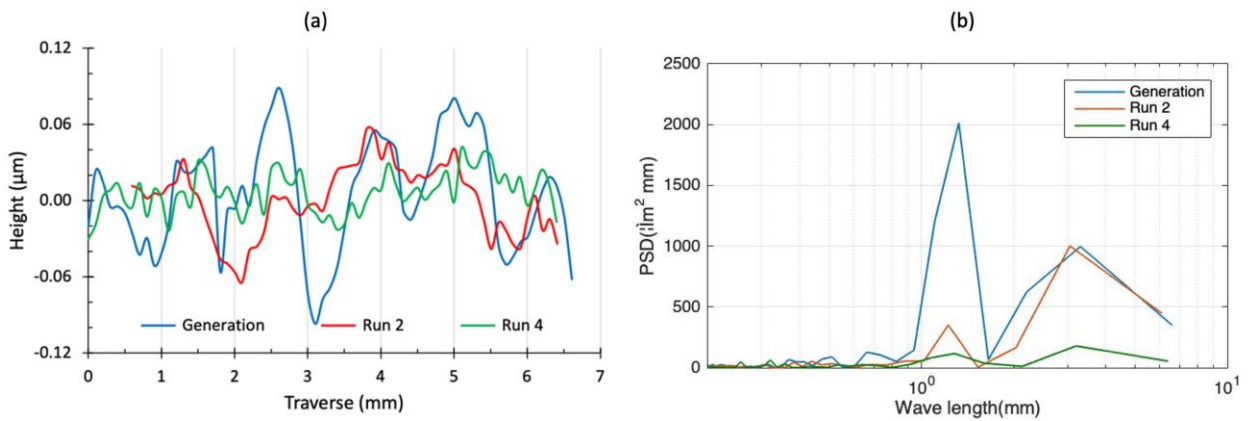
Figure A-2 Profile traces (a) and PSD plot (b) for test 25 zone A: cerium-cornstarch at 1.2mm.
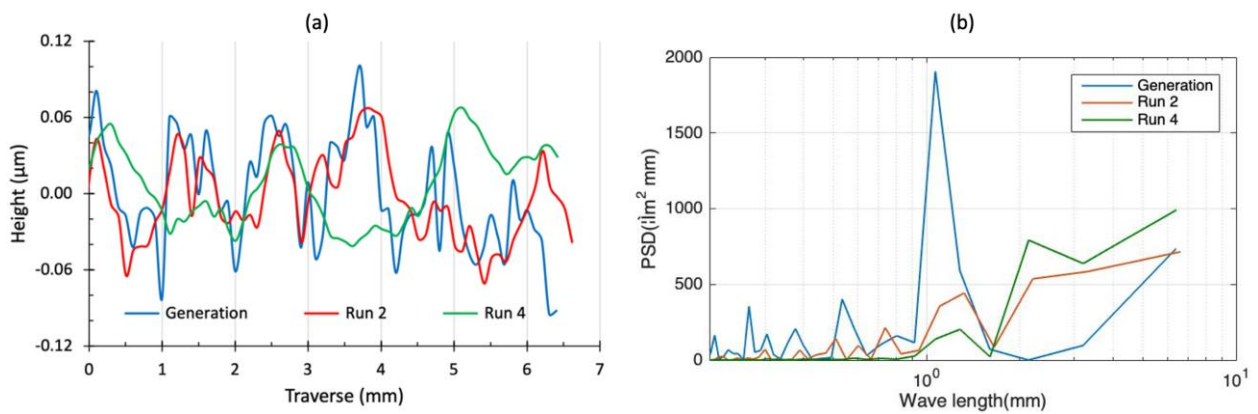
Figure A-3 Profile traces (a) and PSD plot (b) for test 26 zone A: cerium-cornstarch at 1.2mm.
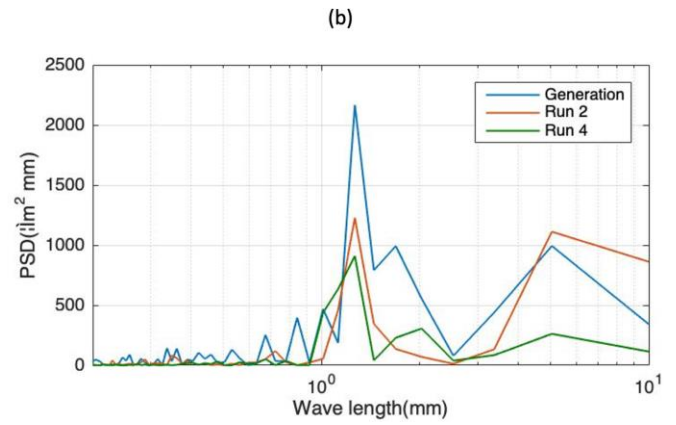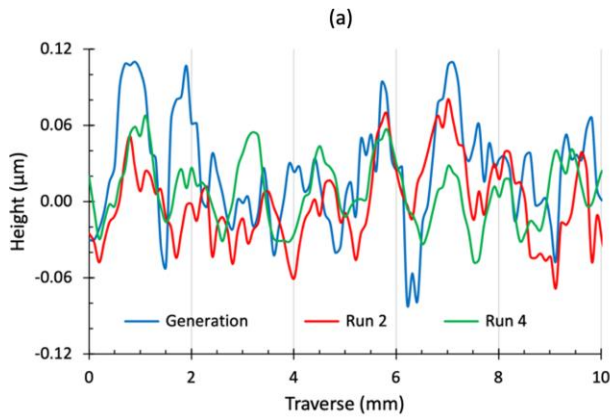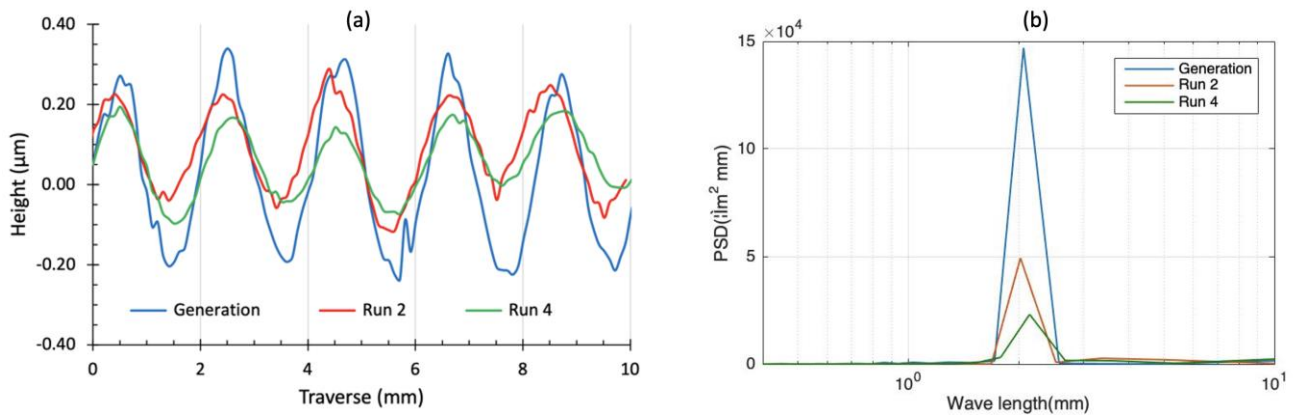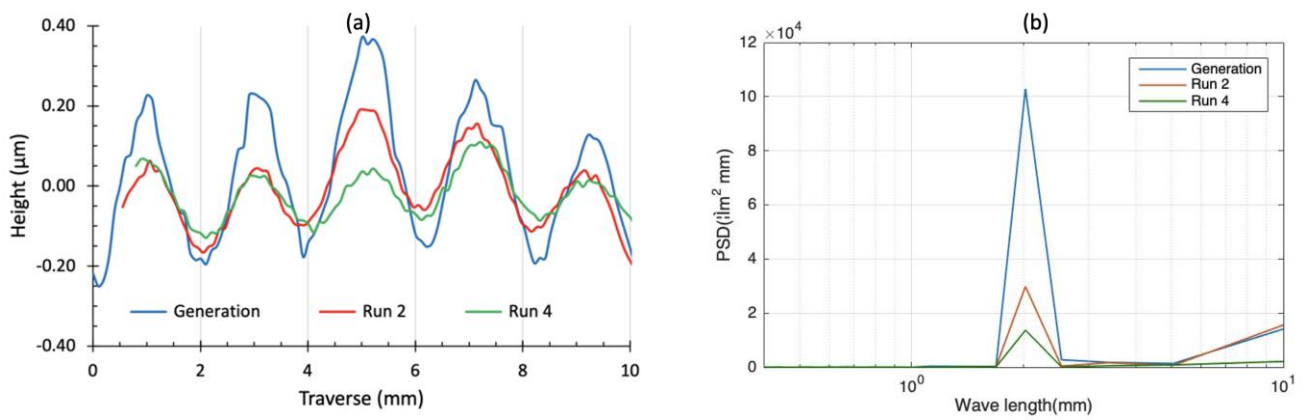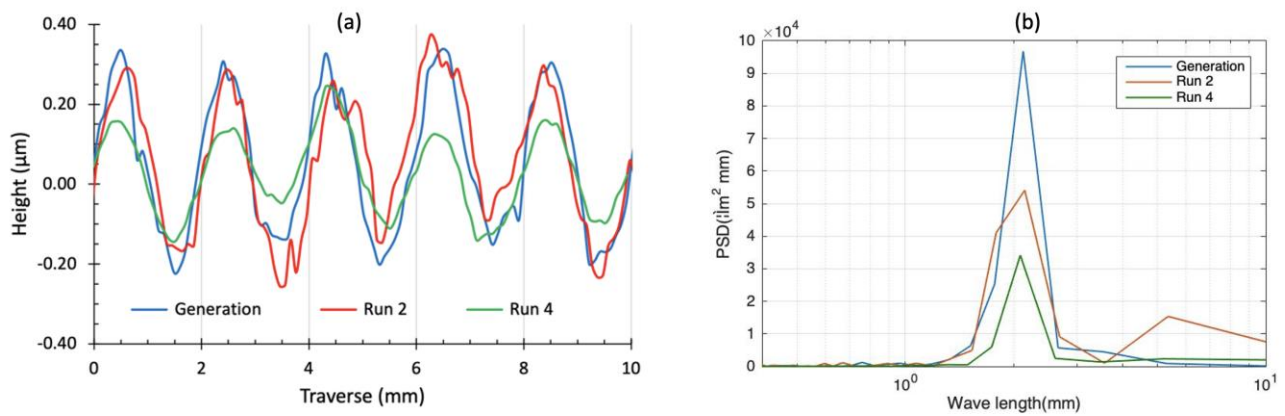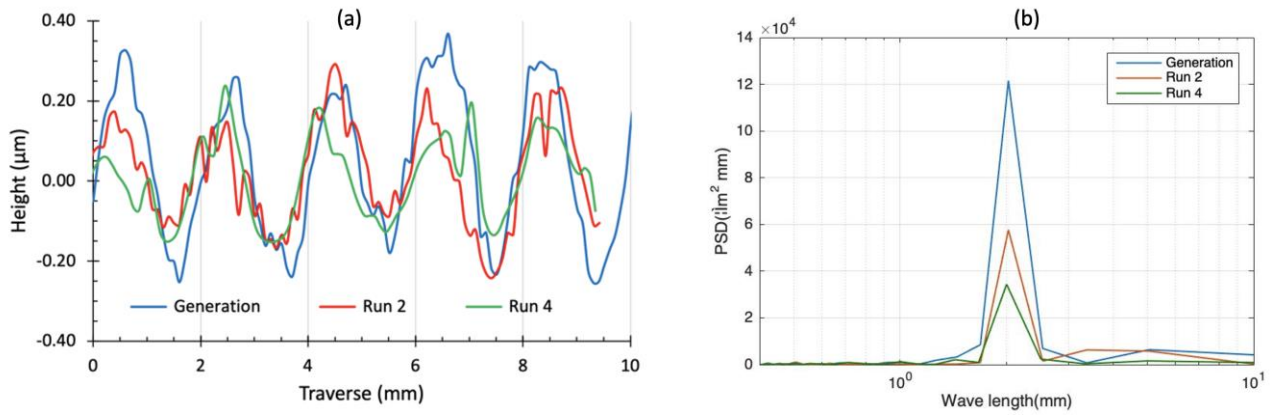
Figure A-4 Profile traces (a) and PSD plot (b) for test 27 zone A: cerium-cornstarch at 1.2mm.
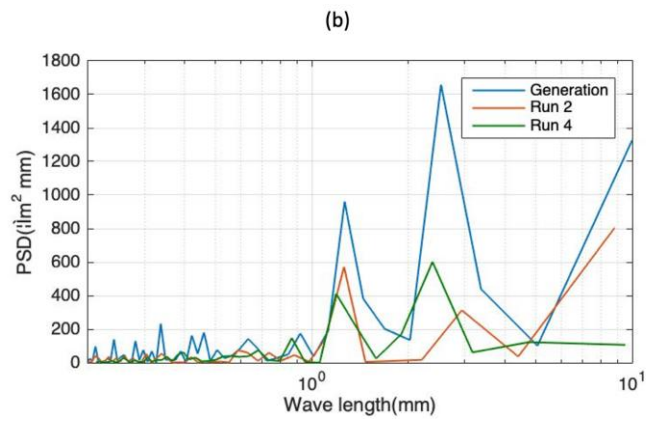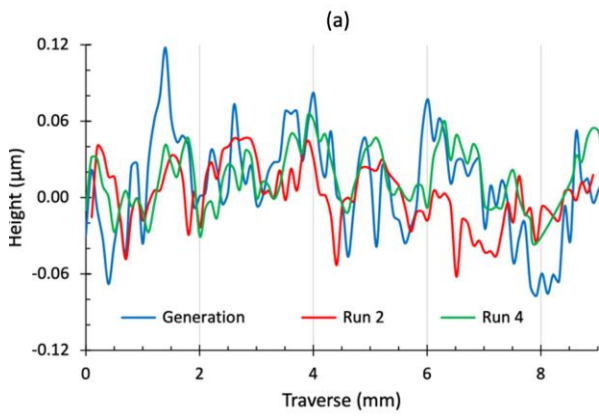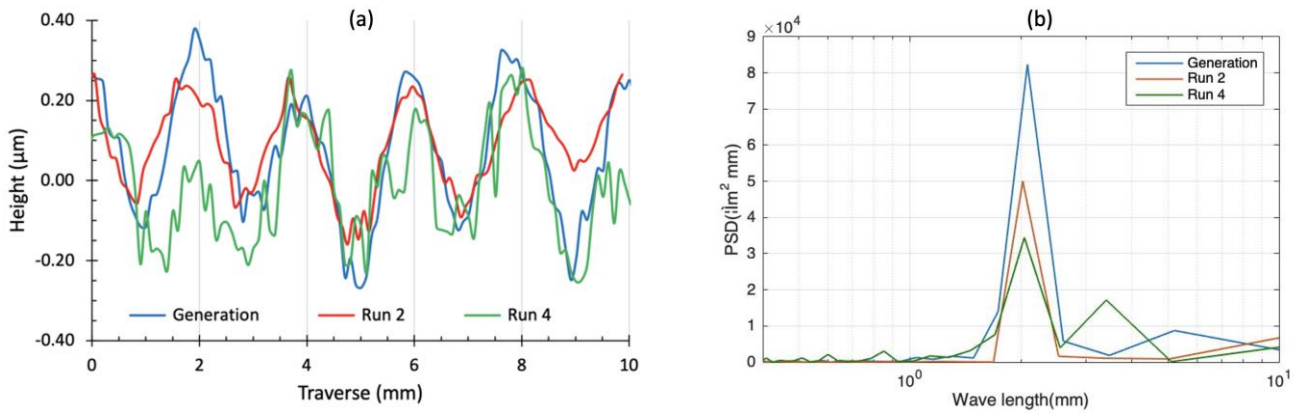

Figure A-5 Profile traces (a) and PSD plot (b) for test 28 zone A: cerium-cornstarch at 1.2mm.

Figure A-6 Profile traces (a) and PSD plot (b) for test 29 zone A: cerium-cornstarch at 1.2mm.

Figure A-7 Profile traces (a) and PSD plot (b) for test 24 zone B: ceria at 2mm.

Figure A-8 Profile traces (a) and PSD plot (b) for test 25 zone B: ceria-cornstarch at 2mm.

Figure A-9 Profile traces (a) and PSD plot (b) for test 26 zone B: ceria-cornstarch at 2mm.
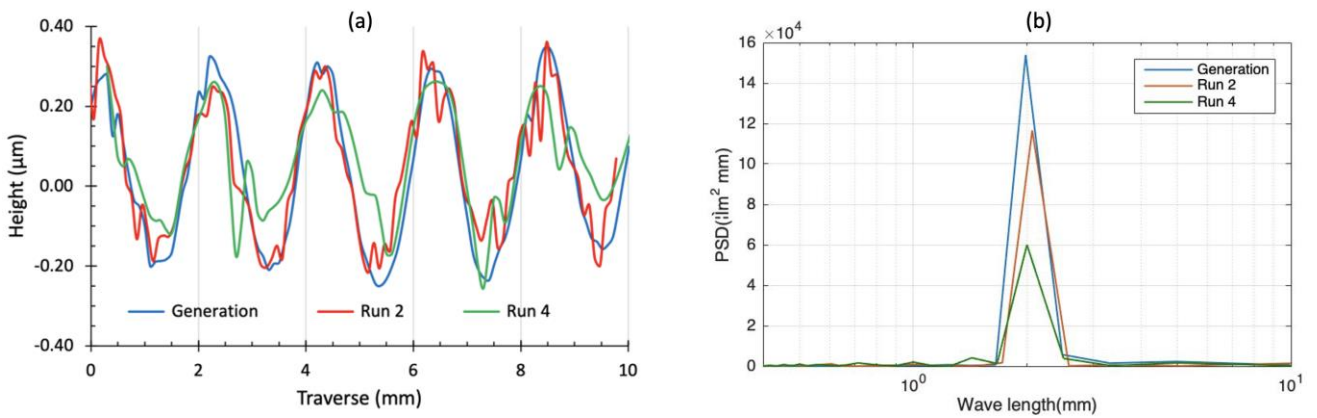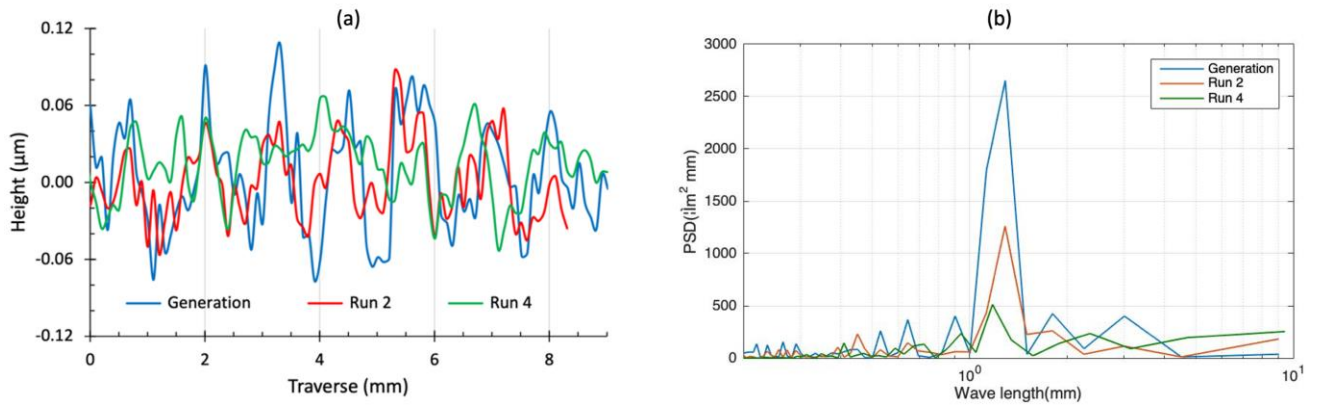
Figure A-10 Profile traces (a) and PSD plot (b) for test 27 zone B: ceria-cornstarch at 2mm.

Figure A-11 Profile traces (a) and PSD plot (b) for test 28 zone B: ceria-cornstarch at 2mm.

Figure A-12 Profile traces (a) and PSD plot (b) for test 29 zone B: ceria-cornstarch at 2mm.

Figure A-13 Profile traces (a) and PSD plot (b) for test 30 zone A: alumina at 1.2mm.
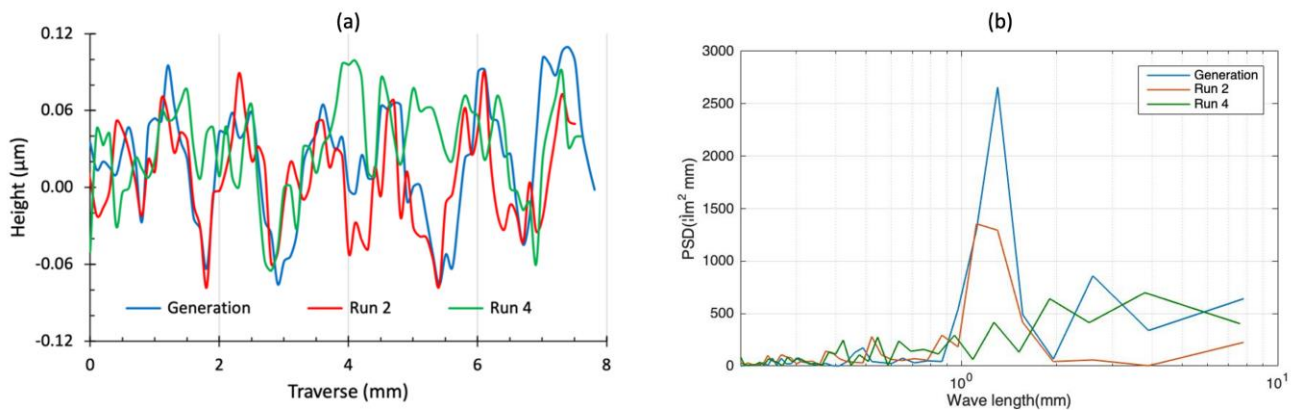

Figure A-14 Profile traces (a) and PSD plot (b) for test 31 zone A: alumina-cornstarch at 1.2mm.
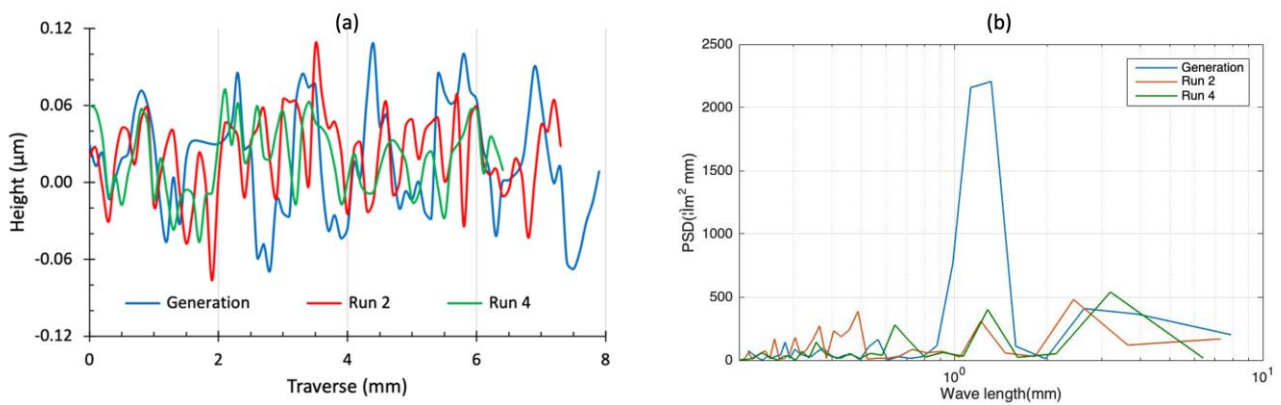

Figure A-15 Profile traces (a) and PSD plot (b) for test 32 zone A: alumina-cornstarch at 1.2mm.
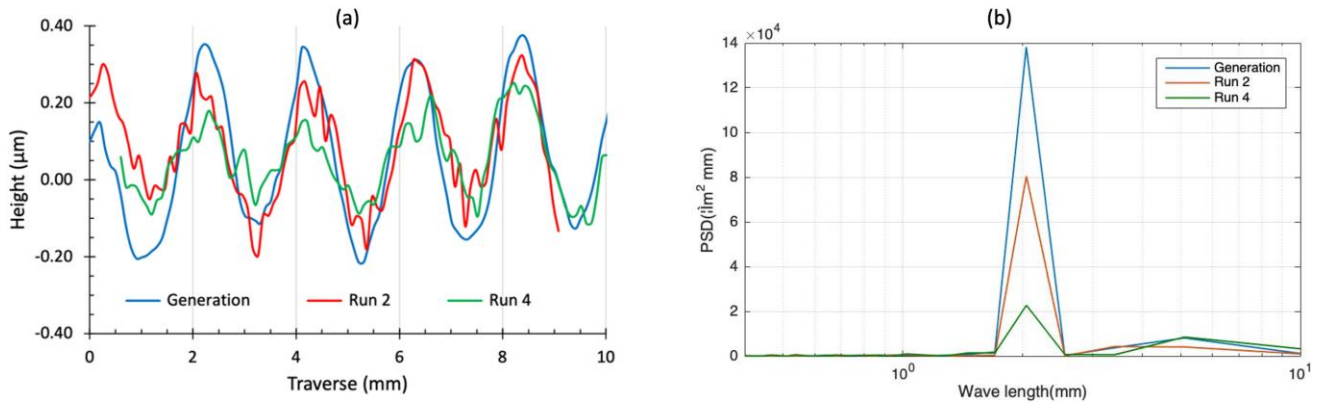
Figure A-16 Profile traces (a) and PSD plot (b) for test 30 zone B: alumina at 2mm.
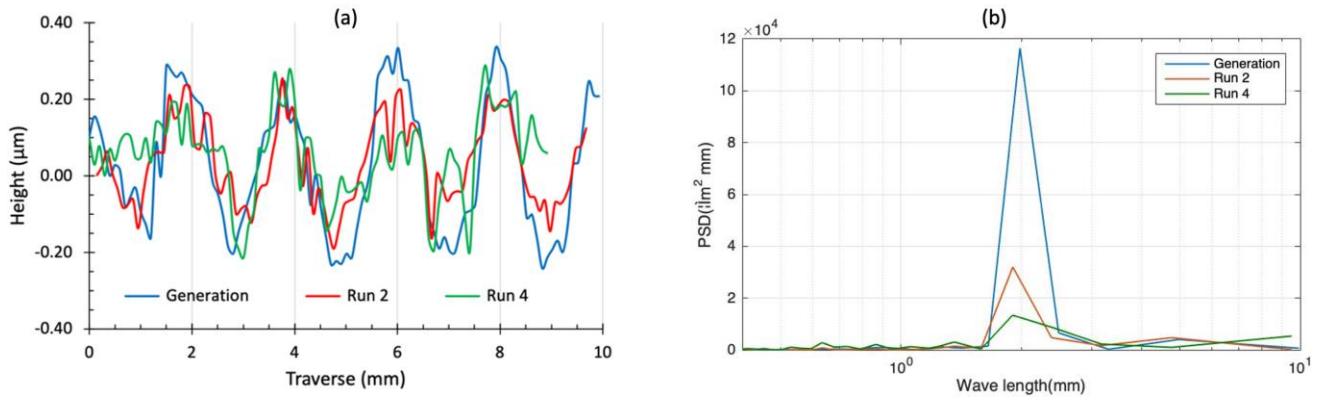

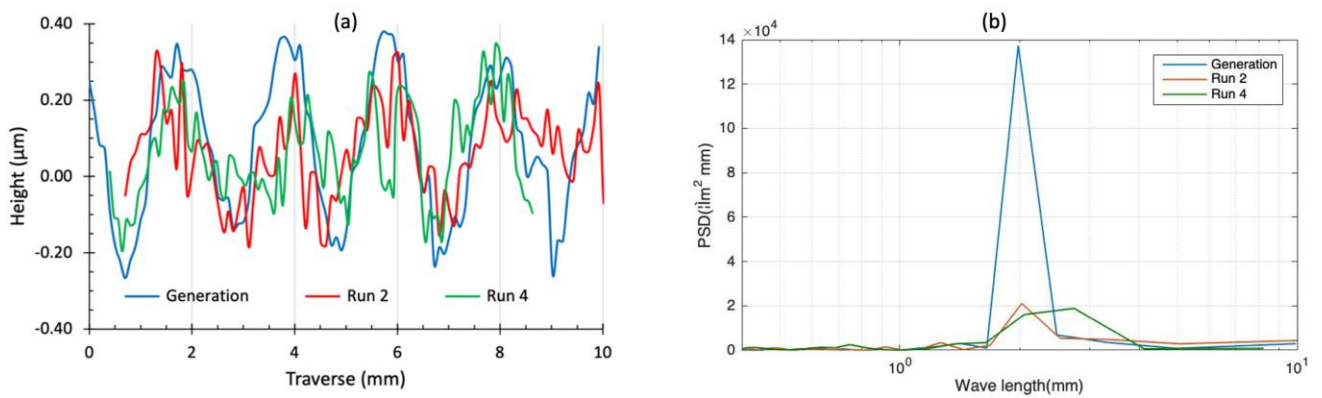*Figure A-17 Profile traces (a) and PSD plot (b) for test 31 zone B: alumina-cornstarch at 2mm.*

Figure A-18 Profile traces (a) and PSD plot (b) for test 32 zone B: alumina-cornstarch at 2mm.

Appendix B

Contents in Appendix B are referenced to in *chapter 6*. Referring to Figure 5-5, the Excel curve-fitting trendline function was used to generate the best fit equations for each of the samples.

```c
#include "udf.h"

DEFINE_PROPERTY(cellViscosity,c,t)
{
    double mu; /* This is the viscosity variable */
    double shRate = C_STRAIN_RATE_MAG(c,t);
    mu = (shRate * −0.000024295 + 1.0188) / 1000;
    return mu;
}
```

Figure B-1 User-defined function for sample CSS-2.

```c
#include "udf.h"

DEFINE_PROPERTY(cellViscosity,c,t)
{
    double mu; /* This is the viscosity variable */
    double shRate = C_STRAIN_RATE_MAG(c,t);
    if (shRate <= 220)
    {
        mu = (0.15343 * pow(shRate,0.46610)) / 1000;
    }
    else {mu = 8.84969 * pow(shRate,−0.28943) / 1000;}
    return mu;
}
```

Figure B-2 User-defined function for sample CSS-3.

```c
#include "udf.h"

DEFINE_PROPERTY(cellViscosity,c,t)
{
    double mu; /* This is the viscosity variable */
    double shRate = C_STRAIN_RATE_MAG(c,t);
    if (shRate <= 205)
    {
        mu = (0.011023 * shRate + 0.50978) / 1000;
    }
    else {mu = (16.8004 * pow(shRate,−0.3513)) / 1000;}
    return mu;
}
```

Figure B-3 User-defined function for sample CSS-4.

```
#include "udf.h"

DEFINE_PROPERTY(cellViscosity,c,t)
{
    double mu; /* This is the viscosity variable */
    double shRate = C_STRAIN_RATE_MAG(c,t);
    if (shRate <= 160)
    {
        mu = (shRate * 0.0254 + 2.0603) / 1000;
    }
    else {mu = (6.355 * exp(-0.00069925 * shRate)) / 1000;}
    return mu;
}
```

Figure B-4 User-defined function for sample CSS-5.

```
#include "udf.h"

DEFINE_PROPERTY(cellViscosity,c,t)
{
    double mu; /* This is the viscosity variable */
    double shRate = C_STRAIN_RATE_MAG(c,t);
    if (shRate <= 182)
    {
        mu = (shRate * 0.2937 - 14.378) / 1000;
    }
    else {mu = (-0.000011681 * pow(shRate,2) + 0.0069725 * shRate + 25.316) / 1000;}
    return mu;
}
```

Figure B-5 User-defined function for sample CSS-6.

```
#include "udf.h"

DEFINE_PROPERTY(cellViscosity,c,t)
{
    double mu; /* This is the viscosity variable */
    double shRate = C_STRAIN_RATE_MAG(c,t);
    if (shRate <= 400)
    {
        mu = (401.42 * exp(-0.00002244 * shRate)) / 1000;
    }
    else {mu = -0.2536 * shRate + 499.3 / 1000;}
    return mu;
}
```

Figure B-6 User-defined function for sample CSS-7.